N° d'ordre : 262 - 2014 Année 2014

THÈSE DE L'UNIVERSITÉ DE LYON

délivrée par

L'UNIVERSITÉ CLAUDE BERNARD LYON 1
Spécialité : Acoustique

L'UNIVERSITÀ DEGLI STUDI DI FIRENZE

ÉCOLE DOCTORALE : MÉCANIQUE, ÉNERGÉTIQUE, GÉNIE CIVIL, ACOUSTIQUE

DOTTORATO DI RICERCA : TECNOLOGIE ELETTRONICHE PER L'INGEGNERIA DELL'INFORMAZIONE

DIPLOME DE DOCTORAT
(arrêté du 7 aout 2006)

soutenue publiquement le 21 Novembre 2014

par

**Matthieu TOULEMONDE**

# New beamforming strategy for improved ultrasound imaging: application to biological tissues nonlinear imaging

Jury

| | | |
|---|---|---|
| Olivier BASSET | Professeur des Universités, Lyon 1 | Co-directeur de thèse |
| Christian CACHARD | Professeur des Universités, Lyon 1 | Co-directeur de thèse |
| Piero TORTOLI | Professore Ordinario, Firenze | Co-directeur de thèse |
| Denis KOUAME | Professeur des Universités, Toulouse | Rapporteur |
| Filippo MOLINARI | Professore, Torino | Rapporteur |
| Enrico BONI | Researcher, Firenze | Examinateur |
| Olivier MICHEL | Professeur des Universités, Grenoble | Examinateur |
| Massimo MISCHI | Associate Professor, Eindhoven | Examinateur |

# Abstract

Nowadays, ultrasound imaging is a common diagnostic tool thanks to its non-invasive behavior and relatively cheap equipment. Classic medical echographic imaging is based on the linear response of the biological tissue. However harmonic imaging, based on the harmonic frequencies generated by the nonlinear properties of the tissue, is more and more used for clinical application. The quantification of nonlinearity is based on the evaluation of the nonlinearity parameter which strongly influences the harmonics generation. The nonlinearity parameter estimation using an echographic approach would bring new modalities for imaging and diagnosis. However the echographic method for nonlinearity estimation is limited by two factors: the presence of speckles in the image and the focalization used during transmission, which concentrates the energy at one particular depth.

The objectives of this thesis work are developing novel approaches to reduce the speckle noise using original smoothing techniques and improving the nonlinearity parameter estimation in echo mode using new transmission-reception strategies.

Firstly, new speckle noise reduction approaches were investigated. The Thomson's multitaper approach was proposed, consisting in using several different orthogonal apodizations during beamforming. This method was combined to a coherent plane-wave compounding transmission-reception strategy improving the spatial resolution and the contrast while improving the frame rate.

In a second time, the nonlinearity parameter was estimated using a comparative method. The second-harmonic pressure field of a reference area was compared to the pressure field of an area where the nonlinearity parameter is unknown. However in echo-mode, the pressure field of the medium is unknown. It is assumed in this thesis work that the local pressure can be derived from envelope image local amplitude if the speckle noise is smoothed. The nonlinearity parameter estimation has been improved using plane-wave transmission and orthogonal apodizations compared to the use of a single focalization transmission.

# Résumé

L'échographie est aujourd'hui une technique d'imagerie de diagnostic répandue. Si l'imagerie dite 'classique' basée sur la réponse linéaire des tissus est couramment utilisée, l'imagerie harmonique, basée sur la réponse non linéaire des tissus, est maintenant aussi utilisée en routine clinique. L'estimation du paramètre de non linéarité d'un milieu par une technique ultrasonore amène de nouvelles perspectives en termes d'imagerie et de diagnostic. Cependant, la méthode de mesure du paramètre de non linéarité est limitée par deux facteurs, la présence du speckle et la concentration de l'énergie à une profondeur donnée (la zone focale).

Cette thèse a pour objectifs de répondre aux deux limitations mentionnées précédemment en proposant de nouvelles méthodes de lissage de l'image pour réduire le speckle et d'améliorer l'estimation du paramètre de non linéarité en mode écho par de nouvelles méthodes d'émission.

Dans un premier temps, il a été proposé d'utiliser une méthode de filtrage spatiale basée sur des filtres orthogonaux (filtres de Thomson) lors de la formation de voie en réception pour lisser le speckle. Ce filtrage spatiale intervient après la transmission d'ondes planes sous différents angles pour améliorer la résolution spatiale et le contraste tout en accélérant la cadence d'imagerie.

Dans un deuxième temps, l'estimation du paramètre de non linéarité est faite avec une méthode comparative. Le champ de pression du second harmonique d'une zone de référence est comparé avec le champ de pression d'une zone dont le paramètre de non linéarité est inconnu. Cependant, dans le cas des images échographiques, le champ de pression du second harmonique n'est pas accessible. Nous faisons l'hypothèse que la pression acoustique locale est liée à l'intensité de l'image échographique si le speckle est réduit et lissé. La transmission d'ondes planes et l'application de filtres orthogonaux permet de mieux délimiter le paramètre de non linéarité par rapport à une transmission focalisée.

# Sommario

Oggigiorno, le tecniche di imaging ad ultrasuoni sono un comune strumento di diagnosi, grazie alla loro non invasività e alla relativa economicità dei sistemi. La risposta lineare dei tessuti biologici è la base per le tecniche di imaging ecografico tradizionali. La generazione di frequenze ad armoniche superiori da parte dei tessuti può essere sfruttata per sviluppare tecniche di imaging innovative (i.e., imaging armonico), che sono sempre più utilizzate per applicazioni cliniche. Tali tecniche sono basate sul metodo di valutazione del parametro di non linearità che influenza fortemente la generazione delle armoniche all'interno dei tessuti. I metodi per la stima dei suddetti parametri sfruttano solitamente un approccio ecografico tradizionale. Di conseguenza, gli effetti legati alla focalizzazione impiegata durante la trasmissione, che concentra l'energia ad una particolare profondità, e la presenza di *speckle* nell'immagine finale, rendono più incerta la stima del parametro di non linearità.

In questa tesi sono proposti metodi innovativi finalizzati a due scopi: ridurre, nelle immagini, il rumore dovuto a *speckle*, tramite l'adozione di nuove tecniche di *smoothing*; migliorare la stima dei parametri di non linearità, tramite l'impiego di nuove strategie di beamforming in trasmissione e ricezione.

Per ridurre il rumore dovuto a *speckle*, è stato proposto un approccio di filtraggio spaziale basato sull'impiego dei filtri di Thomson. Tale tecnica consiste nell'impiego di numerose apodizzazioni ortogonali fra di loro in fase di beamforming. Il metodo è stato in particolare combinato con la tecnica di imaging *coherent plane-wave compounding*, con lo scopo di migliorare la risoluzione spaziale e il contrasto e, al contempo, incrementare il frame rate.

Il parametro di non linearità è stato misurato tramite un approccio comparativo. Il campo di pressione della seconda armonica in un'area di riferimento dell'immagine è stato confrontato con quello di un'area in cui il parametro di non linearità è ignoto. In questa tesi, grazie alla riduzione del rumore *speckle*, è stato possibile assumere che il campo di pressione fosse derivabile direttamente dell'ampiezza locale delle immagini demodulate. Grazie all'utilizzo di onde piane in trasmissione e di apodizzazioni ortogonali nel beamforming, la stima del parametro di non linearità è stata migliorata rispetto al caso in cui vengano utilizzate trasmissioni focalizzate.

# Résumé étendu

L'échographie est aujourd'hui une technique d'imagerie de diagnostic répandue de par son caractère non invasif, son innocuité, sa simplicité d'utilisation, la visualisation en temps réel de la zone concernée et par son coût relativement faible. L'image échographique obtenue a une texture granuleuse, nommée speckle. Selon les applications, le speckle peut être considérée comme une information importante ou bien un artéfact réduisant la qualité d'image.

Si l'imagerie dite 'classique' basée sur la réponse linéaire des tissus est couramment utilisée, l'imagerie harmonique, basée sur la réponse non linéaire des tissus, est maintenant aussi utilisée en routine clinique. Afin de quantifier le comportement non-linéaire des tissus, différentes techniques d'imagerie harmonique sont implantées sur les échographes et utilisées en routine clinique. Chaque tissu peut être caractérisé par la vitesse de propagation dans le tissu, sa densité et son paramètre de non-linéarité *B/A*. Il a été montré que différents tissus (sains ou pathologiques) peuvent avoir des comportements non-linéaires différents et donc un *B/A* différent. L'estimation de *B/A* en échographie pourrait être une nouvelle modalité pour différencier les tissus sains ou pathologiques.

Cette thèse a pour objectif d'estimer le paramètre de non-linéarité *B/A* en se basant sur la méthode d'amplitude finie proposée par F. Varray. La méthode étant limitée par la présence du speckle, de nouvelles techniques de lissage de l'image sont présentées. De plus, de nouvelles transmissions sont mises en place pour améliorer l'estimation du paramètre de non-linéarité par rapport à une transmission dite classique.

## I. Réduction du speckle

Une première partie du travail fut de réaliser une étude bibliographique sur les différentes approches pour améliorer la qualité des images ultrasonores. Plusieurs critères définissent la qualité de l'image : la présence du speckle ou non, le contraste, la résolution spatiale, le rapport signal sur bruit… Afin d'améliorer la qualité de l'image, les approches consistent à réduire le speckle ou bien d'améliorer le contraste, la résolution ou encore le rapport signal sur bruit. Les méthodes peuvent être classées en deux grandes catégories : les méthodes de transmission-réception et les méthodes post-traitement. La première catégorie concerne les techniques s'appuyant sur des transmissions particulières (composition spatiale, ondes planes, signal codé) ou bien sur une réception ou construction différentes (plusieurs sondes en réception, formation de voie différente). La deuxième catégorie concerne les méthodes où un traitement d'image est fait une fois l'image construite (filtrage).

La méthode retenue pour réduire le speckle est le filtrage de Thomson qui provient du traitement du signal. Durant la formation de voie de l'imagerie ultrasonore, au lieu d'utiliser des pondérations classiques (comme une fenêtre de Hanning), plusieurs fenêtres (ou apodisations) orthogonales sont utilisées afin de créer plusieurs images radio fréquences avec différentes réalisation de speckle. Les images B-mode correspondantes sont ensuite

moyennées afin d'avoir une image avec un speckle lissé. Les fenêtres orthogonales ont le nom de : Discrete prolate spheroidal sequences (DPSS).

La méthode de filtrage de Thomson a été évaluée en simulations et acquisitions avec un fantôme comportant des inclusions et des fils. Durant la formation de voie, plusieurs pondérations ont été utilisées afin de comparer le rapport signal sur bruit (SNR), le contraste (CNR), la résolution latérale et la résolution axiale. Les pondérations utilisées sont : une pondération rectangulaire, une pondération de Hanning et plusieurs DPSS (3 à 31). La Figure. I montre les images simulées avec le logiciel CREANUIS en utilisant une seule focale à 30 mm (SF) et les différentes pondérations utilisées pendant la formation de voies. On remarque que le filtrage de Thomson permet de lisser le speckle dans toute l'image. Le SNR et le CNR augmente lorsque les DPSS sont utilisés mais la résolution axiale et la résolution latérale diminuent. De plus, le lissage est plus important en dehors de la zone focale (30 mm). Néanmoins, le contraste diminue lorsqu'un trop grand nombre de pondération DPSS est utilisé. Il a été montré que comme en traitement du signal, même si on augmente le nombre de pondérations orthogonales pendant la formation de voies, une limite est atteinte à partir de 8 pondérations. Le même résultat est obtenu à partir d'images acquises sur un fantôme physique.

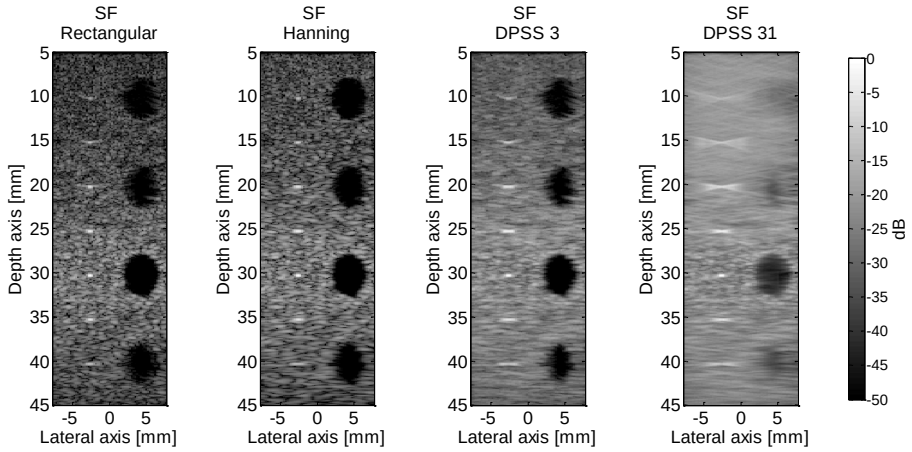


**Figure. I: Images B-mode simulées à partir d'un fantôme comportant des inclusions et des fils en focalisant à 30 mm et en utilisant une fenêtre de pondération (a) rectangulaire, (b) de Hanning, (c) DPSS 3 et (d) DPSS 31.**

Il est proposé d'utiliser ces fenêtres de pondérations orthogonales avec les nouvelles méthodes de transmission composite pour améliorer la résolution : la méthode de l'inversion d'impulsion (PI) et la composition spatiale d'ondes planes.

La méthode d'inversion d'impulsion consiste à la transmission de deux signaux successifs en opposition de phase de même fréquence centrale. Après formation de voies, les images sont sommées et étant donné que les signaux sont transmis en opposition de phase et qu'il y a une propagation non linéaire, la fréquence fondamentale s'annule et uniquement la fréquence du second harmonique est conservée. En simulation et acquisition sur fantôme, la combinaison des deux techniques a permis d'améliorer la résolution axiale de 28% et la résolution latérale de 10%, avec de plus une réduction de 7.6 % du rapport signal sur bruit.

La deuxième méthode est la transmission d'ondes planes avec plusieurs angles d'incidences dans le milieu. Après construction des images pour chaque angle transmis, les images sont moyennées. La Figure. II montre les images simulées avec le logiciel CREANUIS en utilisant une pondération DPSS 3 pour trois méthodes de transmissions : une seule focale à 30 mm (SF), plusieurs focalisations successives de 10 mm à 40 mm tous les 5

mm (MF) et une composition spatiale de 11 ondes planes (MCPWC). Par rapport à une transmission classique avec une seule focalisation dans l'image, la méthode MCPWC a un contraste et une résolution latérale meilleurs dans toute l'image sauf au point focal. Par contre le rapport signal sur bruit diminue dans l'image. La méthode MCPWC est très proche de l'image MF bien que la résolution soit meilleure avec la technique MF. Cependant, un avantage de la transmission d'ondes planes est le temps d'acquisition qui peut être jusqu'à cinq fois plus petit que pour une transmission classique (SF) et pour une qualité d'image très proche.

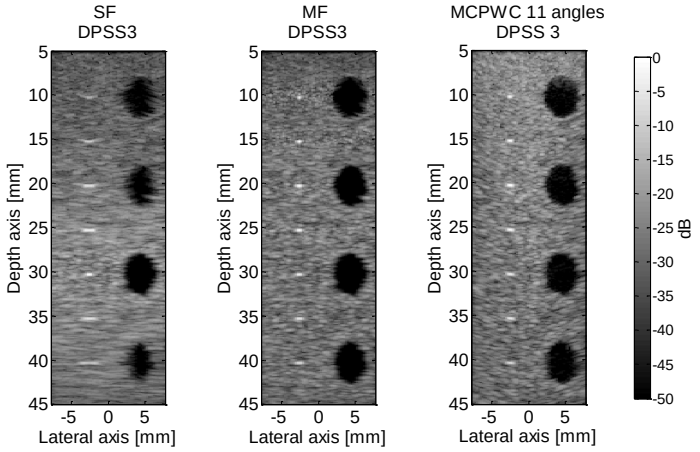


**Figure. II: Images B-mode simulées à partir d'un fantôme comportant des inclusions et des fils. La formation de voie est faite avec 3 DPSS. (a) Une seule focale à 30 mm, (b) plusieurs focales de 10 mm à 40 mm tous les 5 mm et (c) compositions spatiale de 11 onde planes (-15° à 15° tous les 3°).**

## II. Estimation du paramètre *B/A*

Plusieurs techniques existent afin d'estimer le paramètre de non-linéarité et elles peuvent être regroupées dans deux familles : les méthodes thermodynamiques et les méthodes d'amplitude finie. Toutes ces méthodes sont basées sur la détection et la mesure du champ de pression harmonique engendré au cours de la propagation des ultrasons du fait du caractère non linéaire du milieu. Les méthodes thermodynamiques sont reconnues comme étant les plus précises mais nécessitent un matériel complexe et inadéquat pour une utilisation médicale. A l'inverse, les méthodes d'amplitude finie sont utilisables pour une application clinique.

En échographie, une difficulté réside du fait de ne pas accéder directement au champ de pression, mais à la convolution de celui-ci avec les diffuseurs du milieu exploré. Une méthode d'amplitude finie (Varray et al., 2011) a été adaptée pour une application échographique. La méthode consiste à comparer un milieu dont le paramètre de non-linéarité est connu (indice *0*) avec un autre milieu dont le paramètre est inconnu (indice *i*):

$$\beta_i(z) = \beta_0 \frac{\left(\rho c^3\right)_i}{\left(\rho c^3\right)_0}\left[\frac{P_{2i}(z)}{P_{20}(z)} + \frac{1-e^{-(\alpha_2-2\alpha_1)z}}{\alpha_2-2\alpha_1}\frac{d}{dz}\left(\frac{P_{2i}(z)}{P_{20}(z)}\right)\right]$$

$\beta = 1 + B/2A$ est le coefficient de non-linéarité, $\rho$ est la densité du milieu, $c$ est la célérité du milieu, $P_2$ correspond au champ de pression du second harmonique et $\alpha_1$ et $\alpha_2$ désignent l'atténuation du milieu pour le fondamental et le second harmonique.

Cependant, le speckle dans les images échographiques limite l'application de cette méthode. De plus, à cause de la focalisation des ondes ultrasonores lors de la transmission,

l'énergie est concentrée à une profondeur donnée empêchant la bonne estimation et délimitation du paramètre de non-linéarité du milieu dont celui-ci est inconnu.

Pour améliorer l'estimation du paramètre de non-linéarité, il est proposé d'utiliser la composition spatiale par ondes planes pour éviter de concentrer l'énergie à une profondeur privilégiée. Cette technique est testée avec des champs de pressions simulés et sur des images radio fréquences où les champs de pressions ne sont pas connus. Dans le cas des images radio fréquences, le filtrage de Thomson présenté précédemment est utilisé pour réduire le speckle.

Avant d'évaluer l'intérêt des ondes planes pour l'estimation du paramètre de non-linéarité avec les champs de pression, l'impact de la focalisation sur l'estimation du paramètre *B/A* est évalué en simulation. Plusieurs cartes de non-linéarité sont créées, un cas simple avec une seule ellipse et un cas complexe avec plusieurs ellipses. Le cas simple est présenté dans la Figure. III; il s'agit d'un milieu dont le paramètre *B/A* vaut 5 de partout sauf une ellipse où le *B/A* vaut 10. Le milieu de référence défini dans l'équation présentée précédemment et où *B/A* est connu, se trouve entre les deux traits blancs.

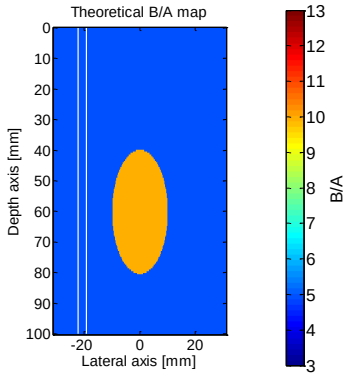


**Figure. III: Carte du paramètre de non-linéarité utilisé en simulation. Le milieu environnant vaut *B/A*=5 tandis que l'ellipse vaut *B/A*=10. La zone comprise entre les deux traits blancs correspond au milieu de référence.**

Pour évaluer l'impact de la focalisation sur l'estimation du paramètre de non-linéarité avec les champs de pression, trois focalisations, à différentes profondeurs, ont été testées : 30, 60 et 90 mm. Ces focalisations correspondent à la région qui précède l'inclusion, à la région de l'inclusion et à la région postérieure du cas simple présenté Figure. III. La Figure. IV montre les images de *B/A* estimées pour les trois focalisations. Le Tableau I donne les valeurs dans les deux zones. Visuellement on voit que la focalisation à 60 mm est celle permettant d'obtenir la valeur la plus proche de *B/A*=10 dans la zone de l'inclusion. Le Tableau. I confirme ce résultat. En revanche, c'est la focalisation à 90 mm qui permet de mieux délimiter la zone de l'inclusion.

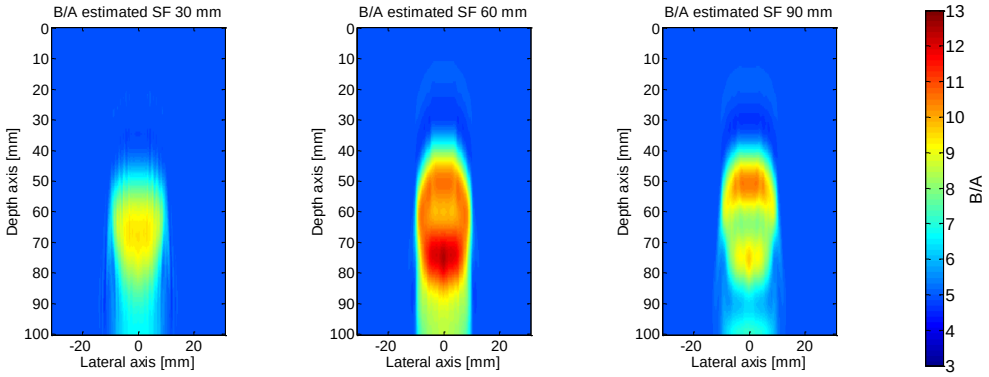


(a) (b) (c)

**Figure. IV: Images de *B/A* estimées avec les champs de pressions dans le cas d'un milieu non-linéaire simple pour trois focalisations (a) 30 mm, (b) 60 mm et (c) 90 mm.**

| *B/A* | SF 30 mm | | SF 60 mm | | SF 90 mm | |
|---|---|---|---|---|---|---|
| | Mean | STD | Mean | STD | Mean | STD |
| 5 | **5.2** | 0.5 | **5.4** | 1.1 | **5.2** | 0.5 |
| 10 | **7.9** | 1.2 | **10.3** | 1.0 | **8.8** | 0.8 |

**Tableau. I: Valeurs de *B/A* estimés avec les champs de pression dans le cas d'un milieu non-linéaire simple pour trois focalisations.**

Pour essayer de mieux délimiter la zone de non-linéarité, la composition spatiale a été utilisé. Il s'agit de réaliser plusieurs tirs successifs avec différents angles de transmission et avec une focale fixe. Les champs de pressions de chaque angle sont sommés. Etant donné que c'est la focalisation à 60 mm qui a donné le meilleur résultat, celle-ci est comparée à deux transmissions de trois angles (-1.5°, 0°, 1.5°) et (-5°, 0°, 5°) avec la même focale à 60 mm. Ces angles sont choisis en se basant sur les résultats de la publication de S.K. Jespersen qui proposent d'utiliser des transmissions obtenues soit avec des angles faiblement différents pour augmenter la détection de zones ayant un faible contraste soit avec des angles de transmission plus largement différents pour améliorer la délimitation de la zone étudiée (Jespersen, Wilhjelm and Sillesen, 1998). La Figure. V montre les images de *B/A* estimées pour la focalisation à 60 mm avec une seule transmission ainsi que les deux compositions spatiales. On remarque que la composition spatiale avec des angles de transmission faiblement espacés, Figure. V.b, améliore la délimitation de la zone avec un *B/A* de 10. Dans le deuxième cas de composition spatiale, Figure. V.c, on observe des artefacts vers 70 mm dû à la présence des lobes de réseaux qui interfèrent avec la zone d'inclusion. Le Tableau. II montre que la méthode de compositions spatiales a tendance à surévaluer le paramètre de non-linéarité dans la zone focale.

Pour l'imagerie du *B/A*, le but est d'améliorer le contraste, qui peut être faible, entre le milieu de référence et le milieu avec un *B/A* inconnu. L'emploie d'angles de transmission faiblement espacé a montré la possibilité d'employer la composition spatiale pour l'estimation du paramètre de non-linéarité mais est encore insuffisante pour parfaitement délimiter les différentes zones de non-linéarité.

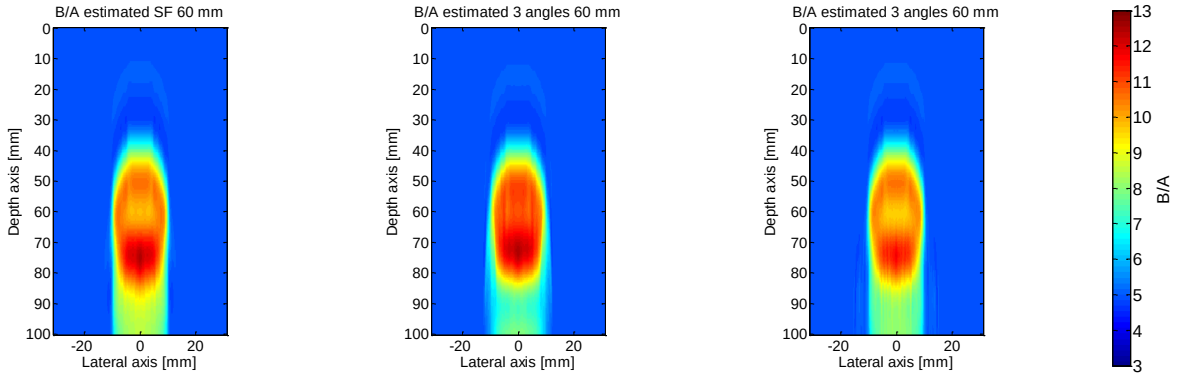


(a) (b) (c)

**Figure. V: Images de *B/A* estimées avec les champs de pressions dans le cas d'un milieu non-linéaire simple pour une focalisation à 60 mm mais pour (a) un seul angle de transmission, (b) trois angles de transmission proches (-1.5, 0°, 1.5°) et (c) trois angles de transmission plus élevés (-5°, 0°, 5°).**

| *B/A* | SF 60 mm | | Spatial 3 (-1.5°, 0°, 1.5°) | | Spatial 3 (-5°, 0°, 5°) | |
|---|---|---|---|---|---|---|
| | Mean | STD | Mean | STD | Mean | STD |
| 5 | **5.4** | 1.1 | **5.3** | 0.9 | **5.3** | 0.5 |
| 10 | **10.3** | 1.0 | **10.6** | 1.1 | **10.1** | 0.8 |

**Tableau. II: Valeurs de *B/A* estimées avec les champs de pression dans le cas d'un milieu non-linéaire simple pour une focalisation à 60 mm mais pour un seul angle de transmission et deux compositions spatiales.**

Les résultats de la composition spatiale focalisée a montré l'intérêt de visualiser la zone de non-linéarité suivant plusieurs angles. Cependant la focalisation influe sur la bonne délimitation du paramètre de non-linéarité. Pour améliorer la délimitation du *B/A*, l'emploi des ondes planes a été testé avec la simulation de champs de pression. Pour pouvoir valider l'emploi des ondes planes sur des données réelles, une plateforme automatique d'acquisitions de champs de pression a été développée. La Figure. VI compare les champs de pression du fondamental ($f_0$) et du second harmonique ($2f_0$) obtenus à partir d'une onde plane, d'une part simulés avec CREANUIS et d'autre part acquis dans de l'eau. La sonde échographique utilisée est composée de 192 transducteurs mais uniquement 64 éléments actifs sont utilisés. Cette limitation est due à l'échographe ULA-OP qui ne peut piloter plus de 64 éléments simultanément. Un hydrophone placé en face de la sonde échographique est piloté grâce à Labview par une plateforme mobile pour ensuite enregistrer une carte de champ de pression. Bien qu'une onde plane soit utilisée, on remarque Figure. VI une certaine inhomogénéité du faisceau qui est due à la géométrie des éléments de la sonde et à leur nombre limité. Dans les champs de pression, on observe la présence de lobes sur les côtés.

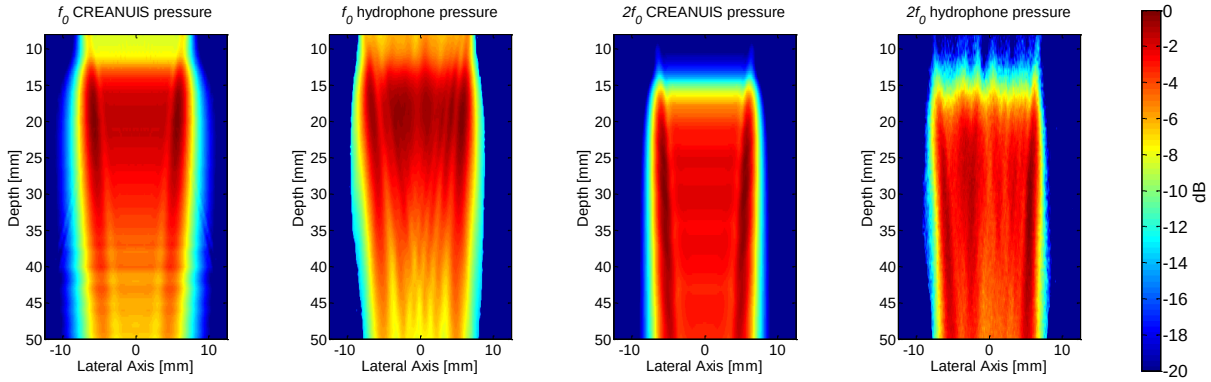


**Figure. VI: Cartes de champs de pression obtenues à partir d'une onde plane simulée (a, c) et à partir d'acquisitions (b, d) du fondamental (a, b) et du second harmonique (c, d).**

L'utilisation d'uniquement 64 éléments actifs est un facteur limitant pour mettre en œuvre la méthode des ondes planes dans le but d'estimer le paramètre de non-linéarité. En simulation, le champ de pression du second harmonique a donc évalué pour différents nombres d'éléments actifs, 64, 128 et 256), d'une sonde. La Figure. VII présente les champs de pression simulés pour 64 et 256 éléments actifs. Dans la Figure. VII.(a, b), nous avons le champ de pression en entier tandis que dans la Figure. VII.(c, d), nous avons un zoom dans la partie centrale de la sonde qui est représentée. Cette zone correspond aux 64 éléments actifs centraux de la sonde. En utilisant 256 éléments actifs, Figure. VII.b, des lobes sont présents sur les bords. En revanche, si nous nous concentrons sur les 64 éléments actifs, Figure. VII.d, le champ de pression est homogène, il est proche de celui produit par un piston parfait (infini).

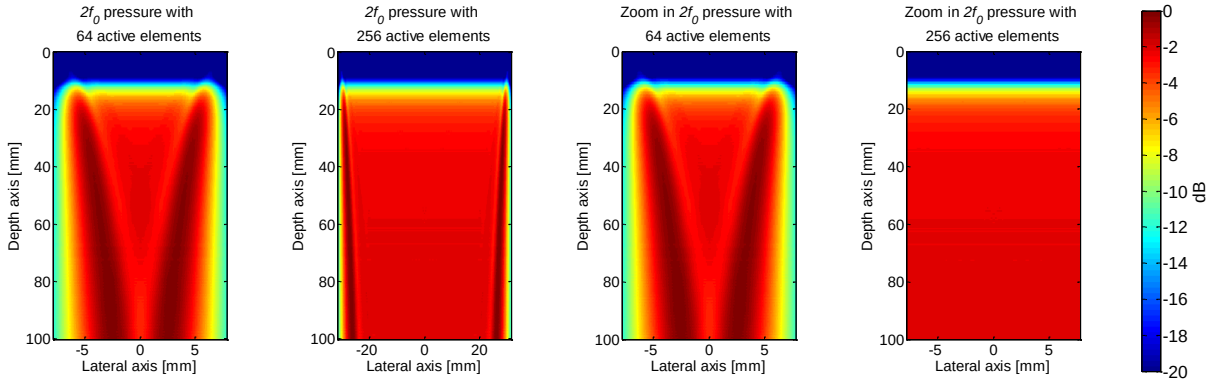


**Figure. VII: Cartes de champ de pression du second harmonique d'une onde plane simulée pour (a, c) 64 ou (b, d) 256 éléments actifs. (a, b) représentent tout le champ de pression pour 64 et 256 éléments tandis que (c, d) ne reporte que le champ en regard des 64 éléments actifs centraux.**

La méthode des ondes planes a donc été évaluée avec le cas d'un milieu non linéaire simple décrit dans la Figure. III. Etant donné que les meilleurs résultats avec la composition spatiale ont été obtenus avec des angles de transmission faiblement espacés, deux méthodes d'ondes planes ont été testées. La première méthode est la transmission d'une seule onde plane sans angle d'incidence et la deuxième méthode est la transmission de 7 angles de -1.5° à 1.5° espacés de 0.5°. La Figure. VIII nous montre les images de *B/A* estimées avec une focalisation à 60 mm et les deux méthodes d'ondes plane. Conformément aux observations faites sur la Figure. VII, des lobes sont présents sur les images de *B/A* estimées avec les techniques d'ondes planes de la Figure. VIII.(b, c). Ceux-ci n'interfèrent pas avec la zone ellipsoïdale où la non-linéarité est différente. Avec l'approche des ondes planes, la zone d'inclusion de non-linéarité élevée est visuellement mieux délimitée. Le Tableau. III montre que la méthode par focalisation est plus performante pour l'estimation du *B/A*. Dans la zone

de *B/A* à 10 la valeur obtenue est par contre plus homogène avec la méthode par composition d'ondes planes. Pour la zone de *B/A* à 5 la valeur est moins homogène du fait des valeurs soit très grandes soit très faibles du champ dans la région des lobes.

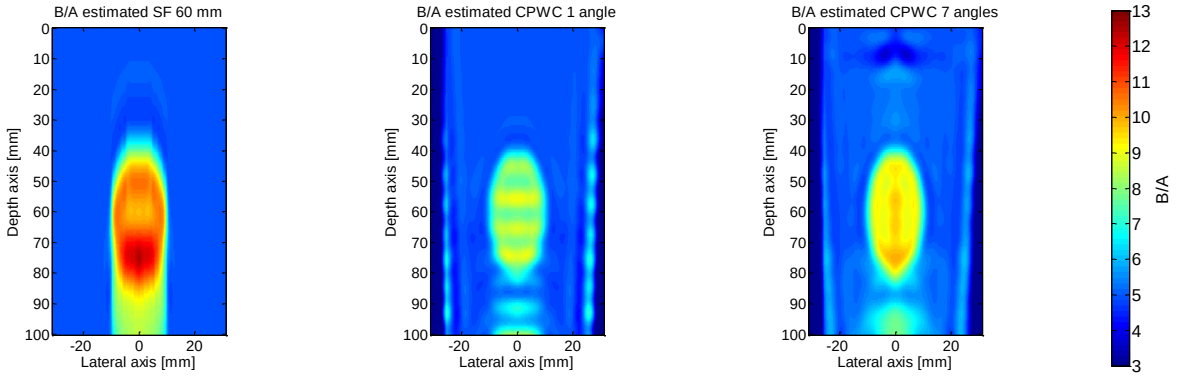


**Figure. VIII: Images de *B/A* estimées avec les champs de pressions dans le cas d'un milieu non-linéaire simple pour (a) une focalisation à 60 mm, (b) une seule onde plane et (c) une composition spatiale d'ondes planes (-1.5° à 1.5° chaque 0.5°).**

| *B/A* | SF 60 mm | | CPWC 1 | | CPWC 7 | |
|---|---|---|---|---|---|---|
| | Mean | STD | Mean | STD | Mean | STD |
| 5 | **5.4** | 1.1 | **4.2** | 1.5 | **4.7** | 1.6 |
| 10 | **10.3** | 1.0 | **8.0** | 0.6 | **8.9** | 0.7 |

**Tableau. III: Valeurs de *B/A* estimées avec les champs de pression dans le cas d'un milieu simple pour une focalisation à 60 mm mais pour un seul angle de transmission et deux compositions spatiales.**

La technique des ondes planes a été appliquée sur des images radio fréquences où les champs de pressions ne sont pas connus. Un milieu homogène en termes de distribution des réflecteurs a été utilisé ainsi que le milieu non-linéaire présenté en Figure. III. Dans le cas de la focalisation à 60 mm, aucune apodisation n'est utilisée pendant la formation de voie. Dans les deux cas d'ondes planes (présentés Figure. VIII), le filtrage de Thomson avec 7 DPSS est utilisé. Ces deux cas montrent l'évolution entre la méthode présentée par F. Varray et ce travail de recherche. La Figure. IX montre que l'approche focalisée ne permet pas de délimiter précisément la zone de non-linéarité tandis que les méthodes d'onde plane la délimitent mieux. Le Tableau. IV montre les valeurs de *B/A* estimés lorsque les champs de pression ne sont pas connus. Comme avec des champs de pression connus (Tableau. III), la valeur de *B/A* dans l'ellipse est mieux évaluée dans le cas de la méthode focalisée.

Avec les ondes planes, les régions de paramètres de non-linéarité différents sont correctement délimitées mais la quantification du paramètre est moins précise. Lorsque seules les données échographiques sont disponibles, l'emploi des ondes planes et des fenêtres de pondérations orthogonales donne de meilleurs résultats que la méthode proposée par F. Varray en utilisant une seule transmission focalisée.

Pour prolonger ce travail, de nouvelles méthodes de transmission ultrasonore (Chirp) sont étudiées pour améliorer l'estimation du paramètre de non-linéarité.

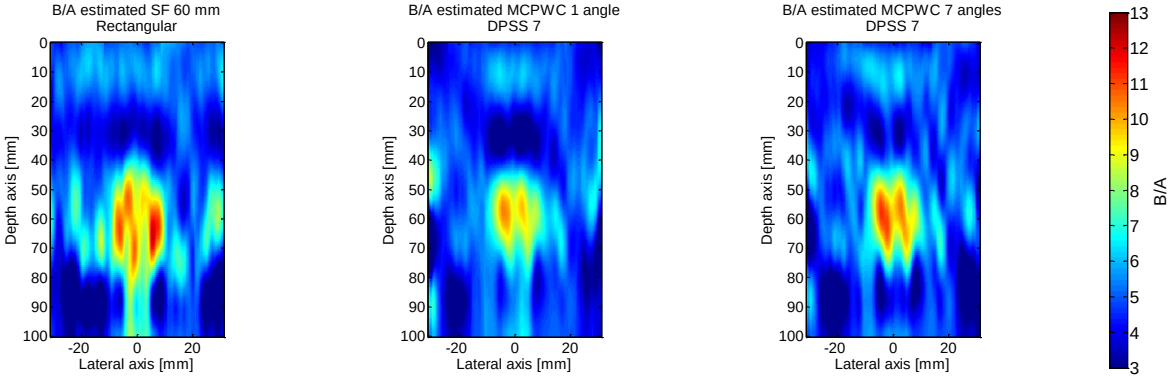


(a) (b) (c)

**Figure. IX: Images de *B/A* estimées avec les champs de pressions dans le cas d'un milieu non-linéaire simple pour (a) une focalisation à 60 mm, (b) une seule onde plane et (c) une composition spatiale d'ondes planes (-1.5° à 1.5° chaque 0.5°).**

| *B/A* | Foc 60 mm | | MCPWC 1 | | MCPWC 7 | |
|---|---|---|---|---|---|---|
| | Mean | STD | Mean | STD | Mean | STD |
| 5 | **4.9** | 1.3 | **4.7** | 1.0 | **4.7** | 1.0 |
| 10 | **9.0** | 1.3 | **7.6** | 1.4 | **8.1** | 1.6 |

**Tableau. IV: Valeurs de *B/A* estimées avec les images radio fréquences dans le cas d'un milieu non-linéaire simple pour une focalisation à 60 mm mais pour un seul angle de transmission et deux compositions spatiales.**

# Contents

# List of symbols and abbreviations

### Latin letter

| | |
|---|---|
| $B/A$ | Nonlinearity parameter |
| $c$ | Sound speed or celerity ($m.s^{-1}$) |
| $f$ | Frequency (Hz) |
| $F$ | F-number |
| $J_n$ | Bessel function of the first kind and *n*-th order |
| $N_\theta$ | Number of plane waves transmitted |
| $P$ | Pressure amplitude (Pa) |
| $P_0$ | Pressure amplitude at equilibrium (PA) |
| $R$ | Intensity reflection coefficient |
| $s$ | Entropy |
| $T$ | Intensity transmission coefficient |
| $t_{acq}$ | Acquisition time (s) |
| $\vec{u}$ | Particle velocity ($m.s^{-1}$) |
| $Z$ | Acoustic impedance of a medium ($kg.m^{-2}.s^{-1}$ or Rayleigh) |

### Greek letter

| | |
|---|---|
| $\alpha_0$ | Attenuation constant of the medium ($dB.MHz^{-1}.cm^{-1}$) |
| $\alpha_1$ | Attenuation of the fundamental wave ($dB.MHz^{-1}.cm^{-1}$) |
| $\alpha_2$ | Attenuation of the second-harmonic wave($dB.MHz^{-1}.cm^{-1}$) |
| $\beta$ | Nonlinear coefficient |
| $\gamma$ | Frequency dependent number (between 1 and 2 for biological media) |
| $\theta$ | Steering angle (degree) |
| $\lambda$ | Wavelength (m) |
| $\mu$ | Mean of the image amplitude in a region-of-interest |
| $\rho$ | Density ($kg.m^{-3}$) |
| $\rho_0$ | Equilibrium density ($kg.m^{-3}$) |
| $\sigma$ | Standard deviation of the image amplitude in a region-of-interest |
| $\omega$ | Angular frequency f (Hz) |

**Abbreviations**

| | |
|---|---|
| ASF | Alternating sequential filter |
| CNR | Contrast-to-noise ratio |
| CPWC | Coherent plane-wave compounding |
| CTR | Contrast-to-tissue ratio |
| DPSS | Discrete prolate spheroidal sequences |
| ECM | Extended comparative method |
| FWHM | Full width at half maximum |
| lpf | Low-pass filter |
| PI | Pulse inversion |
| PSF | Point spread function |
| PWI | Plane wave imaging |
| MACI | Multi-angle compound imaging |
| MCPWC | Multitaper coherent plane-wave compounding |
| MF | Multi-focus |
| MPI | Multitaper pulse inversion |
| MSD | Mean standard deviation |
| NBI's | Narrowband images |
| RF | Radio frequency |
| ROI | Region-of-interest |
| SF | Single transmit focus |
| SNR | Signal-to-noise ratio |
| SSP | Split-spectrum processing |
| STD | Standard deviation |
| TGC | Time gain compensation |
| THI | Tissue harmonic imaging |
| TM | Thomson's multitaper |
| UCA | Ultrasound contrast agents |
| UCT | Ultrasound computed tomography |
| US | Ultrasound |

# Thesis Objectives

The objective of this thesis work is to improve the nonlinearity parameter estimation in echo mode. The first questions which drove this work were: *What is the nonlinearity parameter? What are the limitations in order to estimate the nonlinearity parameter in echo mode?*

The nonlinearity parameter leads to a nonlinear propagation of an ultrasound wave in biological tissue. The nonlinearity parameter has a direct impact on the celerity of the pressure wave transmitted in the biological tissue. Therefore the harmonic signal is impacted, increasing the harmonics amplitude. Each tissue can be characterized by the speed of sound, the density and the nonlinearity parameter (Culjat et al., 2010) (Hamilton and Blackstock, 1998). The estimation of the nonlinear parameter can be a novel modality to distinguish healthy from unhealthy tissues.

Several techniques exist in order to estimate the nonlinearity parameter and they are mainly regrouped in two families: the thermodynamic methods and the finite amplitude methods (Hamilton and Blackstock, 1998). The first ones are recognized as the most accurate methods but involve the use of a complex experimental setup inadequate to medical use (Hamilton and Blackstock, 1998). On the contrary, the finite amplitude methods are suitable for clinical applications. A finite amplitude method proposed by F. Varray was adapted to echographic applications allowing a noninvasive approach (Varray, 2011) (Varray et al., 2011). However the echographic images suffer of speckle noise, which limit the application of the method. Speckle reduction approaches have been proposed, allowing an improvement in the nonlinearity parameter estimation with echographic images. However the previously proposed methods are limited by the unique focalization used in echographic mode, concentrating the energy in the focal depth and avoiding the correct delineation of the nonlinearity area. Moreover, in order to optimize the nonlinearity parameter estimation, the focal depth was set in the investigated nonlinearity area in simulation. However, in an experimental context with unknown tissues, the location of an eventual pathological area with a different nonlinearity parameter is unknown.

In order to respect the objective of this thesis, the work has been guided in two directions: to improve the speckle noise reduction and to propose new transmission methods.

The manuscript is composed of three distinct parts:

- Chapter 1: Ultrasound basics. This first chapter reports on the general aspects of the ultrasound, linear and nonlinear propagation, echographic probes and image formation methods.

- Part I: Ultrasound imaging improvement. This first part is composed of two chapters. Chapter 2 introduces the state of the art of speckle noise reduction, and of contrast or spatial resolution improvement. Different transmission-reception strategies and image processing method are presented and their advantages and drawbacks are discussed in order to identify the method more adapted to reduce the speckle noise. Chapter 3

introduces the Thomson's multitaper approach chosen to reduce the speckle noise. Two original contributions using particular transmission methods are presented to improve the resolution of the Thomson's multitaper approach.

- Part II: Nonlinearity parameter measurement. The last part of the manuscript is composed of two chapters. Chapter 4 report on the state of the art of nonlinear parameter measurement methods. In particular, the extended comparative method (ECM), which is the technique having the most interest for echo mode measurement, is presented. Chapter 5 evaluates the limitation of nonlinear parameter echo mode measurement. The multitaper coherent plane-wave compounding (MCPWC) contribution proposed in Chapter 3 is combined with the ECM method in order to improve the nonlinearity parameter estimation in simulation. The method has been tested on pressure field and radio frequency images simulated with CREANUIS.

A general discussion concludes the thesis. In appendix, additional experimental results are reported.

# Chapter 1

# Ultrasound fundamental

In this chapter, the ultrasound and echographic background are presented. First, generalities about the ultrasound are developed. Then, the linear and nonlinear propagation of an ultrasound wave are presented. Next, the echographic probe and image beamforming are developed. Finally, the methods to evaluate the ultrasound image quality are presented.

## 1.1. Frequency, wave velocity and wavelength

Everywhere around us, the sounds are present and propagate in a medium as a mechanical wave of pressure. It consists of alternating pressure deviations from the equilibrium pressure of the particles in the medium, creating local regions of compression and rarefaction. The sound is characterized by its frequency $f$ in Hz. Human ears are sensible to the sound frequency between 20 Hz – 20 kHz. In medical ultrasound imaging domain, the frequency is mainly comprised between 1 – 20 MHz. During the propagation, the mechanical wave goes through different medium having different density $\rho$ (expressed in $kg.m^{-3}$) influencing the sound speed or celerity $c$ (in $m.s^{-1}$). In function of the celerity $c$, the distance between two compression or rarefaction waves, the wavelength or spatial periodicity $\lambda$, is defined as:

$$\lambda = \frac{c}{f} \tag{1.1}$$

## 1.2. Scattering, transmission and reflection of an ultrasound wave

The characteristic that determines the amount of reflection and transmission is known as the acoustic impedance Z (expressed in $kg.m^{-2}.s^{-1}$ or Rayleigh) and is the product of the density $\rho$ ($kg.m^{-3}$) and the celerity $c$:

$$Z = \rho c \tag{1.2}$$

Moreover, the acoustic impedance also depends on the medium's temperature because the density and the celerity are impacted by the temperature.

The propagation medium contains a huge number of reflectors, named scatterers, impacting the reflection. The reflection type depends on the scatterers' size $s_{scat}$ and the wavelength $\lambda$:

- $s_{scat} << \lambda$, it is a diffuse reflection or Rayleigh scattering. The incident signal is reflected in all directions and it is mostly present with rough surfaces.
- $s_{scat} >> \lambda$, it is a specular reflection. The incident signal is reflected with the same angle in the opposite direction respecting the Snell's law.

The diffuse reflection determines the echo texture of the medium. Ultrasound images have a granular texture, called speckle, which corresponds to the constructive and destructive

interferences of echoes received from scatterers. The work of this thesis is mainly concentrated on the speckle reduction.

The specular reflection is responsible for the brightness of the interfaces between different parts of the medium. When a wave travels through one medium $Z_1$ to a second medium $Z_2$, at the interface of the two media, a part of the energy travels forward as one wave through the second medium while another part is reflected into the first medium. According to the angle with which the incident ultrasonic reaches the interface of the two media, the Snell's Law is applied as illustrated by Figure 1.1. The incident $\theta_i$ and the reflection $\theta_r$ angles have the same value because the two waves travel the same medium and hence have the same velocity. The transmitted $\theta_t$ angle is defined by the Snell's law. The amplitude of the two transmitted and reflected waves depends on the incident angle $\theta_i$ and on the acoustic impedance of the two media.

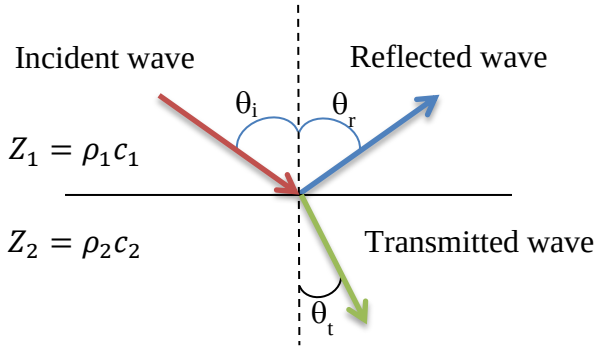


**Figure 1.1: Transmission and reflection of an ultrasound wave between two different media with different acoustic impedance $Z_1$ and $Z_2$. An incident angle $\theta_i$ lead to a reflected angle $\theta_r = \theta_i$ and a transmitted angle $\theta_t$.**

The intensity reflection coefficient R and transmission coefficient T are given by:

$$R = \left( \frac{Z_2 \cos(\theta_i) - Z_1 \cos(\theta_t)}{Z_2 \cos(\theta_i) + Z_1 \cos(\theta_t)} \right)^2$$
$$T = 1 - R = \frac{4 Z_1 Z_2 \cos(\theta_i) \cos(\theta_t)}{\left( Z_2 \cos(\theta_i) + Z_1 \cos(\theta_t) \right)^2} \quad \textbf{(1.3)}$$

If the incident wave arrives perpendicularity to the interface of the two media ($\theta_i = 0°$), the transmitted angle is also equal to 0° and the coefficient $R$ and $T$ are:

$$R = \left( \frac{Z_2 - Z_1}{Z_2 + Z_1} \right)^2$$
$$T = 1 - R = \frac{4 Z_1 Z_2}{\left( Z_2 + Z_1 \right)^2} \quad \textbf{(1.4)}$$

With these two simplified equations, two important cases are presented:

- $Z_2 >> Z_1$, R ≈ 100% and T ≈ 0%, there is a total reflection. This situation occurs when the transducer transmits the ultrasound wave directly in the air. This situation is dangerous for the probe because all the energy is sent back to the transducer which

could be destroyed by heating. In biological media, a similar phenomenon is present when the wave travels from soft tissues to bones.

- $Z_2 \approx Z_1$, T ≈ 100% and R ≈ 0%, there is a total transmission. In biological media the acoustic impedances of the various tissues are closed and only small variation can be observed.

During the propagation of the ultrasound wave, the wave intensity decreases as a function of the depth, meaning that the wave intensity is attenuated. The attenuation is frequency-dependent and the intensity of a plane wave can be modelled as:

$$I(z) = I_0 e^{-\alpha(f)z} \tag{1.5}$$

where $I_0$ is the intensity in the incident wave and $I(z)$ is the intensity at a depth $z$. $\alpha(f)$ is the frequency-dependent attenuation in dB.MHz$^{-1}$.cm$^{-1}$. It is expressed as:

$$\alpha(f) = \alpha_0 \left( \frac{f}{1e^6} \right)^{\gamma} \tag{1.6}$$

with γ a number between 1 and 2 for biological media that translates the frequency dependent law and $\alpha_0$ the attenuation constant of the medium in dB.MHz$^{-1}$.cm$^{-1}$.

Different classical media are presented in Table 1.1 with their density, celerity, acoustic impedance and attenuation. The mean value of the celerity in biological tissue is 1540 m.s$^{-1}$. Thus, the wavelength for the medical ultrasound domain (1 – 20 MHz) is ranged between 0.08 mm and 1.54 mm.

| Medium | Density (kg.m$^{-3}$) | Celerity (m.s$^{-1}$) | Acoustic impedance (MRayl) | Attenuation (dB.MHz$^{-1}$.cm$^{-1}$) |
|---|---|---|---|---|
| Air | 1.2 | 330 | 0.0004 | - |
| Water | 1000 | 1480 | 1.48 | 0.0022 |
| Blood | 1060 | 1584 | 1.68 | 0.2 |
| Biological tissue | 950 – 1100 | 1478 – 1595 | 1.4 – 1.69 | 0.48 – 1.09 |
| Bone (cortical) | 1975 | 3476 | 7.38 | 6.9 |

**Table 1.1: Parameters of classical media (Culjat et al., 2010).**

## 1.3. Linear wave equation

In a homogeneous medium with a negligible viscosity and heat effect during the wave propagation, the ultrasound wave propagation is based on the two linearized Euler's equations (Hamilton and Blackstock, 1988):

Conservation of mass

$$\frac{\partial \rho}{\partial t} + \rho \nabla . \vec{u} = 0 \tag{1.7}$$

Conservation of momentum

$$\rho \frac{\partial \vec{u}}{\partial t} + \nabla P = 0 \tag{1.8}$$

where $\rho$ is the density, $\vec{u}$ the particle velocity in m.s$^{-1}$ and $P$ is the pressure wave in Pa.

The equation (1.7) indicates that during the propagation, there is no mass lost or added in the medium. Equation (1.8) shows that the perturbations in the medium are due to the pressure wave transmitted in the medium.

In linear acoustic, the temperature of the medium is considered constant during the wave propagation. With such a consideration, the compression is adiabatic and can be described as:

$$\frac{P}{P_0} = \left(\frac{\rho}{\rho_0}\right)^{\mathrm{K}} \tag{1.9}$$

where *K* is the ratio of the specific heat. The index *0* indicates that the variables are taken at their equilibrium. The ultrasound propagation is considered isentropic with a constant entropy *s*, so the speed of the propagation can be defined as:

$$c^2 = \left(\frac{\partial P}{\partial \rho}\right)_s \tag{1.10}$$

Using (1.9) and (1.10), the speed of sound at equilibrium is:

$$c_0^2 = \mathrm{K}\frac{P_0}{\rho_0} \tag{1.11}$$

## 1.4. Nonlinear wave equation

The linear propagation of an ultrasound wave in a medium as expressed in the last section is an approximation. The ultrasound propagation is in fact a nonlinear process. The linearized equation (1.8) has to be extended in the case of ultrasound wave propagation through a no viscous and lossless medium (Hamilton and Blackstock, 1988):

$$\rho\left(\frac{\partial \vec{u}}{\partial t} + \left(\vec{u}.\nabla\right)\vec{u}\right) + \nabla P = 0 \tag{1.12}$$

In (1.12), it is the convective acceleration term $(\vec{u}.\nabla)\vec{u}$ compared to (1.8),which makes the ultrasound wave propagation a nonlinear process.

### 1.4.1. Nonlinear coefficient and nonlinearity parameter

In the case of biological tissues, the relation between the pressure and the density variation in function of the pressure wave solicitation is not as simple as the case described by (1.9) which is valid for an ideal gas. It has to expand in a Taylor series to taking into account the nonlinear part:

$$\begin{aligned} P - P_0 &= \sum_{k=0}^{\infty} \frac{1}{k!}\left(\frac{\partial^k P}{\partial \rho^k}\right)_s \left(\rho - \rho_0\right)^k \\ &= \left(\frac{\partial P}{\partial \rho}\right)_s \left(\rho - \rho_0\right) + \frac{1}{2!}\left(\frac{\partial^2 P}{\partial \rho^2}\right)_s \left(\rho - \rho_0\right)^2 + \frac{1}{3!}\left(\frac{\partial^3 P}{\partial \rho^3}\right)_s \left(\rho - \rho_0\right)^3 + \ldots \end{aligned} \tag{1.13}$$

The equation (1.13) can be simplified using $P' = P - P_0$, $\rho' = \rho - \rho_0$ and defining the parameters *A, B* and *C* such as:

$$A = \rho_0 \left( \frac{\partial P}{\partial \rho} \right)_s \equiv \rho_0 c_0^2$$
$$B = \rho_0^2 \left( \frac{\partial^2 P}{\partial \rho^2} \right)_s \quad \textbf{(1.14)}$$
$$C = \rho_0^3 \left( \frac{\partial^3 P}{\partial \rho^3} \right)_s$$

(1.13) can then be written as:

$$P' = \sum_{k=0}^{\infty} \frac{1}{k!} \left( \frac{\partial^k P}{\partial \rho^k} \right)_s \rho'^k = A \frac{\rho'}{\rho_0} + \frac{B}{2!} \left( \frac{\rho'}{\rho_0} \right)^2 + \frac{C}{3!} \left( \frac{\rho'}{\rho_0} \right)^3 + \ldots \quad \textbf{(1.15)}$$

The accuracy of the pressure-density Taylor development is linked to the truncation of (1.15). If only the first order is kept, (1.15) corresponds to the linear ultrasound propagation theory. While in the case of a nonlinear propagation, the parameter *B* is taken into account.

The nonlinear parameter is the ratio between the quadratic, *B*, and the linear, *A*, coefficient of the Taylor development. The nonlinearity parameter *B/A* links the pressure variation with the density variations:

$$\frac{B}{A} = \frac{\rho_0}{c_0^2} \left( \frac{\partial^2 P}{\partial \rho^2} \right)_s \quad \textbf{(1.16)}$$

The nonlinearity parameter has a direct impact on the velocity of the pressure wave:

$$c = c_0 \left( 1 + \frac{B}{2A} \frac{u}{c_0} \right)^{\frac{2A}{B}+1} \quad \textbf{(1.17)}$$

If the ratio between the particle velocity *u* and the celerity $c_0$ is small, the velocity in (1.17) can be express as the first order of:

$$(1+x)^a = 1 + ax + \frac{a(a-1)}{2!} + \ldots \quad \textbf{(1.18)}$$

so,

$$c = c_0 + (1 + \frac{B}{2A})u \quad \textbf{(1.19)}$$

With this equation, the nonlinear coefficient $\beta$ of the medium is defined and it is linked to the nonlinearity parameter *B/A*:

$$\beta = 1 + \frac{B}{2A} \quad \textbf{(1.20)}$$

### 1.4.2. Interpretation of the nonlinear effect

In (1.19) it is demonstrated that the nonlinearity has an effect on the velocity of the pressure wave. Using (1.19), (1.20) and the definition of the particle velocity $u = P/(\rho_0 c_0)$, the celerity can be expressed as:

$$c = c_0 + \beta \frac{P}{\rho_0 c_0} \tag{1.21}$$

The celerity variation $\Delta c = c - c_0$ can be related to the pressure variation $\Delta P$:

$$\Delta c = c - c_0 = \beta \frac{\Delta P}{\rho_0 c_0} \tag{1.22}$$

The equation (1.22) shows that the celerity is not constant during the propagation and is proportional to the local pressure and to the nonlinearity coefficient of the medium.

Two cases are alternatively present during the propagation, the compression and the dilatation:

- Compression : the pressure variation is positive, $\Delta P \sim P$, thus the celerity in the medium is superior to the initial celerity $c > c_0$

$$c^+ = c_0 + \frac{\beta}{\rho_0 c_0} P \tag{1.23}$$

- Dilatation: the pressure variation is negative, $\Delta P \sim -P$, thus the celerity in the medium is inferior to the initial celerity $c < c_0$

$$c^- = c_0 - \frac{\beta}{\rho_0 c_0} P \tag{1.24}$$

During the propagation, the high pressure of the wave travel faster than the low pressure of the wave (Figure 1.2.a). The Figure 1.2.b illustrates in simulation, the distortion of the ultrasound wave after a 300 mm propagation in water (*B/A* = 5). The deformation of the ultrasound wave is visible in their corresponding Fourier spectrum. If the initial ultrasound signal is monochromatic, no harmonics are present in the Fourier transform (Figure 1.2.c). After the propagation, the ultrasound wave is deformed (Figure 1.2.b) and harmonics are generated (Figure 1.2.d).

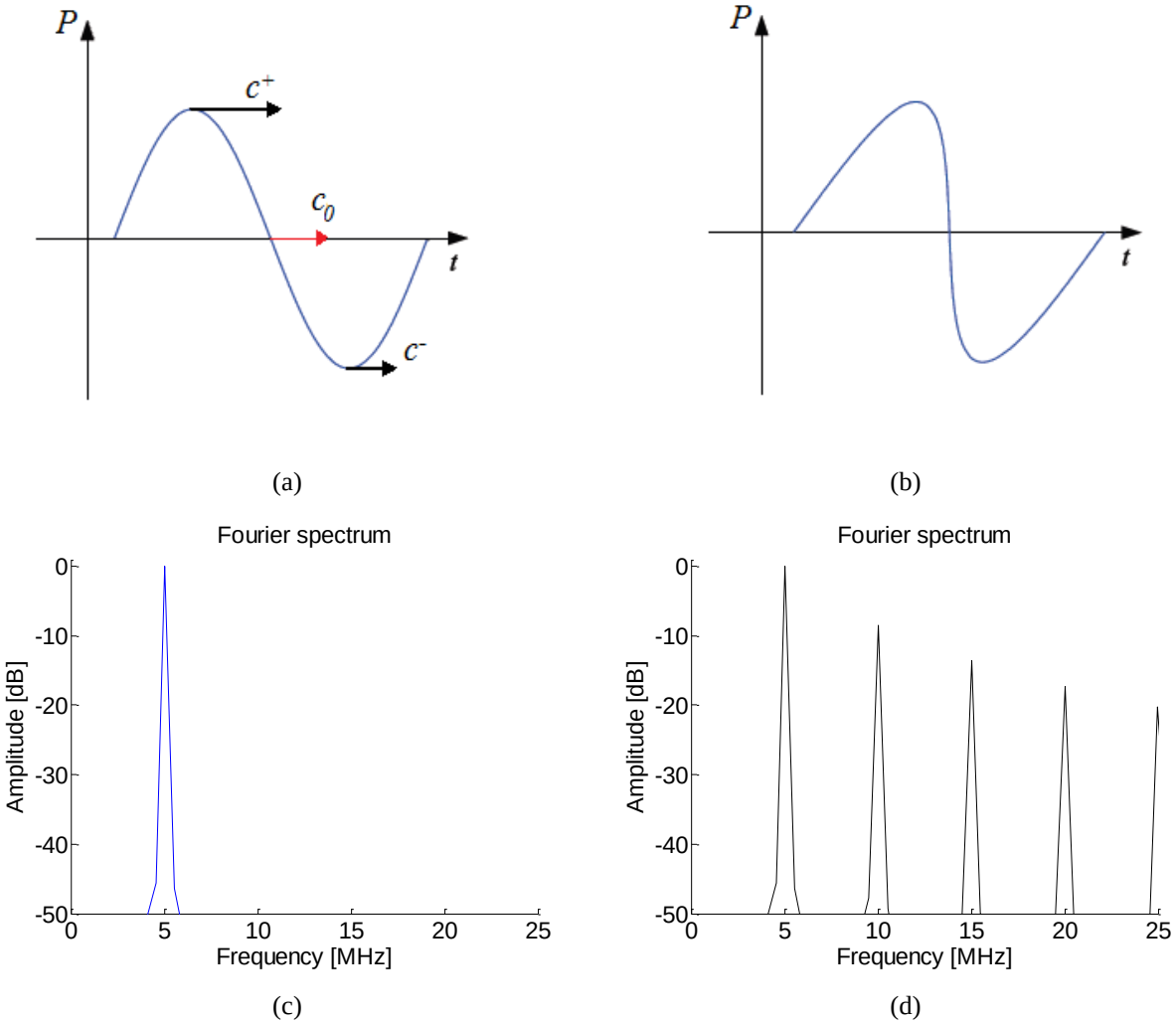


**Figure 1.2: Distortion of a 5 MHz ultrasound wave with an initial pressure of 100 kPa during its propagation in water. (a) Simulated sinusoidal pressure wave transmitted at $z = 0$ and (b) after a propagation $z = 300$ mm. Corresponding Fourier spectrum for both depth propagation are given in (c) and (d). The harmonics appear in (d) during the propagation.**

Theoretically, the ultrasound wave tends to a sawtooth signal until a shock distance length $z_{sh}$ (expressed in $m^{-1}$) (Beyer and Letcher, 1969) (Rudenko and Soluyan, 1977) (Angelsen, 2000):

$$z_{sh} = \frac{\rho_0 c_0^3}{\omega_0 \beta P_0} \tag{1.25}$$

However in medical imaging, first the transmitted pressure is low and second the ultrasound wave is attenuated by absorption during the propagation distance and then prevents the development of infinite pressure gradient. As absorption increases with frequency, the higher harmonic components are more attenuated than the fundamental one.

### 1.4.3. Burgers equation

#### 1.4.3.1. Lossless Burgers equation

During the nonlinear propagation in a lossless medium, the distortion of the pressure wave is given by Burgers lossless equation:

$$\frac{\partial P}{\partial z} = \frac{\beta P}{\rho_0 c_0^3}\frac{\partial P}{\partial \tau} \tag{1.26}$$

where $z$ is the propagation direction and $\tau = t - z/c_0$ is the delayed time. The solution of (1.26) is proposed by (Fubini, 1935):

$$P(z,\tau) = P_0 \sum_{n=1}^{\infty} \frac{2}{n\, z/z_{sh}} J_n\left(n\, z/z_{sh}\right)\sin\left(n\omega_0\tau\right) \tag{1.26}$$

where $n$ is the harmonic number, $\omega_0 = 2\pi f_0$ is the angular frequency and $J_n$ is the Bessel function of the first kind and $n$-th order.

The evaluation of the fundamental and the three first harmonics in function of the depth is given in Figure 1.3 using (1.26). The decrease in the fundamental component as the wave is propagated can easily be seen, as well as the growth of the three first harmonics.

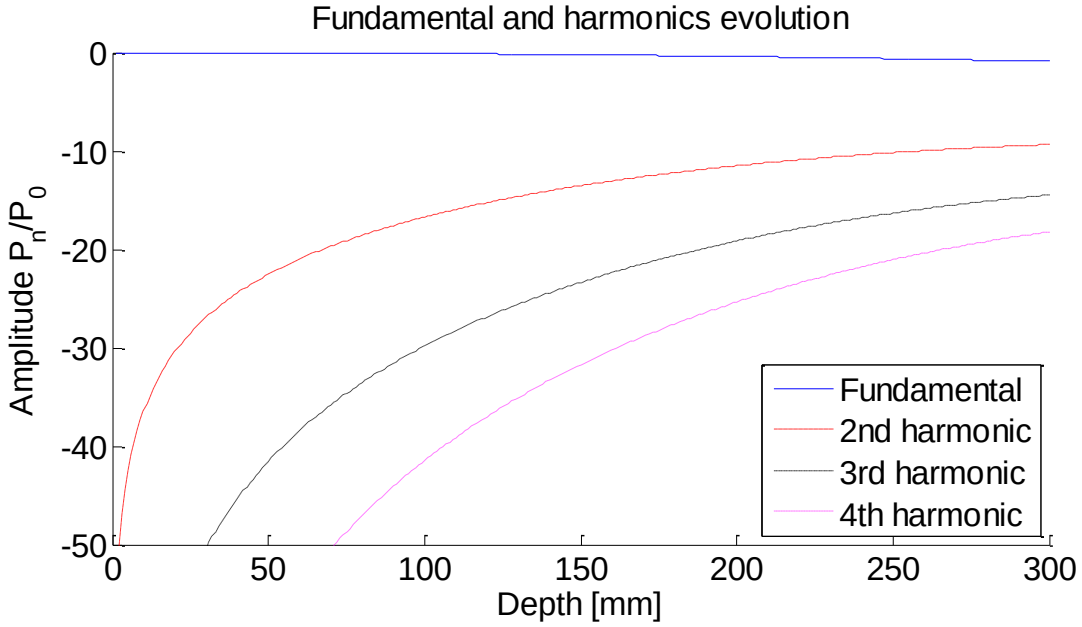


**Figure 1.3: Evolution of the fundamental and three first harmonics in function of the depth for a 5 MHz transmitted signal with an initial pressure $P_0$ of 100 kPa in water ($B/A$ = 5). The amplitude is normalized by $P_0$ and then expressed in dB.**

#### 1.4.3.2. Complete Burgers equation

The equation given in the previous section stands for a nondissipative wave and is an approximation of the reality. When the ultrasound wave travels the medium, it undergoes several changes related to the medium properties. The absorption and dispersion decrease the energy of the propagating ultrasound wave. The absorption converts the ultrasound energy in heat due to the thermo-viscous dissipation. The dispersion effect is lower than absorption and

it is not considered. The extended Burgers equation is expressed (Hamilton and Blackstock, 1998):

$$\frac{\partial P}{\partial z} = \frac{\delta}{2c_0^3}\frac{\partial^2 P}{\partial \tau^2} + \frac{\beta P}{\rho_0 c_0^3}\frac{\partial P}{\tau} \tag{1.27}$$

where $\delta$ is the diffusivity of sound and is composed of different effect of the thermo-viscous dissipation as the thermal conductivity, the sear and bulk viscosity (Hamilton and Blackstock, 1998). The extended Burgers equation is the simplest model that describes the combined effects of the nonlinearity and losses on the propagation of the ultrasound wave.

### 1.4.4. KZK equation

The KZK (Kholkhlov – Zabolotskaya – Kuznetsov) equation is a more complete equation than the Burgers equation (1.27) taking into accounts the combined effects of the medium absorption and also the diffraction of the transducer. The diffraction effect appears due to the finite size of the transducer. KZK equation is expressed as (Hamilton and Blackstock, 1998):

$$\frac{\partial P}{\partial z} = \Delta_\perp P + \frac{\delta}{2c_0^3}\frac{\partial^2 P}{\partial \tau^2} + \frac{\beta P}{\rho_0 c_0^3}\frac{\partial P}{\tau} \tag{1.28}$$

where $\Delta_\perp P$ is the diffraction's effect of the transducers and defines the focalization pattern due to the probe's geometry. The diffraction's effect can be expressed for:

- A circular piston source with a circular elements of radius $r$

$$\Delta_\perp P = \int_{-\infty}^{\tau}\left(\frac{\partial^2 P}{\partial r^2} + \frac{1}{r}\frac{\partial P}{\partial r}\right)d\tau' \tag{1.29}$$

- A linear array source with a lateral and elevation dimension ($x$, $y$) in the probe plane (Figure 1.4)

$$\Delta_\perp P = \int_{-\infty}^{\tau}\left(\frac{\partial^2 P}{\partial x^2} + \frac{\partial^2 P}{\partial y^2}\right)d\tau' \tag{1.30}$$

## 1.5. Echographic probe and image beamforming

### 1.5.1. Probe description

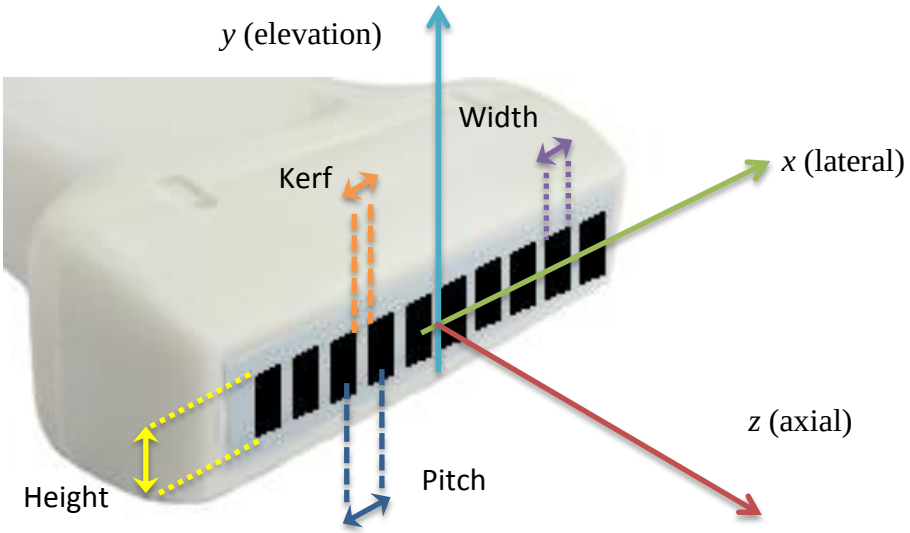


**Figure 1.4: Schematization of a linear array with the width, height, pitch and kerf parameters of the individual element and the landmark (*x*, *y*, *z*).**

In ultrasound medical imaging, different probes are used according to the application, either linear, sectorial or curved probes. The probes are a multi-element transducer and most of them are based on the principle of the piezoelectricity which is the property of some materials to produce an electrical signal when they are submitted to a mechanical force. Moreover, when these materials are excited by an electrical signal, they transmit a mechanical force and reciprocally in reception.

The probe presented in Figure 1.4 is the linear array which is used all along the work. This probe is composed of $N_e$ elements which are characterized by their width and weight in the lateral and elevation direction. Two consecutive elements are spaced out with a kerf distance. The pitch is the distance between the center of two consecutive elements and is equal to the width plus the kerf distance.

### 1.5.2. Image formation

The echographic imaging can be divided in two main steps: the transmission and the reception. The transmission mode is when a subpart of elements of the probe, called aperture, are subjected together to an electrical signal creating an ultrasound (US) wave which travels in the medium. An apodization can be applied in order to reduce sidelobes or to control the transmitting energy. Moreover, to concentrate the beam energy in a focal area, the ultrasound wave transmitted by each element is previously delayed in such way to obtain a summed beam at a focalization point, Figure 1.5. Then the probe switches in reception mode or passive mode meaning that the probe records the pressure that hits its surface and converts it in an electrical signal. Generally the same aperture as in transmission is used. The pressure hitting the aperture's surface is the echoes produced by the scatterers in the medium which arrive at different time to the probe elements according to their position in the medium. Each active transducer of the aperture records the echo and creates a signal called radio frequency (RF) signal. The RF signals providing from one aperture are called pre-beamformed signal. RF signals are then delayed and averaged, with or without any apodization, in order to create one RF-line, Figure 1.6. This operation is named beamforming. The transmission, reception and

beamforming operations are repeated all along the part of the probe in order to obtain one final RF image, also called post-beamformed image.

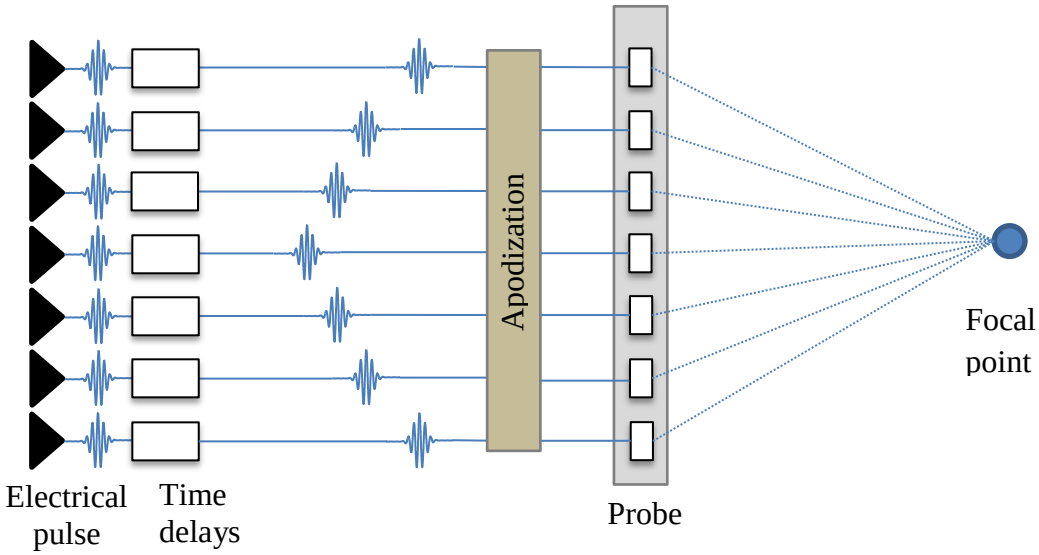


**Figure 1.5: Focalization in transmission used in ultrasound imaging scanners. The time delays applied depend on the distance between one aperture element and the focal area. An apodization can be used to control the transmitted energy.**

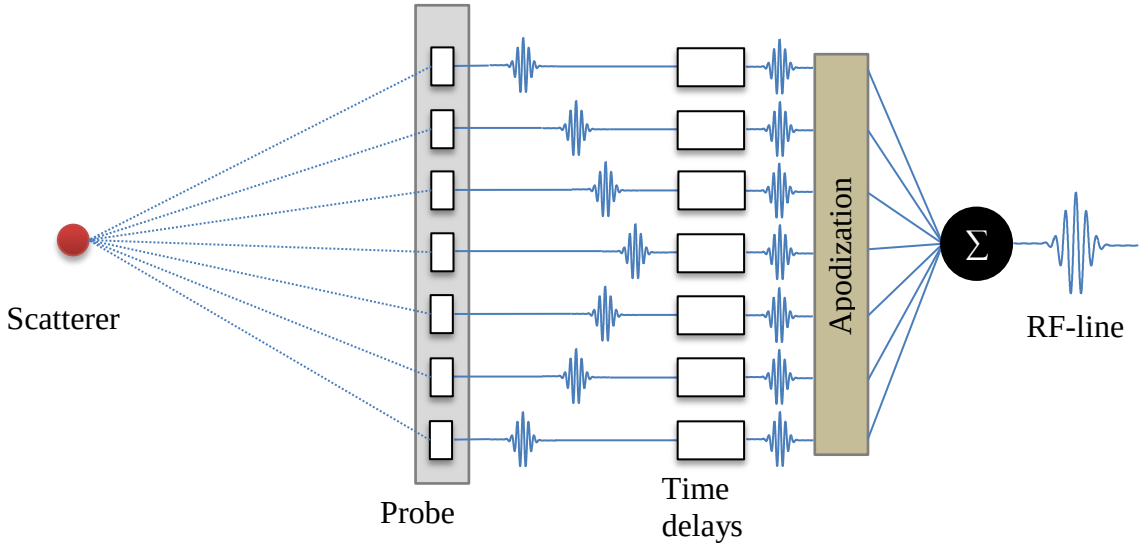


**Figure 1.6: Beamforming in reception used in ultrasound imaging scanners. The time delays applied are proportional to the distance between the considered region and the probe elements. An apodization can be used during the beamforming in order to reduce sidelobes or control the energy.**

Ultrasound images can be represented by different way. The Figure 1.7 shows the RF, B-mode and B-mode log-compressed simulated images of a phantom with wires and hypoechoic cysts (Figure 1.7.a). RF image (Figure 1.7.b) is the first image that can be observed without any other processing after the beamforming. It is difficult to visualize information in the image because of oscillations at the transmitted frequency and its low dynamic. The B-mode image (Figure 1.7.b) is obtained after a demodulation of the RF image or for example by calculating the absolute value of the Hilbert transform of the RF image. The scatterers with the strongest reflection are visible but the image suffers of a low dynamic. In order to improve the dynamic, the B-mode image may be normalized by its own maximum and log-compressed (Figure 1.7.c). The image has a dynamic of 50 dB and the strongest scatterers, the hypo-

echoic cyst and the background are distinguishable. The log-compressed image is the most used imaging mode in medical ultrasound. In the tissue the ultrasound are attenuated when going deep. The attenuation effect is compensated using a time gain compensation (TGC) amplifier. The amplifier increases the signal as a function of the depth.

In section 1.4, it was demonstrated that an ultrasound wave at frequency $f_0$ has a nonlinear propagation generating harmonics, $2f_0$, $3f_0$… Harmonics have the properties to have a higher spatial resolution than the fundamental but a lower energy and penetration depth. The RF image contains all the information backscattered, i.e. the transmitted frequency $f_0$ and its harmonics.

In Figure 1.7, the images are represented with the entire spectrum also call broadband images. From the broadband image, the fundamental image and the second harmonic image, called harmonic image, can be extracted. The fundamental image is the RF image filtered with a low pass filter close to the fundamental frequency of the transmitted ultrasound wave. The second harmonic image is the RF image filtered with a high pass filter.

In Figure 1.8, the broadband, fundamental and second-harmonic B-mode images log compressed are presented with a 50 dB dynamic. All images are normalized by the maximum of the broadband image. Figure 1.8.a and Figure 1.8.b are similar because the level of harmonics component is low. Figure 1.8.c shows that energy of the second harmonic is lower than fundamental image and the second harmonic signal increased as the depth. The granular texture in the Figure 1.8.c is also thinner than the granular texture on the two other images in Figure 1.8.

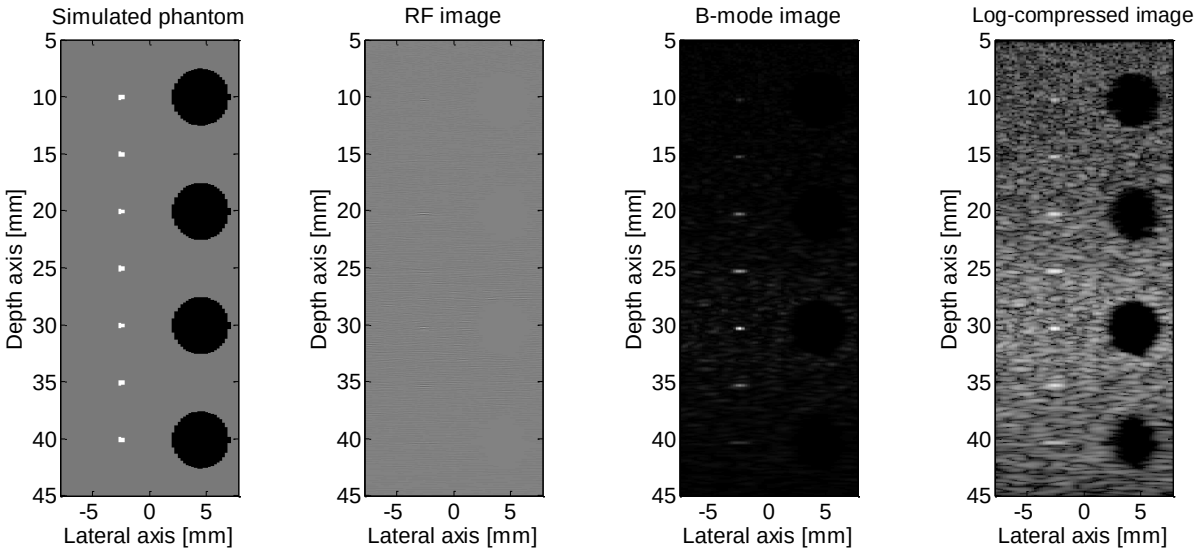


**Figure 1.7: Illustration of different simulated ultrasound image: (a) schematic representation of the simulated phantom, (b) RF image, (c) B-mode image and (d) B-mode image log-compressed with a dynamic of 50 dB.**

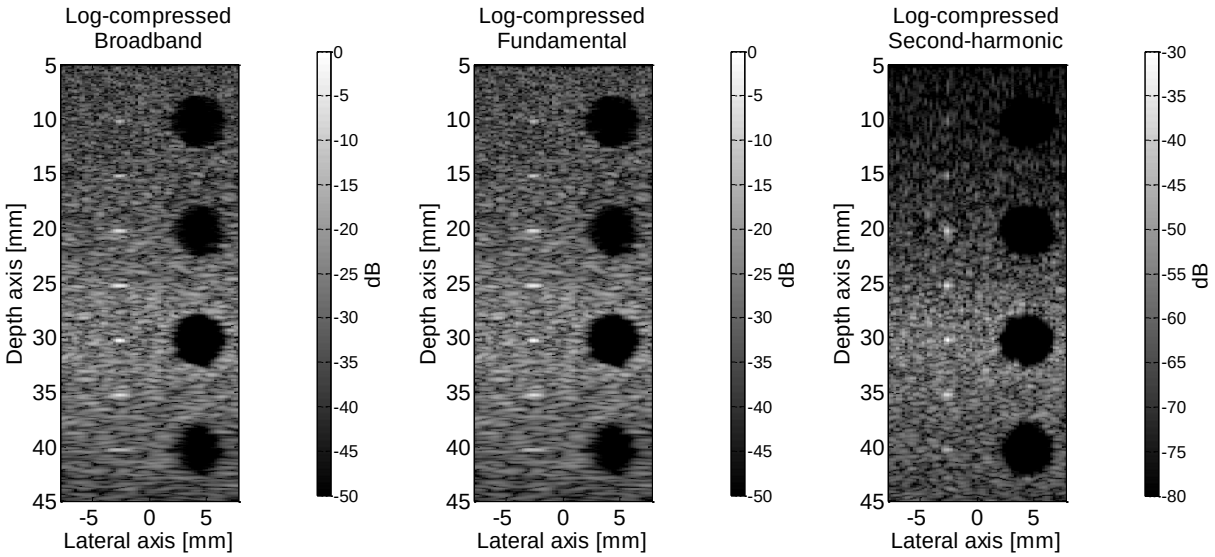


(a) (b) (c)

**Figure 1.8: Illustration of a (a) broadband B-mode image log-compressed, (b) fundamental B-mode image log-compressed and (c) second-harmonic image log-compressed. The broadband, fundamental and second harmonic images are normalized by the maximum of the broadband image. All images have a dynamic of 50 dB.**

The fundamental and the second-harmonic imaging are implemented on commercial scanners. The harmonic imaging is used for its higher resolution than in fundamental imaging and with contrast agents which are highly non-linear scatterers (Mesurolle et al., 2007) (Choudhry et al., 2000).

## 1.6. Evaluation of the image quality

The image quality or the performance of the ultrasound equipment are evaluated with different parameters such as the signal-to-noise ratio (SNR), the contrast-to-noise ratio (CNR), the spatial resolution and the acquisition time (Stetson, Sommer and Macovski, 1997) (Jespersen, Wilhjelm and Sillesen, 1998) (van Wijk and Thijssen, 2002) (Thijssen, 2003).

### 1.6.1. Signal-to-noise ratio

In ultrasound B-mode images, the speckle can be considered from two points of view. On one hand, the speckle is a source of information that can be used for tissue characterization or movement measurement (Thijssen, 2003) (Wagner et al., 1983). On the other hand, the speckle degrades the image and may be considered as noise (Wagner et al., 1983). The speckle noise is quantified by the signal-to-noise ratio (SNR) corresponding to the ratio between the mean, $\mu$, and the standard deviation, $\sigma$, of the image amplitude in a region-of-interest (ROI).

$$SNR = \mu/\sigma \tag{1.31}$$

### 1.6.2. Contrast-to-noise ratio

The quality of an image can be based on its property to distinguish different part in a medium. The lesion detectability is calculated through the contrast-to-noise ratio (CNR), defined as the difference between the mean signal in a region-of-interest (ROI), $\mu_{ROI}$, and the mean signal in the background, $\mu_{back}$, divided by the square root of the sum of squared

standard deviation in the same areas, $\sigma_{ROI}$ and $\sigma_{back}$, respectively (Thijssen, 2003) (Stetson, Sommer and Macovski, 1997) (Jensen et al., 2012):

$$CNR = \frac{\left|\mu_{ROI} - \mu_{back}\right|}{\sqrt{\sigma_{ROI}^2 + \sigma_{back}^2}} \quad \textbf{(1.32)}$$

The ROI is usually the center of a cyst and the background is the surrounding background of the cyst. The considered ROI and surrounding background areas have the same surface. Higher is the CNR, better is the contrast in the image. It is easier to distinguish to different part in the medium if the contrast is high between the two parts.

### 1.6.3. Spatial resolution

The spatial resolution is the capacity to distinguish two close scatterers. The spatial resolution is characterized by the axial resolution, the lateral resolution and the elevation resolution. The axial (or longitudinal) resolution is along the axis of the ultrasound beam whereas the lateral is the scan plane and perpendicular to the axial resolution and the elevation resolution is perpendicular to the scan plane. The spatial resolution is strongly dependent to the beam shape of the transmitted and received signal described by:

- The transmitted frequency
- The number of cycles in the transmitted signal
- The aperture and the geometry of the probe
- The depth of interest

The axial resolution depends on the two first parameters which define the length of the transmitted pulse in the medium:

$$pulse\ length = n_{cycles}\frac{c_0}{f_0} = n_{cycles}\lambda \quad \textbf{(1.33)}$$

Shorter is the pulse length, better is the axial resolution. Decreasing the number of cycles and increasing the pulse frequency improve the axial resolution. Nevertheless, with a short pulse length, the energy transmitted in the medium is low and for a high frequency, the penetration depth of the ultrasound wave is short. There is a tradeoff between the penetration depth and the axial resolution. The lateral and elevation resolutions are impacted by the others parameters.

The spatial resolution is evaluated by using the image of a thin wire or thanks to the point spread function (PSF). The PSF corresponds to the response of a theoretical unique punctual scatterer in the medium. The resolution is evaluated by considering the full width at half maximum (FWHM) in lateral and axial direction on the image of the thin wire or the PSF (van Wijk and Thijssen, 2002). An example is given in Figure 1.9. The PSF is displayed as a RF image (Figure 1.9.a-c) or as a B-mode image (Figure 1.9.d-f). B-mode images are normalized by their own maximum and the FWHM is highlighted by the black line. Higher the number of cycles, lower the axial resolution and higher the frequency, better the both spatial resolutions.

### 1.6.4. Acquisition time and frame rate

One main characteristic of the echographic imaging is the possibility of a real-time implementation. Depending on the number of lines performed to obtain an image, on the depth of the tissue explore, the acquisition time of the echography can be increased or decreased. The acquisition time is calculated by taking into account the maximum investigated depth $z_{img}$, the steering angle, $\theta_i$, of each shot, the number of angles, $N_\theta$, the number of scan lines for each individual angle, $N_{line}$, and the sound velocity in the medium, $c_0$ (Jespersen, Wilhjelm and Sillesen, 1998):

$$t_{acq} = \sum_{i=1}^{N_\theta} \frac{N_{line}}{\cos(\theta_i)} \frac{2z_{img}}{c_0} \tag{1.34}$$

It is more common to speak about the frame rate, so using the acquisition time, it is possible to express the frame rate as:

$$frame\ rate = 1/t_{acq} \tag{1.35}$$

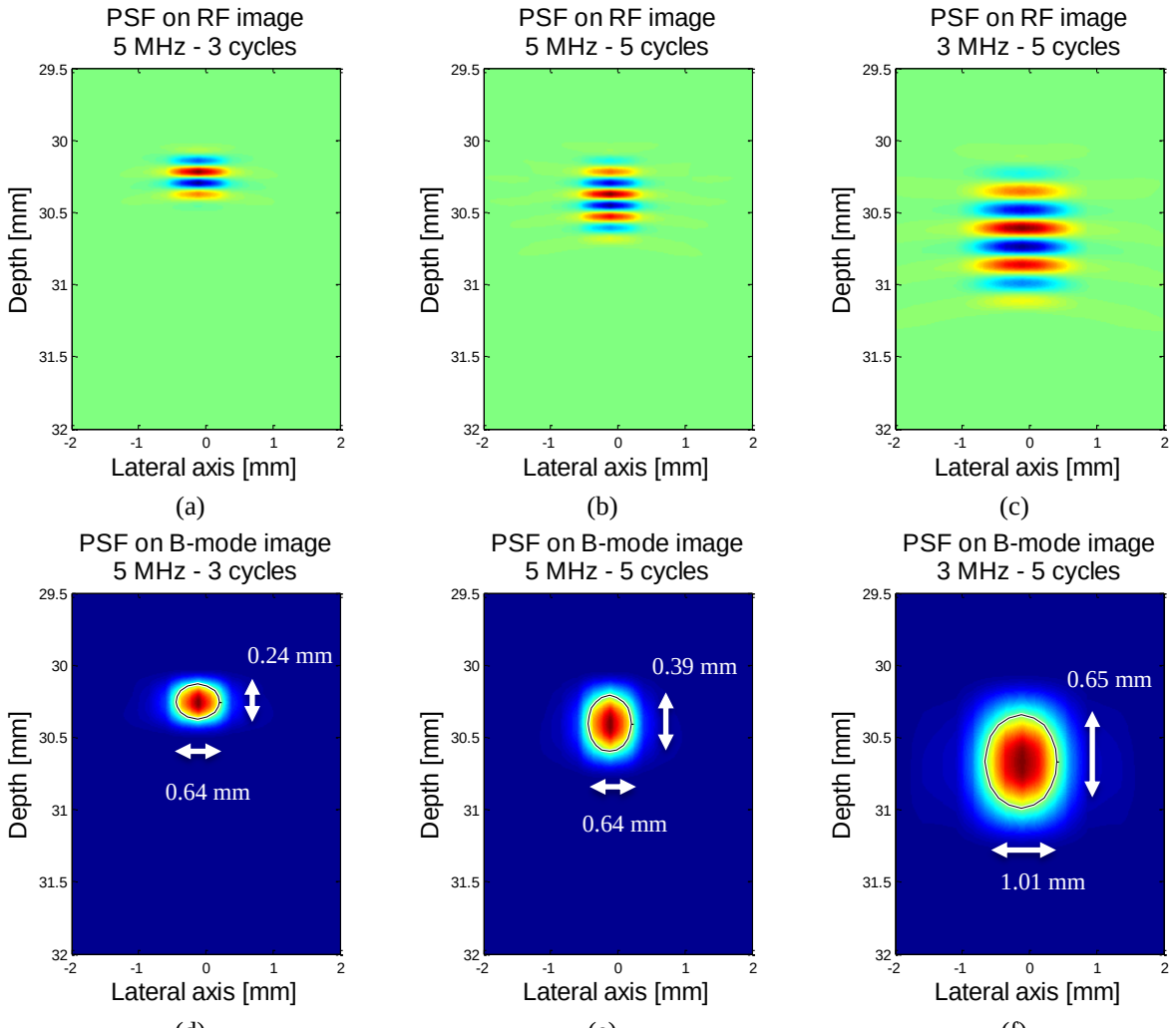


**Figure 1.9: PSF on simulated RF and B-mode image of a punctual scatterer with different transmitted parameters. (a, d) a 3-cycles of a 5 MHz sine, (b, e) a 5-cyles of a 5 MHz sine and (c, f) a 5-cycles of a 3 MHz sine.**

## 1.7. Discussion and conclusion

This chapter introduces a part of the background of medical ultrasound imaging. The linear and nonlinear propagation models have been presented, as well as the image beamforming, the difference between RF images and B-mode images, harmonic imaging and the parameters used to characterize the image quality. Another main parameter for this work has been presented, the nonlinearity parameter *B/A*. The evaluation of the *B/A* parameter can bring a new modality for tissue characterization or parametric imaging.

In the next section, different methods to improve the image quality are presented. The improvement of the image quality is an important part of researcher's work in order to bring new possibility to clinicians to detect healthy or malign organs. It is a compromise between SNR, CNR, spatial resolution and acquisition time. Moreover a state of the art of nonlinearity parameter *B/A* measurement that exist in the literature is presented.

# I. Ultrasound imaging improvement

# Chapter 2

# Speckle noise reduction, contrast and resolution improvement

Nowadays, ultrasound imaging is a common diagnostic tool thanks to its non-invasive behavior and relatively cheap equipment. However, ultrasound imaging has drawbacks usually linked to the ultrasound equipments and ultrasound limitations. A non-exhaustive list of limitations is the speckle and clutter noise, the low contrast and the low resolution outside the focal area. Clutter noise consists of spurious echoes which can often be visualized within a breast cyst (Entrekin et al., 1999). All these limitations are usually linked, and the improvement of one parameter can degrade another one. If the speckle and the clutter noise are reduced, the contrast is improved but the resolution can decrease. Despite its limitations, ultrasound imaging is used more and more in diagnosis imaging, therapy aided by imaging, blood velocity, to detect breast lesion, to track the carotid wall…

In this chapter, a state of the art of techniques improving the ultrasound image is presented in two sections. In the first section, the speckle reduction quantified by the signal-to-noise ratio (SNR) and the contrast improvement techniques are presented. In the second section, the resolution improvement approaches are developed.

## 2.1. Speckle reduction or contrast improvement

The speckle noise reduction or the contrast improvement mainly started since the 80's. The comprehension of the speckle is a primordial point in order to reduce it and to improve the contrast in the image. In a resolution cell, which is the smallest resolvable detail by a scanner, it is assume that there are many scatterers. When the scatterers in the resolution cell are insonified, theirs echoes have phases considered as random (the number of scatterers and their positions are unknown) and their echoes have constructive or destructive interferences. If it is a constructive interference, it gives a bright point. While for a destructive interference, it gives a black point. The works of (Burckhardt, 1978) (Abbott and Thurstone, 1979) (Wagner et al., 1983) (Wagner, Insana and Smith, 1988) (Thijssen, 2003) bring information about the statistics and the behavior of the speckle in ultrasound images.

The resolution cell and the texture of the speckle in an ultrasound image depend on the transducer characteristics and the transmission or the reception set up. Several parameters can interact with the speckle texture such as the change of the transmitted frequency, the shift of the transducer (or the aperture)… In case of two acquisitions with different transmission or reception set up, the speckles of the two acquisitions are uncorrelated. So a combination of these two acquisitions gives a new image with a speckle smoothed. The knowledge of the speckle texture behavior brings the possibility to propose new transmissions set up called pre-treatment techniques. The transmission-reception strategies use particular transmissions or reception so the speckle noise in the image may be reduced and the contrast improved. In the case of image processing techniques the image improvement is done on the final B-mode

image. Moreover the image processing techniques can also be applied on the resulting image of transmission-reception strategies.

## 2.1.1. Transmission-reception strategies

### 2.1.1.1. Frequency compounding

Two types of frequency compounding have been proposed. The first one is the 'real' frequency compounding where different signals at different frequencies are successively transmitted. The second one is closer to image processing techniques but it is commonly named frequency compounding. It consists to insonify the medium with a broadband pulse and use a bank of separate narrow band filters in reception. The two approaches are described below.

The first frequency compounding approach is a technique involving the superposition of images made at different frequencies. P.A. Magnin proposed the frequency compounding with multiple narrow bandwidth excitation for phased array images (Magnin, von Ramm and Thurstone, 1982). It is demonstrated that the frequency compounding increases the SNR (1.31) and the degree of improvement is approximately linearly related to the signal burst length transmitted. The Figure 2.1 shows B-mode images of a tissue phantom with two cysts, one bigger than the second, for a 3.0 µs burst excitation. The Figure 2.1.a is the compound frequency scan composed of eight different frequencies from 1.75 MHz to 2.80 MHz and Figure 2.1.b is the simple scan image made at 1.75 MHz. In both images, the biggest cyst is well delimited but the smallest cyst is not well delineated in the simple scan. Using frequency compounding the ability to perceive structural information in the image is increased. A drawback of this frequency compounding approach is its acquisition time which is increased by the number of frequency transmissions.

(a) (b)

**Figure 2.1: Tissue phantom images made with 3.0 µs burst excitation, (a) simple scan at 1.75MHz and (b) compound frequency scan with eight different frequencies from 1.75 MHz to 2.80 MHz (Magnin, von Ramm and Thurstone, 1982).**

The second frequency compound approach is the combination of the transmission of a broadband pulse and the use of several bandpass filters during the reconstruction. U. Bencharit and P.F. Stetson proposed the same transmission method but they evaluated different way to average the RF images after the bank filter processing (Bencharit et al., 1986) (Stetson, Sommer and Macovski, 1997).

U. Bencharit proposed the split-spectrum processing (SSP) approach for ultrasound (non-medical) application. He shows that a linear averaging and mean / standard deviation (MSD), which is an extension of linear averaging with the summed RF lines weighted nonlinearly according to the inverse of their standard deviations, are not the best image reconstruction method (Bencharit et al., 1986).

P.F. Stetson approach is based on the narrowband images (NBI's) for ultrasound medical application (Stetson, Sommer and Macovski, 1997). He proposed an automated gray level mapping and contrast-weighted filtering working with *a priori* information about the location of a lesion or suspected lesion. The proposed gray level mapping method is based on the histograms of the *a priori* lesion and the background regions in the envelope-detected image. Using both histograms, the new gray level is defined with the maximum and minimum of both histograms. The contrast-weighted filtering approach proposed is based on the spectral estimates calculated from the lesion and background regions. A RF filter improving the contrast between the two regions is designed from the two spectral estimates. The Figure 2.2 shows the comparison with the different techniques for a cyst phantom at 3.5 MHz. The conventional B-mode image is shown in Figure 2.2.a and is compared to the contrast-weighted filtering technique (Figure 2.2.b), the automated grayscale mapping (Figure 2.2.c), the classical frequency compounding with five narrowband filters spaced at 500 kHz (Figure 2.2.d) and the combination of all described techniques, the contrast-weighted frequency compounding (Figure 2.2.e**)**. The CNR for each image is given in the figure caption. The CNR values are close for the conventional processing and the contrast-weighted filtering and automated grayscale mapping proposed method. Using the classical frequency compounding, the CNR is improved, the speckle is smoothed but there is a loss of cyst edges. When all techniques are combined, the contrast is improved and cyst edge is well detected.

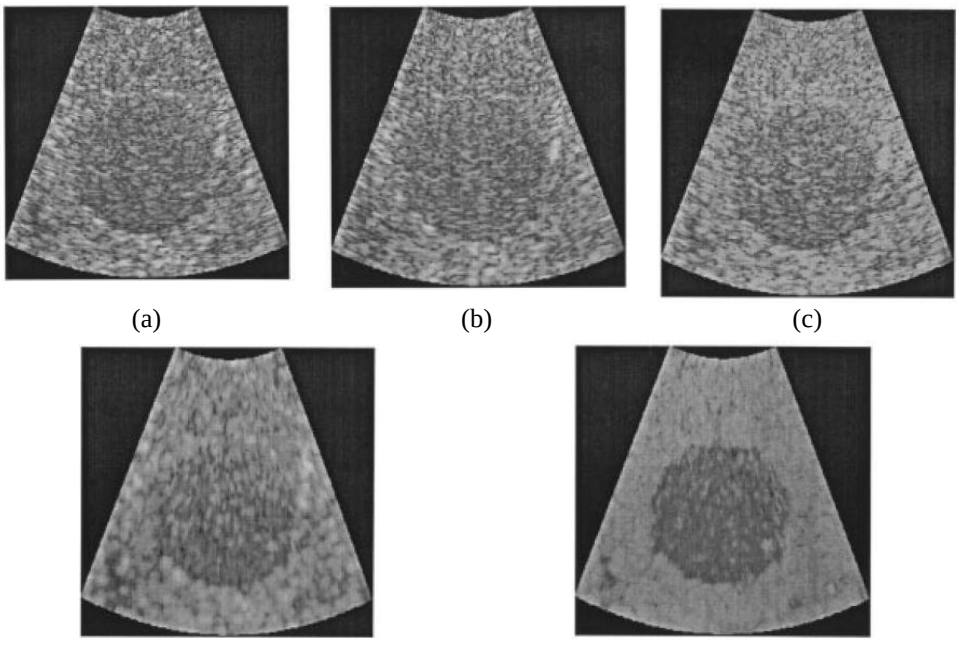


**Figure 2.2: Images of a phantom, normalized to constant mean background gray level at 3.5 MHz and their CNR. (a) conventional processing: CNR = -0.81, (b) contrast-weighted filtering: CNR = -0.85, (c) automated grayscale mapping: CNR = -0.89, (d) classical frequency compounding with five narrowband filters spaced at 500 kHz: CNR = -2.17 and (e) contrast-weighted frequency compounding: CNR = -3.13. The contrast-weighted frequency compounding is the combination of (b), (c) and (d) techniques (Stetson, Sommer and Macovski, 1997).**

#### 2.1.1.2. Spatial compounding

In this state of the art, the spatial compounding is divided in two parts, the spatial incoherent compounding and the plane wave compounding.

Spatial incoherent compounding

The spatial compounding has been more studied than frequency compounding resulting in a large panel of techniques such as transmissions with steered angles (Berson, Roncin and Pourcelot, 1981), the overlap of different phased array scanning with an unique probe (Shattuck and von Ramm, 1982), the combination of spatial and frequency compounding (Jespersen, Wilhjelm and Sillesen, 1998) (Jespersen, Wilhjelm and Sillesen, 1998), the transmission with a phased array probe and the reception with the same probe and two other transducers (Behar, Adam and Friedman, 2003) (Adam et al., 2006),… The spatial compounding also has been studied during clinical experiments (Entrekin et al., 1999) (Entrekin et al., 2001) (Lin et al., 2002) showing its interest to smooth the speckle, improve the contrast and sometimes improve the lateral resolution.

An uncorrelated speckle is obtained by moving the probe manually or with a controlled motor. The development of electronics able to transmit an ultrasound signal without moving the probe but by steering the ultrasound signal transmitted. M. Berson has adapted to a linear array the principle of compound scanning in real-time which consists to explore and visualize the same structure using several beam angles (Berson, Roncin and Pourcelot, 1981). A subset of the elements is selected as the current active aperture and this aperture is used as a phased array to create a beam with one angle. The active aperture is then shifted, as in conventional scanning, all along the probe. Finally, the procedure is repeated for the next beam angle. In reception, the B-mode images have to be corrected in order to have a good superposition of information obtained with different angles of incidence. Figure 2.3 shows the compound B-scan principle. Figure 2.3.a shows the three deflection angles $\phi = 0°$, $12°$ and -12°, Figure 2.3.b illustrates the three images superposed without beam steering correction and Figure 2.3.c illustrates the same images but with beam steering correction. The technique improves the depth of field, but the best quality is obtained only in the central part where the 3 images are superposed.

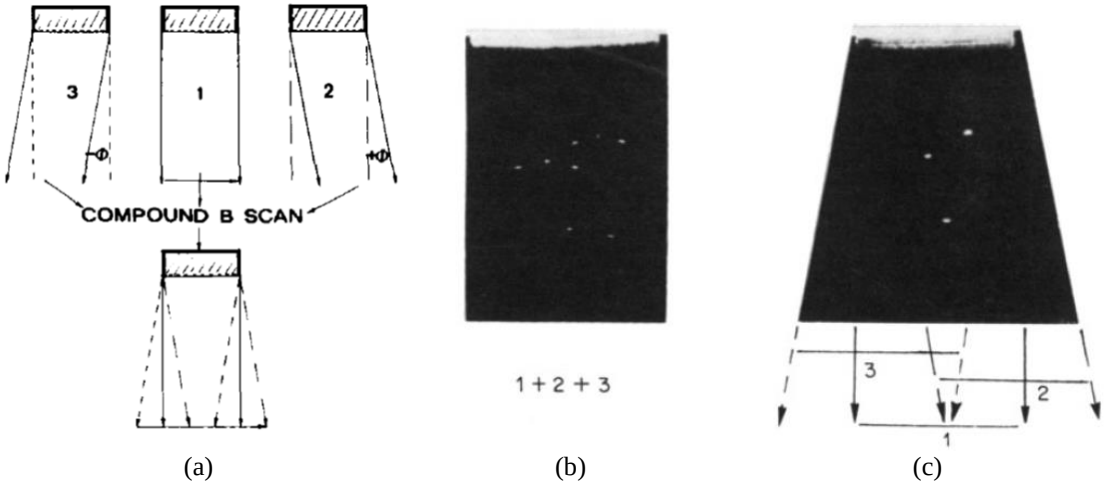


(a) (b) (c)

**Figure 2.3: Ultrasound spatial compounding B-scan principle (Berson, Roncin and Pourcelot, 1981).**

S.K. Jespersen has developed the multi-angle compound imaging (MACI) scanning technique which is the evolution of the M. Berson approach (Jespersen, Wilhjelm and Sillesen, 1998) (Jespersen, Wilhjelm and Sillesen, 1998). The MACI scanning technique combines spatial compounding and frequency compounding in order to reduce sidelobes present when steering uses high angles. The proposition is to decrease the transmitted frequency for the highest angle. The definition of highest angle depends on the system (probe and scanner). The MACI technique improves the boundaries detection and the low contrast

compounded images (Figure 2.4**)**. Figure 2.4 presents the detection of a porcine aorta scanned in water, with, Figure 2.4.a, a compounded images composed of 6 angles ($N_\theta = 6$) and, Figure 2.4.b, the conventional imaging process. Using the MACI technique, the boundaries delimitation is improved and the specular scatterer artefacts are reduced as in the left part of the image where one specular scatterer is suppressed and not the other one which corresponds to information and not a punctual noise. Figure 2.5 shows the contrast improvement and the speckle reduction with the MACI method. Figure 2.5.a is a compounded images composed of 5 angles ($N_\theta = 5$) and Figure 2.5.b is the conventional imaging. Using the MACI method, the cyst detection is improved and the speckle is better smoothed than with the conventional imaging process. The improvement in SNR is close to the theoretical value of $\sqrt{N_\theta}$. Moreover, it was found beneficial to use a smaller angular range for low contrast detection compared to boundaries delimitation improvement. Using a larger angular range might increase grating lobes level obscuring the subtle differences in the scattering level (Jespersen, Wilhjelm and Sillesen, 1998).

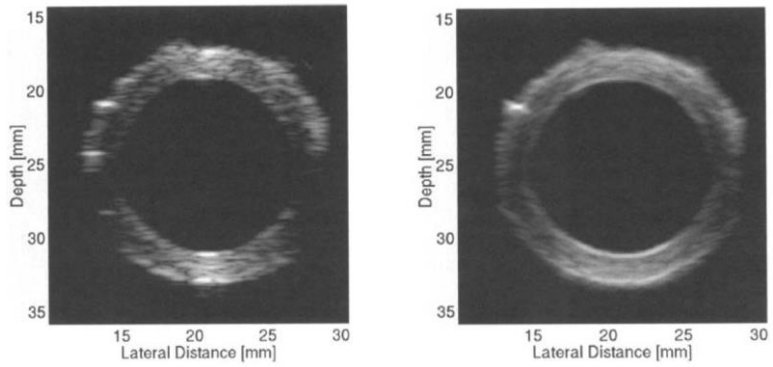


(a) (b)

**Figure 2.4: (a) Conventional image and (b) compounded image with $N_\theta = 6$ angles spaced equally form -25° to 25° of a formalin-fixed thoracic porcine aorta scanned in demineralized water. (Jespersen, Wilhjelm and Sillesen, 1998).**

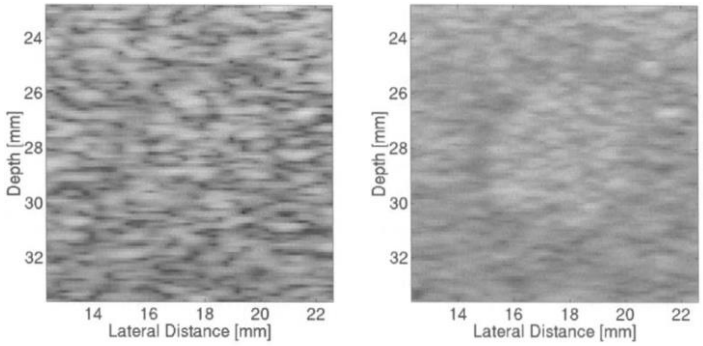


(a) (b)

**Figure 2.5: (a) Conventional image and (b) compounded image with $N_\theta = 5$ angles, spaced equally from -15° to 15° of a 5 mm diameter, +1.5 dB lesion in a low-contrast phantom. (Jespersen, Wilhjelm and Sillesen, 1998).**

D.P. Shattuck developed a 128 array elements composed by 4 adjacent sections of 32 elements (Shattuck and von Ramm, 1982). Each section can be used to produce an independent sector scan. The Figure 2.6 shows the principle of the developed array. Figure 2.6.a corresponds to a simple sector scan and Figure 2.6.b to the compound scan of the 4 adjacent sections. The speckle is the smoothest in the region where all sections are overlapped. G.E. Trahey has developed the same technique for a linear probe where a one-dimensional array is divided into several sub-arrays and an active sub-aperture is translated *N*

times in order to acquire *N* independent images (Trahey, Smith and von Ramm, 1986). The final image is the result of averaging the individual B-mode images. The speckle noise can be reduced as much as $\sqrt{N}$ .

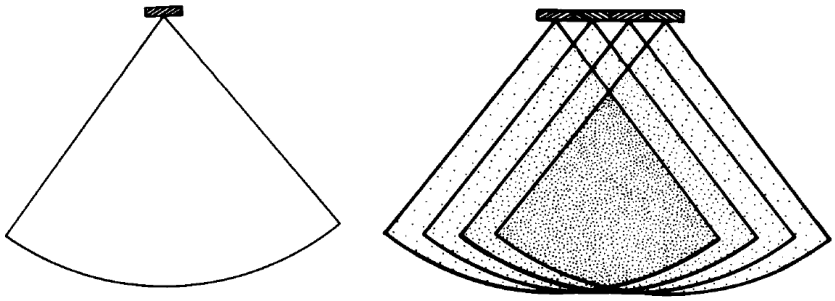

(a) (b)

**Figure 2.6: Sectorial probe for spatial compounding. (a) A simple sector scan and (b) the compound scan with 4 adjacent sections of 32 elements. The center part of the compound scan is overlapped by the fourth sections (Shattuck and von Ramm, 1982).**

V. Behar and D. Adam proposed a new method of spatial compounding imaging using three transducers for data acquisition (Figure 2.7**)** (Behar, Adam and Friedman, 2003) (Adam et al., 2006). The transducer located at the center of the system is a phased array probe that acts as both transmitter and receiver, named Transmitter / Receiver 3 in Figure 2.7. The two other transducers are unfocused pistons that act only as receivers, named Receiver 1 and Receiver 2 in Figure 2.7. The compounded image is obtained by combining the envelope data acquired by each transducer. V. Behar proposed different compounding strategy (Behar, Adam and Friedman, 2003). D. Adam combined the different compounding strategy with a nonlinear filtering in order to decrease the speckle noise (Adam et al., 2006). This method has the advantages to decrease the speckle noise, improve the contrast and do not decrease the lateral resolution without decreasing the image frame rate as required by the conventional spatial compounding imaging.

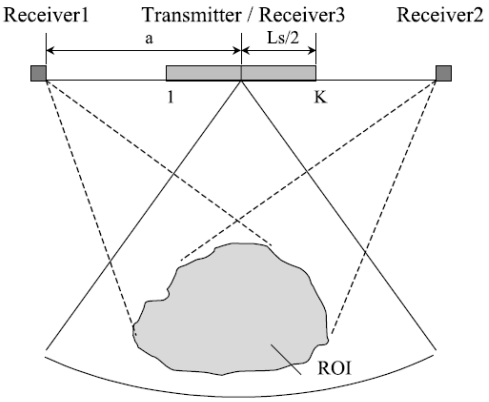


**Figure 2.7: Spatial compounding imaging system with one transmitter / receiver (phased array probe) and two other receivers (pistons) (Behar, Adam and Friedman, 2003) (Adam et al., 2006).**

The advantages of real-time spatial compounding were evaluated in clinical experiments for breast, vascular and musculoskeletal application (Entrekin et al., 1999); (Entrekin et al., 2001); (Lin et al., 2002). The granular appearance of the speckle is decreased with the spatial compounding, the shadowing behind a lesion or a mass is reduced and the delimitation of boundaries is improved. The drawback of the technique is the lost in temporal resolution. With a greater number of frames compounded, motion blurs increases. The number of frames averages has to be adjusted according to the application.

Plane wave compounding

The first objective of plane wave imaging (PWI) was not to improve the image quality but to acquire at a fast frame rate (superior to the classical focalization method) and thus to develop or to improve new imaging modalities such as elastography (Montaldo et al., 2009); (Ramalli et al., 2012), motion estimation (Tanter et al., 2002), cardiac imaging or Doppler imaging (Tanter and Fink, 2014). The principle of PWI is to insonify by a simple plane wave the entire medium in a one shot. The plane wave transmission is produced by the simultaneous excitation of all the probe's elements. The RF echoes are acquired simultaneously by each element. During an offline post processing, backscattered echoes from the unique illumination are set up to form one RF image inducing a short acquisition and reconstruction time.

The offline post processing can be divided in two categories, the time domain and the Fourier domain method. The main difference between the two categories is the computation time, the Fourier method is quicker. G. Montaldo proposed a delay and sum (DAS) method working in the time domain (Montaldo et al., 2009). J.Lu, P. Kruizinga and D. Garcia, proposed three different Fourier methods (Lu, 1997) (Kruizinga et al., 2012) (Garcia et al., 2013). J. Lu proposed a Fourier method using limited diffraction beam (Lu, 1997) (Lu, 1997) (Lu, 1998) (Cheng and Lu, 2006). P. Kruizinga proposed a nonuniform fast Fourier transform for reconstruction (Kruizinga et al., 2012). D. Garcia proposed a method carried out by the Stolt's reconstruction for seismic imaging (Garcia et al., 2013).

An image made with only one plane wave illumination doesn't have a good contrast and lateral resolution. G. Montaldo proposed the coherent plane wave compounding (CPWC) approach (Montaldo et al., 2009). It consists to transmit several slightly tilted consecutive plane waves. The backscattered echoes are coherently compounded improving the contrast and the lateral resolution. The method has also then be applied with the Fourier reconstruction method (Garcia et al., 2013). It is shown by G. Montaldo that in order to keep the same image quality as the focusing approach, a number $N_\theta$ of plane waves should be used (Montaldo et al., 2009):

$$N_\theta = L/\lambda F \tag{2.1}$$

where $L$ is the aperture size, $\lambda$ is the transmitted pulse wavelength and $F$ is the F-number defined by $F = z_f / L$. $z_f$ is the focal depth of the focusing approach. The steering angle for each plane wave $i$ is approximated, for small values of $\theta$ by:

$$\theta_i = \arcsin(i\lambda/L) \approx i\lambda/L, \quad i = -(N_\theta - 1)/2, ..., -(N_\theta - 1)/2 \tag{2.2}$$

After the offline post processing of the $N_\theta$ illuminations in order to reconstruct the $N_\theta$ RF image, the RF images are averaged and the final RF compounded image is obtained. It should be noted that G. Montaldo, P. Kruizinga and D. Garcia proposed a post processing method allowing the use of apodization during the image formation. J. Lu uses limited diffraction beam which are obtained by using particular apodization during the beamforming process.

During this thesis work, the Montaldo method is used so the offline post processing is presented. The post processing beamforming process consists to apply some delay laws and summations, with or without apodization, to focus the backscattered echoes in the receive mode. Each line of the RF image for one illumination is calculated using the same backscattered echoes but with different sets of time delays (Figure 2.8**)**. The final

compounded image is a coherent average of RF image, in the time domain, from all illuminations (Figure 2.9).

The use of different steering angles increases the quality of the B-mode images in terms of noise and artifacts reduction, and resolution improvement, while increasing the acquisition time.

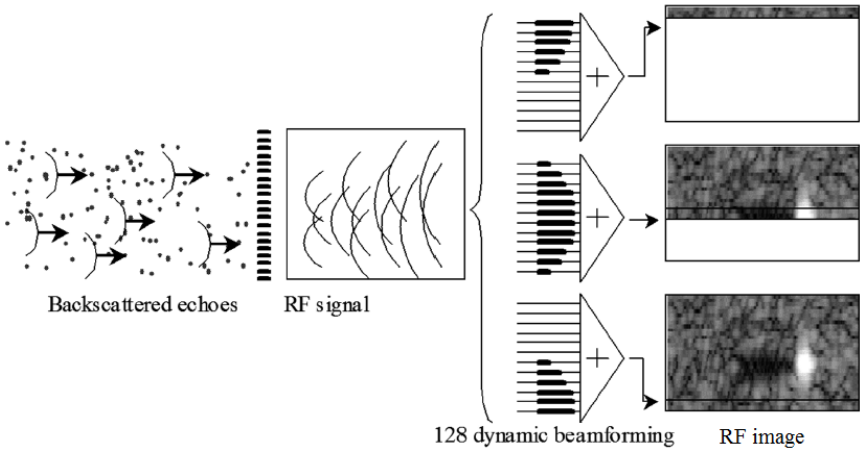


**Figure 2.8: Schematic representation of the Montaldo plane wave reconstruction. The backscattered RF signals are recorded by the transducer array. The beamforming procedure consists in applying time delays laws and summations to the raw RF signals to focus in the receive mode in order to create one RF image. Contrary to standard ultrasonography, each line of the image is calculated using the same RF data set but a different set of time delays (Montaldo et al., 2009).**

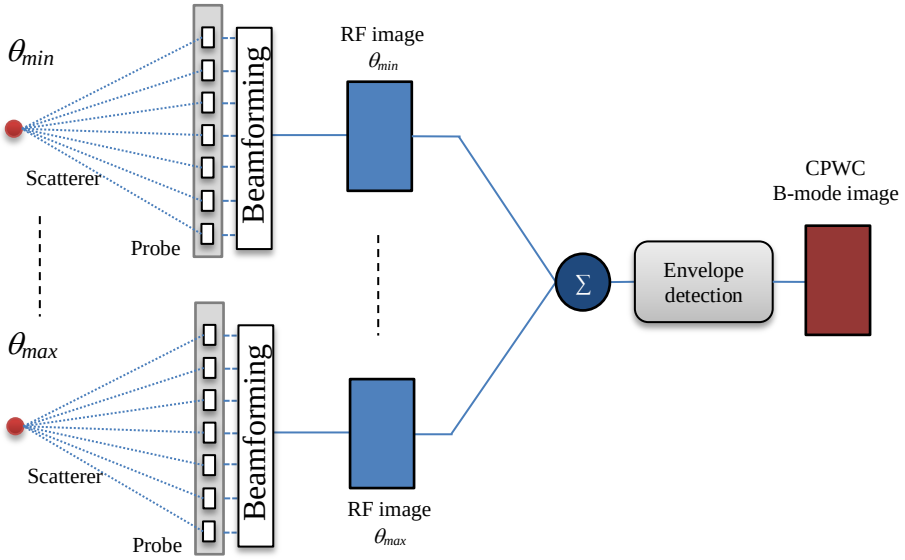


**Figure 2.9: B-mode image reconstruction strategies for coherent plane wave compounding (CPWC). The RF images of all illuminations with different angles are averaged and after an envelope detection, the final CPWC B-mode image is reconstructed.**

#### 2.1.1.3. Harmonic imaging

The second harmonic imaging, called harmonic imaging, is based on the nonlinear property of the tissue. During the propagation of the ultrasound wave transmitted, harmonics are generated because of the nonlinearity of the medium. The harmonic imaging is implemented in ultrasonic scanner and the technique is named tissue harmonic imaging (THI). The principle is to extract the second harmonic component of the backscattered echoes with a high pass filter. The THI is utilized for breast lesions, abdominal disease, liver tissue and the

technique has been evaluated during clinical experiments (Tranquart et al., 1999) (Choudhry et al., 2000) (Frinking et al., 2000) (Rosen and Soo, 2001) (Mesurolle et al., 2007). The use of THI technique improves the contrast, the boundary detection of the lesion and the lesion or disease detection compared to the fundamental imaging. A drawback of the technique is the weak penetration depth due to the attenuation of the second harmonic component.

Moreover, the harmonic imaging can *also* be based on the nonlinear property of ultrasound contrast agents (UCA). The contrast agents are micro-bubbles with sizes less than 10 µm injected into the blood circulation. They allow highlighting the perfused tissues (Frinking et al., 2000) (Bouakaz et al., 2002) (de Jong, Bouakaz and Cate, 2002) (Borsboom et al., 2005). Contrast agents have a strong nonlinear coefficient (Wu and Tong, 1998) and are predisposed for backscattering a lot of energy in harmonics frequencies. The combination of UCA, second harmonic imaging and Doppler technique improves the perfusion imaging application. The UCA are also used with harmonic imaging using coded transmission in order to improve the contrast.

#### 2.1.1.4. Multi pulse and coded transmission

Coded transmissions are based on signal processing using particular transmissions improving the contrast, the SNR or the depth penetration. Two techniques are described in this part, the pulse inversion technique and the coded excitation imaging.

##### Multi pulse: pulse inversion

The pulse inversion (PI) is first proposed to improve the contrast between tissue and microbubbles contrast agent (Simpson, Chin and Burns, 1999) and is dedicated for ultrasonic nonlinear imaging (Shen and Li, 2002). The objective of the technique is to extract second-harmonic component and decrease the fundamental component of the backscattered wave by signal processing, without using a high pass filter. Because when a high pass filter is used to extract second-harmonic, it reduces contrast and axial resolution (Shen, Chou and Li, 2005).

To form a RF line in PI technique, two transmissions are required. A first pulse $x_1(t)$ is transmitted in the media and successively a second pulse $x_2(t)$ in opposite phase is transmitted. The two transmitted pulses and their corresponding received echoes are expressed as:

$$\begin{aligned} x_1(t) &= x(t) \\ x_2(t) &= -x(t) \end{aligned} \xrightarrow{\text{propagation}} \begin{aligned} y_1(t) &= a_1x(t) + a_2x^2(t) + a_3x^3(t) + \dots \\ y_2(t) &= -a_1x(t) + a_2x^2(t) - a_3x^3(t) + \dots \end{aligned} \quad \textbf{(2.3)}$$

where $a_1x(t)$ is the linear component, $a_2x^2(t)$ the second harmonic component, $a_3x^3(t)$ the third harmonic component, etc. The echoes from the first pulse and the second pulse are summed together to obtain a RF PI line:

$$y_{PI}(t) = y_1(t) + y_2(t) = 2a_2x^2(t) + 2a_4x^4(t) + \dots \quad \textbf{(2.4)}$$

The equation (2.4) shows that the second harmonic signal is extracted without interference coming from the signal at fundamental frequency. The PI technique extracts all even harmonics.

The drawbacks of this technique are the frame rate decrease because two pulses are successively sent and so motion artefacts can appear. C.C. Shen reported that the tissue harmonic signal extracted with the PI technique is highly sensitive to motion (Shen and Li, 2002) (Shen, Chou and Li, 2005). When the tissue moves, the linear signal of the tissue is not

correctly suppress, so the linear signal is present in (2.4) and the tissue harmonic signal decreases. Figure 2.10 shows an example of PI images of Levovist® microbubbles associated with different axial motions between the transmission of positive and negative pulse. The contrast-to-tissue ratio (CTR) is estimated for each image. CTR (Figure 2.10.b**)** is calculated using mean intensities of the background and the contrast regions indicated by the two boxes in each B-mode image (Figure 2.10.a**)**. With tissue motion, the background intensity increases and the CTR decreases.

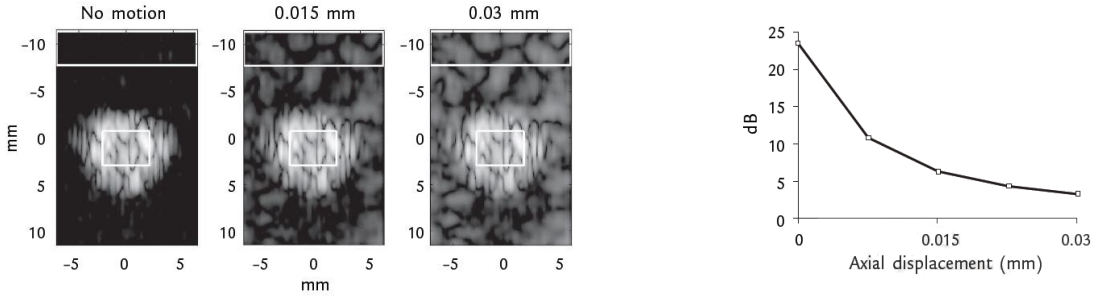


(a) (b)

**Figure 2.10: B-mode images of pulse inversion technique of Levovist® microbubbles associated with (a) different axial motions between the positive and negative pulses, 0 mm, 0.015 mm and 0.03 mm and (b) their corresponding contrast-to-tissue ratio (CTR) (Shen, Chou and Li, 2005).**

Coded transmission

The coded transmission techniques were developed for radar systems for the conflicting requirements of simultaneous long-rang and high-resolution performance in radar systems. Coded excitation operates long pulses transmission in which a code is embedded. After reception, the echo signal is filtered through an autocorrelation-based filter to detect and remove the code. The process is called decoding or compression.

The coded transmission can be classified in two categories, the phase-modulated signals and frequency modulation signals. The first category consists of signals with a constant frequency where the phase is modulated, with Golay code or Barkey code (Takeuchi, 1979) (Peng, Han and Lu, 2006). The second category consists of signal with a constant phase where the frequency is modulated. If the frequency increases, it is an up-chirp or if the frequency decreases, it is a down-chirp. The chirp imaging is the mostly used for ultrasound imaging and improves the penetration depth and SNR improvement for a classic probe (Misaridis et al., 2000) and intravascular probe (Maresca et al., 2012) or for contrast agent imaging (Borsboom et al., 2005). However, side lobes ranges appear in the axial direction due to the chirp compression. The coded excitation has the advantage to increase the energy transmitted without increase the pressure transmitted (Takeuchi, 1979) (Borsboom et al., 2005). Thus, it allows a reduction of the power reducing the possibility of hazardous effect for tissue.

### 2.1.2. Image processing

The image processing techniques presented in this section are the different filters presented in the literature. The filters can find their origin in different domains such as image processing, signal processing… When a new filter is found in one domain, it is usually tested in another domain and for different applications in order to test its efficiencies. The described filters are subdivided in different section as linear filters, nonlinear filters, adaptive filters and multi scale filter.

#### 2.1.2.1. Linear filters

The linear filters have a linear relationship between the initial image *I* and the resulting image *I'* and there action can be described as a convolution based on a kernel representing the shape and size of the neighborhood:

$$I'(x_0, y_0) = FI = \frac{1}{N}\begin{bmatrix} a_{11} & \dots & a_{1m} \\ \vdots & & \vdots \\ a_{n1} & \dots & a_{nm} \end{bmatrix} I \quad \textbf{(2.5)}$$

where $I'(x_0,y_0)$ is the intensity of the pixel at the position $(x_0,y_0)$ where the average is done and $N$ is the average of the weights ($a_{nm}$) of the filter $F$. Larger is the filter higher is the speckle smoothing and more the final image lost details. Different weights might be used as with the Gaussian filter. The weights of the filter follow a Gaussian law $G$:

$$G(x, y) = \frac{1}{2\pi\sigma^2} e^{-\frac{(x^2+y^2)}{2\sigma^2}} \quad \textbf{(2.6)}$$

The $\sigma$ parameter is the standard deviation and the Gaussian width. $\sigma$ is chosen by the user and control the smoothing: higher is $\sigma$ higher is the smoothing.

#### 2.1.2.2. Nonlinear filters

The nonlinear filters can't be described as a convolution filter. A multitude of nonlinear filters exist as median, bilateral, Wiener, homomorphic filter… These filters are used and analyzed for medical imaging (Sivakumar, Gayathri and Nedumaran, 2010). The cited filters are presented and detailed in Appendix A.

#### 2.1.2.3. Adaptive filters

The adaptive filters have been mostly developed for speckle reduction and are widely used in radar and US image restoration. The adaptive filters assume that speckle noise is essentially a multiplicative noise and are based on the local statistical parameters, the mean and the variance. The common adaptive filters are Lee's filter (Lee, 1980), Frost's filter (Frost et al., 1982) and Kuan's filter (Kuan et al., 1985) and papers made comparison of them in radar (Lopes, Touzi and Nezry, 1990) and in US imaging (Coupe et al., 2009) (Sivakumar, Gayathri and Nedumaran, 2010). The name, adaptive filters, informs the user that these filters are not a 'one shot filter', but have to be update during their process in order to make the filter more efficient.

#### 2.1.2.4. Multi scale filter

The multi scale filtering concept is proposed by S.G. Mullat and it is based on the wavelet transform (Mallat, 1989). The concept is to represent an initial signal or image by an approximated signal or image and detailed coefficient at different resolution scales. The approximated subband is obtained by a low pass filter, given the scaling coefficients, and the detail subband is obtained by a high pass filter, given the wavelet coefficients. In image processing, the detailed subband is divided into three orientations, horizontal, vertical and diagonal directions. The Mallat algorithm consists to firstly, extract the approximated and detailed subbands. Thus the same operation is done on the approximated subband at the half

resolution. The algorithm is finished when the approximated subband is totally smooth and all the information is in the detailed subband (Mallat, 1989) (Pizurica et al., 2006).

The wavelet filtering method consists to firstly, calculate the discrete wavelet transform of the image by the Mallat algorithm, then filter the noise from the detailed subbands and finally to reconstruct the image by applying the inverse wavelet transform. This method has been applied in US (Zong, Laine and Geiser, 1998) (Gupta, Chauhan and Sexana, 2004) (Pizurica et al., 2006) (Sivakumar, Gayathri and Nedumaran, 2010) and it is applied to reduce the speckle noise or to improve the contrast. The main work is on the threshold use on the detail subbands to reduce the speckle.

#### 2.1.2.5. Conclusion

Different methods were proposed to reduce the speckle noise and to improve the contrast in the image. The transmission-reception strategies are mostly based on multiple acquisitions unlike the image processing techniques are based on the statistic and local property of the image. It is possible to combine both type of techniques and improve the image quality.

However, the speckle noise reduction is usually linked to a decrease of the resolution. In the next section, a state of the art of spatial resolution improvement is proposed.

## 2.2. Resolution improvement

In different domains, the first perception of the quality of an image is related to its resolution. Nowadays, people used to have an image with an 'infinite resolution' with smartphones, numeric cameras and televisions. This resolution is linked to the density of pixels par inch (ppi) of the screen or of the CCD camera used to take the picture. A high density of ppi gives the illusion of the eyes to don't see the pixels. In image processing the size of the image is not as important as the property to well delimit the boundaries of the different parts in the image or the sensation of sharpness which it is linked to the transmitted and received parameters.

The resolution improvement is generally based on some techniques similar to contrast improvement techniques previously described, so only a short resume is given for these techniques.

### 2.2.1. Spatial compounding

#### 2.2.1.1. Multi-focus imaging

The drawback of the ultrasound approach when a single focalization is used is the concentration of energy in a unique focal area. As it was described in the section 1.6.3, the best resolution is obtain in the focal area. If the region of interest is bigger than the focal area, the user has only a part of the ROI with a good resolution and the rest suffers of a decrease of resolution or worst, a total blur effect. A simple solution is to transmit successive shots with different focal depths and to combine the images in order to create one final image with a field of view and sharpness improved. The method is called multi-focus (MF) imaging and the technique, already implemented in echographic scanner, can be used in real time. However the acquisition time increases proportionally to the number of successive shots.

Figure 2.11 illustrates the resolution improvement in simulation for a hypoechoic cysts and wires phantom. CREANUIS simulator with a 64 elements probe and a pitch of 245 µm was used (Varray et al., 2013). A three-cycle sinusoidal burst at 5 MHz, weighted by a

Hanning window was transmitted. The Figure 2.11.a shows the log compressed ultrasound image with a single transmit focus (SF) depth at 30 mm and Figure 2.11.b consisting to multi-focus imaging method with seven focal depths spaced 5 mm apart between 10 and 40 mm. Outside the focal depth in Figure 2.11.a, the wires and the cyst boundaries are not well delimited. In Figure 2.11.b, the wires and cysts are well delineated. In this transmission conditions, the acquisition time of SF is about 3.7 ms and for MF it is 26.2 ms. The acquisition time of MF is multiplied by seven, the number of focal depths.

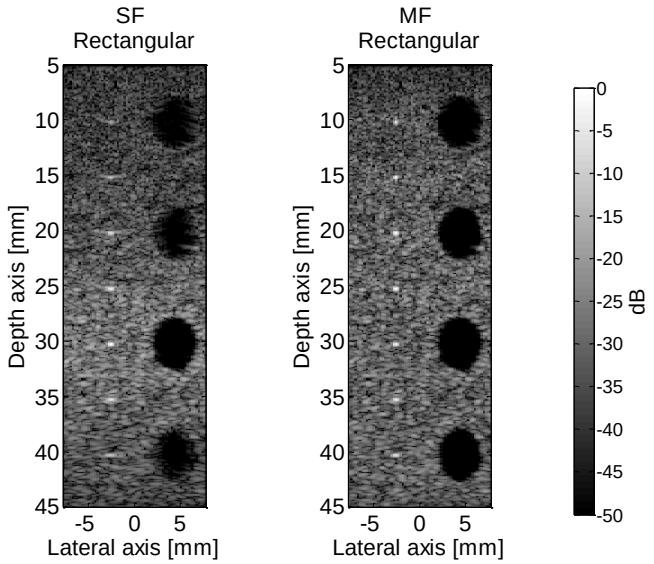


**Figure 2.11: Log compressed CREANUIS ultrasound images of hypoechoic cysts and wires from the CREANUIS simulator for (a) one focal depth at 30 mm and (b) multi-focus image with seven focal depths, spaced 5 mm apart between 10 and 40 mm. A rectangular apodization is used during the beamforming. The dynamic of the image is 50 dB.**

#### 2.2.1.2. Plane wave compounding

The plane wave compounding has been proposed to improve the image quality and more precisely the contrast even if it was not its first interest. It was demonstrated by G. Montlaldo that it is possible to obtain the same image quality as the focusing approach in coherent plane wave compounding (CPWC) approach (Montaldo et al., 2009). The CPWC method as theoretically the same resolution at the focal depth but the approach improves the resolution in all the rest of the image. J. Cheng and D. Garcia also indicate the interest of CPWC for resolution improvement (Cheng and Lu, 2006) and (Garcia et al., 2013). Each team explain that its technique give the best resolution improvement. D. Garcia compared the lateral resolution improvement at different depths for different sets of angles for the DAS reconstruction (Montaldo), Lu reconstruction and f-k reconstruction (Garcia) (Garcia et al., 2013). The f-k method gives the best lateral resolution but the gain in terms of resolution depends on the depth. For a large number of plane waves transmitted, the resolution of all reconstruction's technique is close. One drawback of the evaluation is the change of the set of compounding angles. D. Garcia used either 5 angles (from -2°:+2°, each degree) or 15 angles (from -7°:+7°, each degree). B. Denarie has reported that the resolution in the image is only a function of the maximum angle used and not of the angle sequence (Denarie et al., 2013). It is demonstrated by starting from (2.1). If an odd number of angles $N_\theta$ is used, the F-number can be expressed as:

$$F = \frac{L}{N_\theta \lambda} \approx \frac{1}{N_\theta \Delta\theta} = \frac{1}{2\theta_{\max}} \frac{N_\theta - 1}{N_\theta} \approx \frac{1}{2\theta_{\max}} \quad \textbf{(2.7)}$$

where $\Delta\theta$ is the difference angle between two successive angles and $\theta_{max}$ the maximum angle of the angle sequence. It is so possible to decimate the number of angle and to improve the frame rate without decreasing the lateral resolution. However the reduction of the number of angles introduces grating lobes which can reduce the image quality.

#### 2.2.1.3. Synthetic aperture

Synthetic aperture (SA) finds its origin from the radar application in 1950s and has been investigated in ultrasounds since the late 1960. If during a period the use of the method for ultrasound application was punctual, the technique finds an interest for Doppler and high frame rate imaging (Jensen et al., 2006) (Trots et al., 2011). The SA principle is presented in Figure 2.12. A single element in the transducer aperture is used for transmitting a spherical wave. The wave covers the entire image. During the reception, all the elements of the transducers record the backscattered echoes. After beamforming, a low resolution image is constructed which is only focused in receive due to the un-focused transmission. The same operation is repeated for each elements of the aperture. A final image with a high resolution is reconstructed after the coherent average of the image with a low resolution. The resolution is improved in function of the number of transmissions used.

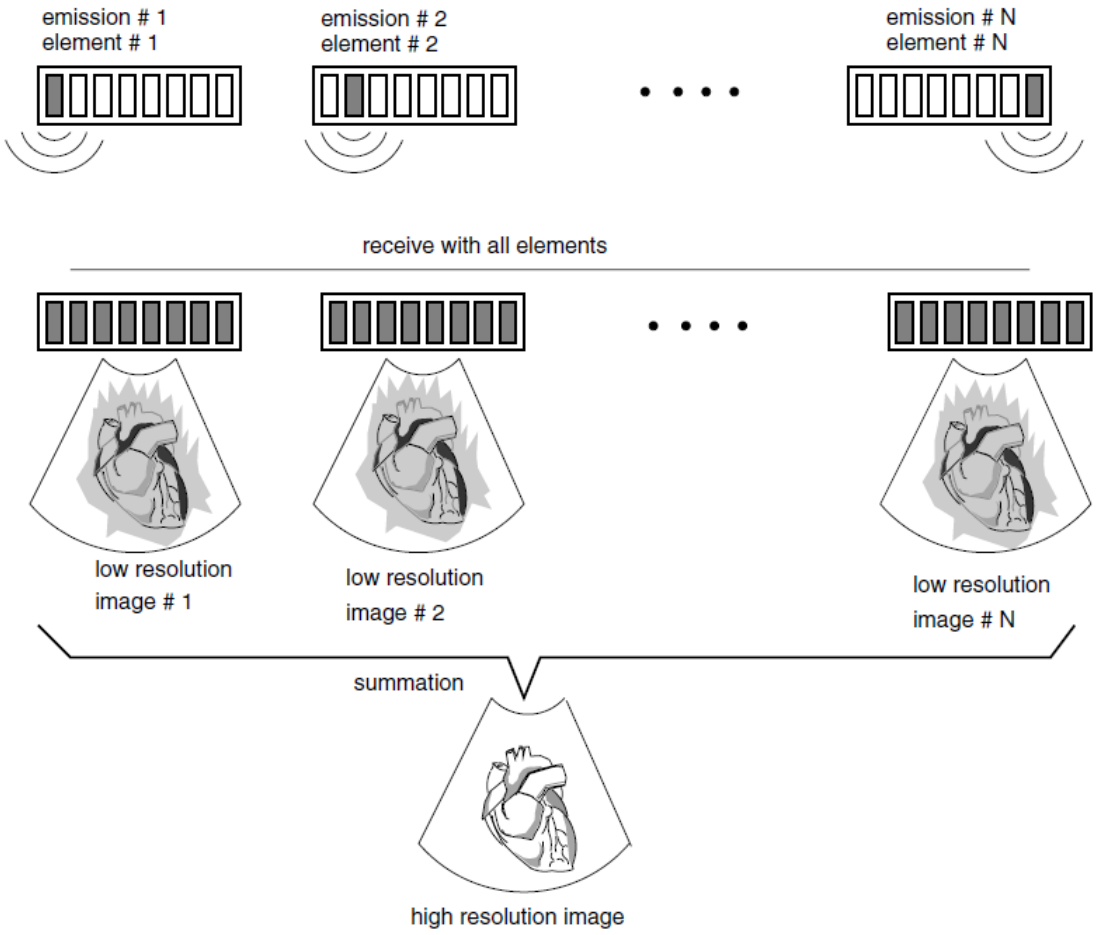


**Figure 2.12: Principle of the synthetic aperture ultrasound imaging. The media is successively insonified by one element of the probe. During the reception all elements acquire backscattered echoes and an image with low resolution is formed. After N emission, and N reception, the N images with low resolution are summed in order to create one final high resolution image (Jensen et al., 2006).**

### 2.2.2. Harmonic imaging

The resolution in ultrasound image is linked to the frequency employed. An easy way to improve the resolution is to increase the frequency. Another solution is to use the nonlinear property of the tissue and extract the harmonics components. This solution have been evaluated and it is used in hospital (Tranquart et al., 1999) (Choudhry et al., 2000) (Frinking et al., 2000) (Rosen and Soo, 2001) (Mesurolle et al., 2007). The resolution improvement is as well as in the axial as the lateral axis. The advantage of this technique is its simple utilization and cost. If the transducer has a large bandwidth, allowing *f0* and *2f0*, the technique is possible. The unique limitation is the highest attenuation of the harmonic compared to the fundamental imaging.

### 2.2.3. Coded transmission

#### Pulse inversion

The PI approach for resolution improvement is close to harmonic imaging. Instead of using a filter in order to extract the second harmonic component, two successive signals in phase opposition are transmitted in the medium. The sum of the two reconstructed images extracts the second harmonic component (2.4). The non-use of filter allows limiting the sidelobes of filters.

#### Coded excitation

It was described in the SNR and contrast enhancements section that coded excitations as chirp improve the SNR and the depth penetration after compression at reception. J.M. Borsboom proposed to use chirp transmission and a nonlinear compression filter that can selectively extract and compress the second harmonic from the received echo (Borsboom et al., 2005). This combination of harmonic imaging and chirp transmission improves the resolution of the chirp. The drawback of chirp imaging is the presence of side lobes in the axial direction due to the chirp compression which is present in fundamental and second harmonic chirp imaging (Borsboom et al., 2005). A novel approach to reduce the side lobes effect and improve the resolution is the resolution enhancement compression (REC) proposed by M.L. Oelze (Figure 2.13**)** (Oelze, 2007). Two different impulse responses, one with a short bandwidth (Figure 2.13.a**)** and the other one with a wide bandwidth **(**Figure 2.13.b**)** convolved by two different chirps can produce the same wave **(**Figure 2.13.e**)**. Thus it is possible to modify the chirp convolved with the small bandwidth impulse response, in order to increase the bandwidth improving the resolution.

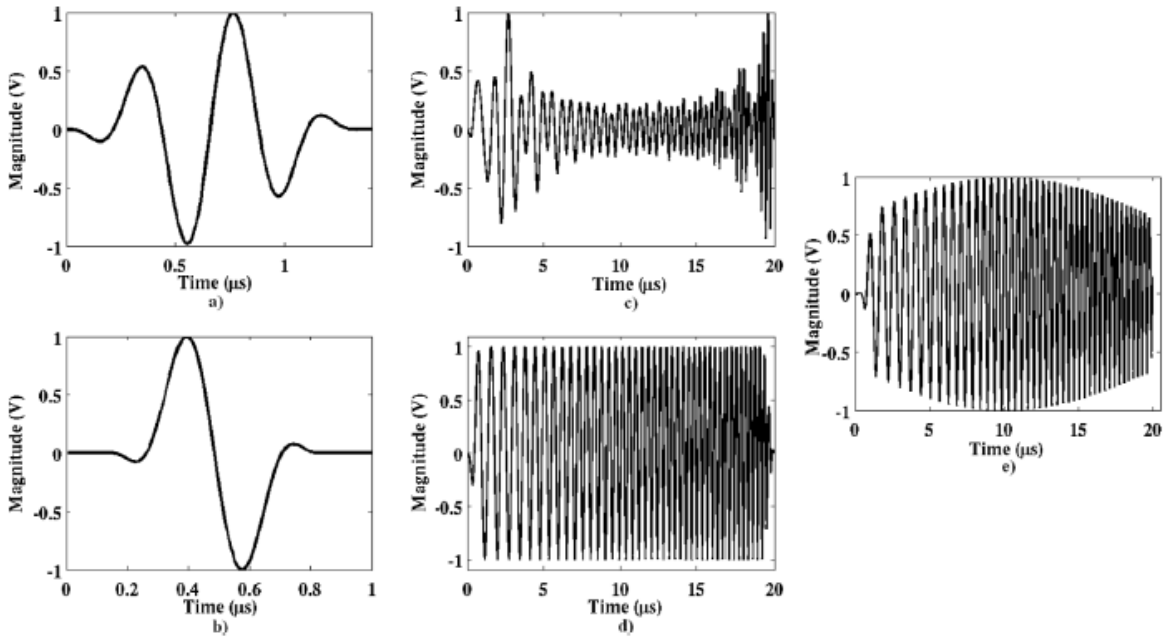


**Figure 2.13: Simulated impulse responses, chirps, and convolutions. (a) Pulse with approximately 48% −3 dB pulse/echo bandwidth. (b) Pulse with approximately 97% −3 dB pulse/echo bandwidth. (c) Modified chirp used to excite the 48% bandwidth source. (d) Linear chirp used to excite the 97% bandwidth source. (e) Convolution of the pulses with their respective chirps sequences (Oelze, 2007).**

### 2.2.4. Conclusion

Different methods were proposed to improve the resolution in ultrasound imaging. The improvement in resolution is usually linked to the contrast improvement for transmission-reception approaches. The coherent plane wave compounding, harmonic imaging, pulse inversion technique are techniques improving the both parameters.

## 2.3. Discussion and conclusion

In ultrasound imaging, since the improvement in electronics and echographic materials, the image quality has been improved. The speckle noise reduction, contrast and spatial resolution improvement have been presented. The speckle noise reduction is a tradeoff with the spatial resolution. If the speckle noise is smoothed, usually, the resolution decreases. That's why a combination of coherent transmission-reception and incoherent method or image-processing can be a solution to decrease the speckle noise while keeping a good spatial resolution.

# Chapter 3

# Thomson filter

In the previous chapter, the review of the existing techniques that reduce the speckle noise and improve the contrast has been presented. The techniques were classified in two mains groups: the transmission-reception strategies and image processing techniques. It is also possible to combine both techniques domain using the spatial compounding and a filter on the resulting compounded image (Adam et al., 2006). Most of the techniques reducing the speckle noise require to select or choose different parameters in order to adapt the speckle reduction in function on the application. One approach does not need parameters: the apodization during the reception or the beamforming of the backscattered echoes. Usually, echographic scanners use a Hanning or Hamming apodization during the reception in order to reduce the side lobes range and to smooth the speckle. The Thomson multitaper approach presented in this contribution has the special feature to use several different apodizations (or tapers) during the beamforming creating images with different speckle realization as spatial compounding. This approach is a combination of transmission-reception and image processing techniques.

The objective of this chapter is firstly to present the Thomson's multitaper method. Furthermore, the Thomson's multitaper signal processing origins is given in Appendix B. Secondly, the Thomson approach is evaluated for the ultrasound application. Then different techniques combined with the Thomson's multitaper method are presented in order to reduce the speckle noise while keeping a good spatial resolution in the whole image.

## 3.1. Thomson's multitaper presentation

Thomson proposes a set of orthogonal data tapers such that each taper provides a good protection against leakage and such that their individual frequency response is as nearly uncorrelated as possible. If the frequency response of each taper is uncorrelated, the average of them produces an estimator with a smaller variance than their individual estimator. The orthogonal data tapers proposed with a good leakage property is the discrete prolate spheroidal sequences (DPSS) or Slepian sequences (Landau and Pollak, 1961) (Slepian and Pollak, 1961) (Slepian, 1978). In this thesis work, the Slepian sequences were implemented in Matlab® to calculate the DPSS tapers using a tridiagonal formulation. The method can be simplified by taking the eigenvectors of the Toeplitz matrix $D_{n,m}$ defined by (Thomson, 1982) (Percival and Walden, 1993):

$$D_{n,m} = \frac{\sin BW(n-m)}{\pi(n-m)}, \quad n,m = 0,1,...N-1 \tag{3.1}$$

where $BW$ corresponds to the half spatial frequency band of the synthesized filter main lobe $\bar{H}(f)$, $N$ the number of samples (the spatial size of tapers) and ($n$, $m$) are indexes to form the Toeplitz matrix. The half spatial frequency band $BW$ is obtained by:

$$BW = k \times 2\pi / N, \quad 1 < k < N/2 \tag{3.2}$$

*BW* is in radian per sample and *k* is chosen so that *2k* is an integer (Thomson, 1982) (Percival and Walden, 1993). The eigenvectors of the Toeplitz matrix are the DPSS tapers and are ordered by their eigenvalues $\lambda$. Eigenvalues indicate the spectral concentration of the eigenvectors. The more their eigenvalues are close to the unit, the more eigenvectors are concentrated. The number of eigenvectors with high spectral concentration is linked to the spatial frequency band *BW* and there are 2*k* eigenvectors with high spectral concentration. This is the "*2k* law" described in (Percival and Walden, 1993). If more than *2k* tapers are used, the sidelobes of the synthesized filter are large and increase the echo artifacts.

The Figure 3.1 shows two examples of three DPSS (Figure 3.1.a**)** and four DPSS (Figure 3.1.c**)** for $N = 64$, $k = 1.5$ and $BW = 1.5 \times 2\pi / N \approx 0.147$ rad/sample. The first case with three DPSS respects the "*2k law*". Their respective eigenvalues are indicated and are close to 1 (Figure 3.1.a**)**. The frequency response of the 3 DPSS tapers and their corresponding synthesize filter (named DPSS 3) is given in Figure 3.1.b. The main lobe of DPSS 3 is large and the sidelobes are principally due to the frequency response of the third taper. In the second case, with four DPSS, the "*2k law*" is respected for the first three tapers, which are the same as in the previous case, but the last taper has an eigenvalue of 0.26 which is too low compared to 1. The frequency response of the 4 DPSS tapers and their corresponding synthesize filter (DPSS 4) is given in Figure 3.1.d. With this fourth taper, the main lobe of DPSS 4 is larger than DPSS 3 but the level of the sidelobes is increased.

Figure 3.2 shows the frequency responses of a rectangular taper, a Hanning taper and a DPSS 3 and DPSS 4 synthesized filter, respectively. All tapers have the same size, $N = 64$, and the DPSS 3 and DPSS 4 have the same properties as in Figure 3.1. The DPSS synthesized filters have a larger main lobe compared to the Hanning and rectangular filters and their sidelobes are slightly lower than the rectangular filter although higher than the Hanning filter. The DPSS 4 filter has higher sidelobes than DPSS 3 confirming that there is only $2k = 2 \times 1.5 = 3$ tapers with high concentration. If a DPSS 4 has to be computed, *2k* must be equal to 4 in order to obtain the optimal DPSS 4 synthesized filter.

The Thomson's multitaper (TM) find its application since its apparition in different domain of application like in medical electroencephalography (Xu, Haykin and Racine, 1999) (Babadi and Brown, 2014), in geophysics (Lees and Park, 1995) (Prieto et al., 2007) and also in sonar signal processing (Wage, 2007). In each case, the multitaper approach was used for spectral analysis. The last publication of B. Babadi proposes an easy explanation of the multitaper approach for signal processing and give a summary of D.J Thomson and D.B Percival papers (Thomson, 1982) (Percival and Walden, 1993) (Babadi and Brown, 2014). Their objective is to facilitate the comprehension of multitaper approach and then its implementation in different fields.

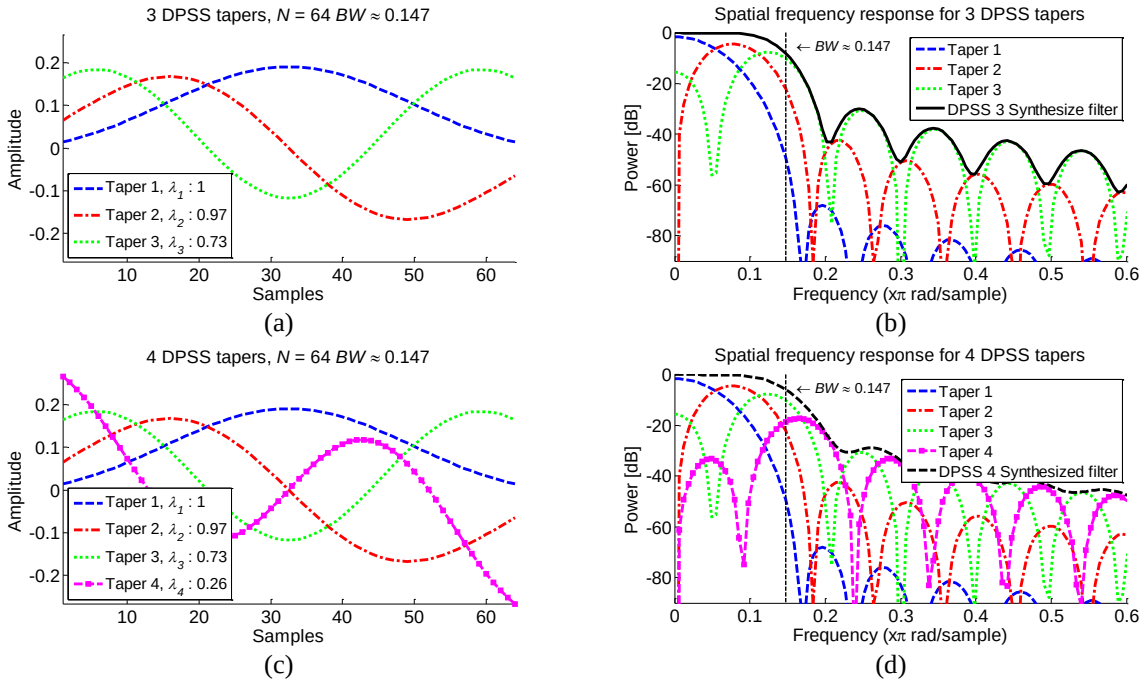


**Figure 3.1: Characteristics of a DPSS 3 and a DPSS 4 synthesized taper for $N = 64$ and $BW = 1.5 \times 2\pi / N \approx 0.147$. (a) the spatial modulation of the 3 DPSS tapers, (b) the spatial frequency response of the 3 DPSS tapers and the DPSS 3 synthesized filter, (c) the spatial modulation of the 4 DPSS tapers and (d) the spatial frequency response of the 4 DPSS tapers and the DPSS 4 synthesized filter.**

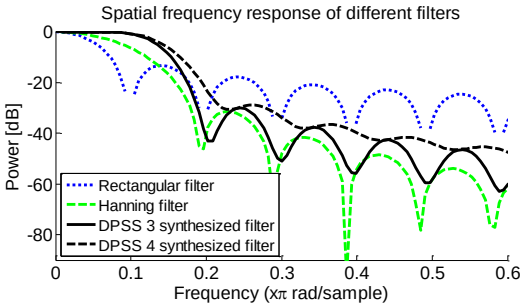


**Figure 3.2: Representation of the spatial frequency response of a rectangular filter, a Hanning filter, the DPSS 3 synthesized filter and the DPSS 4 synthesized filter.**

## 3.2. Thomson's multitaper method for ultrasound

It is only recently that A.C. Jensen proposed to apply the multitaper technique in ultrasound imaging (Jensen et al., 2011) (Jensen et al., 2012). In ultrasound imaging, the use of tapers during beamforming modifies the spatial spectrum of the resulting image. Each taper (e.g. a Rectangular, Hanning, Hamming, or Gaussian window) has a corresponding spatial frequency response that emphasizes or reduces different parts of the spatial spectrum and involves advantages or drawbacks in terms of resolution, sidelobes or speckle noise.

In TM approach, multiple DPSS tapers are used during beamforming (Jensen et al., 2012). In this way, RF images of the same ROI with different speckle realizations are created. The final B-mode image obtained by the weighted average of the incoherent envelope images corresponding to the various tapers, synthesizes a filter that maximizes the power in the large main lobe and reduces the sidelobes leakage. The image formation is explained in the Figure 3.3.

The Figure 3.3.a shows the classical image formation as it was described in the first chapter. After the reception of echoes by an active-aperture of the probe, echoes are delayed

and an apodization can be used before the average of the echoes in order to create one RF-line. After envelope detection, one incoherent B-mode line is obtained.

The Figure 3.3.b explains the image formation using a multitaper approach during the beamforming. Instead of creating one RF-line, several tapers are used in order to obtain different RF-line after the average of the weighted echoes. After envelope detection, the corresponding incoherent B-mode lines are weighted by the eigenvalues of the DPSS tapers and finally are averaged in order to create one final B-mode line.

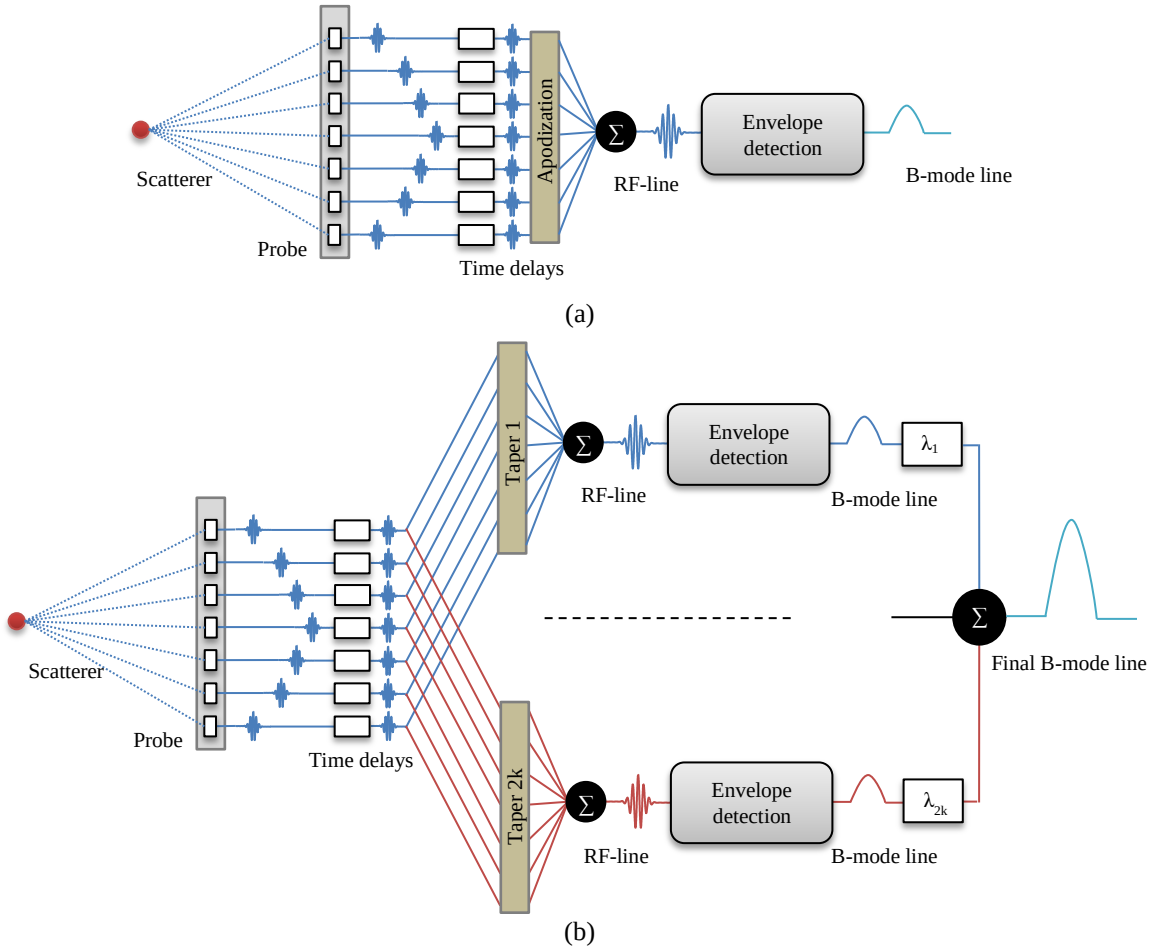


**Figure 3.3: Beamforming in reception (a) with a classical apodization and (b) with the multitaper approach using *2k* tapers.**

## 3.3. Evaluation of Thomson's multitaper approach

In signal processing domain, the frequency resolution and the bias limitation of the TM have been controlled by several authors (Thomson, 1982) (Percival and Walden, 1993). In image processing, A.C. Jensen evaluated the multitaper approach by computing the SNR and the CNR of a simulated cyst phantom (Jensen et al., 2011) (Jensen et al., 2012). A.C. Jensen compared the multitaper technique with the spatial compounding and a weighted and partly overlapping compounding approach (Welch method). All methods are been compounded with 1 and 3 tapers or steering angles.

In this section, the SNR, CNR, spatial resolution and the improvement perception of the TM approach is evaluated in simulation and acquisition by two different ways. The first one is the evaluation of the multitaper approach in function of the number of tapers used during the beamforming. The second evaluation is the comparison of the method with different filters

used in image processing approach and the spatial compounding approach. The techniques are evaluated using a cyst phantom including wires, in both simulations and experiments. Simulations are done with the CREANUIS software (Varray et al., 2013) and acquisitions are done with the ULA-OP scanning system (Tortoli et al., 2009). Simulations and acquisitions are made using the same probe parameters, given in Table 3.1, and are based on the 192-element LA533 (Esaote SpA, Firenze, Italy) linear probe. The geometry and the ROI of the simulated and acquired phantoms are described on Figure 3.4. The simulated phantom, Figure 3.4.a, had 100 000 randomly distributed scatterers (13.6 scatterers / $mm^3$) and included seven wires and four hypoechoic cysts. The acoustic characteristics of the medium are given in Table 3.2. SNR, CNR and spatial resolutions have been calculated at different depths (squares and circles in Figure 3.4.a). The phantom utilized during acquisitions (Gammex 404GS LE) is described on Figure 3.4.b and Figure 3.4.c. One part of the phantom includes seven wires and a hyperechoic cyst, as shown on Figure 3.4.b. Another part shown on Figure 3.4.c, has only a hypoechoic cyst. SNR, CNR and spatial resolutions have been calculated at different depths (squares and circles in Figure 3.4.b and Figure 3.4.c).

The ULA-OP was programmed to drive only the 64 central elements of the linear array. In simulations and experiments, a 3-cycle sinusoidal burst signal at 5 MHz weighted by a temporal Hanning window focalized at 30 mm was transmitted from each element. No spatial apodization was used on the 64 active elements during transmission. In both cases, a $5^{th}$ Butterworth band-pass filter is used to extract the fundamental component.

| Parameters | Value |
|---|---|
| Number of active elements | 64 |
| Pitch | 245 µm |
| Kerf | 30 µm |
| Height | 6 mm |
| Elevation focus | 23 mm |

**Table 3.1: Summary of the probe parameters used in simulation and acquisition.**

| Parameters | Value |
|---|---|
| Density | 1000 $kg.m^{-3}$ |
| Speed of sound | 1540 $m.s^{-1}$ |
| Attenuation | 0.2 $dB.MHz^{-1}.cm^{-1}$ |
| $\gamma$ | 1 |

**Table 3.2: Simulated acoustic characteristics**

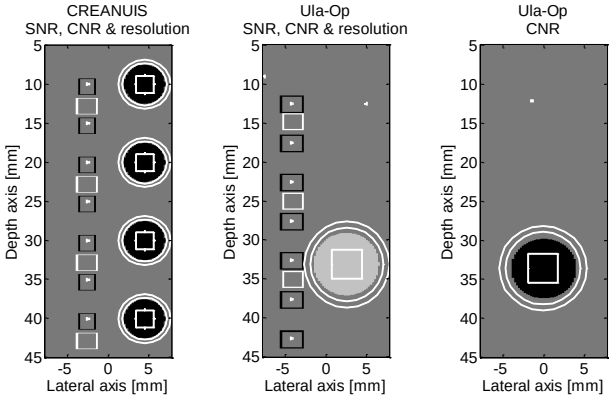


(a) (b) (c)

**Figure 3.4: Geometry of the phantoms used for (a) CREANUIS simulation and (b-c) ULA-OP acquisitions with wires and cysts areas. Areas drawn in phantoms are used for the measurement of SNR (white squares), CNR (white squares inside the cysts and the area between white circles outside the cysts) and resolution parameters estimation.**

### 3.3.1. Evaluation in function of number of tapers

As it was explained in the first part of this chapter, the maximum of tapers that can be used theoretically is inferiors to *N* which corresponds to the number of active elements of the probe used simultaneously (3.1). In signal processing, it was reported by D.B. Percival that the number of tapers used is usually limited to 8 but some applications can use more tapers (Percival and Walden, 1993). If a high number of taper with a good leakages property is used, the variance decreases but the resolution lost in the frequency domain is too important. The interest of the evaluation of the SNR, CNR and spatial resolution as a function of the number of tapers is to determine if there is a limit for the number of tapers to use during the beamforming.

In simulations and acquisitions, three different kinds of apodization were compared during the offline beamforming: a rectangular one, corresponding to no particular apodization, a Hanning apodization and DPSS tapers. The rectangular one was chosen because this apodization gives theoretically the best resolution but with a lot of sidelobes (Figure 3.2). The Hanning apodization was chosen because it is the most common apodization used with standard echographic scanner. The DPSS tapers chosen for the comparison are ranged between 3 to 31 and an odd number of tapers is chosen (DPSS 3, DPSS 5, DPSS 7…). Any number of DPSS apodization can be used, according to the author preference as recalled by D.B Percival (Percival and Walden, 1993). The resulting simulated images are given in Figure 3.5 and SNR, CNR and spatial resolution are given in Figure 3.6, Figure 3.7, and Figure 3.8, respectively. The images are normalized by their own maximum and are log compressed with a dynamic of 50 dB. The SNR and CNR values are normalized by the corresponding value of the SF images, using the rectangular apodization, close to 30 mm and are expressed in decibel. The resulting acquisitions images are given in Appendix B.

#### 3.3.1.1. CREANUIS simulation

Figure 3.5 shows the simulated phantom beamformed with a rectangular and Hanning apodizations and with 6 different DPSS. The use of DPSS tapers during the beamforming reduces the speckle noise compared to the rectangular one and Hanning apodization. The areas outside the focal area are the zone where the speckle is the smoothest. A visual observation shows that the speckle is smoothed, in the lateral direction leading to a lateral blur effect. This can be explained by the fact that during the beamforming, the apodization is performed in the lateral axis. The Hanning apodization also produces a blur effect, but the multitaper approach accentuates it.

The Figure 3.6 shows the speckle reduction with the SNR calculated at different depths. Higher is the SNR, lower is the speckle noise. The speckle noise is reduced when DPSS apodization are used compared to rectangular one and Hanning apodization (Figure 3.5). Without DPSS apodization, the SNR values for all different areas are close. But in three of the fourth cases where the SNR is calculated for DPSS apodization, the SNR value tends to a plateau starting from the DPSS 11. When the speckle noise is reduced, the quality of the edges of the cysts and the size of the wires decrease. It is noticeable with Figure 3.5.(e-f) where the cysts outside the focal area are totally blurred.

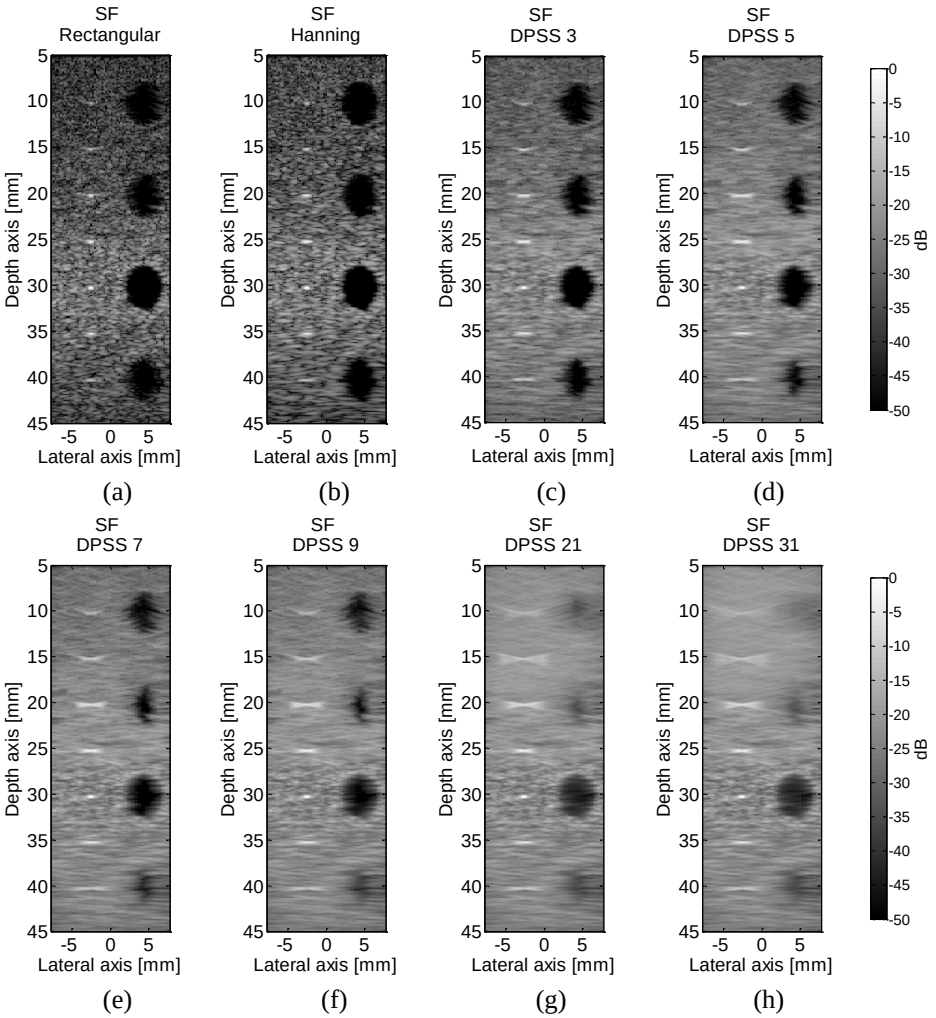


**Figure 3.5: Log compressed CREANUIS simulated ultrasound images of hypoechoic cysts and wires for one focal depth at 30 mm for (a) a rectangular apodization, (b) an Hanning apodization and (c-h) DPSS apodization.**

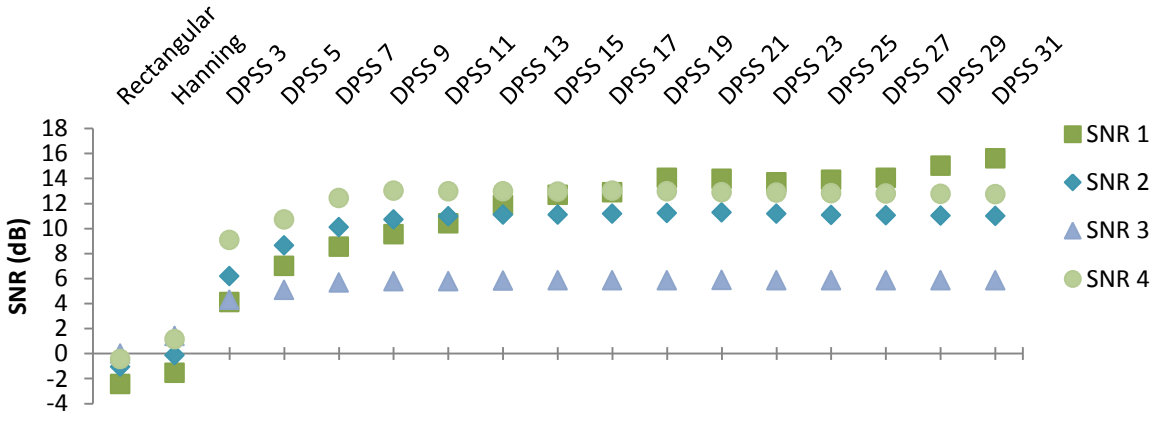


**Figure 3.6: SNR in dB for CREANUIS simulation calculated at different depths given in Figure 3.4.a. The SNR is evaluated for a rectangular, a Hanning and different DPSS apodization. SNR 1 is the SNR area in the top of the image and SNR 4 is the SNR area in the bottom of the image. The SNR is normalized by the measurements performed on SF rectangular image, close to 30 mm and are expressed in decibel.**

If the cysts are incorrectly delimited, the contrast decreases (Figure 3.7). The CNR evaluation shows that in the focal area (cyst 3), the best contrast is obtained when the DPSS 3 or DPSS 5 apodization are used. The same effect is observed on the cyst 2 while for the cyst 4 only the DPSS 3 is optimal. As with SNR values for DPSS apodization, the CNR value in the focal area tends to a plateau starting from the DPSS 5. For the cysts 2 and 4, the CNR reaches a maximum with the DPSS 3 or DPSS 5 then for a larger number of tapers, the cyst edges are totally blurred and the contrast decreases.

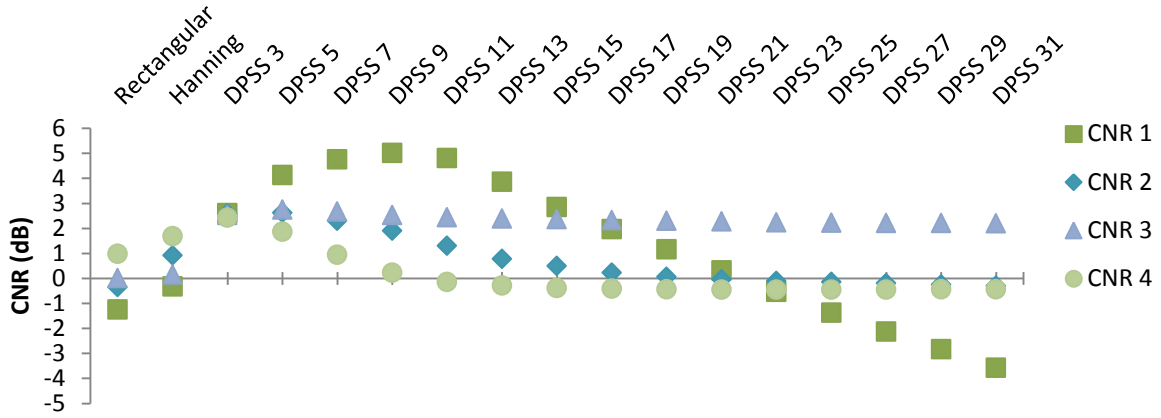


**Figure 3.7: CNR in dB for CREANUIS simulation calculated at different depths given in Figure 3.4.a. The CNR is evaluated for a rectangular, a Hanning and different DPSS apodization. Cyst 1 is the cyst in the top of the image and Cyst 4 is the cyst in the bottom of the image. The CNR is normalized by the measurements performed on SF rectangular image, close to 30 mm and are expressed in decibel.**

The DPSS apodizations have an important blur effect outside of the focal area and it is characterized by the measurement of the spatial resolution (Figure 3.8). Figure 3.8.a gives the lateral resolution and Figure 3.8.b gives the axial resolution in function of the apodization used. The vertical axis of Figure 3.8.a has been shortened because the values of wire 1 is too important with the last DPSS apodization. It is important to distinguish different areas: in and outside the focal area. In the focal area, the resolution is the best and as it is observed in Figure 3.5, the image is less blurred in this area. Thus the resolution decreases less in function of the apodization in this area. This observation is confirmed by the lateral resolution values of the wire 5 (Figure 3.8.a). For all wires, except the wire 1, the lateral resolution decreases when DPSS tapers are used but it tends to a limit value starting from different DPSS tapers. If the wire is close to the focal area, the lateral resolution tends to a limit from a low number of DPSS apodization. The lateral resolution at the wire 5, at the focal depth, tends to a limit starting from the DPSS 3 taper, while the lateral resolution of the wire 2 tends to a limit starting from the DPSS 19 taper. In the case of the axial resolution (Figure 3.8.b) the resolution is less sensible to the use of DPSS taper, except for the wire 1. The axial resolution is sensible to the depth where the resolution is calculated. This effect was obtained because the axial resolution depends on the transmitted signal parameters and the speed of the sound in the medium and it is less sensible to the apodization used during beamforming.

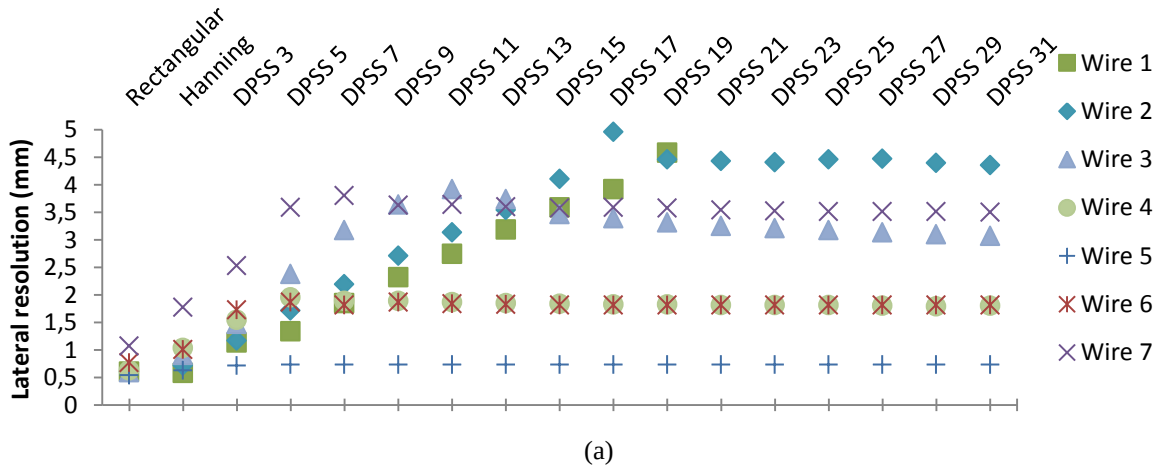


(a)

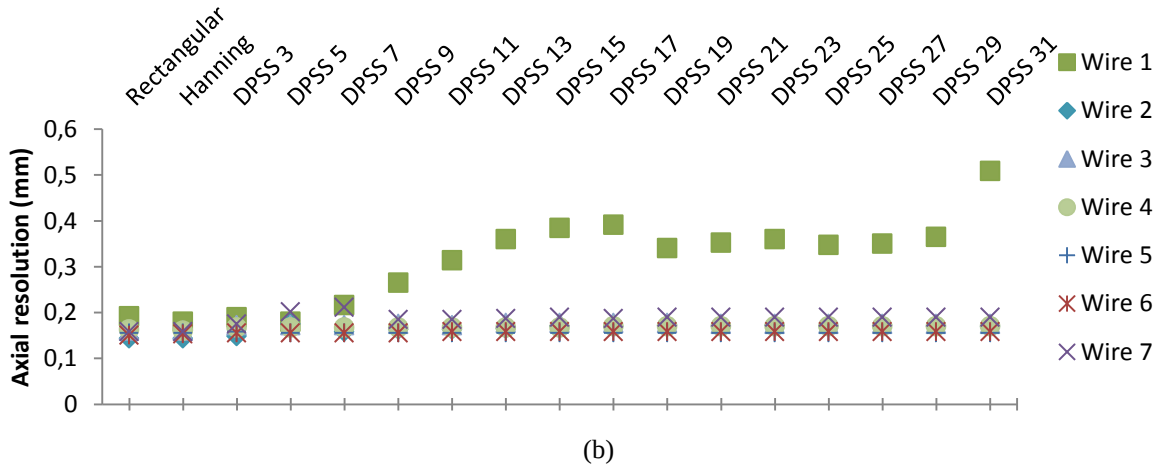


(b)

**Figure 3.8: Spatial resolution, (a) lateral resolution and (b) axial resolution, evaluated at different depths given in Figure 3.4.a in the phantom simulated with CREANUIS. The spatial resolutions are evaluated for a rectangular, a Hanning and different DPSS apodization. Wire 1 is the wire in the top of the image and Wire 7 is the wire in the bottom of the image.**

When the SNR, CNR and spatial resolutions are calculated, the values in the top of the image (SNR 1, CNR 1 and wire 1) vary differently than others or have an unexpected behavior. For SNR, when a high number of DPSS is used, the top of the image is totally smooth so the standard deviation calculated in the ROI tends to 0. Thus the ratio of the mean and the standard deviation tends to the infinite. In the case of the CNR, the cyst and its surrounding background tend to be uniform and similar, so the difference of the mean value in both areas tends to 0 when the blur effect is too important. That's why the CNR decreases. Finally for spatial resolution, -6dB estimation technique reaches its limit because the -6dB of the wire isn't detectable due to the total blur of the speckle. The axial resolution shows the same behavior.

#### 3.3.1.2. ULA-OP acquisition

The results on SNR, CNR and spatial resolution performed on data acquired on a physical phantom with ULA-OP machine exhibit the same behavior as in simulation (Appendix C). The use of DPSS apodization improves the SNR and CNR but decreases the lateral resolution. The top of the image also have a particular behavior. As in simulation SNR, CNR and lateral resolution tend to a limit value when a DPSS apodization with a high number of taper are used.

#### 3.3.1.3. Discussion and conclusion

The evaluation of the TM approach in function of the number of tapers confirms the results shown in other studies reported in the literature: it is not relevant to use a too large number of tapers. SNR, CNR and lateral resolution usually tend to a limit value starting to from DPSS 11. The effect in terms of speckle noise reduction is the most important outside the focal area at the cost of contrast and resolution reduction. In the focal area, the DPSS 3 or the DPSS 5 apodization are sufficient to keep a good contrast, resolution and to reduce the speckle noise.

## 3.4. Comparison of image processing techniques with spatial compounding approaches

The TM approach proved its efficiency to smooth the speckle compared to the classic apodization used during the beamforming in simulation and acquisition. The objective in this section is to compare the TM performance for the speckle noise reduction of spatial compounding and some classic image processing approaches. Only the simulated results are presented because of the same behavior are obtained with simulated and acquired data.

The reference image is the image beamformed with a rectangular apodization. The several methods compared are a mean, a Gaussian, a median, a bilateral filter, a DPSS 3 apodization and two spatial compounding approaches. The characteristics of the different methods employed are given in the Table 3.3. All filters are defined on the same neighborhood (5 x 5). The DPSS 3 apodization is chosen for its capability to smooth the speckle without a large decrease of the resolution. For both spatial compounding approaches, the number of angles and the angular separation are chosen from echographic scanner consideration and from the literature. In echographic scanner, the number of steering angles is usually limited to 5 or 7 angles because a too large number of angles leads to a reduced frame rate and movement artefacts can appear. For the angular separation, S.K. Jespersen and A. Gering showed that with an angular separation of less than 5°, the images are partly correlated (Jespersen, Wilhjelm and Sillesen, 1998) (Gerig et al., 2004).

The log compressed simulated images are represented in the Figure 3.9. The SNR, CNR and spatial resolution are evaluated at different depths (Figure 3.4.a) and are normalized by the value of the reference image close to 30 mm. Moreover the normalized values are averaged. The mean and the standard deviation of SNR, CNR and spatial resolution are given in Figure 3.10.

| Original | Mean | Gaussian | Median | Bilateral filter | DPSS | Spatial 3 | Spatial 5 |
|---|---|---|---|---|---|---|---|
| | 5 x 5 | 5 x 5<br>$\sigma = 0.8$ | 5 x 5 | 5 x 5<br>$\sigma_c = 3$<br>$\sigma_s = 0.1$ | 3 | [-5° : 5° : 5°] | [-10° : 5° : 10°] |
| (a) | (b) | (c) | (d) | (e) | (f) | (g) | (h) |

**Table 3.3: Characteristics of the different methods employed for the comparison of the DPSS filter, image processing and spatial compounding methods.**

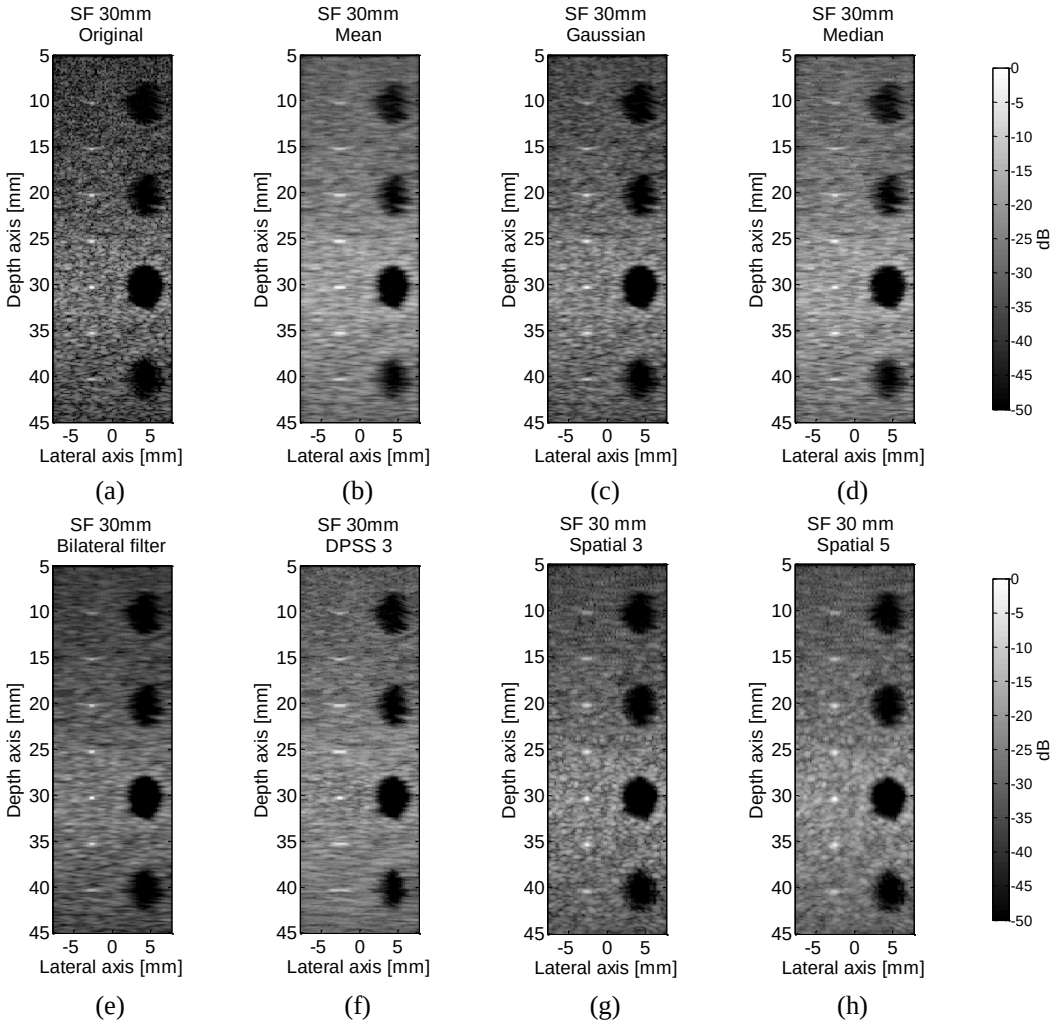


**Figure 3.9: Log compressed CREANUIS simulated ultrasound images of hypoechoic cysts and wires for one focal depth at 30 mm for different speckle noise reduction methods, (a) original image, (b) Mean (5 x 5), (c) Gaussian (5 x 5, σ = 0.8), (d) Median (5x5), (e) bilateral filter (5 x 5, $\sigma_c$ =3, $\sigma_s$=0.1), (f) DPSS3, (g) spatial 3 (-5°:5:5°) and (h) spatial 5 (-10°:5:5°).**

The Figure 3.9 shows that all the proposed techniques smooth the speckle. However different reductions of the speckle noise are obtained (Figure 3.9). The techniques given the best SNR are the image-processing approaches (Mean and bilateral filters) and the DPSS approach. The SNR improvement is more than 5 dB. The spatial compounding approaches do not smooth the speckle as well as the other techniques but the cyst areas are still well delimited. This property allows the spatial compounding with 5 angles to have the best CNR (Figure 3.9.b). The DPSS approach improves the CNR about 2.5 dB. The Mean and bilateral filters are still better than the DPSS approach. The lateral resolution of the DPSS approach is the worst (Figure 3.9.c). Moreover, the standard deviation of the DPSS method is the largest because, as it is demonstrated in the previous section, the speckle noise reduction for DPSS varies in function of the depth. In the focal depth the resolution is better than outside the focal depth for the DPSS method. The same explanation can be done for the standard deviation of the SNR values. The axial resolution of the DPSS approach is close to the one of the original image (Figure 3.9.d). Only the spatial compounding approaches have a variation of the axial resolution.

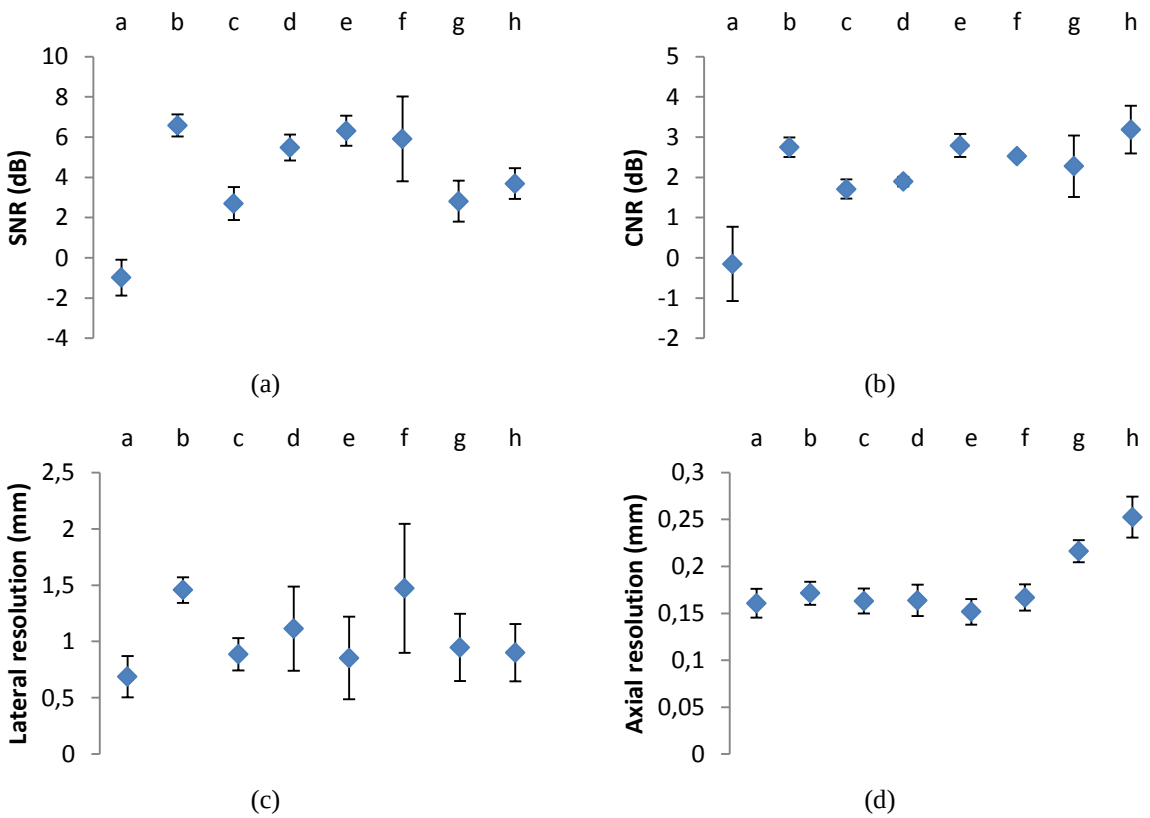


a: Original, b: Mean, c: Gaussian, d: Median, e: Bilateral filter, f: DPSS 3, g: Spatial 3 and h: Spatial 5

**Figure 3.10: Evaluation of different speckle noise reduction approaches. Averaged and standard deviation of (a) SNR and (b) CNR in dB and (c) lateral and (d) axial resolutions for CREANUIS simulation calculated at different depths given in Figure 3.4.a. The SNR is evaluated for several techniques given in Table 3.3. The SNR values have been normalized by the measurements performed on the original image, close to 30 mm and then have been averaged and expressed in decibel. The spatial resolution values of all depths have been averaged.**

The comparison of the TM approach with image processing and spatial compounding approaches proves the usefulness of the technique for speckle noise reduction. Compared to the image processing approaches, the TM approach results are closed to the Mean and bilateral filter for speckle reduction and contrast improvement. However the lateral resolution is lower than the one obtained with these two image processing techniques. Compared to the spatial compounding, the TM method is better for the speckle reduction and close for the contrast. The lateral resolution of spatial compounding is better however its axial resolution is not as well as the Thomson approach.

Furthermore, the TM approach has two advantages. First, there is no reduction of the frame rate as for spatial compounding techniques. A single acquisition is required to reduce the speckle noise. The second advantage lies in the setting parameters. For TM, the number of DPSS tapers is limited because as it was demonstrated in the previous part, when a large number of DPSS are used, the image quality decreases. It is advised to test with the DPSS 3 until the DPSS 7 apodization. While for image processing, several parameters have to be adapted to the medium: the neighborhood, the standard deviation for Gaussian filter… Moreover for spatial compounding the number of angles or the angular step have an important impact on the image quality and depends on the medium or the area investigated. The TM approach is easier to use and requires the selection of a single parameter, the number of DPSS tapers.

## 3.5. Improvement of the Thomson's multitaper approach

The TM approach reduces the speckle noise but the spatial resolution decreases. In view to improve the resolution and the contrast while reducing the speckle noise, two different techniques are proposed to be combined with the TM method:

- The pulse inversion (PI) approach
- The coherent plane wave compounding technique (CPWC)

Both approaches are based on the average of coherent images to improve the resolution and contrast and an incoherent average allowing a speckle noise reduction. The coherent average is the proposed methods, using PI and CPWC, and the incoherent average is the TM approach. The first proposed technique is the multitaper pulse inversion (MPI) and the second is the multitaper coherent plane wave compounding (MCPWC) (Toulemonde et al., 2012) (Toulemonde et al., 2013) (Toulemonde et al., 2014).

In the following part, first the MPI technique is presented and evaluated. Then the same work is done with the MCPWC method. Both techniques are evaluated from their SNR, CNR, spatial resolutions and acquisition time.

### 3.5.1. Multitaper pulse inversion (MPI)

In the section 2.2.3, it was recalled that PI is based on a multi pulse transmission and allow to improve the contrast and the resolution (Simpson, Chin and Burns, 1999) (Shen, Chou and Li, 2005). The resolution improvement is due to the decrease of the fundamental component of the backscattered wave and the extraction of the second harmonic component without using filtering. Two successive pulses in opposite phase are transmitted in the media and the average of the backscattered echoes extracts the second harmonic signal (equation (2.4)).

The MPI technique consists to emit two pulses successively such as for PI technique and to use in reception several DPSS tapers. In order to have MPI image, the RF image *i* obtained with the DPSS taper *i* from the first pulse is coherently summed with the RF image *i* obtained with the same DPSS but from the second pulse. By averaging incoherently the set of resulting B-mode images obtained by envelope detection of each RF images, the final MPI image is obtained (Figure 3.11).

The MPI technique is compared to the fundamental $f_0$ image, the second-harmonic $2f_0$ image and the PI image. The fundamental image is extracted from the broadband image with a $5^{th}$ order Butterworth band-pass filter. The second-harmonic image is extracted with a $5^{th}$ order Butterworth high-pass filter. The broadband image is beamformed with a rectangular and DPSS 3 apodization. PI image is only computed with a rectangular apodization while MPI is constructed with a DPSS 3 apodization. No spatial apodization was used on the 64 active elements during transmission.

The techniques are evaluated using a cyst phantom including wires in simulations while in experiments, a homemade phantom was created. The geometry and the ROI of the simulated phantoms is described on Figure 3.4.a. The homemade phantom is presented in Appendix D, Figure D. 1. Simulations and experiments are made using the same probe and acoustics parameters, given in Table 3.1 and Table 3.2, respectively.

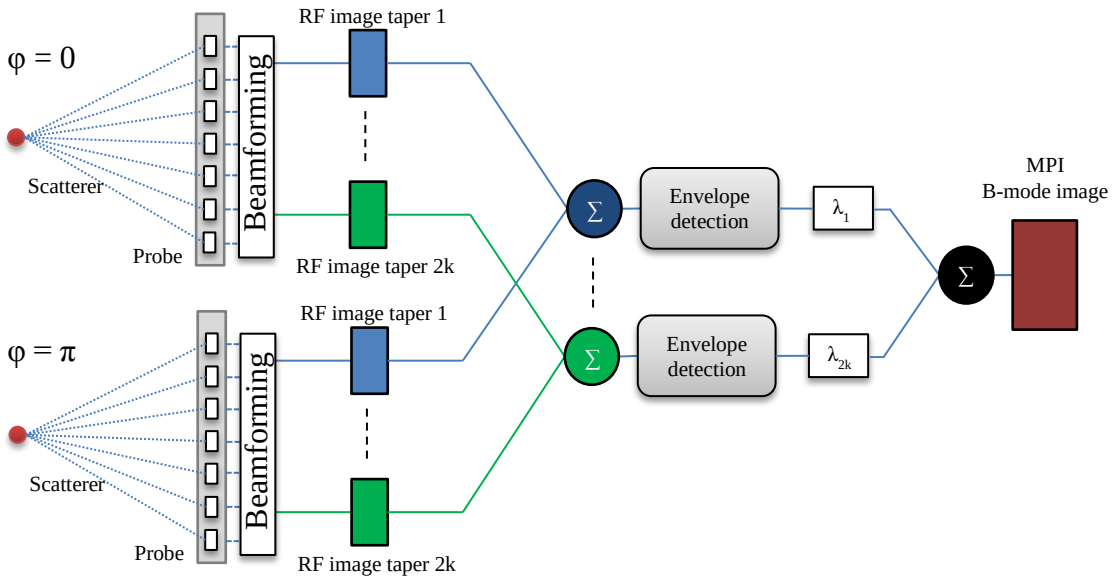


**Figure 3.11: Multitaper pulse inversion beamforming. The backscatters echoes from the two successive transmitted signals in opposite phase and the same taper *i* are averaged. After the envelope detection, all the B-mode images are averaged obtaining the MPI B-mode image.**

#### 3.5.1.1. CREANUIS simulation

Two successive 3-cycle sinusoidal burst signals at 5 MHz weighted by a temporal Hanning window focalized at 30 mm were transmitted in opposite phase from each element. The log compressed simulated images are represented in the Figure 3.12. The SNR, CNR and spatial resolution are evaluated at different depths (Figure 3.4.a) and are normalized by the value of the fundamental image close to 30 mm. Moreover the normalized values are averaged. The mean and the standard deviation of SNR, CNR and spatial resolution are given in Figure 3.13.

The Figure 3.12 and Figure 3.13.a show that the TM approach smoothes the speckle in fundamental, second-harmonic and MPI images. The CNR (Figure 3.13.b) is also improved with the TM approach. However the standard deviation of SNR and CNR for TM approach is significant because the speckle smoothing is dependent of the distance between the depth investigated and the focal depth. In the top of PI and MPI images (Figure 3.13.c, f), because of the weak depth propagation, few second harmonic signal is created. So the contrast is reduced because of the weak difference between the cyst and the surrounding medium.

In standard second harmonic imaging, in order to improve the spatial resolution, a high pass filter is used to extract the second harmonic image. The lateral resolution is improved (Figure 3.13.c), however the axial resolution decreases (Figure 3.13.d). Using the PI or MPI technique, the lateral resolution is better than the one resulting from the second-harmonic image. Moreover, the MPI technique improves the axial resolution because it is only a signal processing second-harmonic extraction without second-harmonic filter artefacts.

The MPI technique improves spatial resolution compared to the fundamental and second-harmonic TM approach, but this resolution improvement induces a SNR decrease. However the SNR and the CNR of the MPI technique are 4.8 dB and 1.9 dB, respectively, better than on the fundamental image with a rectangular apodization.

#### 3.5.1.2. ULA-OP acquisition

The homemade phantom was created in order to generate more harmonics during the propagation than the Gammex phantom presented in section 3.3. Two successive 7-cycle sinusoidal burst signals at 4 MHz with a temporal Hanning window, focused at 20 mm were transmitted in the medium with opposite phase. The SNR, CNR, and resolution results are given in Appendix D.

As in simulation, multitaper methods smooth the speckle. The second-harmonic, or PI / MPI imaging improve a lot the contrast (Figure D. 2). For the CNR, the MPI approach is always the best method (Figure D. 3.b). Moreover, the use of multitaper approach improves the contrast. In the whole image the gain in term of resolutions is less visible than in simulation. The spatial resolution of MPI is closed to the second-harmonic using the TM approach (Figure D. 3.c-d).

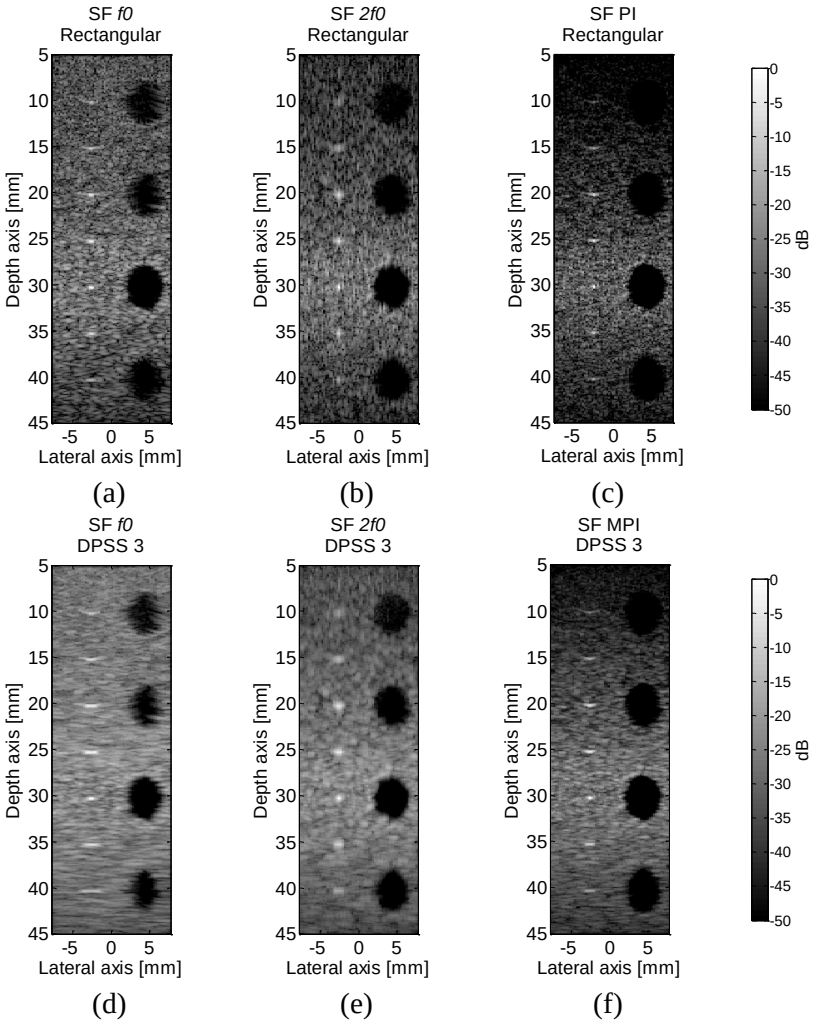


**Figure 3.12: Log compressed CREANUIS simulated ultrasound images of hypoechoic cysts and wires for one focal depth at 30 mm for fundamental, second harmonic and pulse inversion approach with or without DPSS apodization. (a) fundamental rectangular, (b) second-harmonic rectangular, (c) PI rectangular, (d) fundamental DPSS 3,(e) second-harmonic DPSS 3 and (f) MPI DPSS 3 method.**

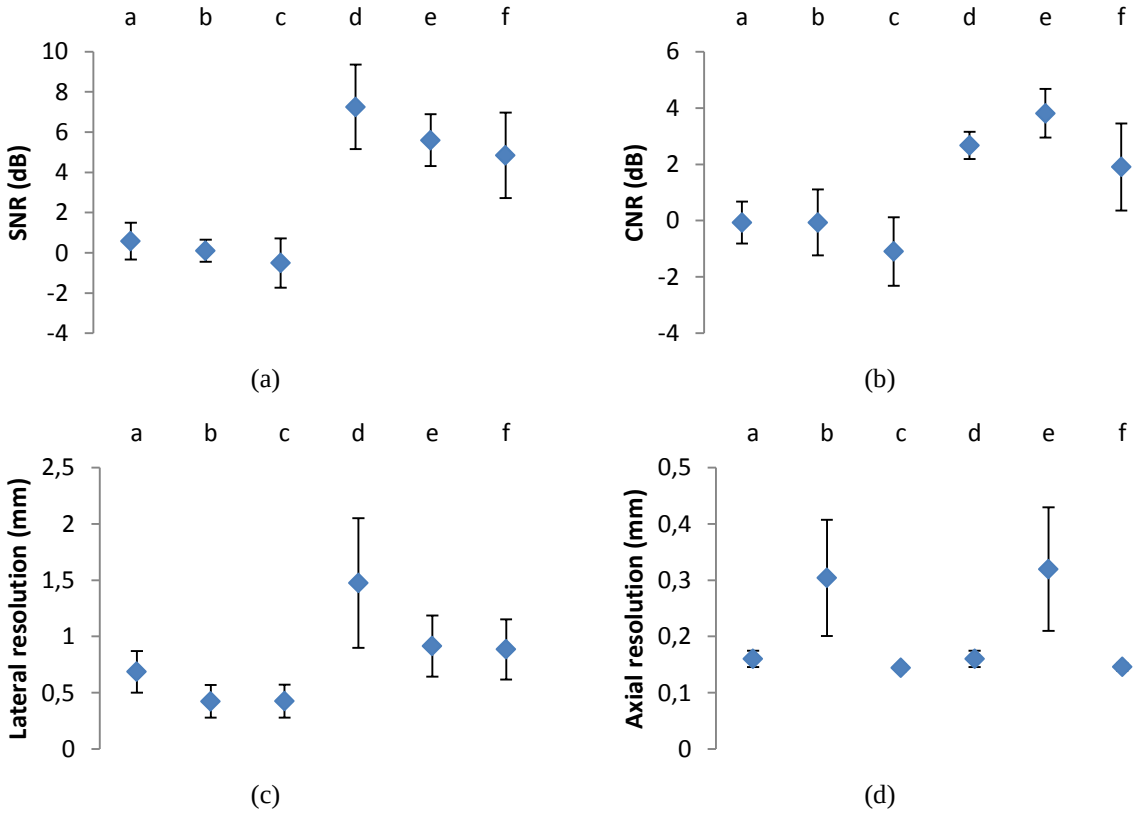


a: Rectangular $f_0$, b: Rectangular $2f_0$, c: Rectangular PI, d: DPSS 3 $f_0$, e: DPSS 3 $2f_0$, f: DPSS 3 MPI

**Figure 3.13: Evaluation of the MPI approach. Averaged and standard deviation of (a) SNR and (b) CNR in dB and (c) lateral and (d) axial resolutions for CREANUIS simulation calculated at different depths given in Figure 3.4.a. The SNR values have been normalized by the measurements performed on the original image, close to 30 mm and then have been averaged and expressed in decibel. The spatial resolution values of all depths have been averaged.**

#### 3.5.1.3. Discussion and conclusion

Combining PI and TM techniques, which give MPI technique, it is possible to increase the TM resolutions. In simulation, the results give an improvement of about 40% and 3% in lateral resolution compared to fundamental and second-harmonic TM, respectively. In axial resolution, the improvement is about 8.7 % and 54 % compared to fundamental and second-harmonic TM, respectively. In acquired data, results show that the resolutions improvement is inhomogeneous in the medium. It has been observed that the best gain of resolutions is in the top of the image. However this resolution improvement induced a SNR decrease but not a CNR decrease. Another drawback of the MPI technique is the frame rate decrease. Two successive signals have to be transmitted reducing the frame rate by two.

### 3.5.2. Multitaper coherent plane-wave compounding (MCPWC)

In the sections 2.1.1.2 and 2.2.1.2, the coherent plane wave compounding (CPWC) was proposed to improve the contrast and the spatial resolution (Montaldo et al., 2009). Multiple steered plane waves, covering a sector angle [$\theta_{min}$ $\theta_{max}$], are consecutively transmitted with a linear array probe. G. Montaldo proved that to obtain the same image quality, in terms of resolution, SNR and contrast, than in a standard image at its focal depth, the number of plane waves is obtained with:

$$N_\theta = L/\lambda F \quad \textbf{(3.3)}$$

where $L$ is the aperture size, $\lambda$ is the transmitted pulse wavelength and $F$ is the F-number defined by $F = z_f / L$. $z_f$ is the focal depth of the focusing approach. The steering angle for each plane wave $i$ is approximated, for small values of $\theta$, by:

$$\theta_i = \arcsin(i\lambda/L) \approx i\lambda/L, \quad i = -(N_\theta - 1)/2, ..., (N_\theta - 1)/2 \tag{3.4}$$

As an example, to achieve the same quality as in the focal region of a 5 MHz image focused at 30 mm, from an aperture size of 15.68 mm (corresponding to 64 active elements), $N_\theta$ must be 27 and the $\theta_i$ angles range from -14.63° to 14.63° with $\Delta\theta$ = 1.13°.

In the CPWC approach (Figure 2.9), $N_\theta$ RF images are averaged before envelope detection. In MCPWC with *2k* DPSS tapers (Figure 3.14), *2k* beamforming is done for each of the $N_\theta$ transmissions. The $N_\theta$ RF images built for the same DPSSS taper are averaged. After the envelope detection, the *2k* B-mode images obtained with different tapers are weighted by their own eigenvalues, $\lambda$, and averaged to produce the final MCPWC B-mode image.

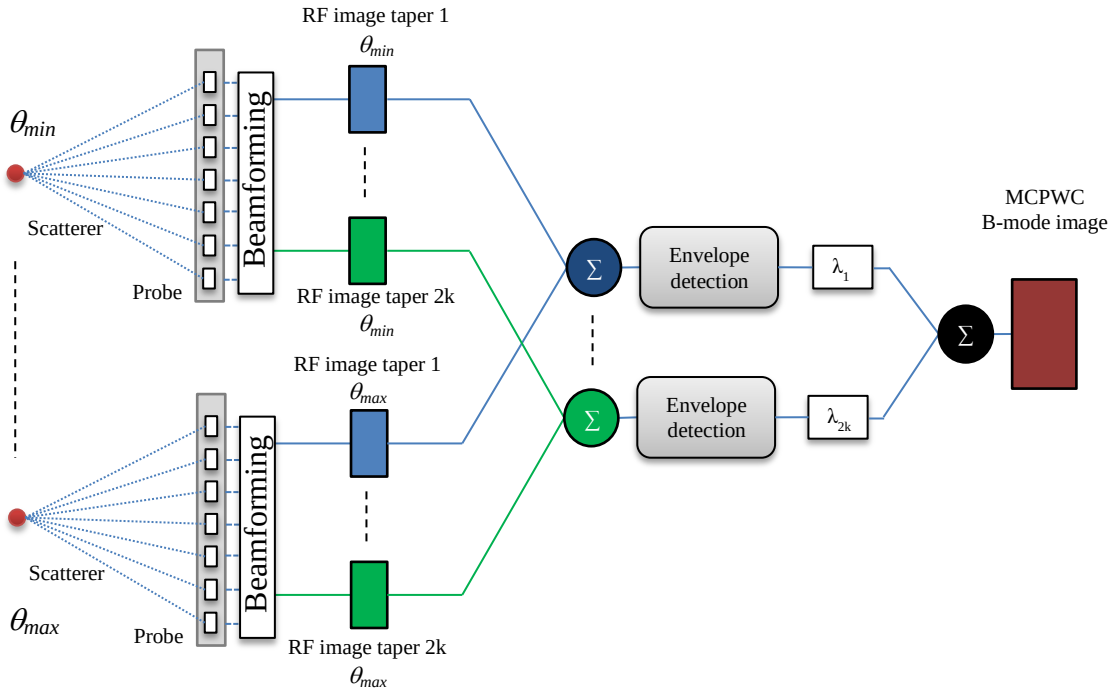


**Figure 3.14: B-mode image reconstruction strategies for multitaper coherent plane wave compounding (MCPWC). The RF images of all illuminations with different angles and built for the same taper are averaged. After the envelope detection, the B-mode images obtained with different tapers are averaged to produce the final MCPWC B-mode image.**

The MCPWC technique was evaluated by two ways. The first goal was to evaluate the influence of the number $N_\theta$, and the effect of beamforming apodization on the image SNR, CNR, and lateral and axial resolutions. The second objective was to compare the speckle noise, CNR, and lateral resolution of the classic single transmit focus (SF) technique, the multi-focus (MF), the CPWC and MCPWC approach. The MF technique may in fact represent a reference, since it offers the best resolution at all depths. The techniques were evaluated using the same cyst phantom presented above and including wires in both simulations and experiments (Figure 3.4). Simulations were done with the CREANUIS software and acquisitions were done with the ULA-OP scanning system with the same probe parameters (Table 3.1).

The ULA-OP was programmed to drive the 64 central elements of the probe. In simulations and experiments, a three-cycle sinusoidal burst at 5 MHz, weighted by a Hanning window, was transmitted from each element. No spatial apodization was used during transmission and reception, but different apodizations were compared during offline beamforming. All along the reported results, the images are normalized using their own maximum amplitude and are log compressed. A 50 dB dynamic is used in the figures issued from simulation or acquired data.

#### 3.5.2.1. CREANUIS simulation

Evaluation of the different beamforming apodization and number of steering angles

The parameters used in MCPWC simulations are given in Table 3.4 and Table 3.5. $\theta_{min}$ and $\theta_{max}$ were fixed, and only the angle step was changed. Figure 3.15 shows the influence of compounding on MCPWC images with DPSS 3 apodization. Figure 3.16 shows the behavior of the SNR, CNR, and lateral and axial resolutions as a function of the number of transmission angles for different reception apodizations windows. All parameters are calculated at a depth of 30 mm (Figure 3.4.a) and SNR and CNR values are expressed in decibel. The values are normalized by the SNR or the CNR of the image obtained from a single plane wave and with a rectangular apodization.

| $\theta_i$ | -15° to 15° | | | | | | | | | 0° |
|---|---|---|---|---|---|---|---|---|---|---|
| $\Delta\theta$ (°) | 0.5 | 1.0 | 1.5 | 2 | 2.5 | 3.0 | 6.0 | 10 | 15 | 0 |
| $N_\theta$ | 61 | 31 | 21 | 17 | 13 | 11 | 7 | 5 | 3 | 1 |
| $\frac{1}{t_{acq}}$ (kHz) | 0.28 | 0.55 | 0.80 | 0.99 | 1.3 | 1.5 | 2.4 | 3.4 | 5.6 | 17.1 |

**Table 3.4: Transmission angles and frame rate**

| | Rectangular | Hanning | DPSS 3 | DPSS 5 | DPSS 7 | DPSS 9 |
|---|---|---|---|---|---|---|
| $k$ | | | 1.5 | 2.5 | 3.5 | 4.5 |

**Table 3.5: Apodization parameters**

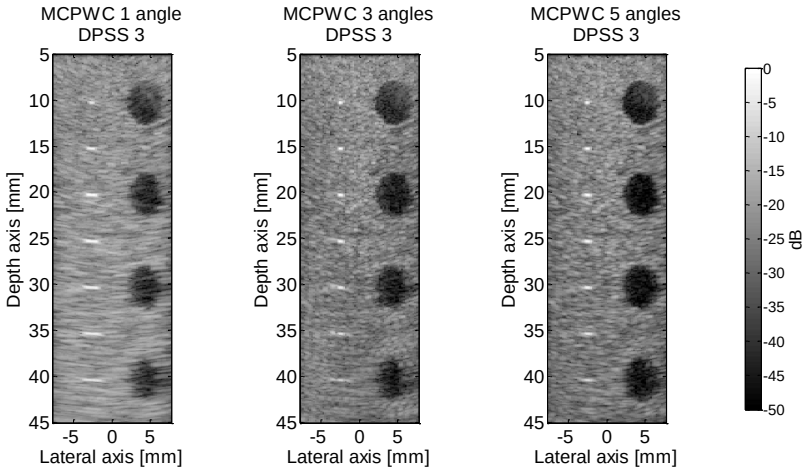


(a) (b) (c)

**Figure 3.15: MCPWC Log compressed ultrasound images of wires and hypoechoic cysts simulated by CREANUIS, for (a) one transmitted angle, (b) three transmitted angles and (c) five transmitted angles.**

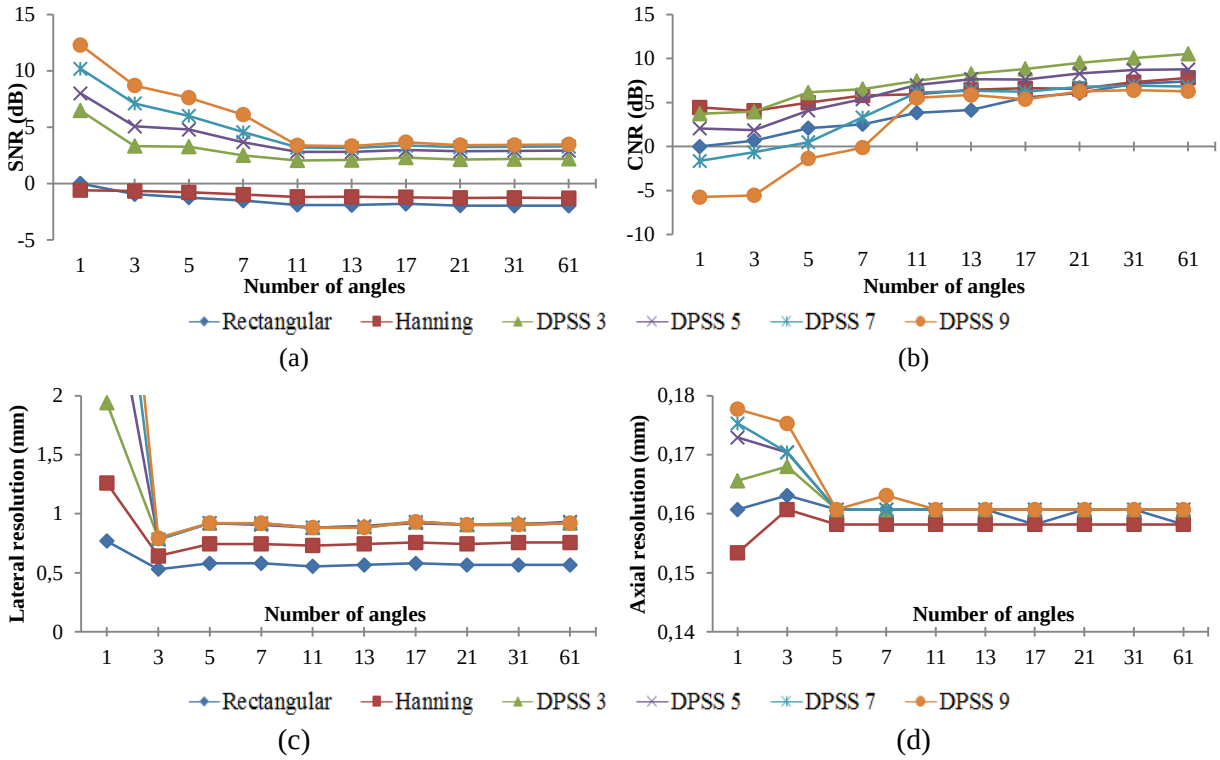


**Figure 3.16: CREANUIS simulations on the phantom described in Figure 3.a. (a) SNR, (b) CNR, and (c) lateral resolution and (d) axial resolution as a function of the number of angles in transmission and for different apodization during beamforming. The parameters were calculated at a depth of 30 mm.**

When a single plane wave transmission is combined with a DPSS apodization during the beamforming, the speckle noise is smoothed but with a significant decrease in image quality (Figure 3.15.a). Increasing the number of steered plane waves for the same DPSS apodization, the contrast and the resolution are improved but the speckle is less smoothed (Figure 3.15.c) while the frame rate decreases (Table 3.5).

Figure 3.16.a shows that the SNR obtained with Hanning and rectangular apodization is nearly constant for all sets of angles, while it is higher for the DPSS apodization. In the latter case, only when the number of transmissions is less than 11 the SNR increases with the DPSS order. Moreover, the SNR is better when the number of angles is low, which can be explained by observing the Figure 3.15. In Figure 3.15.a, the speckle pattern is in fact more uniform, i.e the local variance is lower, than in Figure 3.15.c.

Figure 3.16.b shows that the best CNR (at a 30 mm depth) is obtained with the DPSS 3 taper. Whatever the apodization, the CNR increases when more steered angles are involved because of the coherent contributions of several RF images. The same effect was observed in (Montaldo et al., 2009) (Cheng and Lu, 2006) and is confirmed by Figure 3.16.

Figure 3.16.c and Figure 3.16.d show the effect of apodization on lateral and axial resolutions. The axial resolution is not impacted by the use of several apodizations during beamforming or by the use of different set of angles. The best resolution is obtained with the rectangular apodization for all of the considered sets of angles. The DPSS tapers give the same lateral resolution when 3 or more angles are used but largely differ for a single transmission angle. The constant value of the lateral resolution can be explained from the considerations developed in (Denarie et al., 2013) by using the F-number. Equation (2.7) shows that the resolution in the image only depends on the maximum angle used during transmission. It does not take into account the transmitted angle sequence. The number of

angle can be decimated introducing grating lobes, reducing the lateral resolution, and improving the frame rate.

Comparison of the results obtained with SF, MF, CPWC and MCPWC

The results in Figure 3.16 suggest the parameters to be used in order to compare the SF, MF, CPWC and MCPWC images. Concerning the apodization, the rectangular and the DPSS 3 apodizations offer the best performance in terms of resolution and CNR, respectively. Table 3.6 indicates the main parameters used in SF (col.1), MF (col.2), CPWC and MCPWC (col.3-5) modes. In particular the 3rd column, CPWC and MCPWC have the same acquisition time as in SF mode (3.7 ms). In the last column, the CPWC or MCPWC methods implemented with few angles (11) have a frame rate about 5 and 40 times higher than the SF and MF techniques respectively. The spatial resolutions are the same for these three MCPWC cases as demonstrated in Figure 3.16. Furthermore, the Figure shows that working with more than 10 angles guarantees that the optimal SNR is achieved, while only the CNR continues to increase with the number of angles.

According to these indications, the analysis of SNR, CNR and spatial resolutions for CPWC and MCPWC has been concentrated on the case of 11 angles, which significantly reduces the acquisition time. For the SF images the focalization was set at 30 mm. For the MF images seven focal depths were spaced 5 mm apart between 10 and 40 mm.

| | **SF** | **MF** | **CPWC or MCPWC** | | |
|---|---|---|---|---|---|
| $\theta_i$ | 0° | 0° | -15° to 15° | | |
| $\Delta\theta$ | | | 0.5° | 1° | 3° |
| $N_\theta$ | 1 | 1 | 61 | 31 | 11 |
| $N_{line}$ | 64 | 64 | 1 | 1 | 1 |
| $t_{acq}$ **(ms)** | 3.7 | 26.2 | 3.6 | 1.8 | 0.65 |
| $\frac{1}{t_{acq}}$ **(kHz)** | 0.27 | 0.04 | 0.28 | 0.55 | 1.53 |

**Table 3.6: Summary of transmission parameters and acquisition time**

A comparison of simulated images for SF, MF, CPWC and MCPWC is given in Figure 3.17. SF and MF images were computed with both rectangular apodization and DPSS 3 apodization. CPWC and MCPWC images used the rectangular and the DPSS 3 window, respectively. The top panels make use of a rectangular reception apodization while the bottom panels use the DPSS 3 apodization. The SNR, CNR and resolutions results are given in Figure 3.18. The SNR and CNR values are normalized by the corresponding value of the SF image close to 30 mm and are expressed in decibel. Positive values indicate SNR or CNR improvement compared to the values obtained at 30 mm on the SF image with rectangular apodization.

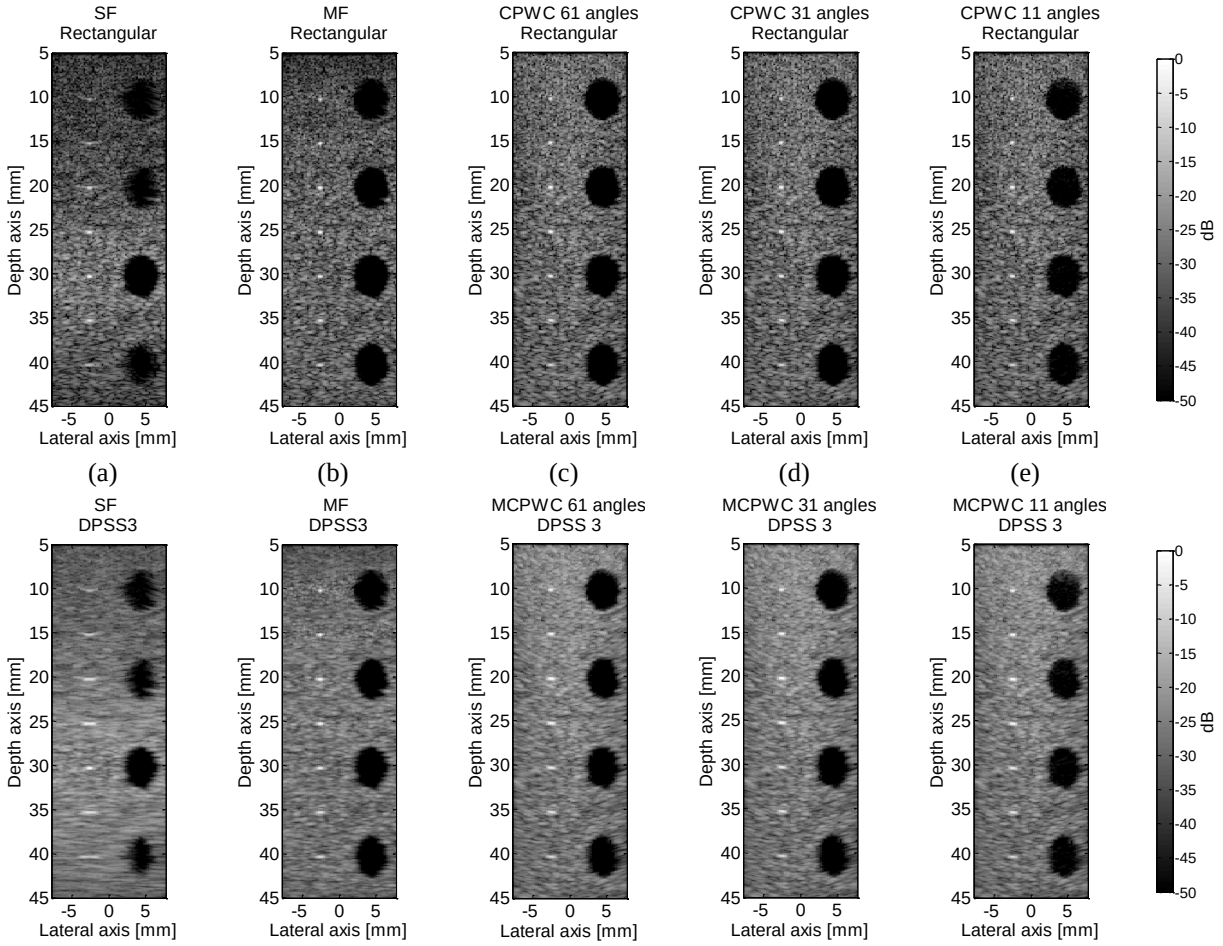


**Figure 3.17: Log compressed ultrasound images of hypoechoic cysts and wires simulated by the CREANUIS simulator, (a, f) one focal depth at 30 mm without and with three apodization tapers on reception, (b, g) MF without and with three apodization tapers on reception, (c-e) CPWC and (h-j) MCPWC with three apodization tapers on reception and 61, 31 and 11 transmitted angles.**

The images built with a DPSS apodization improve the SNR and the CNR for all methods at each depth. The SNR or CNR values obtained with DPSS apodization are always higher than with rectangular apodization. However, the results given for the SF approach in Figure 3.18.c show that the lateral resolution, outside the focal depth, decreases more quickly with the DPSS 3 taper than with the rectangular apodization. The CPWC 11 and MCPWC 11 techniques are able to improve the resolution outside the focal depth. The Figure 3.16.d shows that the axial resolution is not influenced by the method employed. In this case, outside of the focal area, the MCPWC 11 improves the lateral resolution by a factor two and the CNR by about 2 dB. Visually, Figure 3.17 shows that the differences between MF and CPWC, with rectangular apodization or with DPSS 3 apodization, are low. The only noticeable difference is the artifact noise present in the top of the first cyst for DPSS 3 apodization.

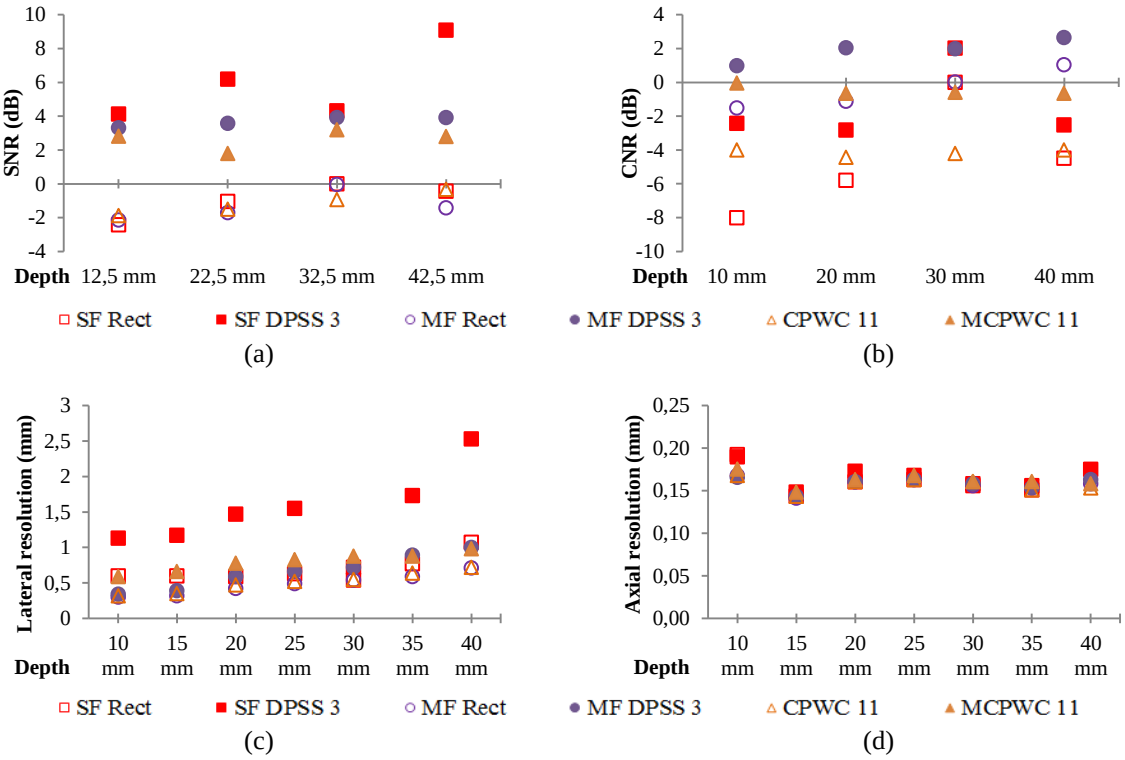


**Figure 3.18: CREANUIS simulations on the phantom described in Figure 3.4.a. (a) SNR, (b) CNR, (c) lateral resolution and (d) axial resolution estimated at different depths for different transmission methods (SF, MF, CPWC / MCPWC) and different apodizations (Rectangular and DPSS3) during beamforming.**

#### 3.5.2.2. ULA-OP acquisition

The MCPWC technique was applied to an actual phantom using the ULA-OP system. Only the comparison with SF, MF, CPWC and MCPWC has been realized (Appendix E). The experimental SF, MF, CPWC and MCPWC images confirm the simulation results: in the upper images the speckle is less smooth than in the lower images (Figure E. 1, Figure E. 2). The SNR and the CNR increase for the DPSS images, whereas the lateral resolution decreases and the axial resolution is not influenced (Figure E. 3). Unlike the simulations, cysts edges are less degraded with the DPSS tapers.

#### 3.5.2.3. Conclusion

The choice of the best set of MCPWC parameters to optimize criteria such as the acquisition time, SNR, CNR and resolution is not trivial, because contradictory effects can be obtained depending on the criteria to emphasize. In conclusion, it has been shown that using 11 steering angles (-15° to 15°) with a DPSS 3 taper is the optimum set-up to smooth the speckle and to have a better contrast and spatial resolution compared to SF approach. The DPSS 3 taper is the optimum DPSS apodization for the CNR. Due to the property of the coherent plane wave compounding, it is possible to increase the resolution and CNR by about 2 dB outside the focal area. The low number of steering angles (11) yields an acceptable tradeoff between the contrast quality and the frame rate, which is significantly improved with respect to the standard SF technique.

## 3.6. Discussion and conclusion

The study of Thomson's multitaper approach proved its effectiveness to reduce the speckle noise and to improve the contrast. However the method suffers of limitations such as

the resolution reduction when it is utilized with the classic single focalization. Two methods have been proposed to improve the TM approach. The best method is the multitaper coherent plane wave compounding allowing resolution and contrast improvement in the entire image. Moreover, the frame rate is improved 5 times when 11 steering angles are used.

In the next part, several methods to estimate the nonlinear parameter are proposed. Furthermore, the TM approach and plane wave compounding are proposed to improve the nonlinear parameter estimation in echo mode.

# II. Nonlinearity parameter measurement

# Chapter 4

# Nonlinearity parameter estimation: State of the art

In this chapter, a state of the art of the different methods allowing the measurement of the nonlinearity parameter is presented. The objective of the work is to find a method which can be easily used for clinical application. The literature presents the different methods for nonlinearity parameter estimation as two main families: the thermodynamic methods and the finite amplitude methods (Hamilton and Blackstock, 1998). The first one are recognized as the most accurate methods but employing a complex experimental setup (Hamilton and Blackstock, 1998). The finite amplitude methods are thus suitable for clinical applications. This review is mainly based on F. Varray publications (Varray, 2011) (Varray et al., 2011).

## 4.1. Thermodynamic methods

In section 1.4, the nonlinearity *B/A* parameter has its origin in the Taylor series expansion of the celerity variation in terms of the pressure for an adiabatic transformation. The nonlinearity parameter is expressed by (Beyer, 1960) (Hamilton and Blackstock, 1998) as:

$$\frac{B}{A} = 2\rho_0 c_0 \left(\frac{\partial c}{\partial P}\right)_{\rho_0,s} \tag{4.1}$$

The classical thermodynamic method is expressed by developing this expression (4.1) (Beyer, 1960) (Hamilton and Blackstock, 1998)**:**

$$\begin{aligned}\frac{B}{A} &= 2\rho_0 c_0 \left(\frac{\partial c}{\partial P}\right)_{\rho_0,T} + \frac{2c_0 T\chi_p}{\rho_0 c_p}\left(\frac{\partial c}{\partial T}\right)_{\rho_0,P} \\ &= \left(\frac{B}{A}\right)' + \left(\frac{B}{A}\right)''\end{aligned} \tag{4.2}$$

where $\chi_P = (1/V)(\delta V/\delta T)_P$ is the volume coefficient of thermal expansion and $c_P$ is the specific heat at constant pressure. *B/A* is described as the sum of two terms:

$$\begin{cases}\left(\frac{B}{A}\right)' = 2\rho_0 c_0 \left(\frac{\partial c}{\partial P}\right)_{\rho_0,T} \\ \left(\frac{B}{A}\right)'' = \frac{2c_0 T\chi_p}{\rho_0 c_p}\left(\frac{\partial c}{\partial T}\right)_{\rho_0,P}\end{cases} \tag{4.3}$$

The first term, $(B/A)'$, corresponds to the pressure derivative term for an isothermal process. The second term, $(B/A)''$, corresponds to the temperature derivative term for an isobar process. It has been shown for organic liquids, that the dominant part of the expression is the pressure derivative term. The measure of the nonlinearity parameter is thus

approximated by several authors to the measurement of the pressure derivative term $(B/A)'$ (Law, Frizzell and Dunn, 1983) (Beyer, 1960).

Different evaluations of the pressure derivative term have been proposed by. Z. Zhu measures the change in the travel time of ultrasonic tone burst which are caused by prescribed changes in the ambient pressure (Zhu et al., 1983). Two transducers are separated by a fixed distance *L*. The wave propagates through the medium between the two transducers in a duration time $\tau$. The change in the sound speed in the medium due to variation of the static pressure is:

$$\frac{\partial c}{\partial P} = \frac{-L}{\tau^2}\frac{\partial \tau}{\partial P} \tag{4.4}$$

The nonlinearity parameter is approximated to:

$$\frac{B}{A} = \frac{-2\rho_0 c_0^2}{\tau}\left(\frac{\Delta\tau}{\Delta P}\right)_s \tag{4.5}$$

Z. Zhu reported that the changes in transit time $\tau$ are equivalent to phases shifts in the acoustic wave which has propagated in the medium (Zhu et al., 1983). C.M. Shegal proposed to simplify the equation (4.1) and the first term of (4.2) using directly the phase difference (Sehgal, Bahn and Greenleaf, 1984) (Sehgal, Porter and Greenleaf, 1986):

$$\frac{\partial \phi}{\partial P} = -\frac{L\omega}{c_0^2}\frac{\partial c}{\partial P} \tag{4.6}$$

where $\phi$ is the phase. The equation (4.1) and the first term of (4.2) can be expressed as:

$$\begin{cases} \dfrac{B}{A} = 2\rho_0 c\left(\dfrac{\partial c}{\partial P}\right)_{\rho_0,s} = -\dfrac{2\rho_0 c_0^3}{L\omega}\dfrac{\Delta\phi_s}{\Delta P} \\ \left(\dfrac{B}{A}\right)' = 2\rho_0 c\left(\dfrac{\partial c}{\partial P}\right)_{\rho_0,T} = -\dfrac{2\rho_0 c_0^3}{L\omega}\dfrac{\Delta\phi_T}{\Delta P} \end{cases} \tag{4.7}$$

where $\Delta\phi_s$ and $\Delta\phi_T$ are the two phases differences during an adiabatic and isothermal process, respectively. Estimating $(B/A)$ and $(B/A)'$ at two different moments, the measurement of $\Delta\phi_T$ is done half an hour after $\Delta\phi_s$, C.M. Shegal gets two close values improving the *B/A* estimation.

B.T. Sturtevant estimated the nonlinearity of liquid water at high temperature (250°C) and at high pressure (14 MPa) (Sturtevant, Pantea and Sinha, 2012). The proposed method evaluates the sound speed in water using a swept frequency acoustic interferometry technique for different temperature and for different pressures (Sturtevant, Pantea and Sinha, 2012). The variation of the speed in function of the temperature and the pressure are used in (4.3) to estimate *B/A*. The *B/A* parameter estimated at ambient temperature is close to the literature but at high temperature and at high pressure, the *B/A* is 20% higher than the values calculated with the international standard speed.

The thermodynamic method is a technique usually used by chemist for evaluating the nonlinearity parameter of liquid mixture. The *B/A* parameter is interesting for liquid because he can provides information about properties such as internal pressure, intermolecular

potential, spacing, acoustic diffraction… A specific study on the glycol-water mixture has been conducted by J. Khelladi and B.B. Nanda (Khelladi et al., 2009) (Nanda, Nanda and Mohanty, 2012). Sulfate in polyvinyl alcohol (PVA) solutions and benzyliden aniline Schiff base liquid crystalline systems have been studied by S. Ravichandran and M.V.V.N. Reddy (Ravichandran and Ramanathan, 2010) (Reddy et al., 2011). J. Khelladi employed the phase method proposed above. B.B. Nanda, S. Ravichandrand and M.V.V.N. Reddy utilized the linear relation between the nonlinearity parameters of liquids and sound speed obtained from the empirical rule of Ballou employed by Hartmann (Hartmann, 1979):

$$\frac{B}{A} = -0.5 + \left( \frac{1.2 \times 10^4}{c} \right) \tag{4.8}$$

Hartmann proposed a derived equation to improve the *B/A* estimation:

$$\frac{B}{A} = 2 + \left( \frac{0.98 \times 10^4}{c} \right) \tag{4.9}$$

The *B/A* parameter of alkanediols has been evaluated by thermodynamic method under high pressure (Zorebski and Zorebski, 2014). The goal of E. Zorebski is to analyze the experimental relation between *B/A* and internal pressure. The internal pressure measures the energy variation of a system when the system expands or contracts at a constant temperature. A relationship between *B/A* and internal pressure is proposed and the relationship allowed to verify the *B/A* value using the internal pressure values reported in literature.

The nonlinearity parameter has been evaluated for different liquid such as water, mixed liquid but also for biological media. W. Law did some measures of the nonlinear parameter in biological materials and also compared the thermodynamic and finite amplitude methods (Law, Frizzell and Dunn, 1983) (Law, Frizzell and Dunn, 1985). R.L. Errabolu evaluated the nonlinear parameter in excised human and animal fat tissues and some simple solution such as milk (Errabolu et al., 1988).

## 4.2. Finite amplitude methods

The finite amplitude methods have two advantages: it is experimentally easier to implement and there is the possibility to simulate the pressure wave propagation. The methods are differentiated by their transmissions along the axial direction of the probe. The three main groups of finite amplitude methods are: the single frequency transmission, the composite frequency transmission and the pump wave method. Their principle is schematized in Figure 4.1. The first group (Figure 4.1.a) consists in the transmission of one wave at a frequency *f* and to the evaluation of the increase of the second harmonic during the propagation. The second group (Figure 4.1.b) is composed of several transmission signals at different frequencies in the medium. The nonlinear parameter is estimated using the complementary waves created at the sum ($f_+$) and difference ($f_-$) frequencies. The last group (Figure 4.1.c) involves a pumping wave perpendicular to the transmitted wave. The interaction between the two waves creates a phase shift that is related to the nonlinear parameter.

During the thermodynamic methods presentation, the nonlinearity parameter *B/A* is directly given. In finite amplitude methods, the literature deals with the nonlinear parameter $\beta$ which is linked to the *B/A* parameter (1.20).

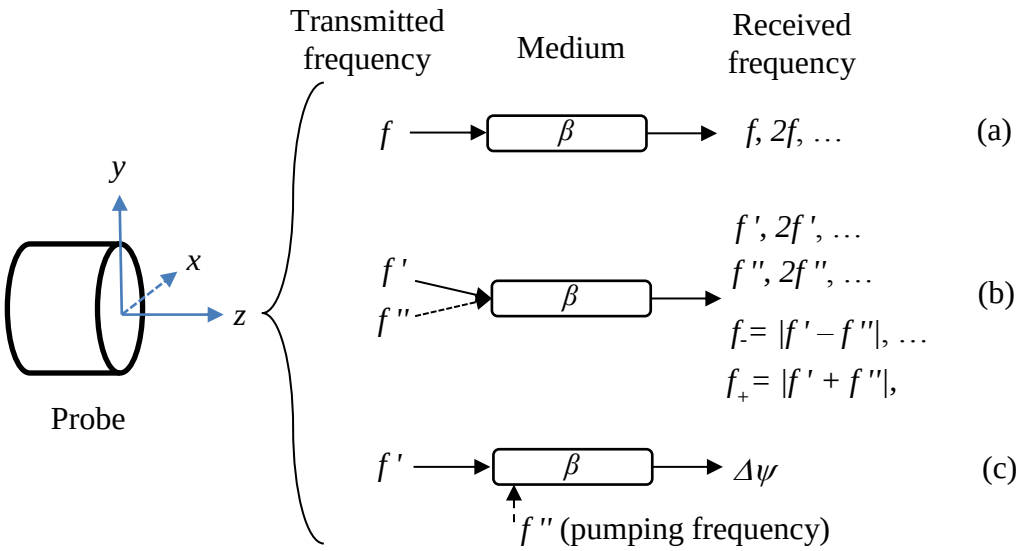


**Figure 4.1: Schematic representation of the three different approaches to determine the nonlinear parameter *β* of the propagation medium by finite amplitude methods. The groups are differentiated by the transmitted interrogative wave: (a) methods with a single frequency transmission, (b) methods with composite signal transmission and (c) methods using pumping waves during the propagation of a single transmission.**

### 4.2.1. Single frequency transmission

#### 4.2.1.1. Direct method

The direct method is the simplest method to estimate the nonlinear parameter consisting to transmit a wave with amplitude $P_1$ with a single frequency. In reception, the amplitude of the second harmonic component $P_2$ is measured. L. Adler and W.K. Law proposed an expression of the nonlinear coefficient depending on the ratio of the pressure amplitude of the second harmonic component $P_2(z)$, along the propagation axis, by the fundamental at the source $P_1(0)$ (Adler and Hiedemann, 1962) (Law, Frizzell and Dunn, 1981) (Law, Frizzell and Dunn, 1985):

$$\beta = \frac{2\rho_0 c_0^3}{\omega} \frac{P_2(z)}{zP_1^2(0)} \tag{4.10}$$

However the expression of the nonlinear coefficient is imprecise due to the attenuation. Thus W.K. Law completed the equation (4.10) by taking into account the attenuation in the medium (Law, Frizzell and Dunn, 1985):

$$\beta = \frac{2\rho_0 c_0^3}{\omega} \frac{P_2(z)}{zP_1^2(0)} e^{-(\alpha_1+\alpha_2/2)z}\Big|_{z\to 0} \tag{4.11}$$

where $\alpha_1$ and $\alpha_2$ are the attenuation of the fundamental and the second harmonic components. The $z \to 0$ indicates the limited range of validity and the necessity to be close to the transducer. Moreover, to take into account the diffraction loss in the medium for a piston source, W.K. Law corrected the second harmonic expression with a diffraction correction term, F(z) defined for an ideal piston source (Law, Frizzell and Dunn, 1985):

$$\beta = \frac{2\rho_0 c_0^3}{\omega} \frac{P_2(z)}{zP_1^2(0)} e^{-(\alpha_1+\alpha_2/2)z} F^{-1}(z)\Big|_{z\to 0} \quad \textbf{(4.12)}$$

C. Pantea proposed to not employ approximations related to attenuation and to measure pressure values of the fundamental and second harmonic component at various transmitter-receiver distances (Pantea, Osterhoudt and Sinha, 2013). The nonlinear parameter is given as:

$$\beta = \frac{2\rho_0 c_0^3}{\omega} \frac{P_2(z)}{zP_1^2(z)} \quad \textbf{(4.13)}$$

The determination of $\beta$ with the equation (4.13) is ambiguous due to several limitations such as the transducer nonlinearity or the shock formation length. However in medical imaging, the ultrasound wave is attenuated before the shock formation length. Moreover beyond the near-field distance, the values of $\beta$ are possibly erroneous. C. Pantea proposed to re-arranged the equation (4.13) and to use the slope of $P_2(z)/P_1^2(z)$ obtained at different transmitter-receiver distances:

$$slope\left(\frac{P_2(z)}{P_1^2(z)}\right) = \frac{\beta\pi f}{\rho_0 c_0^2} z \quad \textbf{(4.14)}$$

From this slope, or a fitted one passing by the origin, the nonlinear parameter is estimated.

When the several direct methods presented above are used during experiments, the authors proposed three different methods to evaluate the fundamental pressure at the source and the second harmonic pressure after the propagation. The first approach proposed by L. Adler used an optical system (Adler and Hiedemann, 1962). The second approach used a transmitter and a hydrophone or another transducer to quantify the pressure component after a propagation distance (Law, Frizzell and Dunn, 1981) (Gong et al., 1984) (Law, Frizzell and Dunn, 1985) (Wallace et al., 2007) (Pantea, Osterhoudt and Sinha, 2013). The third approach used the same transmitter in transmission and reception (Gupta, Chauhan and Sexana, 2004) (Vander Meulen and Haumesser, 2008) (Vander Meulen and Haumesser, 2008). The second harmonic pressure component is measured after a reflection on a metallic plate. For a constant attenuation in the medium, the second harmonic is expressed as:

$$P_2(z) = \frac{\beta\omega}{2\rho_0 c_0^3} P_1^2(0) R(1+R) \int_0^z e^{-2\alpha_1 u - \alpha_2(2z-u)du} \quad \textbf{(4.15)}$$

where $R$ is a reflection coefficient if the metallic plate is not perfect. The nonlinear coefficient is thus:

$$\beta = \frac{2\rho_0 c_0^3}{\omega} \frac{P_2(z)}{R(1+R)P_1^2(0)} \frac{\alpha_2 - 2\alpha_1}{e^{-(2\alpha_1+\alpha_2)z} - e^{-2\alpha_2 z}} \quad \textbf{(4.16)}$$

A recent method proposed by T. Kujawska is the combination of modeling and experimental data (Kujawska, Nowicki and Lewin, 2011). The hybrid method is based on the comparison of the predicted and experimentally determined amplitudes of harmonic components in a two-layer configuration of parallel media. The numerical model used is the JW model which is an extension of the nonlinear propagation equation developed in the KZK

model (Wojcik et al., 2006). The two-layer media is composed of water (6 cm) and the tested fluid (0 – 6 cm). The first centimeters of water are used in order to avoid measurement in the near field. The ratio of the fundamental to the second harmonic amplitude measured and simulated is done for several depths. Several nonlinear parameters are used in simulation in order to fit the fundamental and second harmonic ratio.

#### 4.2.1.2. Insertion-substitution method

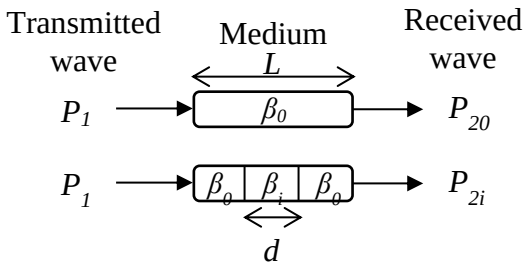


**Figure 4.2: Illustration of the insertion-substitution method. The second harmonic pressure is measured in a reference medium with a known $\beta_0$ and in a medium having a nunknown $\beta_i$ inserted in the reference medium.**

The insertion-substitution method consists to measure twice the second harmonic in a medium which has been partially modified (Figure 4.2). In a reference medium (subscript 0) of length $L$ which nonlinear parameter $\beta_0$ is known, the second harmonic pressure $P_{20}$ is measured. Then, a part of the reference medium, length $d$, is substituted by a medium (subscript i) which nonlinear parameter $\beta_i$ is unknown. The second harmonic pressure is once again measured, $P_{2i}$.

X. Gong showed that the unknown nonlinear coefficient $\beta_i$ can be expressed as (Gong et al., 2004):

$$\frac{\beta_i}{\beta_0} = \left( \frac{P_{2i}}{P_{20}} \frac{1}{D'D''} \frac{L}{d} - \frac{L}{d} + 1 \right) \frac{\left(\rho c^3\right)_i}{\left(\rho c^3\right)_0} \frac{1}{D''} \tag{4.17}$$

where $D'$ and $D''$ are :

$$\begin{cases} D' = 2(\rho c)_0 / \left[ (\rho c)_0 + (\rho c)_i \right] \\ D'' = 2(\rho c)_i / \left[ (\rho c)_0 + (\rho c)_i \right] \end{cases} \tag{4.18}$$

However the expression of the nonlinear coefficient is imprecise due to the attenuation. Thus X. Gong modified the (4.17) by taking into account the attenuation in the medium (Gong et al., 1989):

$$\frac{\beta_i}{\beta_0} = \left( \frac{P_{2i}}{P_{20}} \frac{L}{d} \frac{1}{I_1 I_2} - \left[ \frac{L}{d} - 1 \right] \frac{I_2}{I_1} D'D'' \right) \frac{\left(\rho c^3\right)_i}{\left(\rho c^3\right)_0} \frac{1}{D''^2 D'} \tag{4.19}$$

where $I_1$ and $I_2$ are the attenuation terms of the fundamental and the second harmonic, respectively:

$$\begin{cases} I_1 = e^{-\alpha_1 d} \\ I_2 = e^{-\alpha_2 d/2} \end{cases} \quad \textbf{(4.20)}$$

Moreover, to take into account the diffraction loss in the medium for a piston source, X. Gong corrected the expression with a diffraction correction term, *F(k, $z_0$, z)* defined for an ideal piston source of radius *a* (Gong et al., 1989):

$$F(k, z_0, z) = 1 - \frac{2}{z - z_0} \int_{z_0}^{z} \frac{1 - \xi(z - \mu/2)/2k^2a^2}{\sqrt{\pi\xi(z - \mu/2)}} d\mu \quad \textbf{(4.21)}$$

with

$$\xi(z) = k \frac{\sqrt{z^2 + 4a^2} - z}{2} \quad \textbf{(4.22)}$$

The final expression proposed by X. Gong is expressed as:

$$\frac{\beta_i}{\beta_0} = \left( \frac{P_{2i}}{P_{20}} \frac{L}{d} \frac{1}{I_1 I_2} - \left[ \frac{L}{d} - 1 \right] \frac{I_2}{I_1} D'D'' \frac{F(k_0, d, L)}{F(k_0, 0, L)} \right) \times \frac{(\rho c^3)_i}{(\rho c^3)_0} \frac{1}{D''^2 D'} \frac{F(k_0, 0, L)}{F(k_0, 0, d)} \quad \textbf{(4.23)}$$

The attenuation and diffraction corrections of the nonlinear parameter estimation for the insertion-substitution and for a piston source by X.Gong are close to the correction proposed by W.K. Law for the direct method approach.

The insertion-substitution method has been employed by several authors (Gong et al., 1984) (Gong et al., 1989) (Saito, 1993) (Zhang, Gong and Ye, 1996) (Wu and Tong, 1998) (Zhang and Gong, 1999) (Dong et al., 1999) (Harris et al., 2007). All authors use the same reference medium, water, to measure the unknown nonlinear parameter. However the authors did not use the same techniques.

X. Gong and G.R. Harris use two transducers, one transmitter and one receiver (Gong et al., 1984) (Gong et al., 1989) (Harris et al., 2007). The sample with an unknown nonlinear parameter is set between the two transducers. The distance between the two transducers has to be less than 10 cm (Harris et al., 2007). J. Wu utilizes the same approach to evaluate the nonlinear parameter of ultrasound contrast agent (UCA) (Wu and Tong, 1998). The contrast agents have a nonlinear parameter much higher than the biological tissues with the different concentrations used (B/A > 100). F. Dong utilizes the same disposition previously described but the distance between the two transducers is higher (60 cm) (Dong et al., 1999). The receiver is far enough from the transmitter so that plane waves are well approximated at the interrogated sample with an unknown nonlinear parameter. During the propagation in the reference medium, second harmonic is generated. A glycerol attenuator is set before the sample to guarantee that the plane waves contain very few second-harmonic component.

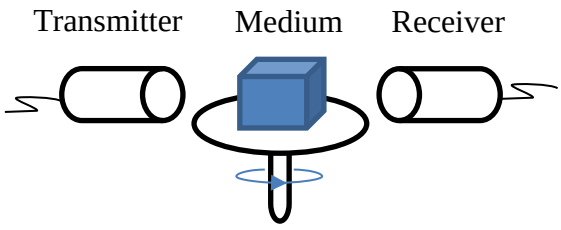


**Figure 4.3: Ultrasound computer tomography (UCT) scanning system. The nonlinear parameter image is obtained by rotating the medium or the transmitter/receiver couple.**

The previous authors calculate the nonlinear parameter giving only one value of the sample. D. Zhang proposed to use the ultrasound computed tomography (UCT) to obtain a nonlinear parameter image (Zhang, Gong and Ye, 1996) (Zhang and Gong, 1999). Y. Nakagawa was the first obtaining an experimental image of the nonlinear parameter with the UCT method (Nakagawa et al., 1984) (Nakagawa et al., 1986). As in the previous settings, two transducers are used (Figure 4.3). Furthermore, by rotating the transmission-reception setup around the medium, different acquisitions are made and a reconstruction algorithm provides an image of the nonlinear coefficient. With biological media, the UCT technique indicates that values of acoustic nonlinearity parameters of pathological tissues are obviously higher than those of healthy counterparts.

Another method proposed by S. Saito uses a focused source to insonified the medium (Saito, 1993)**.** However the previous formulations are no more correct. The mathematical theory for focalized source is given by S. Saito and start by introducing a new variable $R$ for plane wave transmission:

$$R(z) = \frac{\beta_i \rho_0 c_0^3}{\beta \rho_i c_i^3} \frac{T_I}{\left(T_I T_O\right)^{a_2/a_1 - 1}} = \left(\frac{P_{2i}(z)}{P_{20}(z)}\right)\left(\frac{P_{10}(z)}{P_{1i}(z)}\right)^{a_2/2a_1 - 1} \tag{4.24}$$

where $T_I$ and $T_O$ are the transmission coefficients of the sound pressure at the water-sample and sample-water interface, respectively, which are defined by the linear acoustic properties of two media. For a focused source, the pressure amplitude of the second harmonic component generated at the focal region can be detected by employing the phase parameter $\phi_i$ and $\phi_0$:

$$\begin{aligned} \phi_0 &= \phi_{20} - 2\phi_{10} \\ \phi_i &= \phi_{2i} - 2\phi_{1i} \end{aligned} \tag{4.25}$$

A new quantity $R_F$ defined for focused sources which is derived from $R$ and the phase parameter $\phi_i$ and $\phi_0$:

$$\begin{aligned} R_F &= \left(\frac{P_{2i}(z)}{P_{20}(z)} \frac{\sin\phi_i}{\sin\phi_0}\right)\left(\frac{P_{10}(z)}{P_{1i}(z)}\right)^{a_2/2a_1 - 1} \\ &= R\frac{\sin\phi_i}{\sin\phi_0} \end{aligned} \tag{4.26}$$

Prior to the measurement for $R_F$, the linear acoustic properties $c_i$, $\rho_i$ and attenuation $\alpha_1$ and $\alpha_2$ are measured. The experimental setup design by S. Saito is composed of a Gaussian focused source and a hydrophone. The sample is placed at the focal point of the focused source in order to have accurate results.

#### 4.2.1.3. Comparative method

The comparative method finds its origin in the insertion-substitution method. It is a particular case where the inserted medium has the same length as the reference medium. Thus the (4.19) can be simplified as:

$$\beta_i = \beta_0 \frac{P_{2i}}{P_{20}} \frac{1}{I_1 I_2} \frac{(\rho c^3)_i}{(\rho c^3)_0} \frac{1}{D''^2 D'} \tag{4.27}$$

The comparative method can be used in simple transmission but also after a reflection on a metallic plate. As in insertion-substitution method, the comparative formulation has to be modified. D. Kourtiche updated the comparative method with reflections and sensitivity coefficients (Kourtiche et al., 2001):

$$\beta_i = \beta_0 \frac{P_{2i}}{P_{20}} \frac{R_{ri}}{R_{r0}} F_\eta F_{diff} F_\alpha \frac{(\rho c^3)_i}{(\rho c^3)_0} \tag{4.28}$$

where $R_{ri}$ and $R_{r0}$ are the reflection coefficients between water and reflector and the studied medium and the reflector, respectively. $F_\eta$ is the sensitivity function, $F_{diff}$ the diffraction function and $F_\alpha$ is the attenuation function.

X. Gong proposed a similar application (Gong et al., 2004). Starting from the equation (4.15), the ratio of the second harmonic components between the unknown medium and the reference medium is expressed as:

$$\frac{P_{2i}(z)}{P_{20}(z)} = \frac{\beta_i}{\beta_0} \frac{(\rho c^3)_i}{(\rho c^3)_0} \frac{R_{ri}(1+R_{ri})}{R_{r0}(1+R_{r0})} \frac{\int_0^z e^{-2\alpha_{1i}u - \alpha_{2i}(2z-u)} du}{\int_0^z e^{-2\alpha_{10}u - \alpha_{20}(2z-u)} du} \tag{4.29}$$

where $\alpha_{10}$, $\alpha_{20}$, $\alpha_{1i}$ and $\alpha_{2i}$ are respectively the fundamental and second harmonic attenuation of the reference and unknown medium. The nonlinear coefficient of the unknown medium can then be extracted:

$$\beta_i = \beta_0 \frac{P_{2i}(z)}{P_{20}(z)} \frac{(\rho c^3)_0}{(\rho c^3)_i} \frac{R_{r0}(1+R_{r0})}{R_{ri}(1+R_{ri})} \frac{\int_0^z e^{-2\alpha_{10}u - \alpha_{20}(2z-u)} du}{\int_0^z e^{-2\alpha_{1i}u - \alpha_{2i}(2z-u)} du} \tag{4.30}$$

The proposed methods are applied for a planar source. S. Saito extended its proposed method using a focalized source for insertion-substitution approach (Saito, 1993) to comparative method (Saito, Kim and Nakamura, 2006) (Saito, 2010) (Saito and Kim, 2011). S. Saito used the formulation (4.28) and created an experimental system measuring the celerity, the density and the attenuation of the inserted sample. Moreover in (Saito and Kim, 2011), the experimental system has been automated applying two-dimensional measurements of excised biological samples. The focus of the sound beam is shifted by moving an *x-y* stage creating a two-dimensional nonlinear parameter image of excised biological samples.

### 4.2.2. Composite frequency transmission

The composite frequency transmission is based on the nonlinear interaction between two waves transmitted in a medium at the same time. In addition to the harmonic generation during the propagation for both waves, the nonlinear interaction between two waves creates

components at the sum and difference frequencies (Westervelt, 1963) (Fenlon, 1972). The nonlinear interaction is related to the nonlinearity *B/A* parameter and several authors have attempted to determine the nonlinear parameter through this composite emission. The composite frequency transmission is subdivided in several approaches to determine the nonlinear coefficient.

#### 4.2.2.1. Composite signal with two different frequencies

D. Zhang proposed to combine the composite frequency transmission and UCT technique (Zhang, fen Gong and Chen, 2001). A high $f_h$ and a low $f_l$ frequency signals are transmitted in the medium by a piston source. The initial amplitude of both high and low frequency signals are $P_{h0}$ and $P_{l0}$ respectively. Moreover the initial amplitude of the low frequency signal is superior to the high frequency signal ($P_{l0} \gg P_{h0}$). The total pressure wave is expressed as:

$$P(t, z=0) = P_{h0}\sin(2\pi f_h t) + P_{l0}\sin(2\pi f_l t) \quad \textbf{(4.31)}$$

Due to a nonlinear interaction between the two waves, sum and difference frequency components are generated. F.H. Fenlon gave a solution to the lossless Burgers' equation describing the evolution of the maximal pressure of the wave created at the sum ($P_s$) and difference ($P_d$) frequencies (Fenlon, 1972):

$$P_{s/d}(z) = \frac{2}{(\varepsilon_h \pm \varepsilon_l)u_0} J_1((\varepsilon_h \pm \varepsilon_l)u_h) J_1((\varepsilon_h \pm \varepsilon_l)u_l) \quad \textbf{(4.32)}$$

with:

$$\varepsilon_{h/l} = \frac{\beta \omega_{h/l} z}{c_0^2} \quad \textbf{(4.33)}$$

Where $J_1$ is the first order Bessel function, $u_0$, $u_l$ and $u_h$ are the particle velocities at the source for respectively the total, the low and the high frequency waves. D. Zhang combined the difference formulation with the insertion substitution method (Zhang, fen Gong and Chen, 2001). The difference frequency component provides a better source for acoustic nonlinearity parameter tomography because the pressure of the difference frequency grows almost linearly with distance from the piston source compared with the second harmonic wave. There is no attenuation of the difference frequency wave compared to the second harmonic wave (Westervelt, 1963). The error of the measurements was under 10%.

#### 4.2.2.2. Composite signal with two close frequencies

When two close high-frequency ($f_h$ and $f_h + f_d$) waves are transmitted in the same direction, a low frequency ($f_d$) wave is generated by nonlinear interaction of sound waves. Y. Nakagawa proposed to derive the pressure $P_d(z)$ of the low frequency wave to access to the nonlinear parameter (Nakagawa et al., 1984) (Nakagawa et al., 1986):

$$\frac{dP_d(z)}{dz} = \frac{\beta(z)\omega_d}{2\rho_0 c_0^3} P_1(z) P_2(z) - \alpha_d(z) P_d(z) \quad \textbf{(4.34)}$$

where $\alpha_d(z)$ is the attenuation of the difference wave. The nonlinear parameter is thus expressed as:

$$\beta(z) = \frac{2\rho_0 c_0^3}{\omega_d P_{f_h}(z) P_{f_h+f_d}(z)} \left( \frac{dP_d(z)}{dz} + \alpha_d(z) P_d(z) \right) \quad \textbf{(4.35)}$$

Y. Nakagawa used his method with the UCT approach given the first nonlinear parameter image. A. Cain adapted the equation (4.34) in three algorithms to compute the *B/A* parameter for three, weakly, moderately and strongly scattering medium (Cai, Sun and Wade, 1992). The different approaches have been implemented and simulated data shows a good correlation with their theoretical results.

#### 4.2.2.3. Second-order ultrasound field technique

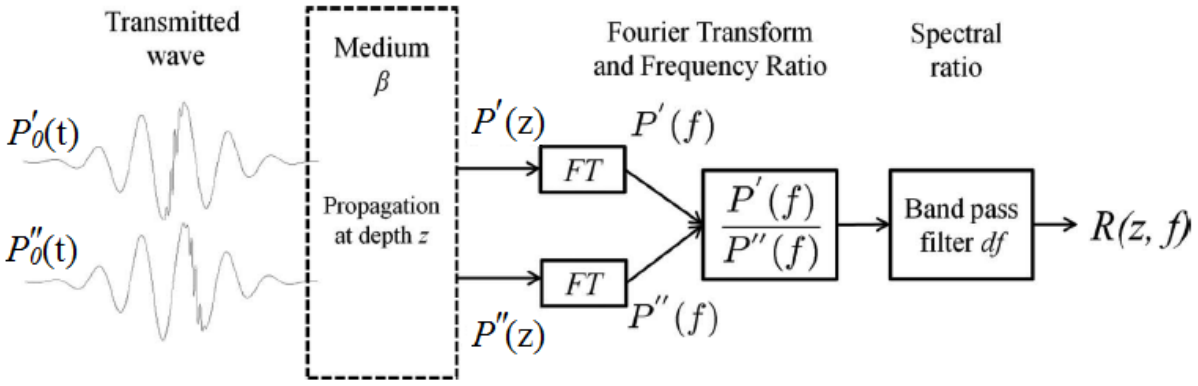


**Figure 4.4: Second-order ultrasound field (SURF) method: transmission of two consecutive waves with the different high-frequency pulse localizations. The nonlinear coefficient is computed from the pair of recorded pulses (Ueno et al., 1990) (Varray et al., 2011).**

The second-order ultrasound field (SURF) technique is proposed by S. Ueno (Ueno et al., 1990). The method is based on the nonlinear interaction between two specific waves which are superimposed and propagated in the same direction. The specificity of these waves is the presence of a high frequency ($f_h$) component during the increasing part or the decreasing part of a low frequency ($f_l$) wave (Figure 4.4). $P'_0$ and $P''_0$ are the two different transmitted signals. During the propagation, the high pressure of the wave travels faster than the low pressure of the wave as it was demonstrated in the section 1.4.2.The high frequency pulse coinciding with the increasing part of the low pressure ($P'_0$) has an increase of the speed, thus the frequency decrease. While the high frequency pulse coinciding with the decreasing part of the low pressure ($P''_0$) has a reduction of the speed, thus the frequency increases.

The theoretical background to compute the nonlinear coefficient has been developed by H. Fukukita (Fukukita, Ueno and Yano, 1996). In the Figure 4.4, for a given depth *z*, the two waves $P'(z)$ and $P''(z)$ are transformed into the frequency domain to produce $P'(f)$ and $P''(f)$, respectively. Then, the spectrum ratio $R(z, f)$ is computed over a bandwidth $\pm df$ around the high frequency $f_h$. This ratio corresponds to the spectral variation of the compression and the dilation of the high-frequency pulse on the two different low frequency waves:

$$R(z, f) = \frac{P'[f_h - df; f_h + df]}{P''[f_h - df; f_h + df]} \quad \textbf{(4.36)}$$

From (4.36), the crossover frequency $f_x$ is obtained when:

$$\log\left(R(z, f = f_x)\right) = 0 \quad \textbf{(4.37)}$$

The slope of the spectral ratio $S_x$ at $f_x$ is also needed to obtain the final value of the nonlinear coefficient:

$$S_x(z) = \left( \frac{\delta \log[R(z, f)]}{\delta f} \right)_{f=f_x} \tag{4.38}$$

$$\beta(z) = \frac{\rho_0 c_0^3 B_0^2}{2\omega_l P_0} \frac{S_x(z)}{z f_x(z)} \tag{4.39}$$

where $B_0^2$ is the frequency variance of the spectrum defined by H. Fukukita (Fukukita, Ueno and Yano, 1996).

### 4.2.3. Pump wave method

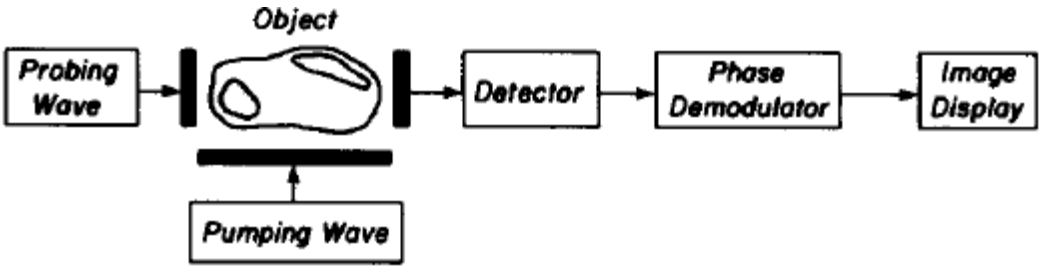


**Figure 4.5: Imaging system using the pump wave method. A probe wave and pump wave are transmitted at the same time. The pump wave modified the probe wave propagation and a phase modulation is present on the probe pulse and is related to the nonlinear parameter (Kim, Greenleaf and Sehgal, 1990).**

The pump wave method consists to use a low frequency with a high amplitude pump wave and a relatively low amplitude and high frequency probe wave at the same time. The pressure field generated by the pump wave $P_p$ is uniform along the path of the probe wave and interacts with the medium inducing a variation in the sound speed of the probe wave. This speed variation produces a cumulative phase shift which is detected at the receiver (Figure 4.5). This method has been presented by N. Ichida and the nonlinear parameter is expressed in function of the phase modulation $\Delta\psi$ along a short distance $\Delta z$ (Ichida, Sato and Linzer, 1983) (Ichida et al., 1984):

$$\frac{B}{A} = -\frac{2\rho_0 c_0^3}{\omega P_p} \frac{\Delta\psi}{\Delta z} \tag{4.40}$$

N. Ichida and D. Kim have presented an extended formulation of this formulation to take into account the possible variation of the nonlinear parameter along the studied direction (Ichida, Sato and Linzer, 1983) (Kim, Greenleaf and Sehgal, 1990). The extended formulation is:

$$\Delta\Psi\left(\frac{1}{\lambda_p}, y\right) = \frac{\omega}{2\rho_0 c_0^3} P_p \int_0^z \frac{B}{A}(x, y) \cos\left(\frac{2\pi x}{\lambda_p}\right) dx \tag{4.41}$$

with $\lambda_p$ the pump wavelength. The equation (4.41) implies that the phase shift of the probe wave, due to the pump wave of the spatial frequency $1/\lambda_p$, is the Fourier transform of the distribution of the nonlinear parameter $B/A$ in the z direction (Kim, Greenleaf and Sehgal, 1990). Doing different estimation of the phase shift at different position, the inverse Fourier transform yields a nonlinear parameter map.

C.A. Cain proposed an approach using a pump wave transmitted with the same transducer as the probe wave (Cain, 1986). A plane reflector is placed at a distance $L$ of the transducer. To image the entire line along the propagation path, a probe wave of duration $2L/c_0$ must be used and the total time for the transmission and the reception of the signal is $4L/c_0$. During the incident propagation, the probe wave only interacts with the medium. While during the reflected propagation, the probe wave also interacts with the pump wave. The phase modulation corresponds to the difference between the phase of the signal during the incident propagation (without pump wave interaction) and during the reflected propagation (with pump wave interaction) which takes into accounts the nonlinear parameter. The phase shift depends on the received time $\tau$ which is in the range of [0; $2L/c_0$]. The equation proposed by C.A. Cain is expressed as the convolution between the pump waveform $P_p(x,t)$ and the spatial distribution of the nonlinear parameter (Cain, 1986):

$$\Delta\Psi(\tau) = -\frac{\omega}{2\rho_0 c_0^3}\int_0^{c_0\tau/2} P_p\left(\frac{c_0\tau}{2}-x\right)\frac{B}{A}(x)dx \qquad \textbf{(4.42)}$$

## 4.3. Nonlinear parameter estimation: extensions in echo mode

In the previous parts, the thermodynamic and finite amplitude approaches has been presented. The thermodynamic is the method allowing the best estimation of the nonlinear parameter but because of the specific equipment required, the technique is inappropriate for clinical application. F. Varray presented several extensions of potential methods of *B/A* measurements in echo mode: the extended direct method (EDM), the extended comparative method (ECM) and the extended SURF method (ESURF) (Varray, 2011) (Varray et al., 2011). All techniques are based on the finite amplitude methods. The finite amplitude methods are privileged for their experimental simplicity and the possibility to evaluate the ultrasound pressure wave propagation with simulators. Pressure field of the ultrasound simulations have been done using a plane wave transmission with or without taking into account the effect of diffraction. The ECM method allows a better estimation, compared to EDM and ESURF, of the nonlinear parameter without diffraction and a good estimation with diffraction. Moreover the method shows its ability to estimate the nonlinear parameter in simulated echographic B-mode image.

The extended comparative method (ECM) is presented and it is implemented in this work to estimate the nonlinearity parameter. The ECM finds its origin in insertion-substitution method developed in (Zhang and Gong, 1999). The objective is to compare a reference medium with a known nonlinear coefficient $\beta_0$ (subscript *0*) and another medium with an unknown nonlinear coefficient $\beta_i$ (subscript *i*). ECM is based on the expression of the amplitude pressure of the second-harmonic wave $P_2$ which is expressed as (Zhang and Gong, 1999):

$$P_2(z) = \frac{\omega P_0^2}{2\rho_0 c_0^3}\int_0^z \beta(u) e^{\int_0^u -2\alpha_1(v)dv - \int_0^u \alpha_2(v)dv} du \qquad \textbf{(4.43)}$$

This equation can also be expressed as:

$$P_2(z) = \frac{\omega P_0^2}{2\rho_0 c_0^3} e^{-\int_0^u \alpha_2(v)dv}\int_0^z \beta(u) e^{\int_0^u (\alpha_2(v)-2\alpha_1(v))dv} du \qquad \textbf{(4.44)}$$

In the case of a homogeneous nonlinear coefficient and attenuation in the reference medium, (4.43) could be expressed as:

$$P_{20}(z) = \frac{\beta_0 \omega P_0^2}{2\rho_0 c_0^3} I_0(z) \tag{4.45}$$

where

$$I_0(z) = \frac{e^{-2\alpha_{10}z} - e^{-\alpha_{20}z}}{\alpha_{20} - 2\alpha_{10}} \tag{4.46}$$

The subscript *0* is also used for the attenuation. Indeed, the reference medium and the unknown one can have different attenuation values. Based on the comparative method, which is a particular case of insertion-substitution method, the ratio between the amplitude pressure of the second harmonics of the unknown medium and the reference medium can be expressed using (4.44) and (4.45):

$$\frac{P_{2i}(z)}{P_{20}(z)} = \frac{\left(\rho c^3\right)_i}{\left(\rho c^3\right)_0} \frac{e^{-\int_0^u \alpha_{2i}(v)dv} \int_0^z \beta_i(u) e^{\int_0^u (\alpha_{2i}(v) - 2\alpha_{1i}(v))dv} du}{\beta_0 I_0(z)} \tag{4.47}$$

$$\beta_i(z) = \beta_0 \frac{\left(\rho c^3\right)_i}{\left(\rho c^3\right)_0} \left[ V(z) \frac{P_{2i}(z)}{P_{20}(z)} + W(z) \frac{d}{dz}\left( \frac{P_{2i}(z)}{P_{20}(z)} \right) \right] \tag{4.48}$$

where *V(z)* and *W(z)* are two terms depending on attenuations of the two different media:

$$\begin{cases} V(z) = \dfrac{e^{-2\alpha_{10}z}\left(\alpha_{2i}(z) - 2\alpha_{10}\right) - e^{2\alpha_{20}z}\left(\alpha_{2i}(z) - 2\alpha_{10}\right)}{\alpha_{20} - 2\alpha_{10}} e^{\int_0^z 2\alpha_{1i}(v)dv} \\ W(z) = I_0(z) e^{\int_0^z 2\alpha_{1i}(v)dv} \end{cases} \tag{4.49}$$

The final equation in (4.48) is valid in media with different densities, celerities and attenuations. If the attenuations are considered equal in the two media and homogeneous during the propagation, *V(z)* and *W(z)* are simplified as:

$$\begin{cases} V(z) = 1 \\ W(z) = \dfrac{1 - e^{-(\alpha_2 - 2\alpha_1)z}}{\alpha_2 - 2\alpha_1} \end{cases} \tag{4.50}$$

which leads to a simplified expression of the nonlinearity coefficient:

$$\beta_i(z) = \beta_0 \frac{\left(\rho c^3\right)_i}{\left(\rho c^3\right)_0} \left[ \frac{P_{2i}(z)}{P_{20}(z)} + \frac{1 - e^{-(\alpha_2 - 2\alpha_1)z}}{\alpha_2 - 2\alpha_1} \frac{d}{dz}\left( \frac{P_{2i}(z)}{P_{20}(z)} \right) \right] \tag{4.51}$$

The equation (4.51) shows that $\beta_i$ depends on the ratio, $P_{2i}/P_{20}$, of the local pressures. This approach is thus feasible in simulation or when the pressure is directly measurable in the media with a hydrophone.

## 4.4. Discussion and conclusion

In this chapter, different techniques to measure the nonlinear parameter have been presented. The thermodynamic methods have a good accuracy but need specific equipment to perform the measurement, while the finite amplitude methods can be used in echo mode and are thus suitable for clinical applications (Law, Frizzell and Dunn, 1983) (Varray, 2011). In the Table 4.1, the nonlinearity parameter of several biological media is presented and the techniques used, thermodynamic or finite amplitude, are given. R.T. Beyer summarizes a large variety of nonlinearity parameter of fluids, gases, biological tissues and proteins in the book (Hamilton and Blackstock, 1998). The recent study of F. Varray proposed the ECM approach to image the *B/A* parameter in inhomogeneous nonlinear media. However, the single focalization transmission method employed with the ECM technique presents drawbacks. First, the focalization used during the transmission concentrates the energy at one particular depth and is then not homogeneous on the image. Second is the inaccurate delimitation of areas with different *B/A* in the media. Finally, the accuracy is limited by the presence of speckles in the image.

In the next chapter, several methods to improve the nonlinear parameter estimation in echo mode are proposed.

| Medium | Temperature | *B/A* | Method | Reference |
|---|---|---|---|---|
| Water | 20°C | 5.0 | Thermo. | (Beyer, 1960) |
| | 20°C | 4.8 | Thermo. | (Sturtevant, Pantea and Sinha, 2012) |
| | 250°C | 10 | Thermo. | |
| | | 5.0 | F.A. | (Pantea, Osterhoudt and Sinha, 2013) |
| Beef liver | | 6.88 | Thermo | (Law, Frizzell and Dunn, 1983) |
| | 30°C | 6.42 | F.A. | |
| Breast fat | 22°C | 9.21 | Thermo. | (Sehgal, Bahn and Greenleaf, 1984) |
| | 30°C | 9.91 | Thermo. | |
| | 37°C | 9.63 | Thermo. | |
| Porcine liver | | 6.8 ± 0.3 | F.A. | (Zhang and Gong, 1999) |
| | | 6.9 | F.A. | (Gong et al., 2004) |
| | | 7.27 ± 0.19 | F.A. | (Saito and Kim, 2011) |
| Pig fat | 25°C | 10.9 | Thermo. | (Law, Frizzell and Dunn, 1985) |
| | 25°C | 11.0 – 11.3 | F.A. | |
| Human multiple myeloma | 22°C | 5.6 | Thermo. | (Sehgal, Bahn and Greenleaf, 1984) |
| | 30°C | 5.8 | Thermo. | |
| | 37°C | 6.2 | Thermo. | |

**Table 4.1: Nonlinear parameters of several media as reported in the literature and estimated by thermodynamic (Thermo.) or finite amplitude (F.A.) approach.**

# Chapter 5

# Nonlinearity parameter estimation in echo mode

In the previous chapter, several approaches to estimate the nonlinear parameter were presented. Unfortunately, only few techniques can be used for clinical application and moreover in echo mode. The extended comparative method (ECM) proposed by F. Varray is suitable but he mentioned some limitations: the energy concentration due to the focalization prevents to obtain an homogeneous evaluation on the whole image and the delimitation of the nonlinearity parameter is inaccurate (Varray et al., 2011). The ECM approach is based on the second-harmonic pressure however in echo mode, only RF or envelope images which are measurements of the local echogenicity and not of the pressure are obtained. F. Varray supposed that the local pressure field can be derived from envelope images local amplitude if the speckle noise is smoothed. F. Varray proposed to use an alternative sequential filter (ASF) but the speckle noise is not effectively suppressed.

In this chapter the methods proposed in the Chapter 3, the Thomson's multitaper (TM) and the multitaper coherent plane wave compounding (MCPWC), are combined with the ECM approach in order to improve the nonlinearity parameter estimation in echo mode.

## 5.1. Pressure field *B/A* estimation

The ECM approach has been evaluated only in single transmit focus (SF) approach (Varray, 2011) (Varray et al., 2011). However the SF has the drawback to concentrate the energy at one depth. If the nonlinearity area is inside or outside the focal depth, the ECM method can overestimated or undervalue the *B/A* parameter. In pressure field simulation, it is proposed to evaluate the effect of the focal depth for the *B/A* estimation. Moreover, a plane wave transmission is proposed to overcome the focalization effect.

The measurement of the nonlinearity parameter from the ECM approach has been evaluated with pressure field simulation on complex media. Two nonlinearity media, simulated with CREANUIS are given in Figure 5.1. One medium (Figure 5.1.a) is composed of a background with $B/A = 5$ and an elliptic inclusion with $B/A = 10$. The second medium (Figure 5.1.b) is similar, excepted that inside the elliptic inclusion, two regions with different nonlinearity parameters (3 and 9) were included. The first nonlinearity medium is called 'simple' nonlinearity medium and the second is named 'complex' nonlinearity medium. The two vertical lines in each figure indicate the medium used as a reference in the ECM. The nonlinearity parameter is homogeneous inside this region. A 5-cycle sinusoidal burst at 3 MHz weighted by a Gaussian window was transmitted from each element. No spatial apodization was used in both transmission and reception. The probe parameters are given in the Table 3.1. The acoustic characteristics of the medium are given in Table 3.2.

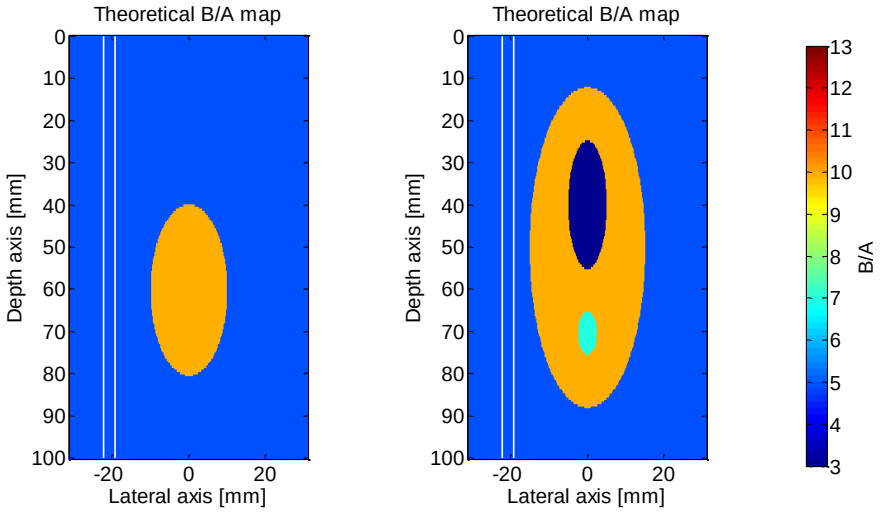


(a) (b)

**Figure 5.1: Schematic nonlinearity parameters medium used in CREANUIS simulation. The reference medium is between the two white lines. (a) Simple and (b) complex nonlinearity media.**

### 5.1.1. Single focalization limitation

In order to test the ECM method in function of the focalization, pressure field simulations have been realized for three single transmit focus (SF) at different depths. The focalizations are chosen: before, inside and after the simple nonlinearity area (Figure 5.1.a). These three depths correspond to 30, 60 and 90 mm.

A probe with 256 elements and an aperture of 64 actives elements, corresponding to the aperture of the LA 533 probe (Table 3.1), has been used for pressure field simulation. 256 pressure fields are thus been simulated and they are based on the aperture. The aperture is moved 256 times in order to compute the entire image. For each pressure field simulation, the corresponding nonlinear coefficient map in front of the aperture has to be used. Then, the central line of the produced second-harmonic is saved in the second-harmonic field image. Finally the ECM approach is applied on the second-harmonic field image. As an example, the second-harmonic pressure field image of the 60 mm focalization with the simple nonlinearity medium is given in Figure 5.2.a. The area between the two white lies is considered as the reference medium where the nonlinearity is constant. Figure 5.2.b shows the pressure field ratio between the unknown and reference medium. The attenuation and the celerity of the reference and unknown mediums are equal, thus the equation (4.51) is used to calculate the nonlinear parameter. The nonlinearity parameter *B/A* is then calculated (1.20). Figure 5.3 shows the nonlinearity parameter estimation for the several SF focalizations for the two nonlinear medium. The mean and the standard deviation (STD) of the *B/A* parameter estimated in each area are given in the Table 5.1 and Table 5.2.

The resulting *B/A* images and values show that in function of the focal depth, the ECM has difficulties to estimate the *B/A*. For simple or complex medium, focalization at 30 mm has the worst *B/A* estimation. This is due to the weak second-harmonic energy transmitted after the 30 mm. The *B/A* values for the focalizations 60 and 90 mm are close but the 90 mm focalization has the advantage to better delimit the *B/A* areas. The spread effect below the *B/A* area is less important. However, the ECM provided promising results for *B/A* imaging but has to be improved in terms of delimitation and energy concentration.

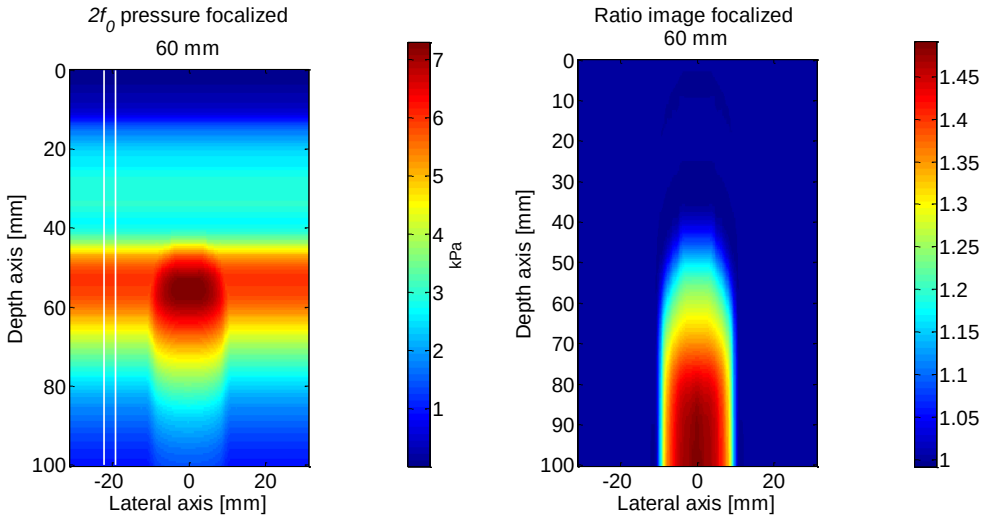


**Figure 5.2: (a) Second-harmonic pressure field and (b) pressure field ratio of the 2nd harmonic in the unknown and reference media for the simple nonlinear media with a focalization at 60 mm.**

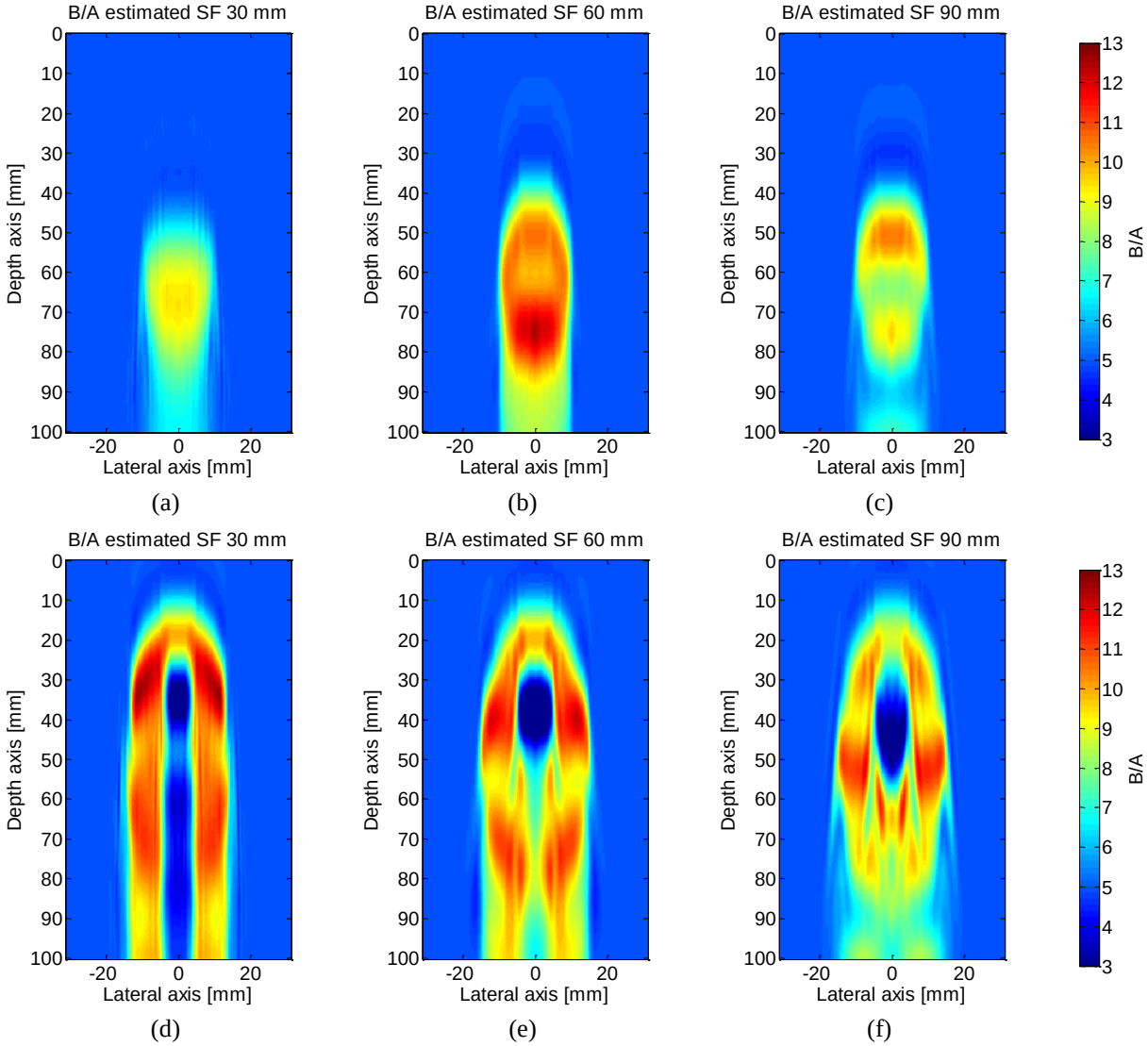


**Figure 5.3: CREANUIS *B/A* estimation with second-harmonic pressure field for SF approaches for simple (a-c) and complex (d-f) *B/A* media and three focalizations: (a, d) 30 mm, (b, e) 60 mm and (c, f) 90 mm.**

| *B/A* | SF 30 mm | | SF 60 mm | | SF 90 mm | |
|---|---|---|---|---|---|---|
| | Mean | STD | Mean | STD | Mean | STD |
| 5 | **5.2** | 0.5 | **5.4** | 1.1 | **5.2** | 0.5 |
| 10 | **7.9** | 1.2 | **10.3** | 1.0 | **8.8** | 0.8 |

**Table 5.1: Nonlinearity *B/A* parameter estimated with pressure field for three single focalizations (30, 60 and 90 mm) for the simple *B/A* medium.**

| *B/A* | SF 30 mm | | SF 60 mm | | SF 90 mm | |
|---|---|---|---|---|---|---|
| | Mean | STD | Mean | STD | Mean | STD |
| 3 | **5.4** | 2.1 | **4.1** | 2.1 | **4.5** | 1.6 |
| 5 | **5.5** | 1.3 | **5.5** | 1.3 | **5.4** | 0.8 |
| 7 | **4.1** | 0.2 | **8.6** | 0.5 | **9.0** | 0.5 |
| 10 | **9.3** | 2.4 | **9.8** | 1.1 | **9.2** | 1.1 |

**Table 5.2: Nonlinearity *B/A* parameter estimated with pressure field for three single focalizations (30, 60 and 90 mm) for the complex *B/A* medium.**

### 5.1.2. Spatial compounding improvement

In section 2.1.1.2, the spatial incoherent composition approach improving the contrast and reducing the speckle noise was presented (Berson, Roncin and Pourcelot, 1981) (Entrekin et al., 1999). Moreover was demonstrated the gain in term of shadowing reduction was demonstrated. For *B/A* imaging, the hypothesis is that the spatial compounding method reduces the spread effect when the *B/A* is estimated. Two spatial compounding are proposed. The first one has three transmitted angles with an angular step of 1.5°. The second also has three transmitted angles but the angular step is larger, 5°. These two approaches have been chosen from S.K. Jespersen results (Jespersen, Wilhjelm and Sillesen, 1998). He proposed to use small angular range to improve low contrast detection and a larger angular range to improve delimitation. The two angular ranges are tested in order to know which one is better for *B/A* imaging.

The two spatial compounding, (-1.5°, 0°, 1.5°) and (-5°, 0°, 5°), are focalized at 60 mm and are compared to the SF focalized at 60 mm. The second-harmonic pressure field of spatial compounding approaches is computed by averaging the pressure field of each transmitted angle. Figure 5.4, Table 5.3 and Table 5.4 show the *B/A* estimation for the two *B/A* mediums.

The *B/A* images show that the spatial compounding with low angular separation (Figure 5.4.b, e) reduces more efficiently the spread effect than the two others approaches. Moreover the *B/A* estimation is better with the low angular separation. With the higher angular separation, there are artefacts in *B/A* images close to 70 mm (Figure 5.4.c, f). These results were expected because large angular range can have grating lobes influencing with the nonlinear media and reducing the nonlinearity estimation precision (Jespersen, Wilhjelm and Sillesen, 1998). S.K. Jespersen also reported that low angular range is interesting for low contrast detection. In *B/A* imaging, the goal is to improve the contrast between the reference and the unknown medium which may have low intensity difference and the spatial compounding may be a possibility.

The spatial compounding improves the *B/A* imaging when low angular separation is used. However the technique has the drawback to focalize the energy at one particular depth, like the SF method. To overcome this problem, plane wave transmission is proposed.

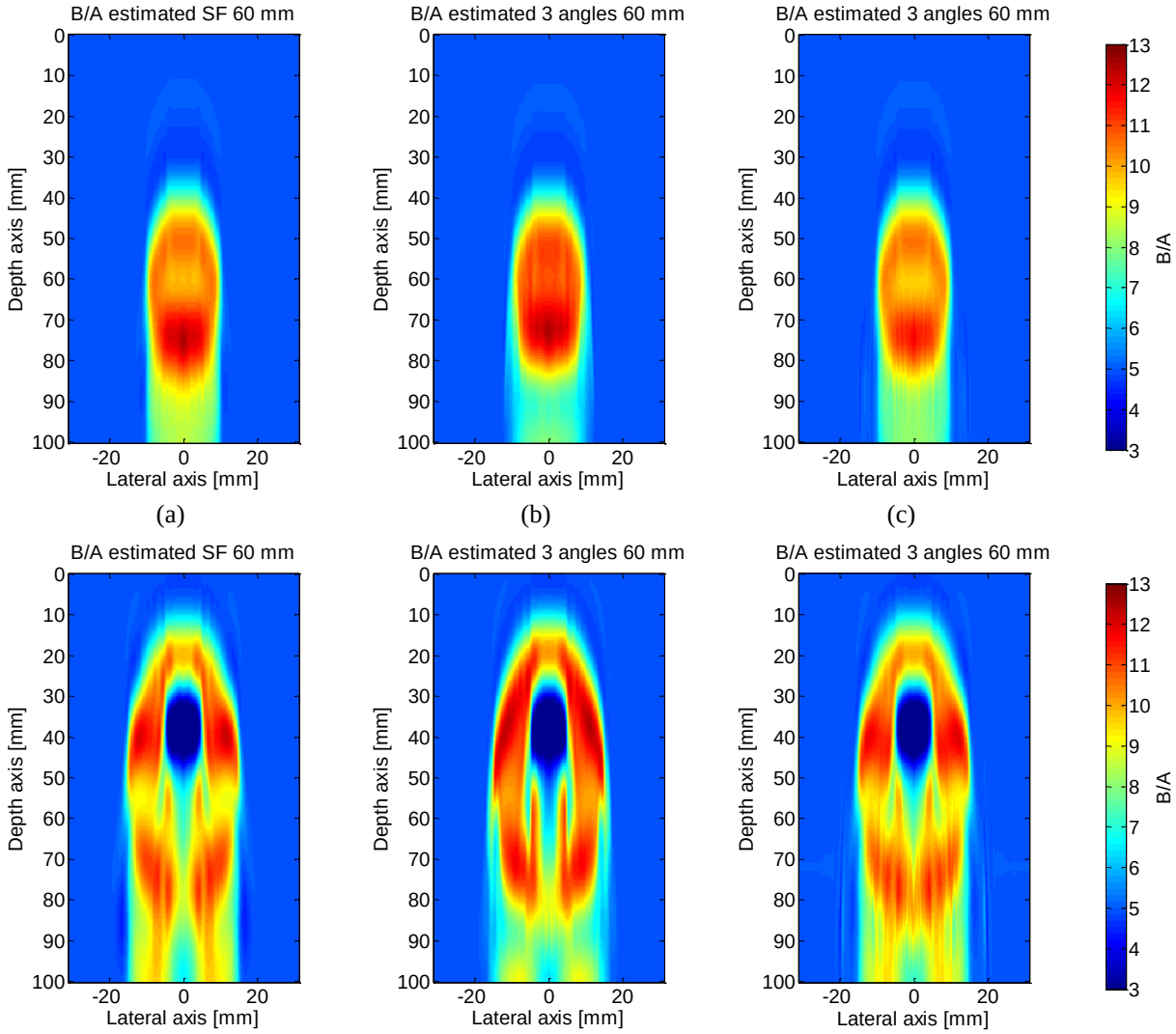


**Figure 5.4: CREANUIS *B/A* estimation with second-harmonic pressure field for SF approaches for simple (a-c) and complex (d-f) *B/A* media and three tranmissions: (a, d) SF 60 mm, (b, e) spatial (-1.5°, 0°, 1.5°) and (c, f) spatial (-5°, 0°, 5°).**

| *B/A* | SF 60 mm | | Spatial 3 (-1.5°, 0°, 1.5°) | | Spatial 3 (-5°, 0°, 5°) | |
|---|---|---|---|---|---|---|
| | Mean | STD | Mean | STD | Mean | STD |
| 5 | **5.4** | 1.1 | **5.3** | 0.9 | **5.3** | 0.5 |
| 10 | **10.3** | 1.0 | **10.6** | 1.1 | **10.1** | 0.8 |

**Table 5.3: Nonlinearity *B/A* parameter estimated with pressure field for one single focalization (60 mm) and two spatial approaches (-1.5°, 0°, 1.5°) and (-5°, 0°, 5°) for the simple *B/A* medium.**

| *B/A* | SF 60 mm | | Spatial 3 (-1.5°, 0°, 1.5°) | | Spatial 3 (-5°, 0°, 5°) | |
|---|---|---|---|---|---|---|
| | Mean | STD | Mean | STD | Mean | STD |
| 3 | **4.1** | 2.1 | **3.7** | 1.9 | **4.1** | 2.02 |
| 5 | **5.5** | 1.3 | **5.5** | 1.1 | **5.6** | 1.2 |
| 7 | **8.6** | 0.5 | **8.0** | 0.6 | **9.4** | 0.6 |
| 10 | **9.8** | 1.1 | **10.1** | 1.4 | **9.8** | 1.1 |

**Table 5.4: Nonlinearity *B/A* parameter estimated with pressure field for one single focalization (60 mm) and two spatial approaches (-1.5°, 0°, 1.5°) and (-5°, 0°, 5°) for the complex *B/A* medium.**

### 5.1.3. Plane-wave compounding improvement

The plane-wave transmission compounding is proposed to insonify the whole nonlinear media without any focalization. Moreover, the use of steering angle offers a better delimitation of the *B/A* areas and avoid shadowing than the spatial compounding approach. However, the plane-wave transmission has two drawbacks which are the energy reduction and the aperture limitation. First, these limitations are analyzed in a first part, and second the plane-wave compounding is evaluated for *B/A* imaging.

#### 5.1.3.1. Plane-wave analysis

The energy reduction is linked to the excitation of all active elements at the same time, creating a plane wavefront. The energy is theoretically homogeneously distributed, there is no energy concentration, and thus the mean energy is reduced compared to the energy on the focal area.

The aperture is linked to the geometry of the probe. In the case of a perfect piston, the wave front is perfectly plane. With an echographic probe, the element's aperture has a finite size. So there is edges interference during the propagation of the signal. The Figure 5.5 shows the simulated second-harmonic pressure field for several sizes of the aperture: 64, 128 and 256 active elements. All the active elements have the same size (Table 3.1). The 64 active elements aperture is the actual limitation of the ULA-OP scanner and 256 active elements will be the future version of the ULA-OP. Even if no focalization was selected with the 64 active elements, two intense lobes are present showing a 'virtual' focalization. Using a higher number of active elements (Figure 5.5.a-c) the lobes are still present, but they are shifted, allowing a 'real' plane wave in the center of the pressure field image (Figure 5.5.d-f).

The presence of lobes has been analyzed in acquisition using the ULA-OP system and a pressure field platform (Appendix E). A 3-cycle sinusoidal burst signal at 5 MHz weighted by a temporal Hanning window was transmitted from each element of the LA533 linear array. No spatial apodization was used on the 64 active elements during transmission. The fundamental and second-harmonic pressure fields have been measured by a needle hydrophone at several positions in water. The simulation and experimental pressure field are compared in Figure 5.6. The presence of several small lobes in the central part of the experimental pressure field is probably due to a small misalignment of the hydrophone and the echographic probe.

The experimental and CREANUIS simulated results are similar and they exhibit lobes in the edges of the fundamental and second-harmonic pressure field. It demonstrates the importance to have a large aperture in order to avoid artefacts during plane wave transmission for *B/A* imaging. Moreover, if the steering angles used during plane wave compounding are important, the two large lobes of the second-harmonic field can interfere with the central part of the image. Thus only small angle and small angular range are used for *B/A* estimation.

#### 5.1.3.2. Plane-wave compounding B/A imaging

Two different transmission strategies are used in coherent plane wave compounding (CPWC): either a single plane wave transmission or compounding with seven illuminations from -1.5° to 1.5° with 0.5° angle step. The first method is proposed in order to evaluate the limitation of only one plane wave. The second is based on the S.K. Jespersen method where a small angular range and low contrast detection are emphasized. Moreover, with the 1.5°

angle, there is no interaction between the second-harmonic lobes and the area of the nonlinear media investigated.

For plane wave transmission, the 256 probe elements are simultaneously fired to explore the entire nonlinear medium. The second-harmonic pressure field image is directly obtained from this single transmission. With seven transmissions, the second-harmonic pressure field image is the average of second-harmonic pressure field obtained for each angle. For comparison, a SF focused at 60 mm was also simulated.

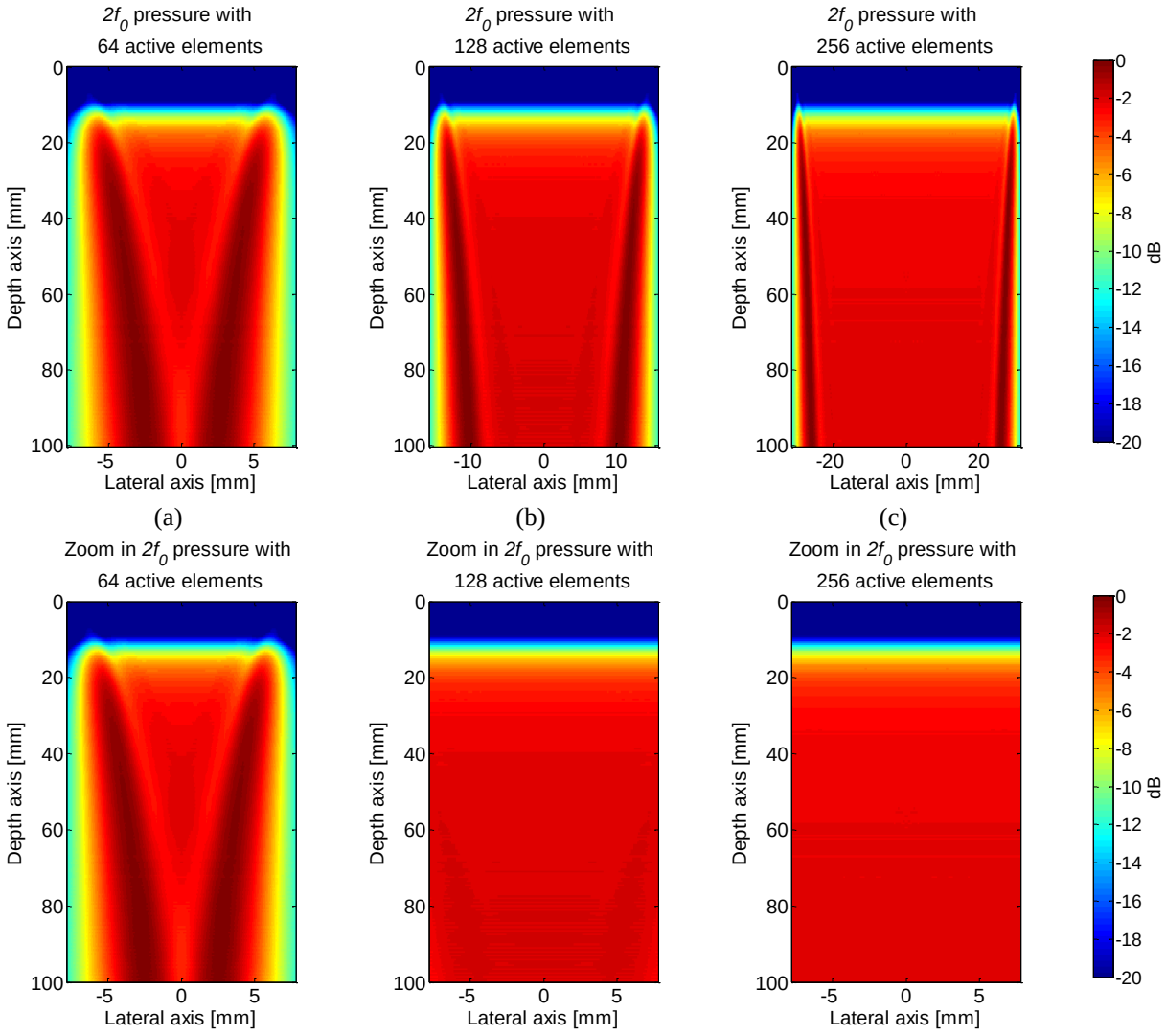


**Figure 5.5: Plane wave second-harmonic pressure field simulated with CREANUIS for different number of active elements. (a-c) Pressure field with 64, 128 and 256 actives elements and (e-g) zoom in the pressure field of 64, 128 and 256 active elements.**

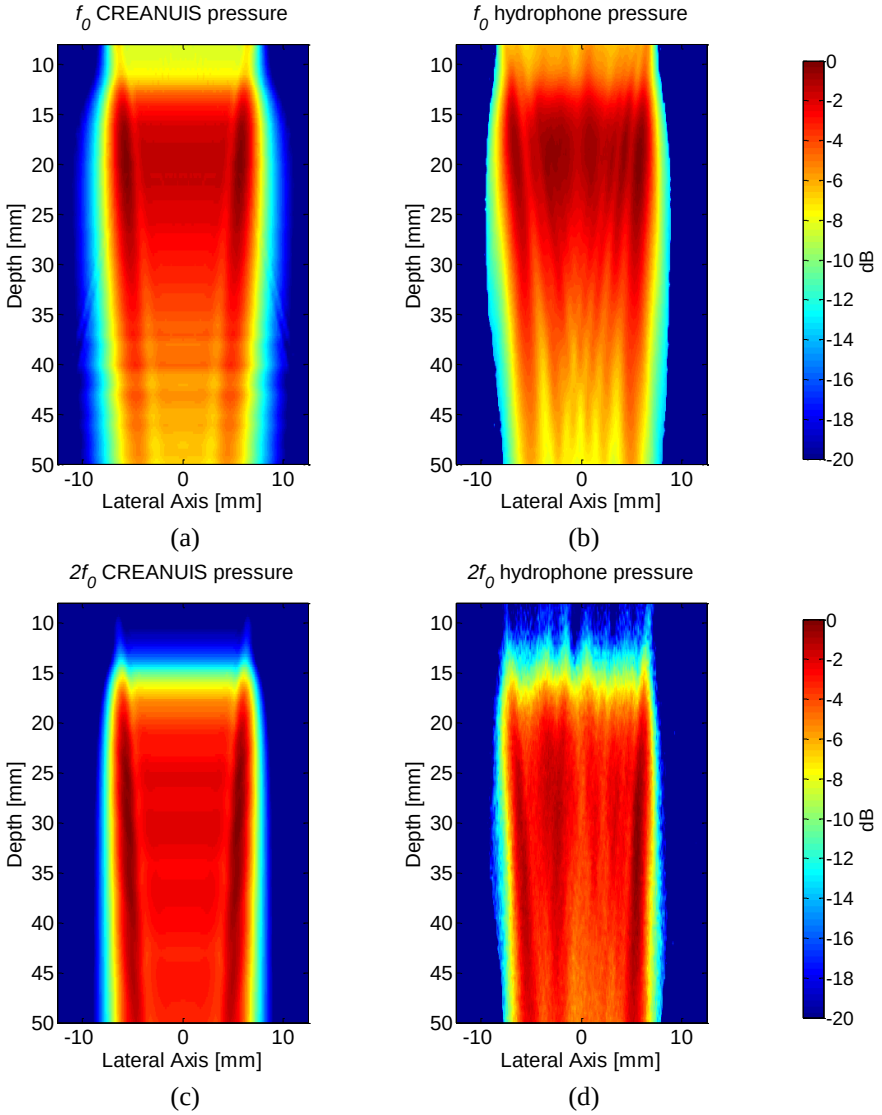


**Figure 5.6: (a, c) Simulated and (b, d) experimental fundamental and second harmonic pressure field in water.**

The Figure 5.7 shows the *B/A* estimated images of the two *B/A* media (Figure 5.1). The *B/A* estimated in each area of the two *B/A* media are given in Table 5.5 and Table 5.6.

The two CPWC methods show an important improvement in terms of *B/A* delimitation for simple and complex medium. In the complex medium, the low *B/A* area (3) is well delimited and the second *B/A* ellipse (7) starts to be visible in the CPWC 7. The second-harmonic plane wave lobes are also visible (Figure 5.7), limiting the ROI for nonlinearity estimation. F. Varray reports that the ECM approach has difficulties to estimate variations in the nonlinearity parameter (Varray, 2011). The CPWC approach is less sensitive to the variations in the nonlinearity parameter than the SF method because the CPWC approach uses different views of the same linear media. The *B/A* estimated with CPWC 7 is better than using CPWC 1. The *B/A* the estimation of SF 60 mm and CPWC 7 are closed.

Even if the plane wave transmission is limited by lobes, the CPWC transmission combined with the ECM method show a real improvement for *B/A* estimation from the pressure field. However, in clinical acquisition, the pressure field is not accessible. The proposed method is thus evaluated on simulated RF images.

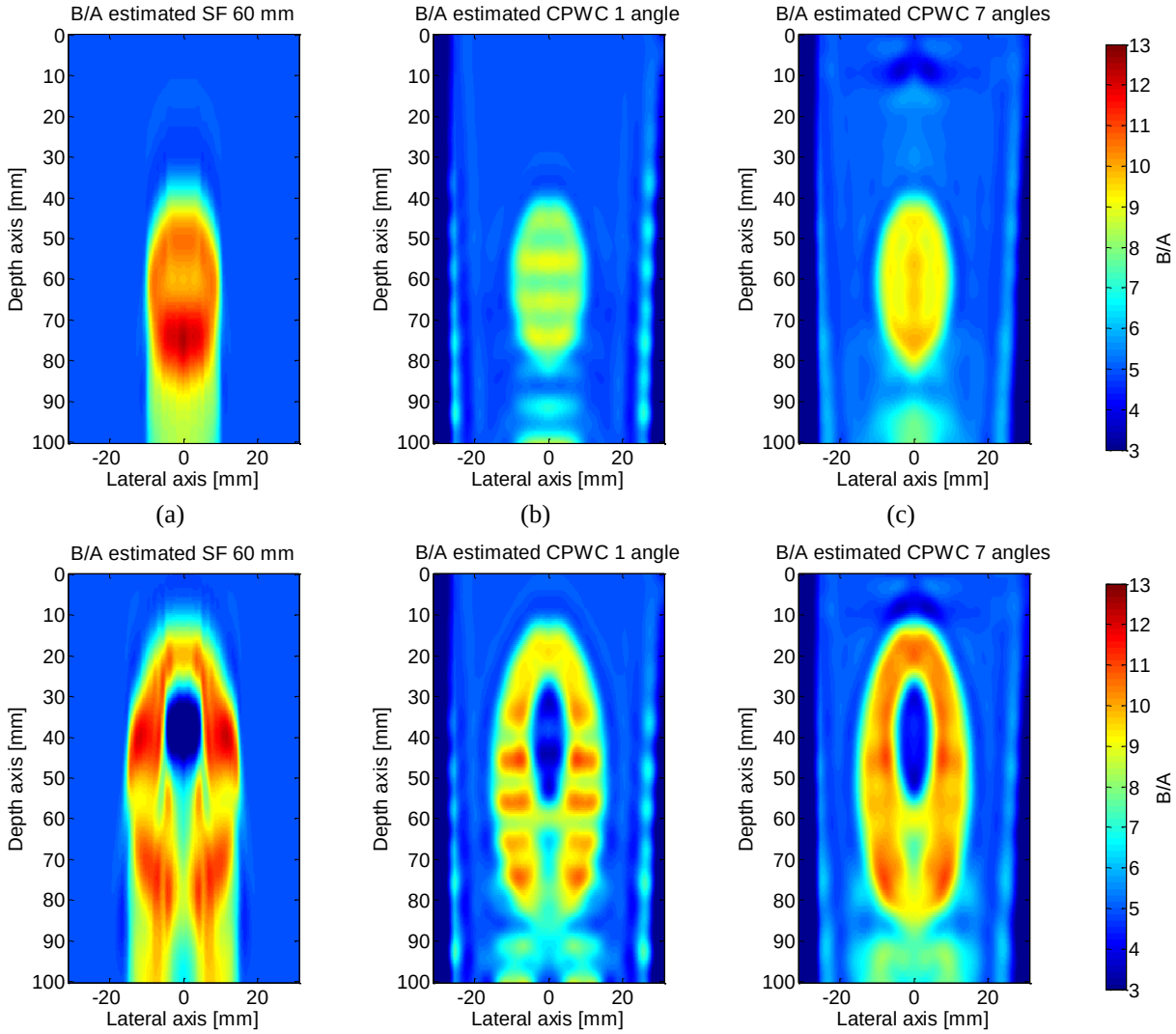


**Figure 5.7: CREANUIS *B/A* estimation with second-harmonic pressure field for SF approaches for simple (a-c) and complex (d-f) *B/A* media and two coherent plane wave compounding approaches: (a, d) SF 60 mm, (b, e) CPWC 1 and (c, f) CPWC 7.**

| *B/A* | SF 60 mm | | CPWC 1 | | CPWC 7 | |
|---|---|---|---|---|---|---|
| | Mean | STD | Mean | STD | Mean | STD |
| 5 | **5.4** | 1.1 | **4.2** | 1.5 | **4.7** | 1.6 |
| 10 | **10.3** | 1.0 | **8.0** | 0.6 | **8.9** | 0.7 |

**Table 5.5: Nonlinearity *B/A* parameter estimated with pressure field for one single focalization (60 mm) and two coherent plane wave compounding approaches CPWC 1 and CPWC 7 for the simple *B/A* medium.**

| *B/A* | SF 60 mm | | CPWC 1 | | CPWC 7 | |
|---|---|---|---|---|---|---|
| | Mean | STD | Mean | STD | Mean | STD |
| 3 | **4.1** | 2.1 | **5.0** | 1.1 | **5.1** | 1.1 |
| 5 | **5.5** | 1.3 | **4.7** | 1.8 | **4.7** | 1.9 |
| 7 | **8.6** | 0.5 | **7.1** | 0.4 | **8.2** | 0.5 |
| 10 | **9.8** | 1.1 | **8.8** | 1.0 | **9.4** | 0.9 |

**Table 5.6: Nonlinearity *B/A* parameter estimated with pressure field for one single focalization (60 mm) and two coherent plane wave compounding approaches CPWC 1 and CPWC 7 for the complex *B/A* medium.**

## 5.2. *B/A* estimation on radio frequency images

In echo-mode, the pressure field of the medium is unknown, since RF images or B-mode images are acquired. B-mode images exhibit a speckle texture created by the scatterers in the medium. However, ECM cannot be directly applied on B-mode images because the speckle has a deleterious effect on the derivative term in the equation (4.51). F. Varray proposed that the local pressure can be derived from B-mode images local amplitude. The hypothesis is that with a fully developed speckle, the B-mode image is related to its pressure field if the effects of the scatterers are successfully suppressed (Varray, 2011). The objective is thus to obtain an estimation of the second-harmonic pressure field from B-mode images.

To reduce the speckle noise, the alternative sequential filter (ASF) has been proposed by F. Varray. The ASF is based on mathematical morphology operations (Sternberg, 1986). It consists in the composition of several opening $\gamma_i$ and closing $\varphi_i$ operations on fundamental and second-harmonic B-mode images with masks of increasing sizes *i*. The resulting filtered fundamental $I_{f_0}^n$ and second-harmonic $I_{2f_0}^n$ filter images after an ASF of *n* successive iteration are expressed as:

$$I_{f_0/2f_0}^n = \gamma_n \circ \varphi_n \circ ... \gamma_1 \circ \varphi_1 (I_{f_0/2f_0}) \quad \textbf{(5.1)}$$

where $I_{f_0}$ and $I_{2f_0}$ are the fundamental and second-harmonic envelope images.

It is also supposed that the intensity variation of fundamental images is only related to the scatterers' distribution. It is assumed that the fundamental image did not depend on the nonlinearity parameter map. In second-harmonic images, the intensity variation depends on scatterers' distribution and also on the nonlinearity parameter. So the normalization, pixel by pixel, of the second-harmonic by the fundamental image may suppress the intensity variation coming from the scatterer's distribution. Moreover, a low pass filtering (*lpf*) is applied on the normalized image to ensure the reduction of high frequency information. The final second-harmonic image $I_{2f_0}^f$ is computed and only the nonlinearity parameter intensity variation remains.

$$I_{2f_0}^f = lpf\left(\frac{I_{2f_0}^n}{I_{f_0}^n}\right) \quad \textbf{(5.2)}$$

In summary, the first step to estimate *B/A* consists in applying a low or high pass 5$^{th}$ order Butterworth filter on the RF simulated data to separate the fundamental and second harmonic RF images, followed by an envelope detection to obtain B-mode images. Then, the ASF technique is applied on both B-mode images. Next, the second-harmonic image is normalized by the fundamental image. The resulting image is the input of the ECM method.

In order to improve speckle noise reduction and nonlinearity parameter delimitation, the MCPWC approaches is proposed. The method is evaluated in two media with different scatterer's density: a homogeneous and inhomogeneous scattering medium. Moreover, the two nonlinearity media (Figure 5.1) have been utilized for both scattering medium. The same nonlinearity reference for ECM is used. The homogeneous medium includes 700 000 scatters (11.16 scatters / mm$^3$) randomly distributed in space and amplitude. The inhomogeneous medium includes 525 000 scatterers. From the homogeneous medium, 175 000 scatterers have been removed half of the simulated medium (in the positive *x*-axis region) to decrease the

backscattered signal in this part of the tissue. The amplitude of each scatterer is still random. The negative *x*-axis still has a 11.16 scatterers / $mm^3$ density while the positive *x*-axis has a 5.58 scatterers / $mm^3$ density.

A 5-cycle sinusoidal burst at 3 MHz weighted by a Gaussian window was transmitted from each element. A rectangular apodization is used as reference while a DPSS 7 apodization is used so smooth the speckle noise. Three approaches are compared, the SF at 60 mm and the MCPWC technique with one (MCPWC 1) and seven (MCPWC 7) transmitted angles. The two same strategy angles as in the pressure field approach are used for the transmission: 0° and -1.5° to 1.5° each 0.5°. The probe parameters are given in the Table 3.1. The acoustic characteristics of the medium are given in Table 3.2.

#### 5.2.1.1. Homogeneous scattering medium

In this section, the media with the homogeneous scatterer's density is used. The resulting fundamental and second-harmonic B-mode images of the simple nonlinearity media for the three approaches are displayed in Figure 5.8, Figure 5.9 and Figure 5.10. Moreover, the filtered fundamental and second-harmonic are given in (c, d) of each Figure. Figure 5.11 shows the *B/A* images for the two nonlinearity medium and *B/A* parameters estimated are given in Table 5.7 and Table 5.8.

The final second-harmonic SF image given in Figure 5.8.e is close to the second-harmonic pressure field (Figure 5.2.a). This similarity allows to have a correct *B/A* estimate but with the same spread artifact beyond the nonlinearity area (Figure 5.11.a). Moreover, some false nonlinearity areas appear due to the not perfect suppression of the speckle noise.

In the fundamental MCPWC 1 B-mode image (Figure 5.9.a), the top of the image is degraded by intense lines. This artefact comes from the delay and sum and DPSS combination. Because of the use of a large probe (256 active elements) and a short distance, the backscattered echoes are not correctly received. Thus during the beamforming, the DPSS apodization emphasizes this artefact. In plane wave pressure field analysis section, the presence of lobes in the second-harmonic pressure field is shown. In Figure 5.9.b, the lobes are visible. Furthermore, the nonlinearity area is also visible and the lobes do not interfere with the nonlinearity area. In Figure 5.10.b, the lobes are smoothed as well as the nonlinearity area. As with pressure field *B/A* estimation, the *B/A* area is better delimited with plane wave transmission than with SF (Figure 5.11.b-c).

With the complex nonlinearity medium, the SF and the MCPWC 7 methods are close for the *B/A* value (Table 5.8). However the MCPWC 7 approach improves the *B/A* delimitation in the top of the nonlinearity area. Furthermore, the MCPWC 7 does not concentrate the energy at 60 mm as well as the SF approach.

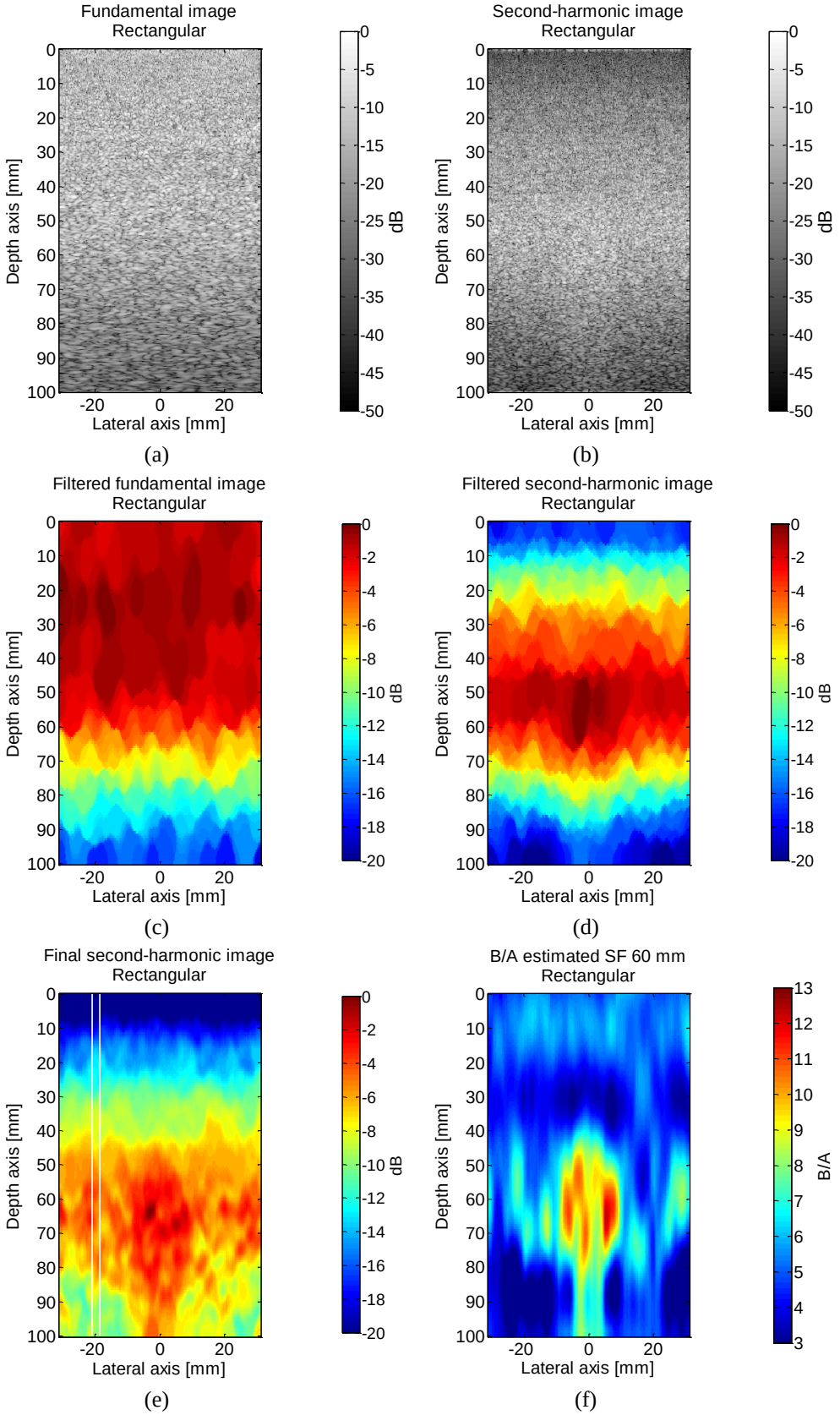


**Figure 5.8: CREANUIS single focalization B-mode log compressed (a) fundamental and (b) second-harmonic images obtained with the rectangular apodization, the simple nonlinearity medium and a homogeneous scatterer's distribution. (c,d) are the ASF filtered fundamental and second-harmonic images and (e) is the final second-harmonic image. (f) is the resulting *B/A* image.**

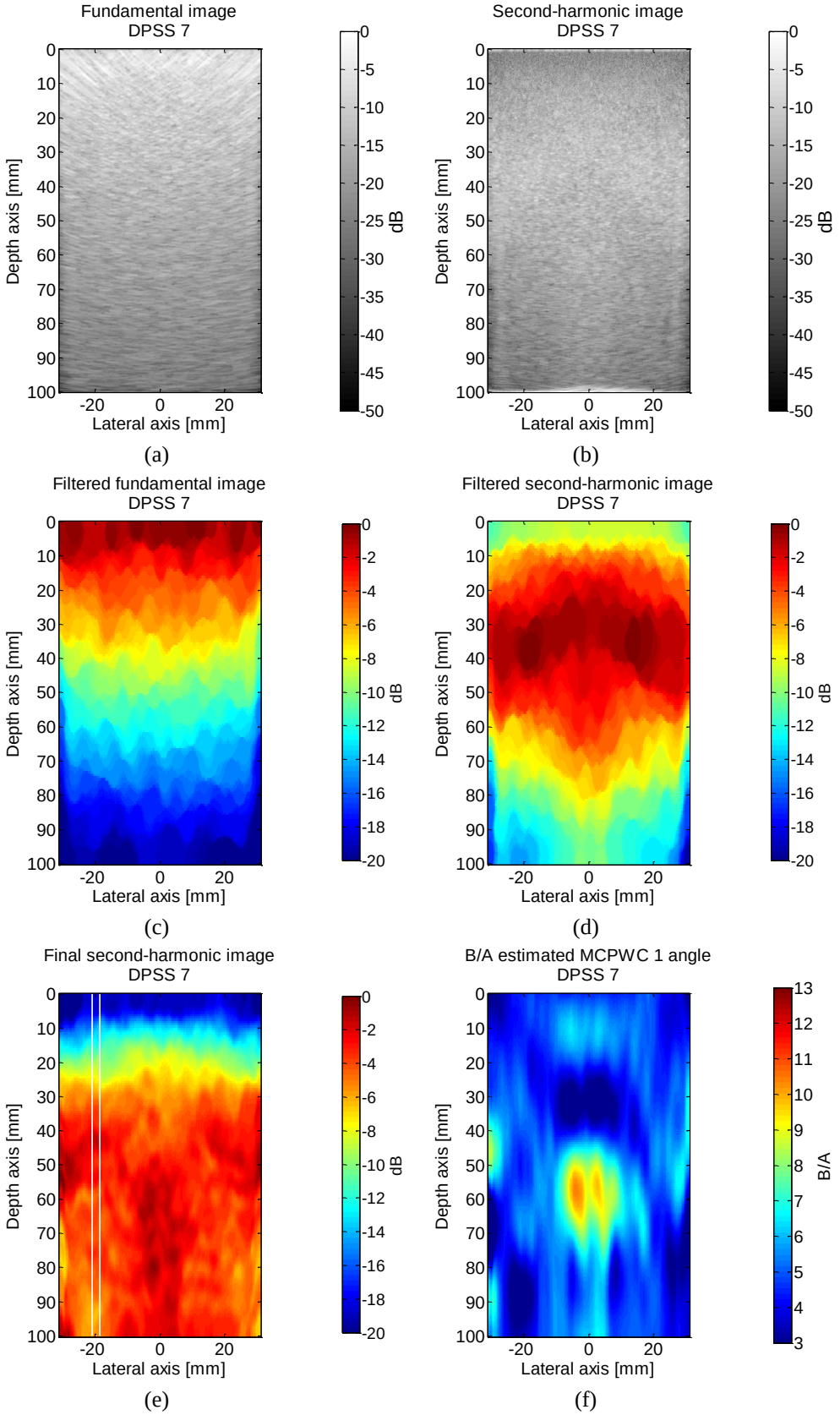


**Figure 5.9: CREANUIS MCPWC 1 B-mode log compressed (a) fundamental and (b) second-harmonic images obtained with the DPSS 7 apodization, the simple nonlinearity medium and a homogeneous scatterer's distribution. (c,d) are the ASF filtered fundamental and second-harmonic images and (e) is the final second-harmonic image. (f) is the resulting *B/A* image.**

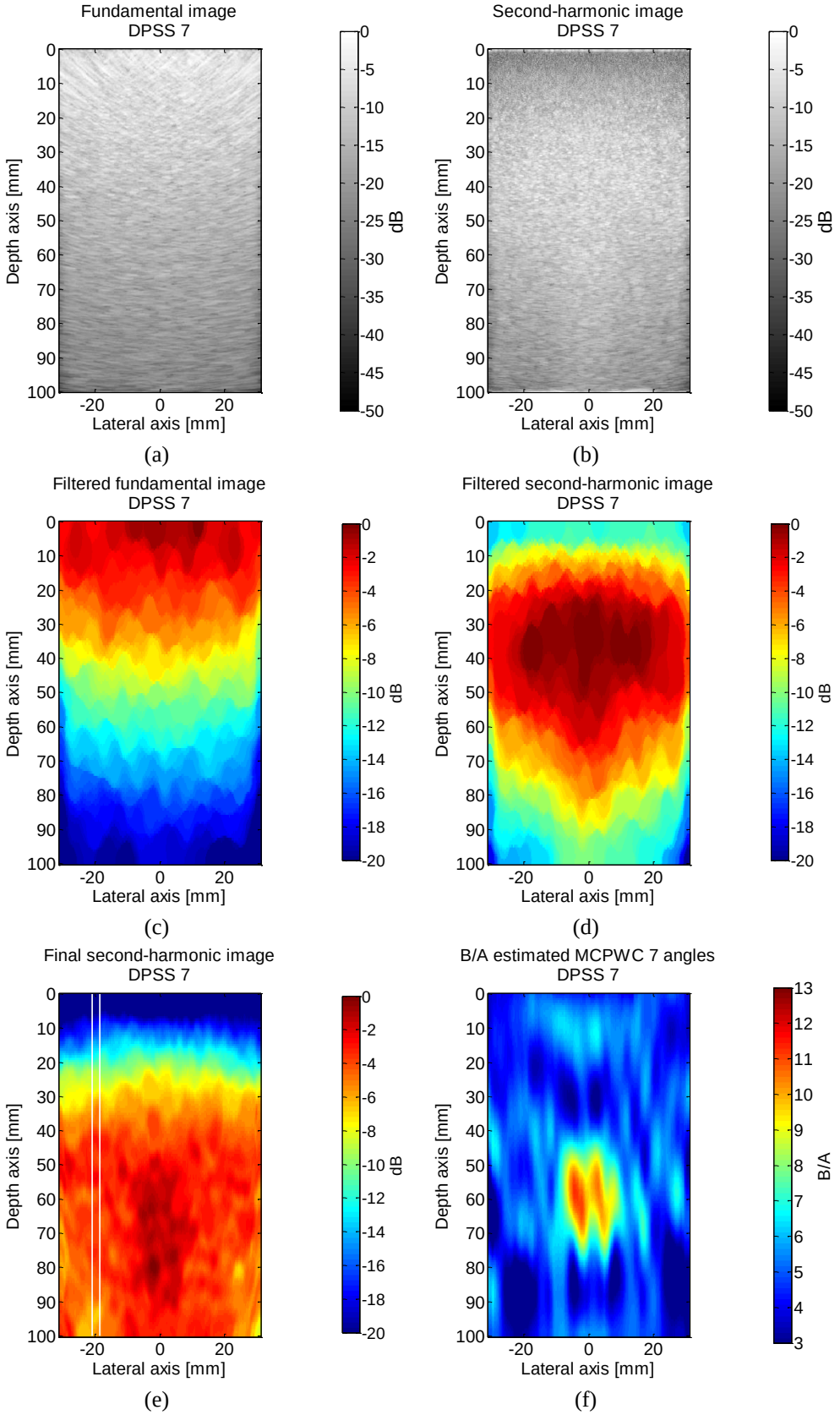


**Figure 5.10: CREANUIS MCPWC 7 B-mode log compressed (a) fundamental and (b) second-harmonic images obtained with the DPSS 7 apodization, the simple nonlinearity medium and a homogeneous scatterer's distribution. (c,d) are the ASF filtered fundamental and second-harmonic images and (e) is the final second-harmonic image. (f) is the resulting *B/A* image.**

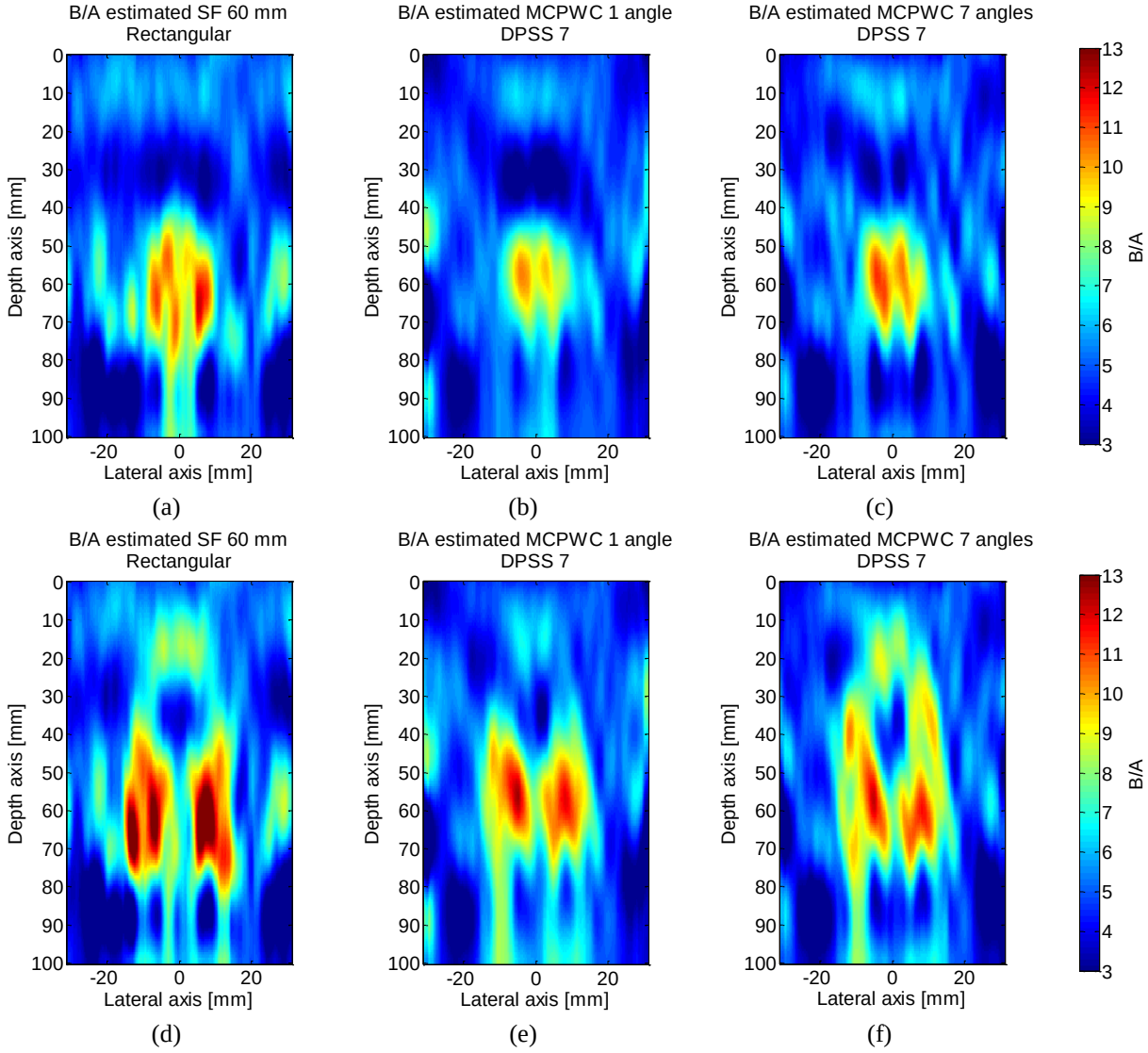


**Figure 5.11: CREANUIS *B/A* estimation with final B-mode second-harmonic image for SF approaches for simple (a-c) and complex (d-f) *B/A* media and two coherent plane wave compounding approaches: (a, d) SF 60 mm, (b, e) CPWC 1 and (c, f) CPWC 7.**

| *B/A* | Foc 60 mm | | MCPWC 1 | | MCPWC 7 | |
|---|---|---|---|---|---|---|
| | Mean | STD | Mean | STD | Mean | STD |
| 5 | **4.9** | 1.3 | **4.7** | 1.0 | **4.7** | 1.0 |
| 10 | **9.0** | 1.3 | **7.6** | 1.4 | **8.1** | 1.6 |

**Table 5.7: Nonlinearity *B/A* estimated with B-mode image for one single focalization with rectangular apodization and two coherent plane wave compounding approaches MCPWC 1 and MCPWC 7 with DPSS 7 apodization for the simple *B/A* and homogeneous scatterer's distribution medium.**

| *B/A* | Foc 60 mm | | MCPWC 1 | | MCPWC 7 | |
|---|---|---|---|---|---|---|
| | Mean | STD | Mean | STD | Mean | STD |
| 3 | **5.6** | 1.4 | **5.6** | 1.7 | **5.9** | 1.2 |
| 5 | **5.1** | 1.6 | **5.0** | 1.3 | **4.8** | 1.2 |
| 7 | **7.5** | 0.9 | **7.0** | 0.8 | **7.6** | 1.1 |
| 10 | **8.7** | 2.3 | **7.7** | 2 | **8.2** | 1.7 |

**Table 5.8: Nonlinearity *B/A* estimated with B-mode image for one single focalization (with rectangular apodization and two coherent plane wave compounding approaches MCPWC 1 and MCPWC 7 with DPSS 7 apodization f for the complex *B/A* and homogeneous scatterer's distribution medium.**

#### 5.2.1.2. Inhomogeneous scattering medium

In this section, the media with the inhomogeneous scatterer's density is used. The resulting fundamental and second-harmonic B-mode images of the simple nonlinearity media for the three approaches are displayed in Figure 5.12, Figure 5.13 and Figure 5.14. Moreover, the filtered fundamental and second-harmonic are given in (c, d) of each Figures presented above. Figure 5.15 shows the *B/A* images for the two nonlinearity medium and *B/A* parameters estimated are given in Table 5.9 and Table 5.10.

For all approaches, when the filtered fundamental and second-harmonic images are analyzed, the negative *x*-axis is more intense than the positive x-axis. This is due to the higher scatterer's density in the negative *x*-axis. Thanks to the ratio of the second-harmonic by the fundamental image (5.2), the final second-harmonic image is homogeneous. The scatterer's effect is suppressed and the ECM method is applied.

The SF approach is less accurate to delimit the *B/A* area in the inhomogeneous case (Figure 5.15**.**(a, d)) than in the homogeneous case. The MCPWC 1 also has difficulties while the MCPWC 7 is less impacted by the inhomogeneous scatterer's distribution. Table 5.9 shows that the SF and MCPWC 7 produce similar results for the simple nonlinear medium. The complex nonlinear medium is quite well delimited by the MCPWC 7 approach but the *B/A* values estimated for the 3 and 7 areas are more overvalued than in homogenous medium.

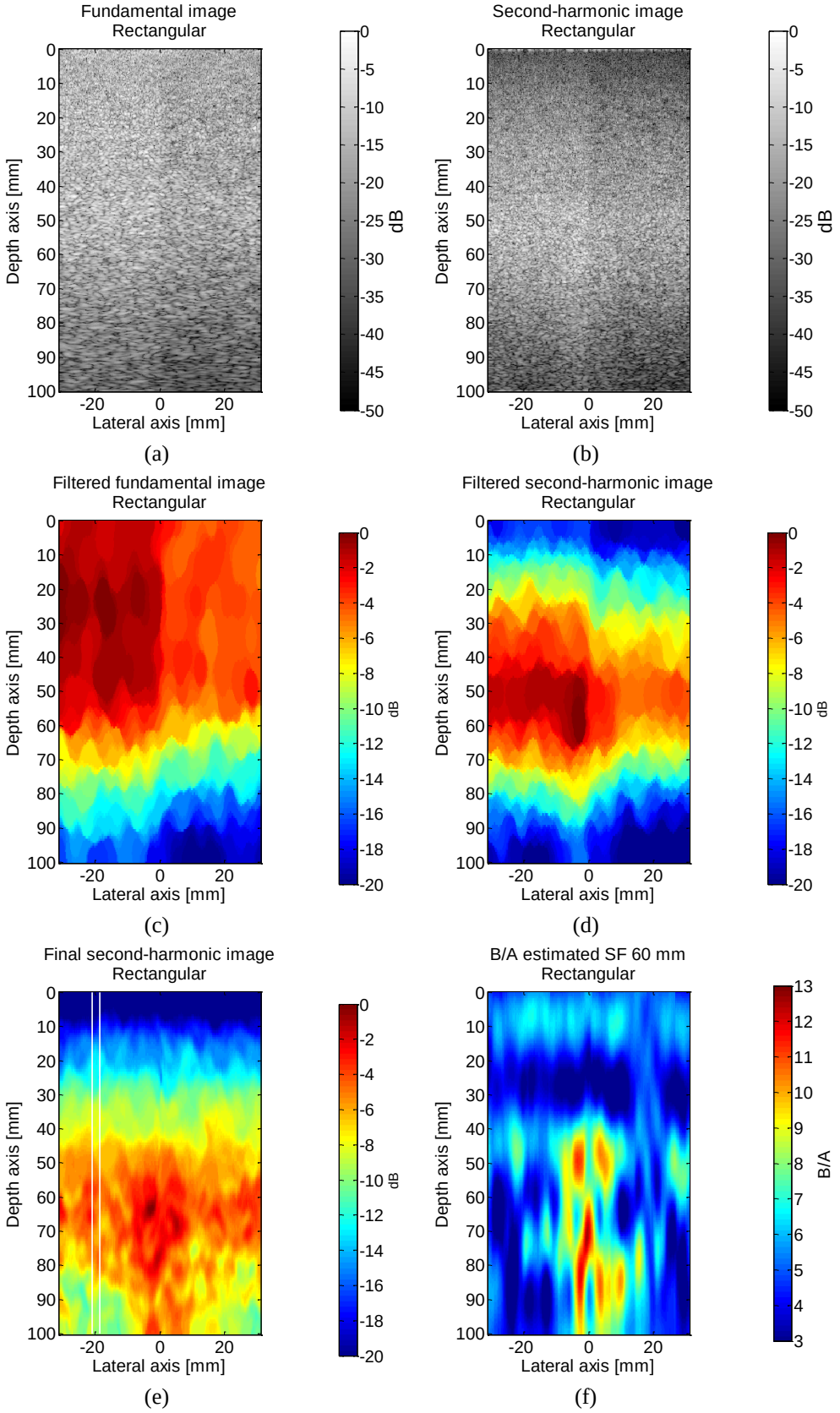


**Figure 5.12: CREANUIS single focalization B-mode log compressed (a) fundamental and (b) second-harmonic images obtained with the rectangular apodization, the simple nonlinearity medium and an inhomogeneous scatterer's distribution. (c,d) are the ASF filtered fundamental and second-harmonic images and (e) is the final second-harmonic image. (f) is the resulting *B/A* image.**

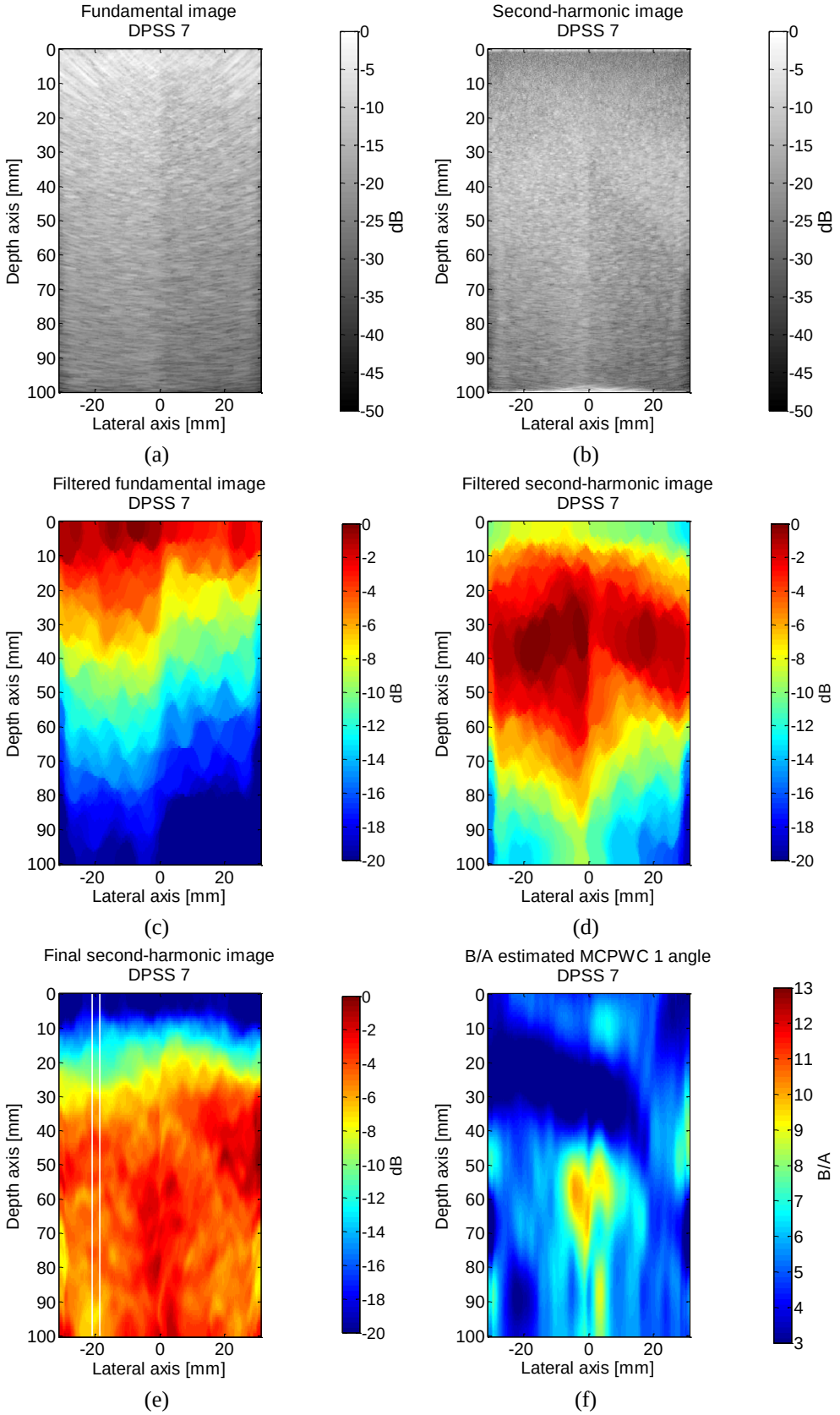


**Figure 5.13: CREANUIS MCPWC 1 B-mode log compressed (a) fundamental and (b) second-harmonic images obtained with the DPSS 7 apodization, the simple nonlinearity medium and an inhomogeneous scatterer's distribution. (c,d) are the ASF filtered fundamental and second-harmonic images and (e) is the final second-harmonic image. (f) is the resulting *B/A* image.**

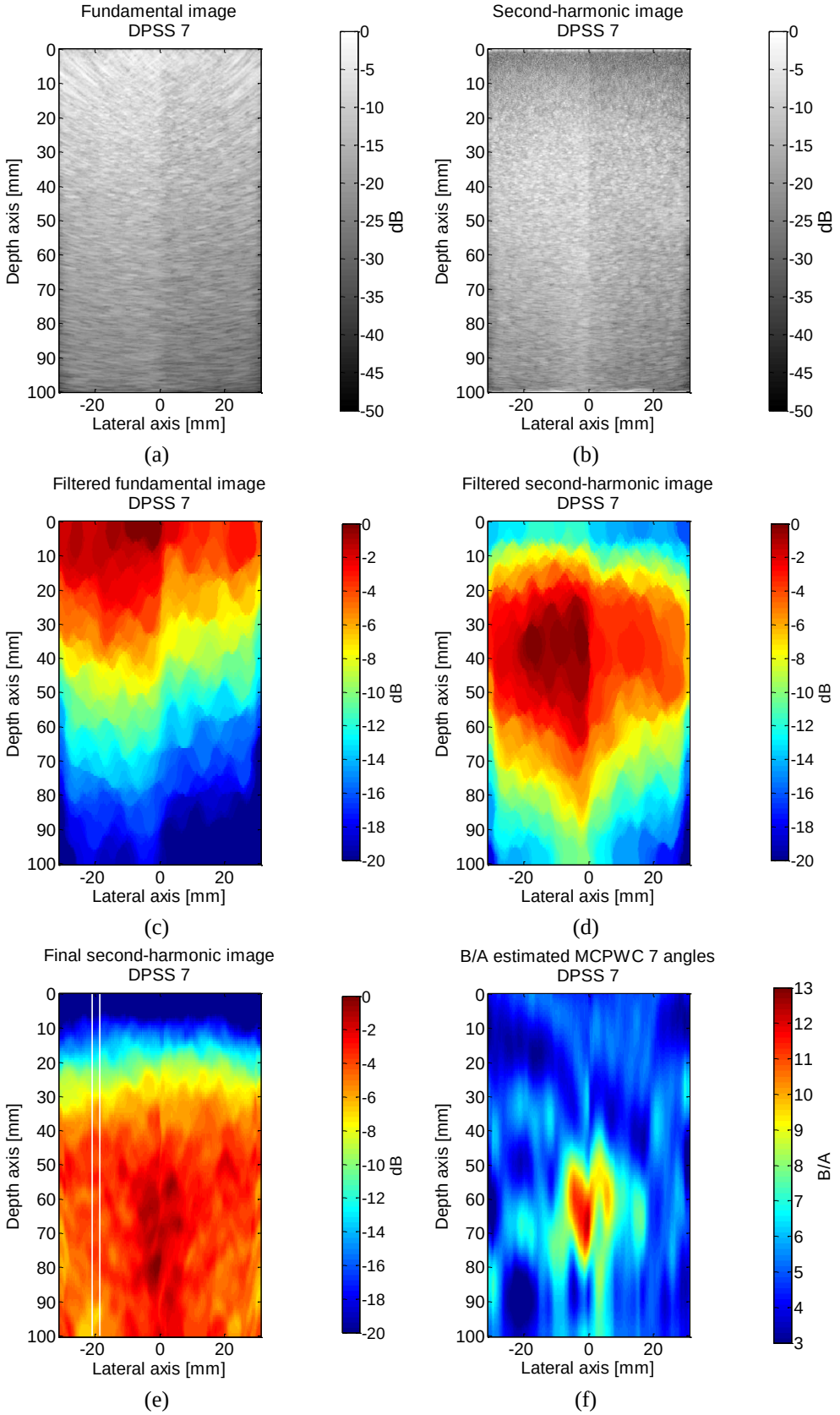


**Figure 5.14: CREANUIS MCPWC 7 B-mode log compressed (a) fundamental and (b) second-harmonic images obtained with the DPSS 7 apodization, the simple nonlinearity medium and an inhomogeneous scatterer's distribution. (c,d) are the ASF filtered fundamental and second-harmonic images and (e) is the final second-harmonic image. (f) is the resulting *B/A* image.**

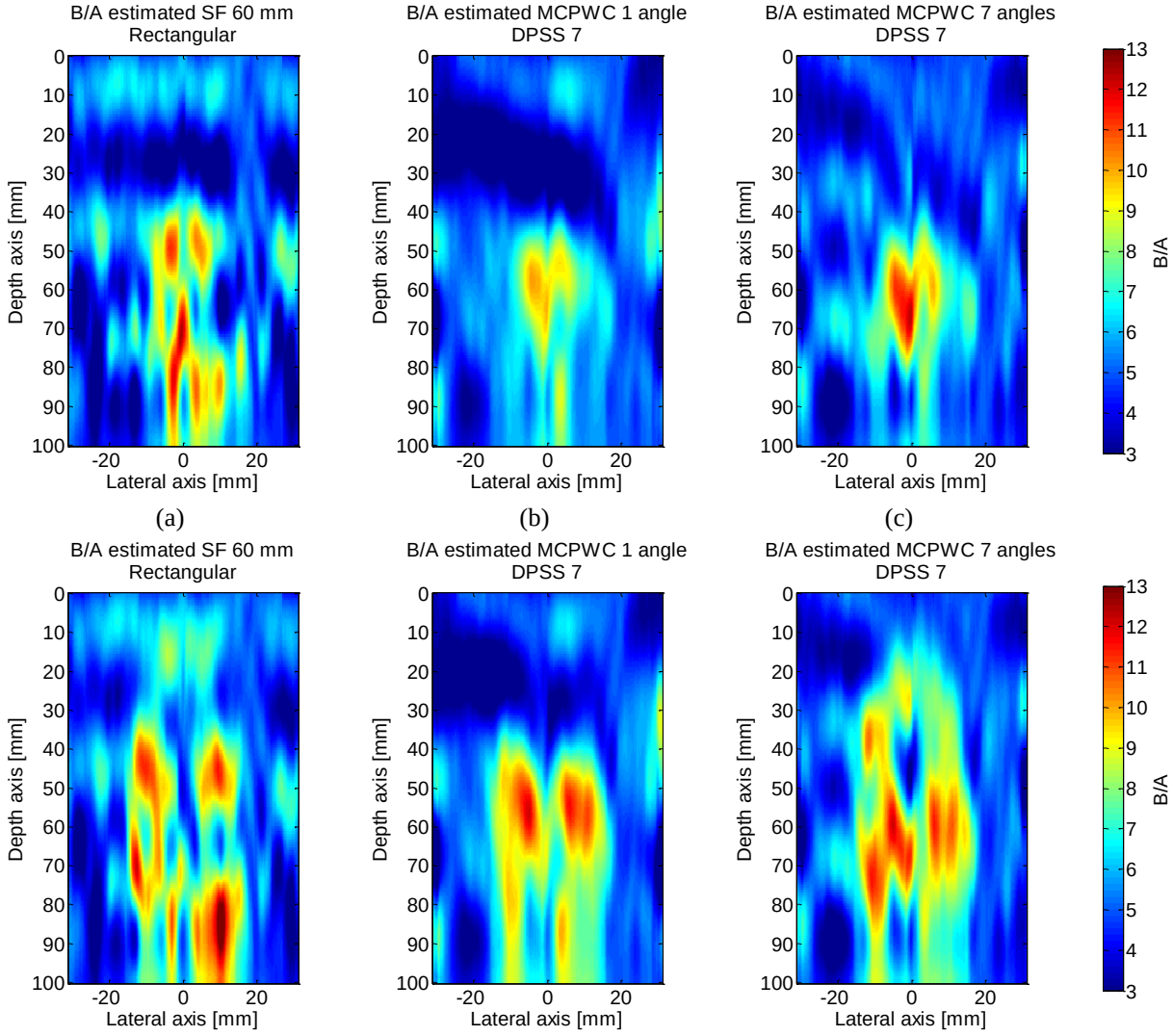


**Figure 5.15: CREANUIS *B/A* estimation with final B-mode second-harmonic images for SF approaches for simple (a-c) and complex (d-f) *B/A* media and two coherent plane wave compounding approaches: (a, d) SF 60 mm, (b, e) CPWC 1 and (c, f) CPWC 7.**

| *B/A* | Foc 60 mm | | MCPWC 1 | | MCPWC 7 | |
|---|---|---|---|---|---|---|
| | Mean | STD | Mean | STD | Mean | STD |
| 5 | **5,1** | 1,6 | **4,8** | 1,4 | **5.0** | 1.0 |
| 10 | **8,3** | 1,7 | **7.8** | 1.2 | **8.4** | 1.6 |

**Table 5.9: Nonlinearity *B/A* estimated with B-mode image for one single focalization with rectangular apodization and two coherent plane wave compounding approaches MCPWC 1 and MCPWC 7 with DPSS 7 apodization for the simple *B/A* and inhomogeneous scatterer's distribution medium.**

| *B/A* | Foc 60 mm | | MCPWC 1 | | MCPWC 7 | |
|---|---|---|---|---|---|---|
| | Mean | STD | Mean | STD | Mean | STD |
| 3 | **5,9** | 1.3 | **5.6** | 1.8 | **6.2** | 1.5 |
| 5 | **5,5** | 1.8 | **5.1** | 1.6 | **4.1** | 1.4 |
| 7 | **7,9** | 1.0 | **7.8** | 0.9 | **9.6** | 1.3 |
| 10 | **7,9** | 1.7 | **7.5** | 2.4 | **8.5** | 1.5 |

**Table 5.10: Nonlinearity *B/A* estimated with B-mode image for one single focalization with rectangular apodization and two coherent plane wave compounding approaches MCPWC 1 and MCPWC 7 with DPSS 7 apodization for the complex *B/A* and inhomogeneous scatterer's distribution medium.**

## 5.3. Discussion and conclusion

The ECM is an interesting approach to detect the different nonlinear regions. However, using a single focalization transmission approach limit the *B/A* estimation and delimitation. Depending on the focal depth, the *B/A* can be over or under estimated. Moreover, the delimitation of the B/A can me more difficult if not enough energy is transmitted in the *B/A* area. A shadow cone is also present with one focal transmission, thus it was proposed to use spatial compounding. However, this approach is also limited by the use of one focal.

Presented in the Chapter 2, the coherent plane wave compounding is a solution to overcome the focalization problem and shadow cone. The pressure field study shows an important improvement for *B/A* delimitation. The estimation of *B/A* from radio-frequency images was improved using the MCPWC approach. With seven transmitted angles and using the DPSS 7 apodization, the *B/A* estimated is close to the SF focalization and the *B/A* delimitation is improved. The more important result is that no depth was privileged in terms of energy with the plane wave transmission. Moreover, the MCPWC was less sensible to the variation of speckle density. Unfortunately, the method still requires a reference area where the nonlinearity parameter has to be known.

# Conclusions and perspectives

## Conclusions

In this thesis work, a method using a plane-wave transmission and an incoherent image formation reducing the speckle noise and improving the nonlinearity parameter estimation is presented.

First, the Thomson's multitaper (TM) approach is presented and evaluated. This method finds its origin in signal processing for spectrum density estimation. In image processing, the method decreases the speckle noise using several apodization during the beamforming of echographic image without reducing the frame rate.

However, the TM approach reduces the spatial resolution, principally the lateral resolution. The possibility to combine the multitaper approach with composite transmission in order to improve spatial resolution is demonstrated. The multitaper coherent plane-wave compounding (MCPWC) method was proposed, improving the spatial resolution and the contrast while reducing the speckle noise in simulation and experiments. Moreover, using only 11 transmitted angles of plane wave, it is possible to increase by a factor of five the frame rate compared to the standard single focalization approach.

Then, the extended comparative method (ECM) for nonlinearity parameter estimation in echo-mode is presented. From pressure field simulations the impact of the focalization -- before, inside and beyond the investigated nonlinearity area-- is demonstrated for the estimation and delineation of the nonlinearity parameter with the ECM approach. The plane-wave transmission is proposed and studied for the nonlinearity estimation. Using 7 transmitted angles, the delimitation of the nonlinearity area in a simple or complex medium is improved compared to the single focalization approach. However two undesirable lobes in the fundamental and second-harmonic appear when plane wave transmission is used. These lobes disturb the plane-wave approach and they oblige to use an aperture with a large number of active elements in order to shift the lobes on the lateral parts of the field and to have a homogeneous area in the center.

Assuming that the local pressure field can be linked to the intensity of image, the ECM combined to the MCPWC approach has been evaluated with radio-frequency images. The proposed method improves the nonlinearity delimitation compared to the single focalization approach. Moreover the method is less sensible when the medium is inhomogeneous. However, the MCPWC couldn't a present be utilized in acquisition because of the lack of echographic scanner with a high number of active elements.

## Perspectives

This thesis work opens the following opportunities:

**Thomson's multitaper approach.** The method has a high capability to reduce the speckle noise. The implementation in an echographic scanner can be a novel modality to reduce the speckle noise.

**ULA-OP with 256 active elements.** The new version of the ULA-OP research scanner (not available at present) with the possibility to use 256 active elements will allow evaluating the impact of the two lobes with plane wave transmission. Moreover the *B/A* plane wave imaging will be possible.

**Chirp transmission for *B/A* imaging.** The plane-wave transmission has the drawback to reduce the transmitted energy. It is proposed to transmit plane wave combined with chirp signal and to use a nonlinear compression filter that can selectively extract and compress the second-harmonic from the received echo (Borsboom et al., 2005). The second-harmonic chirp image has more energy than using pulse transmission. The comparison between the nonlinearity reference area and the unknown nonlinearity area may be improve.

**Backscatter coefficient**. Assuming that the local pressure field can be linked to the intensity of image, the extraction of the backscatter coefficient may provide a better estimation of the local pressure field.

**CMUT array.** The capacitive micromachined ultrasonic transducer (CMUT) is new array having interesting characteristics. The CMUT pressure field is close to the pressure field of a perfect piston. The transmitted bandwidth of such array is upper than 100% and theoretically infinite in reception. The evaluation of CMUT array with the pressure field platform and the use of this array for *B/A* imaging may improve the nonlinearity parameter estimation.

# Appendix

# Appendix A

# Nonlinear filter for speckle noise reduction

The nonlinear filters used in order to reduce the speckle noise or to improve the contrast cited in the section 2.1.2.2, are presented in this appendix.

## A.1. Median filter

The median filter replaces the central pixel where the operation is done by the median of the gray values of its neighborhoods. There is no information loss because the new pixel value is one of its neighborhood. This filter is powerful for salt-and-pepper noise but can be limited for the speckle noise which is bigger.

$$\begin{bmatrix} 6 & 9 & 10 \\ 4 & 20 & 9 \\ 3 & 4 & 6 \end{bmatrix} \rightarrow 3,4,4,6,6,9,9,10,20 \xrightarrow{median} 6 \qquad \textbf{(i)}$$

## A.2. Bilateral filter

The general bilateral filter is expressed as (Balocco et al., 2010):

$$h(p) = \Gamma^{-1} \int_{\Omega(p)} f(\xi) c(\xi, p) s(f(\xi), f(p)) d\xi \qquad \textbf{(ii)}$$

with the normalization factor:

$$\Gamma(p) = \int_{\Omega(p)} c(\xi, p) s(f(\xi), f(p)) d\xi \qquad \textbf{(iii)}$$

where $f$ is the input image, $h$ is the output image, $\Omega(p)$ is the spatial neighborhood of the centered pixel $p$ where the filter is applied and $\xi$ is the integration variable representing pixels coordinates in $\Omega$. $c(\xi,p)$ and $s(f(\xi),f(p))$ are the closeness function and the similarity function defined by C. Tomasi as two Gaussian functions (Tomasi and Manduchi, 1998):

$$c(\xi, p) = \exp\left( -\frac{\|p - \xi\|}{2\sigma_c^2} \right) \qquad \textbf{(iv)}$$

$$s\left( f(\xi), f(p) \right) = \exp\left( -\frac{\left( f(p) - f(\xi) \right)^2}{2\sigma_s^2} \right) \qquad \textbf{(v)}$$

where $\sigma_c$ and $\sigma_s$ are the standard deviation of the both Gaussian functions. The closeness function measures the Euclidean distance in terms of pixel between the central pixel and its neighbors. The similarity function measures a distance between the intensity of the central pixel and its neighbors.

For example, in a homogeneous region, pixel values in a small neighborhood are similar and the normalization factor Γ is close to one. Thus the bilateral filter recognized the area as an unique region and averages the pixel neighborhood and reduces the noise. When the technique is applied in a region with two distinct areas, the normalization factor Γ is closed to one for pixel of the same area as the centered pixel and close to zero for the others (Tomasi and Manduchi, 1998).

## A.3. Wiener filter

The Wiener method is used to filter out noise and the method is also used to restore images in the presence of blur. The images are considered as a stationary process and the noise is considered as an additive noise. The method minimizes the minimum mean square error between the initial image and the restored image.

## A.4. Homomorphic filtering

For Homomorphic filtering, the speckle noise is considered as a multiplicative noise. Homomorphic filtering improves the image by calculating the FFT of the logarithmic compressed image converting the multiplicative noise to additive noise. Then a denoising homomorphic filter function is used and the final image is performed by inverse FFT. The filter may be a band-pass or a high-boost Butterworth filter (Sivakumar, Gayathri and Nedumaran, 2010).

# Appendix B

# Thomson's multitaper signal processing origins

The Thomson's multitaper signal processing origins (section 3.1) is presented in this appendix. In time series or signal analysis, the spectral analysis is an important source of information. The main problem is to choose an algorithm to estimate the spectrum which is not limited by bias. A method proposed to estimate the spectral density is the periodogram also named spectral estimator. Given a time series of $N$ elements that can be regarded as a realization of $X_1$, $X_2 \ldots X_N$, the spectral estimator $\hat{S}^{(p)}(f)$ is expressed as (Percival and Walden, 1993):

$$\hat{S}^{(p)}(f) = \frac{\Delta t}{N}\left|\sum_{t=1}^{N} X_t e^{-i2\pi ft\Delta t}\right|^2 \quad \textbf{(i)}$$

where $\Delta t$ is the sampling interval and $f$ the frequency. During all this part, the circumflex means that the value is an estimator or an estimate of the value. This spectral estimator is described as a simple method due to its important variance and bias (Percival and Walden, 1993). A method proposed to reduce the spectral bias is to use a taper (or apodization) on the time series in order to truncate the sequence gradually rather than abruptly. Another method proposed to reduce the variance is to average several spectral estimator as Bartlett's method but with a loss of resolution in frequency domain. The Bartlett's method consists to split the time series of $N$ elements in $N_B$ blocks of data segments of length $Ns$. For each segment, a periodogram is computed and the final periodogram is the average of the $N_B$ data segments periodograms:

$$\hat{S}_l(f) = \frac{\Delta t}{N_S}\left|\sum_{t=1}^{N_S} X_{t+(l-1)N_S} e^{-i2\pi ft\Delta t}\right|^2, 1 \le l \le N_B$$
$$\hat{S}_l^{(Bartlett)}(f) = \frac{1}{N_B}\sum_{l=1}^{N_B} \hat{S}_l(f) \quad \textbf{(ii)}$$

where $\hat{S}_l(f)$ is the spectral estimator for the block data $l$ and $\hat{S}_l^{(Bartlett)}(f)$ the final spectral estimator averaged. The averaging reduces the variance, compared to the origin estimator but with a loss of resolution in the frequency domain. Welch proposed to improve the Bartlett's method by using a taper on the different blocks and by overlapping the blocks of data segments (Welch, 1967). First, the use of data taper on each block reduces potential bias due to leakage in the spectral estimator. Second, the overlap of the blocks can produce a spectral estimator with better variance properties than when contiguous non overlapping blocks are used. The Welch method is also named WOSA for 'weighted or Welch overlapped segment averaging' (Welch, 1967) (Percival and Walden, 1993). As with Bartlett's method, the time series of $N$ elements is split in blocks of length $N_S$ but now there are $N_{BW}$ blocks defined by $D$, the starting points of overlapped segments:

$$0 < D \leq N_S \text{ and } N_{BW} = \frac{N - N_S}{D} + 1 \quad \textbf{(iii)}$$

The Figure B. 1 illustrates the equation (iii). If the starting point $D$ is equal to $N_S$, the method is the same as Bartlett's method and $N_{BW}$ is equal to $N_B$.

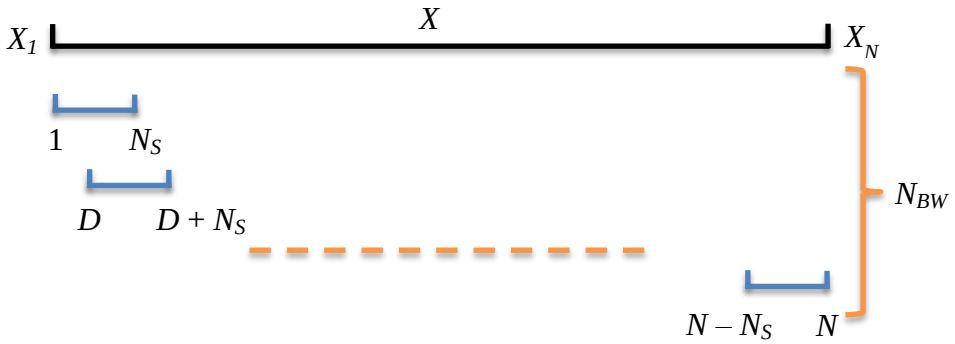


**Figure B. 1: Illustration of the segmentation for a time series X with the Welch periodogram method. The times series has *N* points and the Welch method has $N_{BW}$ segments with a size $N_S$ and the overlapped segments start at the position *D* of the time series.**

The Welch spectral estimator is:

$$\hat{S}_l(f) = \frac{\Delta t}{N_S}\left|\sum_{t=1}^{N_S} h_t X_{t+(l-1)N_S} e^{-i2\pi ft\Delta t}\right|^2, 1 \leq l \leq N_{BW}$$
$$\hat{S}_l^{(WOSA)}(f) = \frac{1}{N_{BW}}\sum_{l=1}^{N_{BW}} \hat{S}_l(f) \quad \textbf{(iv)}$$

where $\hat{S}_l(f)$is the estimator for the block data $l$, $\hat{S}_l^{(WOSA)}(f)$ the final spectral estimator averaged and $h$ is the taper, with a size $N_S$, used on each blocks of the time series.

The importance of tapering time series and averaging several spectral density were introduced in order to reduce variance and bias leakage but with a reduction of the sample size and so a reduction of the frequency resolution. To avoid the information loss, Thomson proposed to apply multiple orthogonal tapers on the same time series (Thomson, 1982). D.B. Percival and A.T. Walden explain the Thomson multitaper approach in (Percival and Walden, 1993). Based on the same time series, the Thomson multitaper spectral estimator using $K$ tapers is expressed as:

$$\hat{S}_k^{(mt)}(f) = \frac{\Delta t}{N}\left|\sum_{t=1}^{N} h_{t,k} X_t e^{-i2\pi ft\Delta t}\right|^2$$
$$\hat{S}^{(mt)}(f) = \frac{1}{K}\sum_{k=1}^{K} \hat{S}_k^{(mt)}(f) \quad \textbf{(v)}$$

where $\hat{S}_k^{(mt)}(f)$ is the estimator using the data taper $h_{t,k}$ and $\hat{S}^{(mt)}(f)$ is the multitaper spectral estimator composed with $K$ spectral estimator. It can be noticed that $\hat{S}_k^{(mt)}(f)$ is the same spectral estimator as $\hat{S}^{(p)}(f)$ in (i), if the taper used on the time series is equal to one.

For each data taper $h_k$, it can be define an associated spectral window $H_k$:

$$H_k(f) = \Delta t \left| \sum_{t=1}^{N} h_{t,k} e^{-i2\pi ft\Delta t} \right|^2 \quad \textbf{(vi)}$$

The first moment properties of $\hat{S}_k^{(mt)}(f)$ are given by:

$$E\left\{\hat{S}_k^{(mt)}(f)\right\} = \int_{-f(N)}^{f(N)} H_k(f - f')S^{(p)}(f')df' \quad \textbf{(vii)}$$

It follows that:

$$E\left\{\hat{S}^{(mt)}(f)\right\} = \int_{-f(N)}^{f(N)} \bar{H}(f - f')S^{(p)}(f')df' \quad \textbf{(viii)}$$

with

$$\bar{H}(f) = \frac{1}{K}\sum_{k=1}^{K} H_k(f) \quad \textbf{(ix)}$$

The function $\bar{H}(f)$ is the average of the *K* spectral windows of the different tapers and $\bar{H}(f)$ corresponds to the spectral window for the estimator $\hat{S}^{(mt)}(f)$. If the function $\bar{H}(f)$ provides a good protection against leakage, the estimator $\hat{S}^{(mt)}(f)$ is leakage-free.

# Appendix C

# TM evaluation from ULA-OP images

The evaluation of the Thomson's multitaper approach (defined in section 3.3.1.2) using the actual images provided by ULA-OP scanning system is presented. Figure C. 1 and Figure C. 2 are the two parts of the same phantom (Gammex 404GS LE) with a hyperechoic cyst with wires and a hypoechoic cyst. The images are normalized by their own maximum and are log compressed with a dynamic of 50 dB. The SNR, CNR and spatial resolution are evaluated at different depths (Figure 3.4.b, Figure 3.4.c) and are given in Figure C. 3, Figure C. 4 and Figure C. 5, respectively.

As in simulation, the speckle is smooth when DPSS apodization are used and the smoothing is more important outside the focal area. The loss of resolution is clearly visible in second line of the Figure C. 1, where the wires outside the focal are spread. The contrast also decreases in the region of the hypoechoic cyst, Figure C. 2. The center of the hypoechoic cyst has signal which appears and degrades the contrast with the surrounding background when a too high number of DPSS apodization is used.

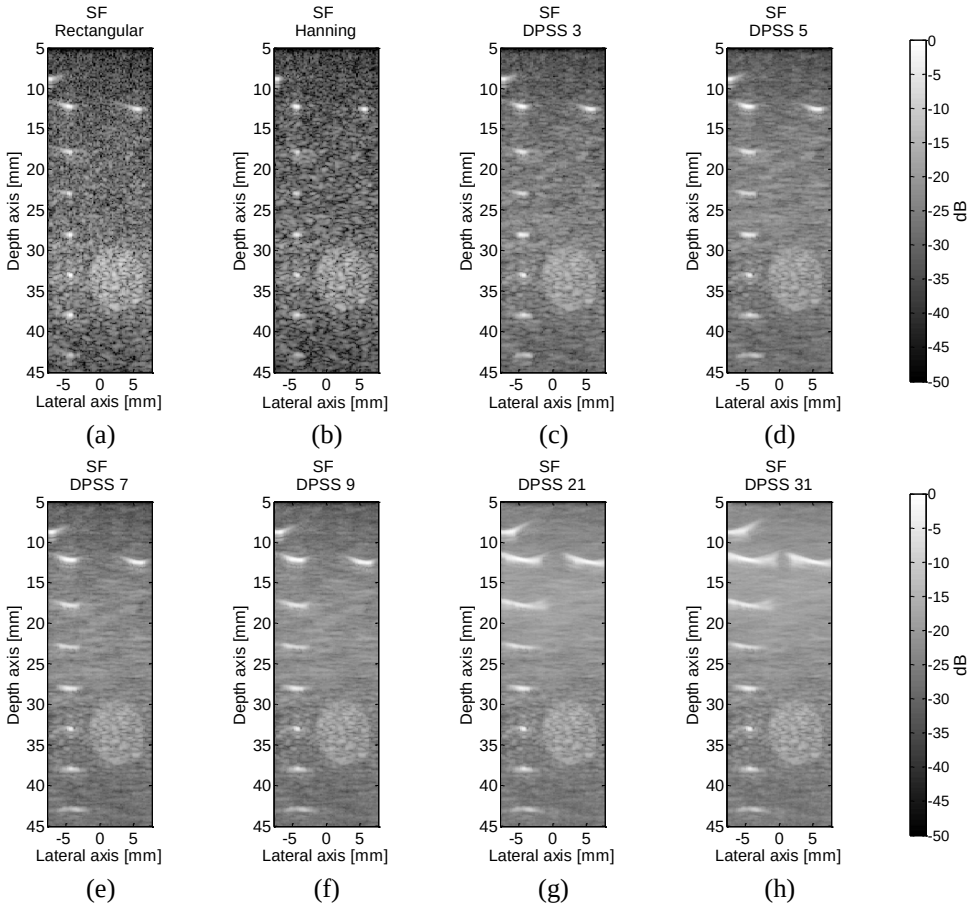


**Figure C. 1: Log compressed ULA-OP ultrasound images of hypoechoic cysts and wires for one focal depth at 30 mm for (a) a rectangular apodization, (b) an Hanning apodization and (c-h) DPSS apodization.**

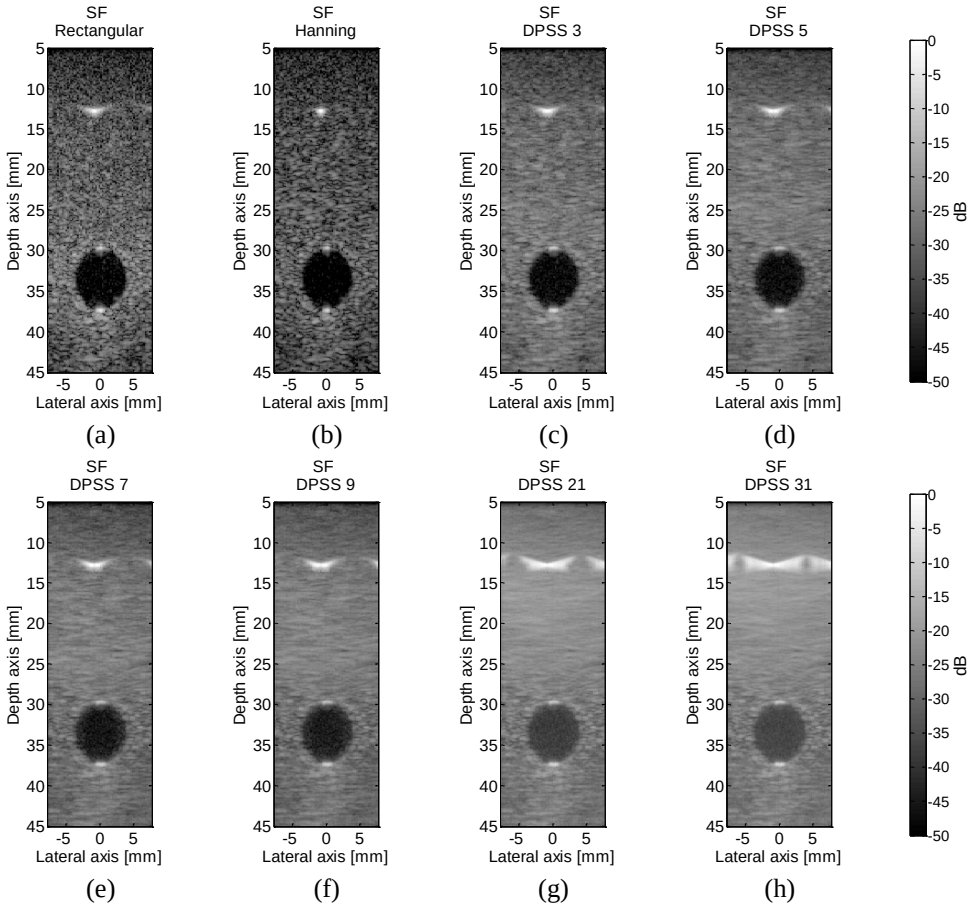


**Figure C. 2: Log compressed ULA-OP ultrasound images of hypoechoic cysts and wires for one focal depth at 30 mm for (a) a rectangular one apodization, (b) an Hanning apodization and (c-h) DPSS apodization.**

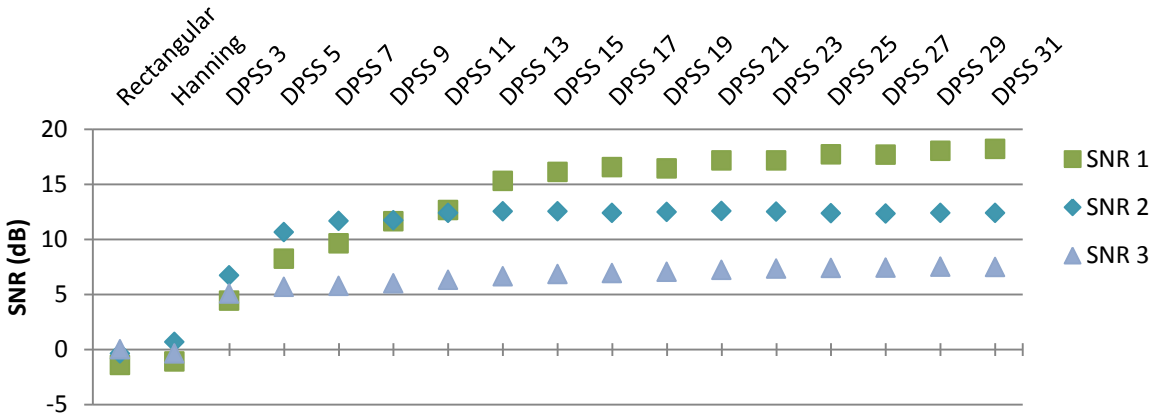


**Figure C. 3: SNR in dB for ULA-OP acquisitions calculated at different depths given in Figure 3.4.b. The SNR is evaluated for a rectangular, a Hanning and different DPSS apodizations. SNR 1, SNR 2 and SNR 3 are the area in the top, middle and bottom of the image, respectively. The SNR is normalized by the measurements performed on SF rectangular image, close to 30 mm and is expressed in decibel.**

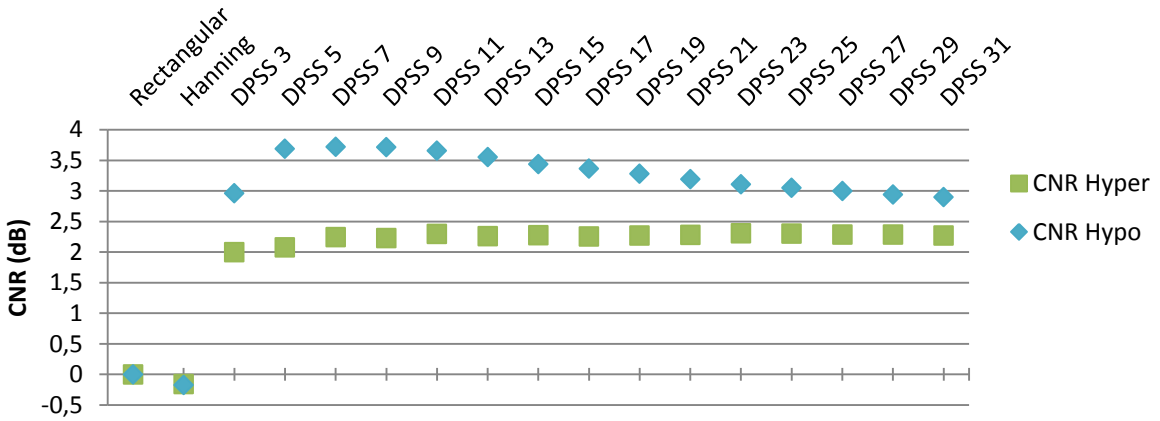


**Figure C. 4: CNR in dB for ULA-OP acquisition calculated in Figure 3.4.b and Figure 3.4.c. The CNR is evaluated for a rectangular, a Hanning and different DPSS apodizations. The CNR is normalized by the measurements performed on SF rectangular image, close to 30 mm and is expressed in decibel.**

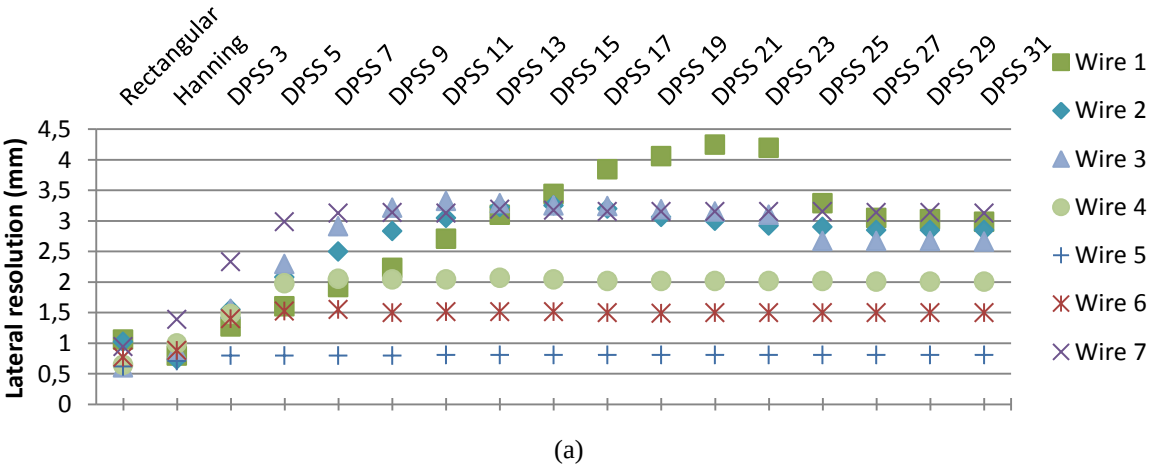


(a)

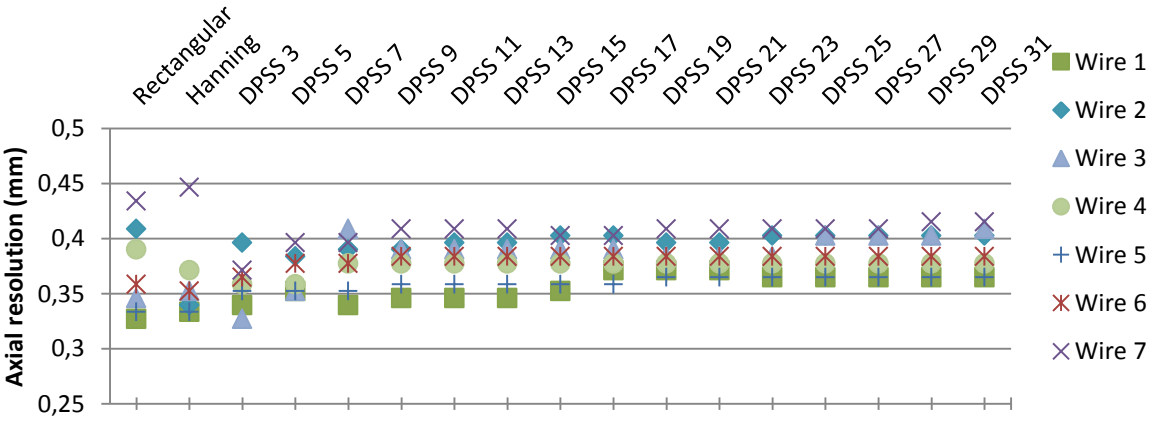


(b)

**Figure C. 5: Spatial resolution, (a) lateral resolution and (b) axial resolution, evaluated at different depths given in Figure 3.4.b in the phantom with ULA-OP acquisitions. The spatial resolutions are evaluated for a rectangular, a Hanning and different DPSS apodization. Wire 1 to 7 are the wires from the to the bottom of the image.**

# Appendix D

# MPI evaluation from ULA-OP data

The evaluation of the multitaper pulse inversion method (defined section 3.5.1.2) from images acquired with the ULA-OP scanning system. Figure D. 1 shows the homemade agar phantom with two holes. The left hole was filed with water silica mixtures (hole 1) and the right hole with only water (hole 2). The log compressed simulated images of fundamental, second-harmonic and PI or MPI techniques are represented in the Figure D. 2. A rectangular or DPSS 3 apodization is used during the beamforming. The SNR, CNR and spatial resolution are evaluated at different depths (Figure D. 1). The SNR and CNR are normalized by the value of the fundamental image close to 20 mm. They are averaged and the mean and the standard deviation of SNR, CNR and spatial resolution are given in are given in Figure D. 3.

The SNR evaluation shows that the multitaper method smoothes the speckle as in simulation (Figure D. 3.a). In the hole 1 (Figure D. 3.b), the second-harmonic or PI / MPI imaging improves strongly the contrast. In the whole image the gain in term of resolutions is less visible than in simulation. The spatial resolution of MPI is closed to the second-harmonic using the TM approach (Figure D. 3.c-d).

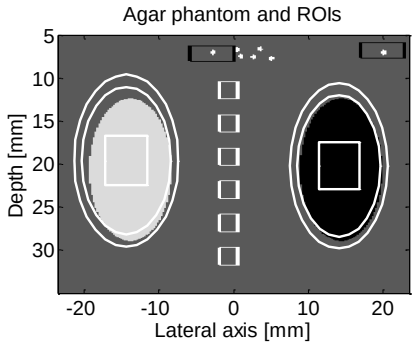


**Figure D. 1: Geometry of the phantoms with wires and holes areas used with ULA-OP acquisitions. Areas drawn in phantoms are used for the measurement of SNR (white squares), CNR (white squares inside the cysts and the area between white circles outside the cysts) and resolutions.**

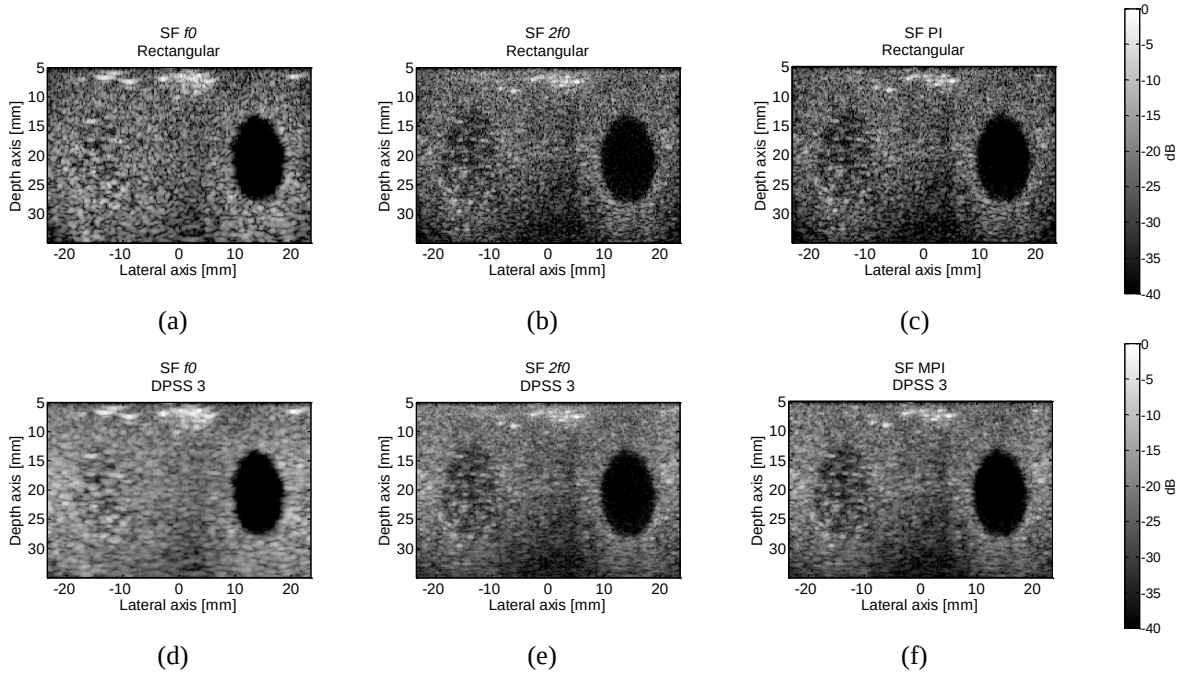


**Figure D. 2: Log compressed ULA-OP ultrasound images of the phantom including two holes. One single focal depth at 20 mm is used. The resulting image for fundamental, second harmonic and pulse inversion approach with or without DPSS apodization are presented: (a) fundamental rectangular, (b) second-harmonic rectangular, (c) PI rectangular, (d) fundamental DPSS 3,(e) second-harmonic DPSS 3 and (f) MPI DPSS 3 method.**

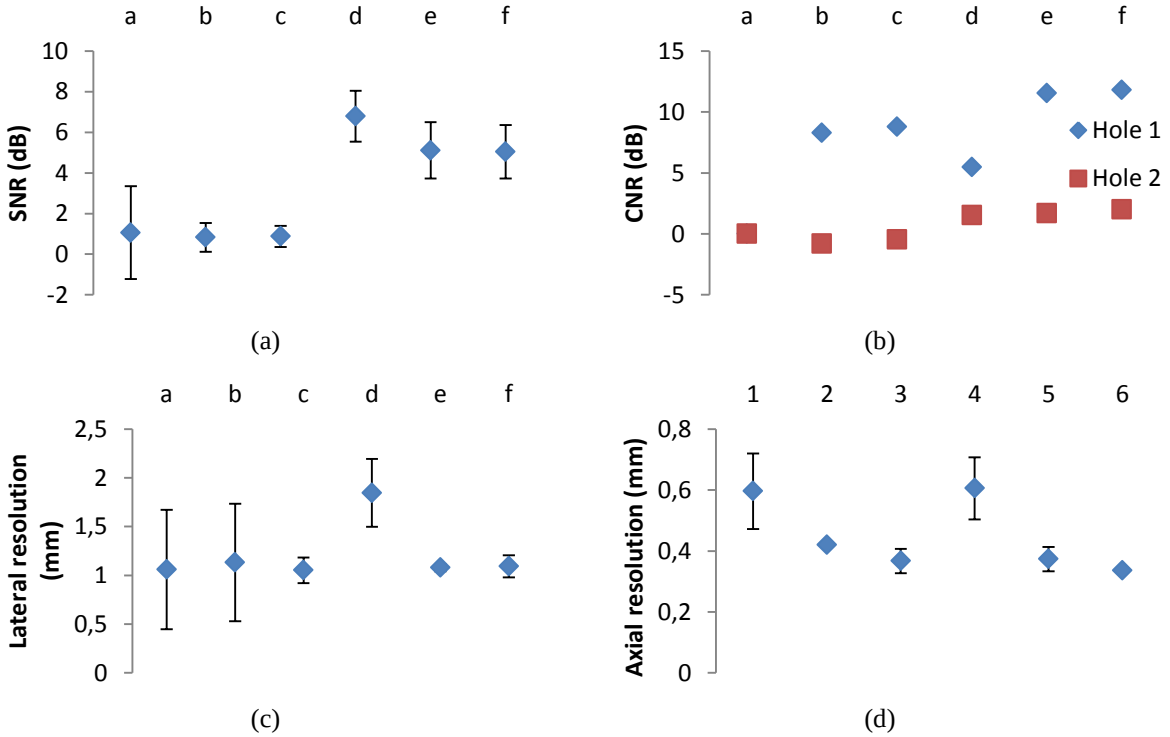


a: Rectangular $f_0$, b: Rectangular $2f_0$, c: Rectangular PI, d: DPSS 3 $f_0$, e: DPSS 3 $2f_0$, f: DPSS 3 MPI

**Figure D. 3: Evaluation of the MPI approach. Averaged and standard deviation of (a) SNR and (b) CNR in dB and (c) lateral and (d) axial resolutions for ULA-OP acquisition calculated at different depth given in Figure D. 1. The SNR values have been normalized by the measurements performed on the original image, close to 20 mm and then have been averaged and expressed in decibel. The spatial resolution values of all depths have been averaged.**

# Appendix E

# MCPWC evaluation from ULA-OP data

The evaluation of the multitaper coherent plane wave compounding (MCPWC) method (defined section 3.5.2.2) from images acquired with the ULA-OP scanning system. The MCPWC technique is compared to the SF, MF and CPWC approaches with rectangular one or DPSS 3 apodization. The SF focus was set at 32.5 mm, which is the depth of the cyst area in Figure 3.4.b. For the MF approach, the seven focalizations were spaced 5 mm apart from 12.5 to 42.5 mm. In MCPWC and CPWC imaging modes, the same (61, 31 and 11) steering angles used in the simulations were considered. Figure E. 1 and Figure E. 2 are the two parts of the same phantom (Gammex 404GS LE) with a hyperechoic cyst with wires and a hypoechoic cyst. The images are normalized by their own maximum and are log compressed with a dynamic of 50 dB. The SNR, CNR and spatial resolution are evaluated at different depths (Figure 3.4.b, Figure 3.4.c) and are given in Figure E. 3. The SNR and CNR are normalized by the value of the fundamental image close to 30 mm.

As in simulation, the use of DPSS apodization increases the SNR (Figure E. 3.a) and CNR (Figure E. 3.b). However the lateral resolution decreases (Figure E. 3.c). The MCPWC improves the resolution in the whole image compared to the SF approach.

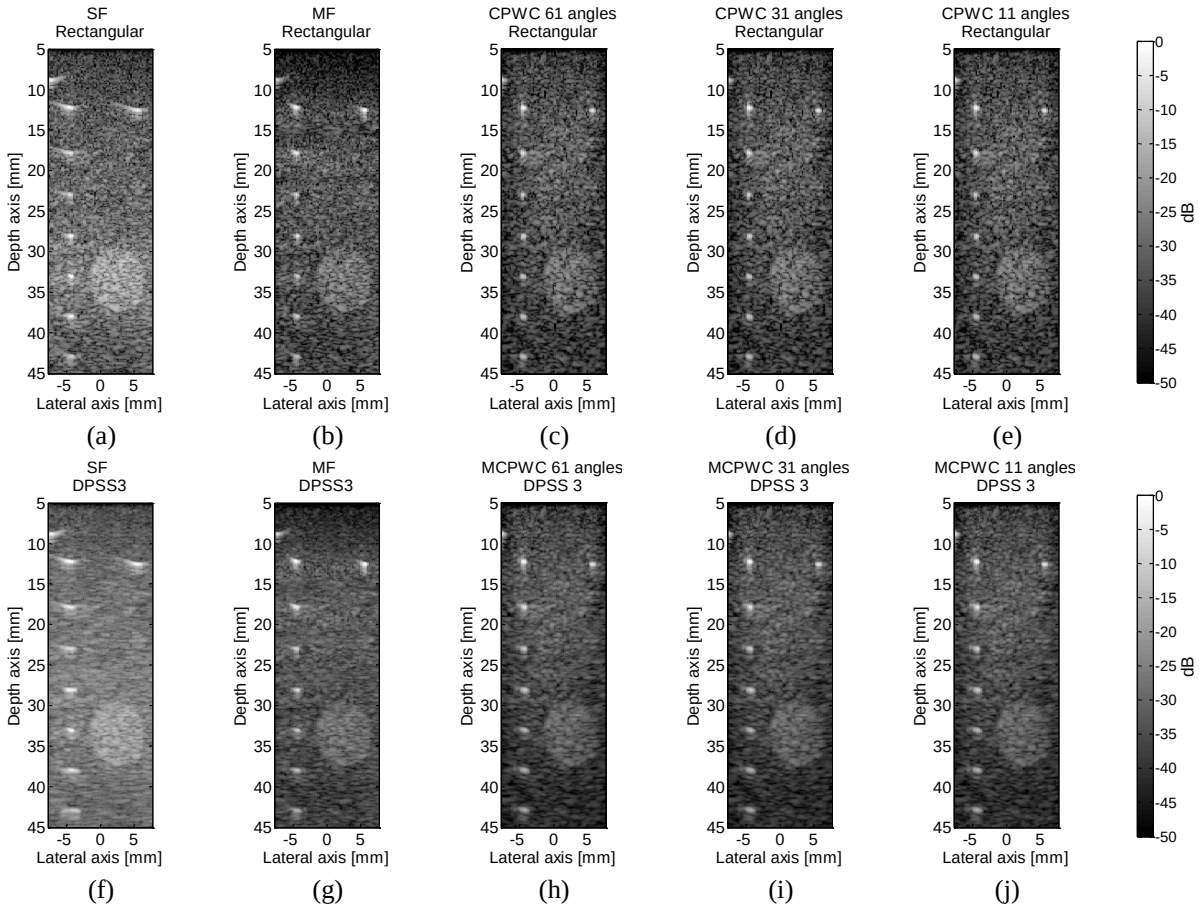


**Figure E. 1: Log compressed images of cyst and wires obtained by the ULA-OP scanner, (a, f) one focal depth at 32.5 mm without and with three apodization tapers on reception. (b, g) MF without and with three apodization tapers on reception, (c-e) CPWC and (h-j) MCPWC with three apodization tapers on reception and 61, 31 and 11 transmitted angles.**

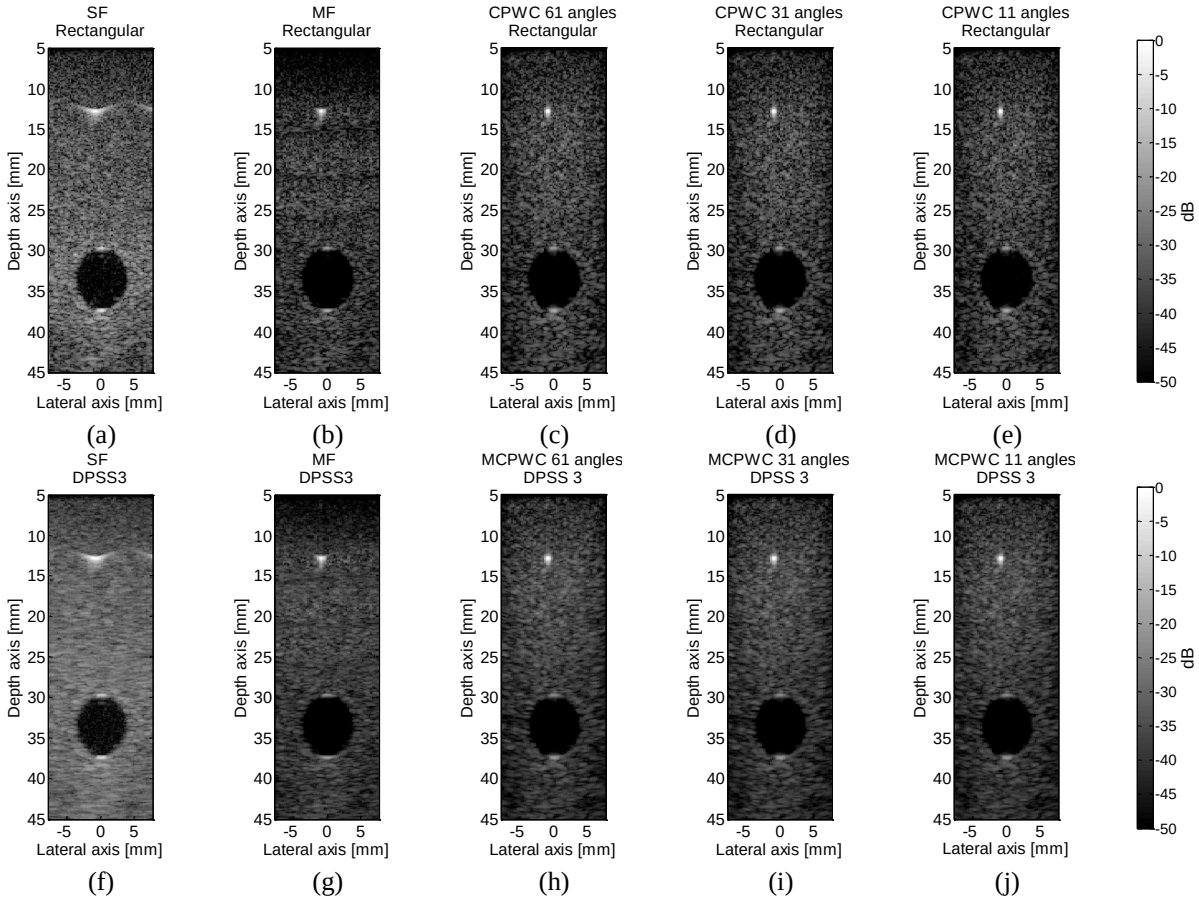


**Figure E. 2: Log compressed images of hypo echoic cyst obtained by the ULA-OP scanner, (a, f) one focal depth at 32.5 mm without and with three apodization tapers on reception, (b, g) MF without and with three apodization tapers on reception, (c-e) CPWC and (h-j) MCPWC with three apodization tapers on reception and 61, 31 and 11 transmitted angles.**

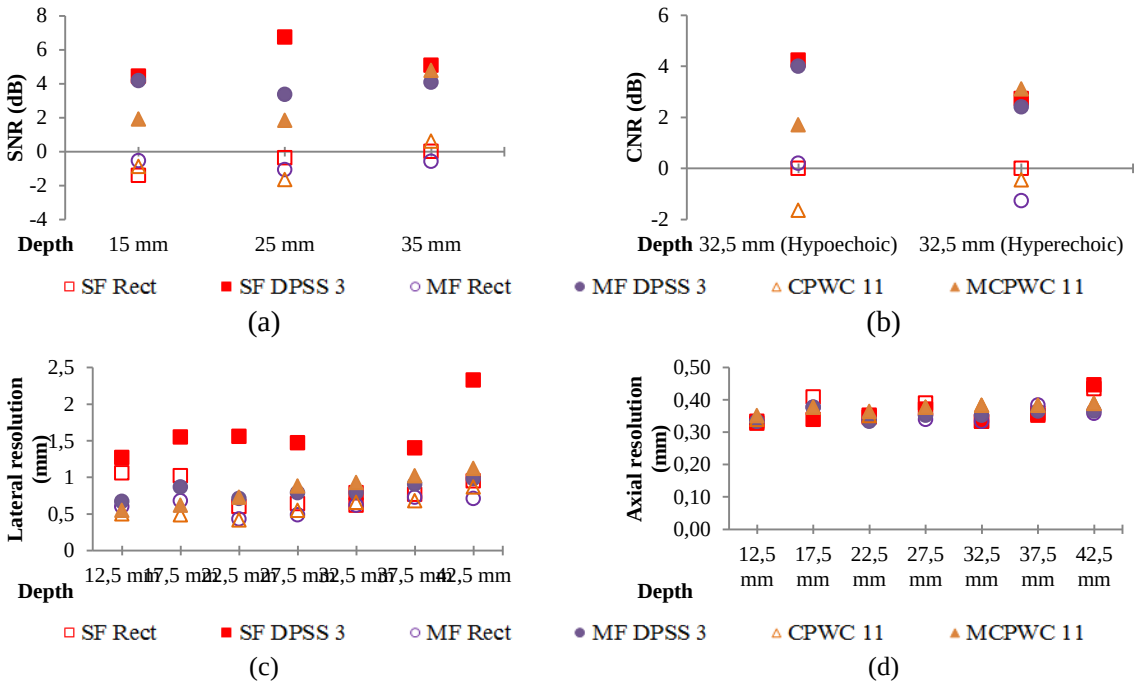


**Figure E. 3: ULAOP acquisitions on the phantom described in Figure 3.4.b and Figure 3.4.c. (a) SNR, (b) CNR, (c) lateral resolution and (d) axial resolution estimated at different depth for different transmission method (SF, MF, CPWC / MCPWC) and different apodization (Rectangular and DPSS3) during beamforming**

# Appendix F

# Pressure field measurement platform

A pressure field estimation platform has been created in order to validate the plane wave pressure field simulation (Figure F. 1). A PVDF needle hydrophone (Precision Acoustics, no. 105) is moved to measure the signal in front of a probe. Then the signal is amplified (DC Coupler Unit no. D/C1 153) and the amplitude of harmonics are estimated using an electronic oscilloscope (LECROY Ware Runner 44MXi-A). The platform is controlled by a Labview® software developed by M. Toulemonde with the help of A. Poizat and A. Bernard.

(a)

(b)

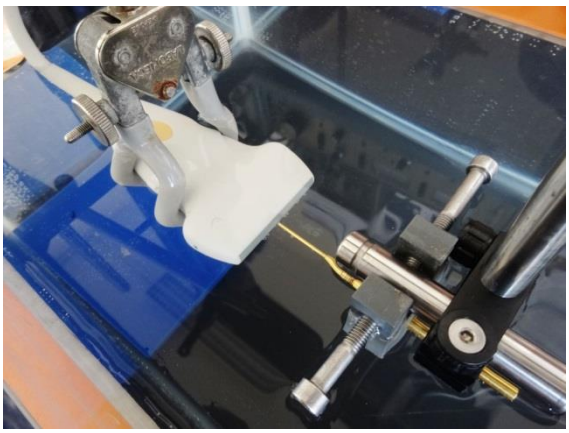

(c)

(d)

**Figure F. 1: Pressure field estimation platform. (a) Pressure field platform with the probe in water, (b) three independent motors and axis (OWIS, Staufen im Breisgau), (c) echographic probe and hydrophone and (d) electronic oscilloscope.**

# Personal bibliography

**International journal**

(Toulemonde et al., 2014): **Toulemonde, M.,** Basset, O., Tortoli, P., & Cachard, C., (2014). 'Thomson's multitaper approach combined with coherent plane-wave compounding for speckle reduction', Ultrasonics, accepted the 9th September 2014.

**International conferences**

(Toulemonde et al., 2014): **Toulemonde, M.**, Varray, F., Basset, O., Tortoli, P., & Cachard, C., (2014). 'High Frame Rate Compounding for Nonlinearity B/A Parameter Ultrasound Imaging in Echo Mode – Simulation Results', IEEE 2014 ICASSP, 5190-5194.

(Toulemonde et al., 2013): **Toulemonde, M.,** Basset, O., Tortoli, P., & Cachard, C., (2013). 'Thomson's multitaper high frame rate compounding for speckle reduction', IEEE 2013 Ultrasonics Symposium, 1452-1455.

(Toulemonde et al., 2012): **Toulemonde, M.**, Basset, O., Varray, F., Tortoli, P., & Cachard, C., (2012). 'Resolution improvement in Thomson's multitaper approach using the pulse inversion technique', IEEE 2012 Ultrasonics Symposium, 1934-1937.

(Varray et al., 2012): Varray, F., **Toulemonde, M.**, Basset, O., & Cachard, C., (2012). 'Fast and accurate nonlinear pressure field simulation : a finite difference scheme into the Fourier domain', IEEE 2012 Ultrasonics Symposium, 1682-1684.

(Toulemonde et al., 2012): **Toulemonde, M.**, Varray, F., Tortoli, P., Cachard, C., & Basset, O., (2012). 'Speckle Reduction with Multitaper approach to improve B/A imaging', Acoustics 2012, 197-202.

(Varray et al., 2012): Varray, F., **Toulemonde, M.**, Basset, O., & Cachard, C., (2012). 'Fast Simulation of Nonlinear Radio Frequency Ultrasound Images in Inhomogeneous Nonlinear Media : CREANUIS', Acoustics 2012, 91-96.

**Educational conference**

(Toulemonde et al., 2013): **Toulemonde, M.**, Rousseau, D., Liebgott, H., Cachard, C., & Neyran, B., (2013). 'En attendant le nouveau bachot', CETSIS 2013.

# Bibliography

Abbott, J.G. and Thurstone, F.L. (1979) 'Acoustic speckle: Theory and experimental analysis', *Ultrasonic Imaging*, vol. 1, no. 4, pp. 303-324.

Adam, D., Beilin-Nissan, S., Friedman, Z. and Behar, V. (2006) 'The combined effect of spatial compounding and nonlinear filtering on the speckle reduction in ultrasound images ', *Ultrasonics* , vol. 44, no. 2, pp. 166-181.

Adler, L. and Hiedemann, E.A. (1962) 'Determination of the Nonlinearity Parameter B/A for Water and m-Xylene', *The Journal of the Acoustical Society of America*, vol. 34, no. 4, pp. 410-412.

Angelsen, B.A.J. (2000) *Ultrasound Imaging*, Emantec.

Babadi, B. and Brown, E.N. (2014) 'A Review of Multitaper Spectral Analysis', *Biomedical Engineering, IEEE Transactions on*, vol. 61, no. 5, pp. 1555-1564.

Balocco, S., Gatta, C., Pujol, O., Mauri, J. and Radeva, P. (2010) 'SRBF: Speckle Reducing Bilateral Filtering', *Ultrasound in Medicine and Biology*, vol. 36, no. 8, pp. 1353-1363.

Behar, V., Adam, D. and Friedman, Z. (2003) 'A new method of spatial compounding imaging ', *Ultrasonics* , vol. 41, no. 5, pp. 377-384.

Bencharit, U., Kaufman, J.L., Bilgutay, N.M. and Saniie, J. (1986) 'Frequency and Spatial Compounding Techniques for Improved Ultrasonic Imaging', IEEE 1986 Ultrasonics Symposium, 1021-1026.

Berson, M., Roncin, A. and Pourcelot, L. (1981) 'Compound scanning with an electrically steered beam ', *Ultrasonic Imaging* , vol. 3, no. 3, pp. 303-308.

Beyer, R.T. (1960) 'Parameter of Nonlinearity in Fluids', *The Journal of the Acoustical Society of America*, vol. 32, no. 6, pp. 719-721.

Beyer, R.T. and Letcher, S.V. (1969) *Physical ultrasonics*, Academic Press.

Borsboom, J.M.G., Chin, C.T., Bouakaz, A., Versluis, M. and de Jong, N. (2005) 'Harmonic chirp imaging method for ultrasound contrast agent', *IEEE Transactions on Ultrasonics, Ferroelectrics and Frequency Control*, vol. 52, no. 2, pp. 241-249.

Bouakaz, A., Frigstad, S., Cate, F.J.T. and de Jong, N. (2002) 'Improved contrast to tissue ratio at higher harmonics', *Ultrasonics* , vol. 40, no. 1-8, pp. 575-578.

Burckhardt, C.B. (1978) 'Speckle in ultrasound B-mode scans', *Sonics and Ultrasonics, IEEE Transactions on*, vol. 25, no. 1, pp. 1-6.

Cain, C.A. (1986) 'Ultrasonic reflection mode imaging of the nonlinear parameter B/A: I. A theoretical basis', *The Journal of the Acoustical Society of America*, vol. 80, pp. 28-32.

Cai, A., Sun, J.-A. and Wade, G. (1992) 'Imaging the acoustic nonlinear parameter with diffraction tomography', *Ultrasonics, Ferroelectrics and Frequency Control, IEEE Transactions on*, vol. 39, no. 6, pp. 708-715.

Cheng, J. and Lu, J.-y. (2006) 'Extended high-frame rate imaging method with limited-diffraction beams', *Ultrasonics, Ferroelectrics and Frequency Control, IEEE Transactions on*, vol. 53, no. 5, pp. 880-899.

Choudhry, S., Gorman, B., Charboneau, J.W., Tradup, D.J., Beck, R.J., Kofler, J.M. and Groth, D.S. (2000) 'Comparison of Tissue Harmonic Imaging with Conventional US in Abdominal Disease', *RadioGraphics*, vol. 20, no. 4, pp. 1127-1135.

Coupe, P., Hellier, P., Kervrann, C. and Barillot, C. (2009) 'Nonlocal Means-Based Speckle Filtering for Ultrasound Images', *Image Processing, IEEE Transactions on*, vol. 18, no. 10, pp. 2221-2229.

Culjat, M.O., Goldenberg, D., Tewari, P. and Singh, R.S. (2010) 'A Review of Tissue Substitutes for Ultrasound Imaging ', *Ultrasound in Medicine \& Biology* , vol. 36, no. 6, pp. 861-873.

de Jong, N., Bouakaz, A. and Cate, F.J.T. (2002) 'Contrast harmonic imaging ', *Ultrasonics* , vol. 40, no. 1-8, pp. 567-573.

Denarie, B., Tangen, T.A., Ekroll, I.K., Rolim, N., Torp, H., Bjastad, T. and Lovstakken, L. (2013) 'Coherent Plane Wave Compounding for Very High Frame Rate Ultrasonography of Rapidly Moving Targets', *Medical Imaging, IEEE Transactions on*, vol. 32, no. 7, pp. 1265-1276.

Dong, F., Madsen, E.L., MacDonald, M.C. and Zagzebski, J.A. (1999) 'Nonlinearity parameter for tissue-mimicking materials ', *Ultrasound in Medicine and Biology*, vol. 25, no. 5, pp. 831-838.

Entrekin, R., Jackson, P., Jago, J. and Porter, B. (1999) 'Real time spatial compound imaging in breast ultrasound: technology and early clinical experience', *medicamundi*, vol. 43, no. 3, pp. 35-43.

Entrekin, R., Porter, B.A., Sillesen, H., Wong, A., Cooperberg, P. and Fix, C. (2001) 'Real-Time Spatial Compound Imaging: Application to Breast, Vascular, and Musculoskeletal Ultrasound', *Seminars in Ultrasound, CT and MRI*, vol. 22, no. 1, pp. 50-64.

Errabolu, R.L., Sehgal, C.M., Bahn, R.C. and Greenleaf, J.F. (1988) 'Measurement of ultrasonic nonlinear parameter in excised fat tissues ', *Ultrasound in Medicine and Biology*, vol. 14, no. 2, pp. 137-146.

Fenlon, F.H. (1972) 'An Extension of the Bessel-Fubini Series for a Multiple-Frequency CW Acoustic Source of Finite Amplitude', *The Journal of the Acoustical Society of America*, vol. 51, no. 1B, pp. 284-289.

Frinking, P.J.A., Bouakaz, A., Kirkhorn, J., Cate, F.J.T. and de Jong, N. (2000) 'Ultrasound contrast imaging: current and new potential methods ', *Ultrasound in Medicine and Biology*, vol. 26, no. 6, pp. 965-975.

Frost, V.S., Stiles, J.A., Shanmugan, K.S. and Holtzman, J. (1982) 'A Model for Radar Images and Its Application to Adaptive Digital Filtering of Multiplicative Noise', *Pattern Analysis and Machine Intelligence, IEEE Transactions on*, vol. PAMI-4, no. 2, pp. 157-166.

Fubini, G. (1935) 'Anomalie nella propagazione di onde acustiche di grande ampiezza', *Altra Frequenza*, vol. 4, pp. 503-581.

Fukukita, H., Ueno, S. and Yano, T. (1996) 'Ultrasound pulse reflection mode measurement of nonlinearity parameter B/A and attenuation coefficient', *The Journal of the Acoustical Society of America*, vol. 99, no. 5, pp. 2775-2782.

Garcia, D., Tarnec, L.L., Muth, S., Montagnon, E., Porée, J. and Cloutier, G. (2013) 'Stolt's f-k migration for plane wave ultrasound imaging', *Ultrasonics, Ferroelectrics and Frequency Control, IEEE Transactions on*, vol. 60, no. 9, pp. 1853-1867.

Gerig, A., Chen, Q., Zagzebski, J. and Varghese, T. (2004) 'Correlation of ultrasonic scatterer size estimates for the statistical analysis and optimization of angular compounding', *The Journal of the Acoustical Society of America*, vol. 116, no. 3, pp. 1832-1841.

Gong, X.-f., Feng, R., Zhu, C.-y. and Shi, T. (1984) 'Ultrasonic investigation of the nonlinearity parameter B/A in biological media', *The Journal of the Acoustical Society of America*, vol. 76, no. 3, pp. 949-950.

Gong, X., Zhang, D., Liu, J., Wang, H., Yan, Y. and Xu, X. (2004) 'Study of acoustic nonlinearity parameter imaging methods in reflection mode for biological tissues', *The Journal of the Acoustical Society of America*, vol. 116, no. 3, pp. 1819-1825.

Gong, X.-f., Zhu, Z.-m., Shi, T. and Huang, J.-h. (1989) 'Determination of the acoustic nonlinearity parameter in biological media using FAIS and ITD methods', *The Journal of the Acoustical Society of America*, vol. 86, no. 1, pp. 1-5.

Gupta, S., Chauhan, R.C. and Sexana, S.C. (2004) 'Wavelet-based statistical approach for speckle reduction in medical ultrasound images', *Medical and Biological Engineering and Computing*, vol. 42, no. 2, pp. 189-192.

Hamilton, M.F. and Blackstock, D.T. (1988) 'On the coefficient of nonlinearity β in nonlinear acoustics', *The Journal of the Acoustical Society of America*, vol. 83, no. 1, pp. 74-77.

Hamilton, M.F. and Blackstock, D.T. (1998) *Nonlinear Acoustics*, Academic Press.

Harris, G.R., Liu, Y., Maruvada, S. and Gammell, P.M. (2007) 'P4H-1 Finite Amplitude Method for Measurement of Nonlinearity Parameter B/A Using Plane-Wave Tone Bursts', Ultrasonics Symposium, 2007. IEEE, 2072-2074.

Hartmann, B. (1979) 'Potential energy effects on the sound speed in liquids', *The Journal of the Acoustical Society of America*, vol. 65, no. 6, pp. 1392-1396.

Ichida, N., Sato, T. and Linzer, M. (1983) 'Imaging the nonlinear ultrasonic parameter of a medium ', *Ultrasonic Imaging* , vol. 5, no. 4, pp. 295-299.

Ichida, N., Sato, T., Miwa, H. and Murakami, K. (1984) 'Real-Time Nonlinear Parameter Tomography Using Impulsive Pumping Waves', *Sonics and Ultrasonics, IEEE Transactions on*, vol. 31, no. 6, pp. 635-641.

Jensen, A.C., Nasholm, S.P., Nilsen, C.C., Austeng, A. and Holm, S. (2012) 'Applying Thomson's multitaper approach to reduce speckle in medical ultrasound imaging', *Ultrasonics, Ferroelectrics and Frequency Control, IEEE Transactions on*, vol. 59, no. 10, pp. 2178-2185.

Jensen, J.A., Nikolov, S.I., Gammelmark, K.L. and Pedersen, M.H. (2006) 'Synthetic aperture ultrasound imaging ', *Ultrasonics* , vol. 44, Supplement, pp. e5 - e15.

Jensen, A.C., Nilsen, C.C., Austeng, A., Nasholm, S.P. and Holm, S. (2011) 'A multitaper approach to speckle reduction for medical ultrasound imaging', Ultrasonics Symposium (IUS), 2011 IEEE International, 397-400.

Jespersen, S.K., Wilhjelm, J.E. and Sillesen, H. (1998) 'Multi-angle compound imaging', *Ultrasonic Imaging*, vol. 20, pp. 81-102.

Jespersen, S.K., Wilhjelm, J.E. and Sillesen, H. (1998) 'Ultrasound spatial compound scanner for improved visualization in vascular imaging', Ultrasonics Symposium, 1998. Proceedings., 1998 IEEE, 1623-1626.

Khelladi, H., Plantier, F., Daridon, J.L. and Djelouah, H. (2009) 'Measurement under high pressure of the nonlinearity parameter B/A in glycerol at various temperatures ', *Ultrasonics* , vol. 49, no. 8, pp. 668-675.

Kim, D., Greenleaf, J.F. and Sehgal, C.M. (1990) 'Ultrasonic imaging of the nonlinear parameter B/A: Simulation studies to evaluate phase and frequency modulation methods ', *Ultrasound in Medicine and Biology*, vol. 16, no. 2, pp. 175-181.

Kourtiche, D., Alliès, L., Chitnalah, A. and Nadi, M. (2001) 'Harmonic propagation of finite amplitude sound beams: comparative method in pulse echo measurement of nonlinear B / A parameter', *Measurement Science and Technology*, vol. 12, no. 11, p. 1990.

Kruizinga, P., Mastik, F., de Jong, N., van der Steen, A.F.W. and van Soest, G. (2012) 'Plane-wave ultrasound beamforming using a nonuniform fast fourier transform', *Ultrasonics, Ferroelectrics and Frequency Control, IEEE Transactions on*, vol. 59, no. 12, pp. 2684-2691.

Kuan, D.T., Sawchuk, A.A., Strand, T.C. and Chavel, P. (1985) 'Adaptive Noise Smoothing Filter for Images with Signal-Dependent Noise', *Pattern Analysis and Machine Intelligence, IEEE Transactions on*, vol. PAMI-7, no. 2, pp. 165-177.

Kujawska, T., Nowicki, A. and Lewin, P.A. (2011) 'Determination of nonlinear medium parameter B/A using model assisted variable-length measurement approach ', *Ultrasonics* , vol. 51, no. 8, pp. 997-1005.

Landau, H.J. and Pollak, H.O. (1961) 'Prolate Spheroidal Wave Functions, Fourier Analysis and Uncertainty - II', *Bell System Technical Journal*, vol. 40, no. 1, pp. 65-84.

Law, W.K., Frizzell, L.A. and Dunn, F. (1981) 'Ultrasonic determination of the nonlinearity parameter B/A for biological media', *The Journal of the Acoustical Society of America*, vol. 69, no. 4, pp. 1210-1212.

Law, W.K., Frizzell, L.A. and Dunn, F. (1983) 'Comparison of thermodynamic and finite amplitude methods of B/A measurement in biological materials', *The Journal of the Acoustical Society of America*, vol. 74, no. 4, pp. 1295-1297.

Law, W.K., Frizzell, L.A. and Dunn, F. (1985) 'Determination of the nonlinearity parameter B/A of biological media ', *Ultrasound in Medicine and Biology*, vol. 11, no. 2, pp. 307-318.

Lee, J.-S. (1980) 'Digital Image Enhancement and Noise Filtering by Use of Local Statistics', *Pattern Analysis and Machine Intelligence, IEEE Transactions on*, vol. PAMI-2, no. 2, pp. 165-168.

Lees, J.M. and Park, J. (1995) 'Multiple-taper spectral analysis: A stand-alone C-subroutine', *Computers and Geosciences*, vol. 21, no. 2, pp. 199-236.

Lin, D.C., Nazarian, L.N., O'Kane, P.L., McShane, J.M., Parker, L. and Merritt, C.R.B. (2002) 'Advantages of Real-Time Spatial Compound Sonography of the Musculoskeletal System Versus Conventional Sonography', *American Journal of Roentgenology*, vol. 179, no. 6, pp. 1629-1631.

Lopes, A., Touzi, R. and Nezry, E. (1990) 'Adaptive speckle filters and scene heterogeneity', *Geoscience and Remote Sensing, IEEE Transactions on*, vol. 28, no. 6, pp. 992-1000.

Lu, J.-y. (1997) '2D and 3D high frame rate imaging with limited diffraction beams', *Ultrasonics, Ferroelectrics and Frequency Control, IEEE Transactions on*, vol. 44, no. 4, pp. 839-856.

Lu, J.-y. (1997) 'Designing limited diffraction beams', *Ultrasonics, Ferroelectrics and Frequency Control, IEEE Transactions on*, vol. 44, no. 1, pp. 181-193.

Lu, J.-y. (1998) 'Experimental study of high frame rate imaging with limited diffraction beams', *Ultrasonics, Ferroelectrics and Frequency Control, IEEE Transactions on*, vol. 45, no. 1, pp. 84-97.

Magnin, P.A., von Ramm, O.T. and Thurstone, F.L. (1982) 'Frequency compounding for speckle contrast reduction in phased array images ', *Ultrasonic Imaging* , vol. 4, no. 3, pp. 267-281.

Mallat, S.G. (1989) 'A theory for multiresolution signal decomposition: the wavelet representation', *Pattern Analysis and Machine Intelligence, IEEE Transactions on*, vol. 11, no. 7, pp. 674-693.

Maresca, D., Jansen, K., Renaud, G., Van Soest, G., Li, X., Zhou, Q., de Jong, N., Shung, K.K. and Van der Steen, A.F.W. (2012) 'Intravascular ultrasound chirp imaging', *Applied Physics Letters*, vol. 100, no. 4, pp. 043703-043703-3.

Mesurolle, B., Helou, T., El-Khoury, M., Edwardes, M., Sutton, E.J. and FAU Kao, E. (2007) 'Tissue Harmonic Imaging, Frequency Compound Imaging, and Conventional Imaging', *Journal of Ultrasound in Medicine*, vol. 26, no. 8, pp. 1041-1051.

Misaridis, T.X., Gammelmark, K., Jorgensen, C.H., Lindberg, N., Thomsen, A.H., Pedersen, M.H. and Jensen, J.A. (2000) 'Potential of coded excitation in medical ultrasound imaging ', *Ultrasonics* , vol. 38, no. 1-8, pp. 183-189.

Montaldo, G., Tanter, M., Bercoff, J., Benech, N. and Fink, M. (2009) 'Coherent plane-wave compounding for very high frame rate ultrasonography and transient elastography',

*Ultrasonics, Ferroelectrics and Frequency Control, IEEE Transactions on*, vol. 56, no. 3, pp. 489-506.

Nakagawa, Y., Hou, W., Cai, A., Arnold, N. and Wade, G. (1986) 'Nonlinear Parameter Imaging with Finite-Amplitude Sound Waves', IEEE 1986 Ultrasonics Symposium, 901-904.

Nakagawa, Y., Nakagawa, M., Yoneyama, M. and Kikuchi, M. (1984) 'Nonlinear Parameter Imaging Computed Tomography by Parametric Acoustic Array', IEEE 1984 Ultrasonics Symposium, 673-676.

Nanda, B., Nanda, B. and Mohanty, P. (2012) 'Effect of concentration on thermo acoustic and nonlinearity parameters (B/A) of barium chloride solutions in glycol--water mixtures at 303.15 K', *Journal of Molecular Liquids*, vol. 171, pp. 50-53.

Oelze, M.L. (2007) 'Bandwidth and resolution enhancement through pulse compression', *Ultrasonics, Ferroelectrics and Frequency Control, IEEE Transactions on*, vol. 54, no. 4, pp. 768-781.

Pantea, C., Osterhoudt, C.F. and Sinha, D.N. (2013) 'Determination of acoustical nonlinear parameter β of water using the finite amplitude method', *Ultrasonics* , vol. 53, no. 5, pp. 1012-1019.

Peng, H., Han, X. and Lu, J. (2006) 'Study on application of complementary Golay code into high frame rate ultrasonic imaging system ', *Ultrasonics* , vol. 44, Supplement, pp. e93 - e96.

Percival, D.B. and Walden, A.T. (1993) *Spectral Analysis for Physical Applications*, Cambridge University Press.

Pizurica, A., Wink, A.M., Vansteenkiste, E., Philips, W. and Roerdink, B.J.T.M. (2006) 'A Review of Wavelet Denoising in MRI and Ultrasound Brain Imaging', *Current Medical Imaging Reviews*, vol. 2, no. 2, pp. 247-260.

Prieto, G., Parker, R., Thomson, D., Vernon, F. and Graham, R. (2007) 'Reducing the bias of multitaper spectrum estimates', *Geophysical Journal International*, vol. 171, no. 3, pp. 1269-1281.

Ramalli, A., Basset, O., Cachard, C., Boni, E. and Tortoli, P. (2012) 'Frequency-domain-based strain estimation and high-frame-rate imaging for quasi-static elastography', *Ultrasonics, Ferroelectrics and Frequency Control, IEEE Transactions on*, vol. 59, no. 4, pp. 817-824.

Ravichandran, S. and Ramanathan, K. (2010) 'Ultrasonic investigations of MnSO4, NiSO4 and CuSO4 aqueous in polyvinyl alcohol solution at 303K', *Rasayan Journal of Chemistry*, vol. 3, no. 2, pp. 375-384.

Reddy, M.V.V.N., Pisipati, V.G.K.M., Latha, D.M. and Prasad, P.V.D. (2011) 'Beyer's non-linearity parameter (B/A) in benzylidene aniline Schiff base liquid crystalline systems', *Physica B: Condensed Matter* , vol. 406, no. 4, pp. 720-724.

Rosen, E.L. and Soo, M.S. (2001) 'Tissue harmonic imaging sonography of breast lesions: Improved margin analysis, conspicuity, and image quality compared to conventional ultrasound ', *Clinical Imaging* , vol. 25, no. 6, pp. 379-384.

Rudenko, O.V. and Soluyan, S.I. (1977) *Theoretical Foundations of Nonlinear Acoustics*, Consultants Bureau.

Saito, S. (1993) 'Measurement of the acoustic nonlinearity parameter in liquid media using focused ultrasound', *The Journal of the Acoustical Society of America*, vol. 93, no. 1, pp. 162-172.

Saito, S. (2010) 'Finite amplitude method for measuring the nonlinearity parameter B/A in small-volume samples using focused ultrasound', *The Journal of the Acoustical Society of America*, vol. 127, no. 1, pp. 51-61.

Saito, S. and Kim, J.-H. (2011) 'Two-dimensional measurement of the nonlinearity parameter B/A in excised biological samples', *Review of Scientific Instruments*, vol. 82, no. 6, pp. 064901-1 - 064901-9.

Saito, S., Kim, J.-H. and Nakamura, K. (2006) 'Automatic measurement of the nonlinearity parameter B/A in liquid media ', *Ultrasonics* , vol. 44, Supplement, no. 0, pp. e1429 - e1433.

Sehgal, C.M., Bahn, R.C. and Greenleaf, J.F. (1984) 'Measurement of the acoustic nonlinearity parameter B/A in human tissues by a thermodynamic method', *The Journal of the Acoustical Society of America*, vol. 76, no. 4, pp. 1023-1029.

Sehgal, C.M., Porter, B.R. and Greenleaf, J.F. (1986) 'Ultrasonic nonlinear parameters and sound speed of alcohol-water mixtures', *The Journal of the Acoustical Society of America*, vol. 79, no. 2, pp. 566-570.

Shattuck, D.P. and von Ramm, O.T. (1982) 'Compound scanning with a phased array ', *Ultrasonic Imaging* , vol. 4, no. 2, pp. 93-107.

Shen, C.-C., Chou, Y.-H. and Li, P.-C. (2005) 'Pulse Inversion Techniques in Ultrasonic Nonlinear Imaging ', *Journal of Medical Ultrasound* , vol. 13, no. 1, pp. 3-17.

Shen, C.-C. and Li, P.-C. (2002) 'Motion artifacts of pulse inversion-based tissue harmonic imaging', *Ultrasonics, Ferroelectrics and Frequency Control, IEEE Transactions on*, vol. 49, no. 9, pp. 1203-1211.

Simpson, D.H., Chin, C.T. and Burns, P.N. (1999) 'Pulse inversion Doppler: a new method for detecting nonlinear echoes from microbubble contrast agents', *Ultrasonics, Ferroelectrics and Frequency Control, IEEE Transactions on*, vol. 46, no. 2, pp. 372-382.

Sivakumar, R., Gayathri, M.K. and Nedumaran, D. (2010) 'Speckle Filtering of Ultrasound B-Scan Images- A Comparative Study of Single Scale Spatial Adaptive Filters, Multiscale Filter and Diffusion Filters', *International Journal of Engineering and Technology, IJET*, vol. 2, no. 6, pp. 514-523.

Slepian, D. (1978) 'Prolate spheroidal wave functions, Fourier analysis and uncertainty', *Bell Syst. Tech. J*, vol. 57, no. 5, pp. 1371-1429.

Slepian, D. and Pollak, H.O. (1961) 'Prolate Spheroidal Wave Functions, Fourier Analysis and Uncertainty - I', *Bell System Technical Journal*, vol. 40, no. 1, pp. 43-63.

Sternberg, S.R. (1986) 'Grayscale Morphology', *Comput. Vision Graph. Image Process.*, vol. 35, no. 3, pp. 333-355.

Stetson, P.F., Sommer, F.G. and Macovski, A. (1997) 'Lesion contrast enhancement in medical ultrasound imaging', *Medical Imaging, IEEE Transactions on*, vol. 16, no. 4, pp. 416-425.

Sturtevant, B.T., Pantea, C. and Sinha, D.N. (2012) 'An acoustic resonance measurement cell for liquid property determinations up to 250°C', *Review of Scientific Instruments*, vol. 83, no. 11, pp. 115106-1-115106-6.

Sturtevant, B.T., Pantea, C. and Sinha, D.N. (2012) 'Determination of the acoustic nonlinearity parameter in liquid water up to 250 °C and 14 MPa', Ultrasonics Symposium (IUS), 2012 IEEE International, 285-288.

Takeuchi, Y. (1979) 'An investigation of a spread energy method for medical ultrasound systems: Part one: Theory and investigation ', *Ultrasonics* , vol. 17, no. 4, pp. 175-182.

Tanter, M., Bercoff, J., Sandrin, L. and Fink, M. (2002) 'Ultrafast compound imaging for 2-D motion vector estimation: application to transient elastography', *Ultrasonics, Ferroelectrics and Frequency Control, IEEE Transactions on*, vol. 49, no. 10, pp. 1363-1374.

Tanter, M. and Fink, M. (2014) 'Ultrafast imaging in biomedical ultrasound', *Ultrasonics, Ferroelectrics and Frequency Control, IEEE Transactions on*, vol. 61, no. 1, pp. 102-119.

Thijssen, J.M. (2003) 'Ultrasonic Speckle Formation, Analysis and Processing Applied to Tissue Characterization', *Pattern Recogn. Lett.*, vol. 24, no. 4-5, pp. 659-675.

Thomson, D.J. (1982) 'Spectrum estimation and harmonic analysis', *Proceedings of the IEEE*, vol. 70, no. 9, pp. 1055-1096.

Tomasi, C. and Manduchi, R. (1998) 'Bilateral filtering for gray and color images', Computer Vision, 1998. Sixth International Conference on, 839-846.

Tortoli, P., Bassi, L., Boni, E., Dallai, A., Guidi, F. and Ricci, S. (2009) 'ULA-OP: an advanced open platform for ultrasound research', *Ultrasonics, Ferroelectrics and Frequency Control, IEEE Transactions on*, vol. 56, no. 10, pp. 2207-2216.

Trahey, G.E., Smith, S.W. and von Ramm, O.T. (1986) 'Speckle Pattern Correlation with Lateral Aperture Translation: Experimental Results and Implications for Spatial Compounding', *Ultrasonics, Ferroelectrics and Frequency Control, IEEE Transactions on*, vol. 33, no. 3, pp. 257-264.

Tranquart, F., Grenier, N., Eder, V. and Pourcelot, L. (1999) 'Clinical use of ultrasound tissue harmonic imaging ', *Ultrasound in Medicine and Biology*, vol. 25, no. 6, pp. 889-894.

Trots, I., Andrzej, N., Lewandowski, M. and Tasinkevych, Y. (2011) 'Synthetic Aperture Method in Ultrasound Imaging' InTech.

Ueno, S., Hashimoto, M., Fukukita, H. and Yano, T. (1990) 'Ultrasound thermometry in hyperthermia', Ultrasonics Symposium, 1990. Proceedings., IEEE 1990, 1645-1652 vol.3.

van Wijk, M.C. and Thijssen, J.M. (2002) 'Performance testing of medical ultrasound equipment: fundamental vs. harmonic mode ', *Ultrasonics* , vol. 40, no. 1-8, pp. 585-591.

Vander Meulen, F. and Haumesser, L. (2008) 'Evaluation of B/A nonlinear parameter using an acoustic self-calibrated pulse-echo method', *Applied Physics Letters*, vol. 92, no. 21, pp. 214106-1-214106-3.

Vander Meulen, F. and Haumesser, L. (2008) 'Towards a simple acoustic method to evaluate the nonlinear parameter B/A of fluids', Ultrasonics Symposium, 2008. IUS 2008. IEEE, 1908-1911.

Varray, F. (2011) *Simulation in Nonlinear Ultrasound. Application to Nonlinear Parameter Imaging in Echo Mode Configuration.*.

Varray, F., Basset, O., Tortoli, P. and Cachard, C. (2011) 'Extensions of nonlinear B/A parameter imaging methods for echo mode', *Ultrasonics, Ferroelectrics and Frequency Control, IEEE Transactions on*, vol. 58, no. 6, pp. 1232-1244.

Varray, F., Basset, O., Tortoli, P. and Cachard, C. (2013) 'CREANUIS: A Non-linear Radiofrequency Ultrasound Image Simulator ', *Ultrasound in Medicine and Biology*, vol. 39, no. 10, pp. 1915-1924.

Wage, K.E. (2007) 'Multitaper Array Processing', Signals, Systems and Computers, 2007. ACSSC 2007. Conference Record of the Forty-First Asilomar Conference on, 1242-1246.

Wagner, R.F., Insana, M.F. and Smith, S.W. (1988) 'Fundamental correlation lengths of coherent speckle in medical ultrasonic images', *Ultrasonics, Ferroelectrics and Frequency Control, IEEE Transactions on*, vol. 35, no. 1, pp. 34-44.

Wagner, R.F., Smith, S.W., Sandrik, J.M. and Lopez, H. (1983) 'Statistics of Speckle in Ultrasound B-Scans', *Sonics and Ultrasonics, IEEE Transactions on*, vol. 30, no. 3, pp. 156-163.

Wallace, K.D., Lloyd, C.W., Holland, M.R. and Miller, J.G. (2007) 'Finite Amplitude Measurements of the Nonlinear Parameter B/A for Liquid Mixtures Spanning a Range Relevant to Tissue Harmonic Mode ', *Ultrasound in Medicine and Biology*, vol. 33, no. 4, pp. 620-629.

Welch, P.D. (1967) 'The use of fast Fourier transform for the estimation of power spectra: A method based on time averaging over short, modified periodograms', *Audio and Electroacoustics, IEEE Transactions on*, vol. 15, no. 2, pp. 70-73.

Westervelt, P.J. (1963) 'Parametric Acoustic Array', *The Journal of the Acoustical Society of America*, vol. 35, no. 4, pp. 535-537.

Wojcik, J., Nowicki, A., Lewin, P.A., Bloomfield, P.E., Kujawska, T. and Filipczynski, L. (2006) 'Wave envelopes method for description of nonlinear acoustic wave propagation ', *Ultrasonics*, vol. 44, no. 3, pp. 310-329.

Wu, J. and Tong, J. (1998) 'Measurements of the nonlinearity parameter B/A of contrast agents', *Ultrasound in Medicine and Biology*, vol. 24, no. 1, pp. 153-159.

Xu, Y., Haykin, S. and Racine, R.J. (1999) 'Multiple window time-frequency distribution and coherence of EEG using Slepian sequences and Hermite functions', *Biomedical Engineering, IEEE Transactions on*, vol. 46, no. 7, pp. 861-866.

Zhang, D., fen Gong, X. and Chen, X. (2001) 'Experimental imaging of the acoustic nonlinearity parameter B/A for biological tissues via a parametric array ', *Ultrasound in Medicine and Biology*, vol. 27, no. 10, pp. 1359-1365.

Zhang, D. and Gong, X.-F. (1999) 'Experimental investigation of the acoustic nonlinearity parameter tomography for excised pathological biological tissues ', *Ultrasound in Medicine and Biology*, vol. 25, no. 4, pp. 593-599.

Zhang, D., Gong, X. and Ye, S. (1996) 'Acoustic nonlinearity parameter tomography for biological specimens via measurements of the second harmonics.', *J Acoust Soc Am*, vol. 99, no. 4 Pt 1, pp. 2397-2402.

Zhu, Z., Roos, M.S., Cobb, W.N. and Jensen, K. (1983) 'Determination of the acoustic nonlinearity parameter B/A from phase measurements', *The Journal of the Acoustical Society of America*, vol. 74, no. 5, pp. 1518-1521.

Zong, X., Laine, A.F. and Geiser, E.A. (1998) 'Speckle reduction and contrast enhancement of echocardiograms via multiscale nonlinear processing', *Medical Imaging, IEEE Transactions on*, vol. 17, no. 4, pp. 532-540.

Zorebski, E. and Zorebski, M. (2014) 'Acoustic nonlinearity parameter B/A determined by means of thermodynamic method under elevated pressures for alkanediols ', *Ultrasonics* , vol. 54, no. 1, pp. 368-374.

## TITRE EN FRANCAIS

Formation de voies en émission et en réception pour l'amélioration de l'imagerie ultrasonore, application à l'imagerie non linéaire des tissus biologique

## RESUME EN FRANCAIS

L'échographie est aujourd'hui une technique d'imagerie de diagnostic répandue. Si l'imagerie dite 'classique' basée sur la réponse linéaire des tissus est couramment utilisée, l'imagerie harmonique, basée sur la réponse non linéaire des tissus, est maintenant aussi utilisée en routine clinique. L'estimation du paramètre de non linéarité d'un milieu par une technique ultrasonore amène de nouvelles perspectives en termes d'imagerie et de diagnostic. Cependant, la méthode de mesure du paramètre de non linéarité est limitée par deux facteurs, la présence du speckle et la concentration de l'énergie à une profondeur donnée (la zone focale).

Cette thèse a pour objectifs de répondre aux deux limitations mentionnées précédemment en proposant de nouvelles méthodes de lissage de l'image pour réduire le speckle et d'améliorer l'estimation du paramètre de non linéarité en mode écho par de nouvelles méthodes d'émission.

Dans un premier temps, il a été proposé d'utiliser une méthode de filtrage spatiale basée sur des filtres orthogonaux (filtres de Thomson) lors de la formation de voie en réception pour lisser le speckle. Ce filtrage spatiale intervient après la transmission d'ondes planes sous différents angles pour améliorer la résolution spatiale et le contraste tout en accélérant la cadence d'imagerie.

Dans un deuxième temps, l'estimation du paramètre de non linéarité est faite avec une méthode comparative. Le champ de pression du second harmonique d'une zone de référence est comparé avec le champ de pression d'une zone dont le paramètre de non linéarité est inconnu. Cependant, dans le cas des images échographiques, le champ de pression du second harmonique n'est pas accessible. Nous faisons l'hypothèse que la pression acoustique locale est liée à l'intensité de l'image échographique si le speckle est réduit et lissé. La transmission d'ondes planes et l'application de filtres orthogonaux permet de mieux délimiter le paramètre de non linéarité par rapport à une transmission focalisée.

## TITRE EN ANGLAIS

New beamforming strategy for improved ultrasound imaging application to biological tissues nonlinear imaging

## RESUME EN ANGLAIS

Nowadays, ultrasound imaging is a common diagnostic tool thanks to its non-invasive behavior and relatively cheap equipment. Classic medical echographic imaging is based on the linear response of the biological tissue. However harmonic imaging, based on the harmonic frequencies generated by the nonlinear properties of the tissue, is more and more used for clinical application. The quantification of nonlinearity is based on the evaluation of the nonlinearity parameter which strongly influences the harmonics generation. The nonlinearity parameter estimation using an echographic approach would bring new modalities for imaging and diagnosis. However the echographic method for nonlinearity estimation is limited by two factors: the presence of speckles in the image and the focalization used during transmission, which concentrates the energy at one particular depth.

The objectives of this thesis work are developing novel approaches to reduce the speckle noise using original smoothing techniques and improving the nonlinearity parameter estimation in echo mode using new transmission-reception strategies.

Firstly, new speckle noise reduction approaches were investigated. The Thomson's multitaper approach was proposed, consisting in using several different orthogonal apodizations during beamforming. This method was combined to a coherent plane-wave compounding transmission-reception strategy improving the spatial resolution and the contrast while improving the frame rate.

In a second time, the nonlinearity parameter was estimated using a comparative method. The second-harmonic pressure field of a reference area was compared to the pressure field of an area where the nonlinearity parameter is unknown. However in echo-mode, the pressure field of the medium is unknown. It is assumed in this thesis work that the local pressure can be derived from envelope image local amplitude if the speckle noise is smoothed. The nonlinearity parameter estimation has been improved using plane-wave transmission and orthogonal apodizations compared to the use of a single focalization transmission.

## MOTS-CLES

Ultrasound, speckle noise, Thomson's multitaper, beamforming, plane wave, nonlinearity parameter,
CREANUIS

## INTITULE ET ADRESSE DE L'U.F.R. OU DU LABORATOIRE

Univeristé de Lyon, CREATIS; CNRS UMR 5220; Inserm U1044; INSA-Lyon; Université Lyon 1, 7 Avenue Jean Capelle, 69621 VILLEURBANNE, France.

Microelectronics Systems Desing Laboratory, Università di Firenze, Italy